The University of Hull

THE INTERACTION OF INFRA-RED LASER RADIATION WITH SOLID TARGETS.

being a Thesis submitted for the Degree of

Doctor of Philosophy

in the University of Hull

by

John Albert Sayers, B.Sc. (Kent), M.Sc. (CNAA).

August, 1981.

CONTENTS

LIST OF FIGURES

LIST OF SYMBOLS

a	coefficient as given on p63
A	atomic mass
b	coefficient as given on p6
B^*	as defined on p19
c	velocity of light
C	constant as given on p5
$\bar{C}$	mean specific heat
d	inter-electrode gap spacing
D	aperture diameter, diffusion coefficient
e	electronic charge
E	incident laser energy
E_{ion}	ion expansion energy
E_{out}	output energy
$\bar{g}$	averaged Gaunt factor
h	Planck's constant, enthalpy
$\hbar$	Planck's constant/2π
I	laser intensity, ionization potential
k	Boltzman's constant
K	absorption coefficient, wave number
L	thermal conduction length
m_e	electron mass
m_i	ion mass
M	resonator magnification factor, target mass
n_e	electron density
n_{ec}	critical density
n_i	ion density
N	total number of particles
p	pressure
p_{SF_6}	partial pressure of SF_6
P	laser power
P_{out}	output power
P_{tot}	total gas pressure
q	latent heat of vaporization

Q	total energy flux
r	partial pressure fluorine doner/partial pressure hydrocarbon
r_o	focal-spot radius
r_k	surface defect dimension
R	reflection coefficient, gas constant per unit mass
t_{ei}	equipartition time
t_p	laser pulse duration
T	temperature
T_e	electron temperature
T_i	ion temperature
T_s	surface temperature
u	particle velocity
U	internal energy, velocity
U_s	adiabatic sound velocity
v	velocity
V	volume
V_c	charging potential
V_d	discharge potential
V_{ion}	asymptotic ion expansion velocity
x	distance
$\bar{z}, \bar{Z}$	mean charge
Z	atomic number
Z_n	nuclear charge
α	$1 + T_i/ZT_e \approx 1 + 1/Z$ for $Z > 3$, thermal coupling coefficient
γ	adiabatic constant, partial pressure hydrocarbon/pressure (hydrocarbon + SF_6), molecular gas flow ratio: $CO_2/(CO_2 + N_2)$
ε_o	permittivity of free space
θ	focal-spot angular radius, temperature rise
κ	absorption coefficient
λ	wavelength
λ_D	Debye length
λ_p	penetration depth
Λ	Spitzer coefficient
μ	inverse bremsstrahlung coefficient

μ'	real refractive index of the plasma
ν	frequency
ν_c	electron-atom collision frequency
ζ	as given on p27
ρ	density
ρ_o	ambient gas density
ℓ	absorption length
τ	half width at half maximum, laser pulse duration
τ_b	breakdown time
ϕ	intensity of radiation, target irradiance
ϕ_o	incident flux
$\hat{\phi}_o$	peak intensity
ϕ_b	breakdown irradiance
ϕ_p	average irradiance
ϕ_T	breakdown threshold irradiance
ω	laser frequency ($rad.s^{-1}$)
ω_{BG}	Bohm-Gross frequency
ω_o	radiation frequency
ω_p	plasma frequency $(4\pi\ e^2\ n_{ec}\ /\ m)^{1/2}$
ω_{pe}	electron plasma wave frequency
Ω	solid angle

LIST OF PUBLICATIONS AND CONFERENCES RELATING TO THIS THESIS

1) "The Interaction of Nanosecond CO_2 laser Pulses with Solid Targets" Dyer P.E., Hill G.A., James D.J., Pert G.J., Ramsden S.A., Sayers J.A. and Skipper M.A. Institute of Physics Laser-Plasma Interactions Conference. Joint winter meeting of the Plasma Physics Group, Quantum Electronics Group and the University of Essex Computational Physics Group. University of Essex 3rd January, 1975.
2) "X-ray Production from CO_2 Laser Plasma" Dyer P.E., Sayers J.A. and Skipper M.A. 8th International Conference of Laser-Plasma Fusion. Warsaw, May 1975.
3) "Interaction of TEA CO_2 Laser Pulses with various Solid Targets" Dyer P.E., Ramsden S.A., Sayers J.A. and Skipper M.A. Second National Quantum Electronics Conference, Oxford, 3rd September, 1975.
4) "The Interaction of CO_2 Laser Radiation with various Solid Targets" Dyer P.E., Ramsden S.A., Sayers J.A. and Skipper M.A. J. Phys. D: Applied Physics, 9, 373-382,1181, 1976.
5) "The Interaction of HF Lasers with Gaseous and Solid Targets" Deka B., Dyer P.E., Ramsden S.A. and Sayers J.A. Invited Paper: IEEE International Conference on Plasma Science. May 23-25, 1977, Troy, New York.
6) "Plasma Production Experiments using a Pulsed HF Laser" Dyer P.E., Sayers J.A. and Salvetti G. Applied Physics Letters (American Journal) 32, 457-60, 1978.
7) "Investigation of Laser Supported Detonation Waves and Thermal Coupling using 2.8μm HF Laser Irradiated Metal Targets" Deka B.K., Dyer P.E. and Sayers J.A. Third International Symposium on Gas-Flow and Chemical Lasers. Marseille, France, September, 1980. Published in Supplement au Journal de Physique 41, C9, 75-79, 1980.

PREFACE

The pulsed HF chemical laser was discovered in 1966 by Deutsch. Early lasers had very low power outputs; it is only more recently that high power pulsed HF/DF lasers have emerged. This thesis is concerned with the development of a 10J HF laser in 1976 and subsequent interaction experiments. The high power HF/DF laser is a potentially valuable new device in view of its large gain coefficient and output intermediate in wavelength to the Nd:glass and CO_2 laser. Information on interactions at this wavelength has been lacking and the solid target interactions presented here help to remedy this deficiency. In addition, certain investigations were carried out using the CO_2 laser. These experiments aided direct comparison of the interaction data at the two infra-red wavelengths.

In the first chapter basic laser-plasma interaction theory is discussed. A vacuum environment is firstly considered, and emphasis is given to those models relevant to target irradiances available in our laboratories. Anomalous heating is only superficially treated as these studies were carried out below the non-linear thresholds. The theoretical variation of plasma parameters with laser wavelength is presented next, followed by a consideration of the gaseous environment. A brief review of pulsed HF laser design is given in chapter 2 followed by an account of our own design studies in the next chapter. Chapters 4 and 5 are devoted to laser-target interaction studies employing vacuum and gaseous environments respectively. The first published comprehensive vacuum interaction study, using the HF laser, is presented in chapter 4. The Z dependence of ion-velocity scaling, ion-number scaling, and reflection variation is recorded, together with the first x-ray temperature measurements at this wavelength. The gaseous environment is considered in the following chapter, where thermal coupling and laser supported detonation wave observations are given. Chapter 6 deals with vacuum interaction studies carried out at the CO_2 wavelength. The final chapters deal with the comparison of experimental results with theory, together with a general review of other published interaction investigations.

CHAPTER 1

LASER-PLASMA INTERACTION THEORY

1.1. Introduction

The interaction of laser radiation with solid targets in vacuum is discused. Simple modelling - the self-regulating and deflagration models - is introduced, together with a correction for thermal conduction. Instability heating is briefly treated and a section on wavelength scaling is used to establish a regime diagram.

Thermal coupling of laser radiation with solid targets in a gaseous environment is examined, together with the theory of laser supported detonation waves and gas breakdown.

Numerical values for the irradiance levels set out below have not been given. Such values are meaningless unless relevant parameters, including laser wavelength, pulse duration and shape, focal spot size, target material and nature of surface, are specified. In the case of low irradiances, simple thermal calculations employing known specific and latent heats, together with thermal diffusion constants can be employed to obtain rough values. For the medium and high regime, Fig. 1.5. can be employed.

1.2. Very Low Target Irradiances

Laser radiation incident on a plane opaque target under these conditions is partially reflected and partially absorbed by the process of electron excitation. The effect is to raise the temperature of the target material without change of state. Three-dimensional thermal diffusion occurs, but to a fair approximation conduction normal to the surface can be assumed for $r_o >> \lambda_p$, where r_o is the focal-spot radius and λ_p is the penetration depth. The rate of change of surface temperature, $\dot{T}_s$, has been calculated to initially increase rapidly[1] due to the surface optical properties being a function of temperature. For $\dot{T}_s$ large, shock waves are generated.

1.3. Low Target Irradiances

At slightly higher irradiances changes of state occur. At the melting point the reflectivity suddenly decreases. Liquid flow during the laser pulse duration can be ignored, although the effect of melting can be observed from the wave paterns produced around many target craters. Of far greater importance is the change into the vapour state. The vapour may start to strongly absorb radiation. Hughes[2] has pointed out that the latent heat of vapourization is much greater than the latent heat of fusion, and that the boiling point is drastically changed by the high radiation and ablation pressures.

The transition from the vapour into the plasma state is also acompanied by a large latent heat. Ionization occurs by direct excitation, collisional excitation and multi-photon processes. The free electrons are now heated by the process of inverse bremsstrahlung. Multi-photon ionization involves the excitation of a bound electron by two or more photons, a process employing virtual intermediate states, as permitted by the uncertainty principle. Weingartshofer et al[3] have carried out single particle collision experiments to directly measure the differential cross-sections for multi-photon inverse bremsstrahlung. Theoretical expressions have been developed to treat the more complex multi-particle situation of inverse bremsstrahlung absorption in an intense laser field under laser produced plasma conditions[4]. The high atomic density in the solid and vapour phases favours a large Stark broadening and depresses the ionization limit.

1.4. Medium Target Irradiances

At still higher irradiances the plasma state is rapidly produced. Radiation is now absorbed by the plasma, which is heated and fans out into the vacuum. However, this plasma becomes optically thick, resulting in a decrease in the vapour and ion production at the target surface. This in turn decreases the optical thickness and

so increases the production. The process is thus self-regulating. A shock wave is generated by the ablation pressure. The Self-Regulating (S-R) model has been developed to deal with this situation.

1.5. High Target Irradiances

At high irradiances the absorption occurs in a thin region near to the critical density, n_{ec}. The one-dimensional situation is a deflagration wave-front following the shock wave-front. The Deflagration wave (DW) model is used under these conditions.

1.6. Very High Target Irradiances

At very high irradiances a number of non-linear effects are important. Resonant absorption is a major process. Instabilities greatly effect the plasma reflectivity and energy coupling.

1.7. The Self-Regulating Model

1.7.1. General Principles

Various treatments of this model have been presented[5-11]. Here we shall follow the approach of Puell. This model is particularly relevant to the experimental results of chapters 4 and 6, and so the treatment will be fairly detailed.

At high irradiances the initial plasma production time ($\lesssim 10^{-10}$s) is very much shorter than the laser pulse duration, and so may be neglected. Puell makes the following four assumptions :-

i) The plasma is divided into three regions, as shown schematically in Fig.1.1. Region I represents the unperturbed solid, region II one-dimensional plasma flow, and region III a fan-out into the vacuum. Region II extends to a good approximation to a distance r_o from the target surface[5]. This region is the dominant plasma heating zone, as the density and the strength of the radiation field is rapidly decreasing in the subsequent region. The energy transfered by the

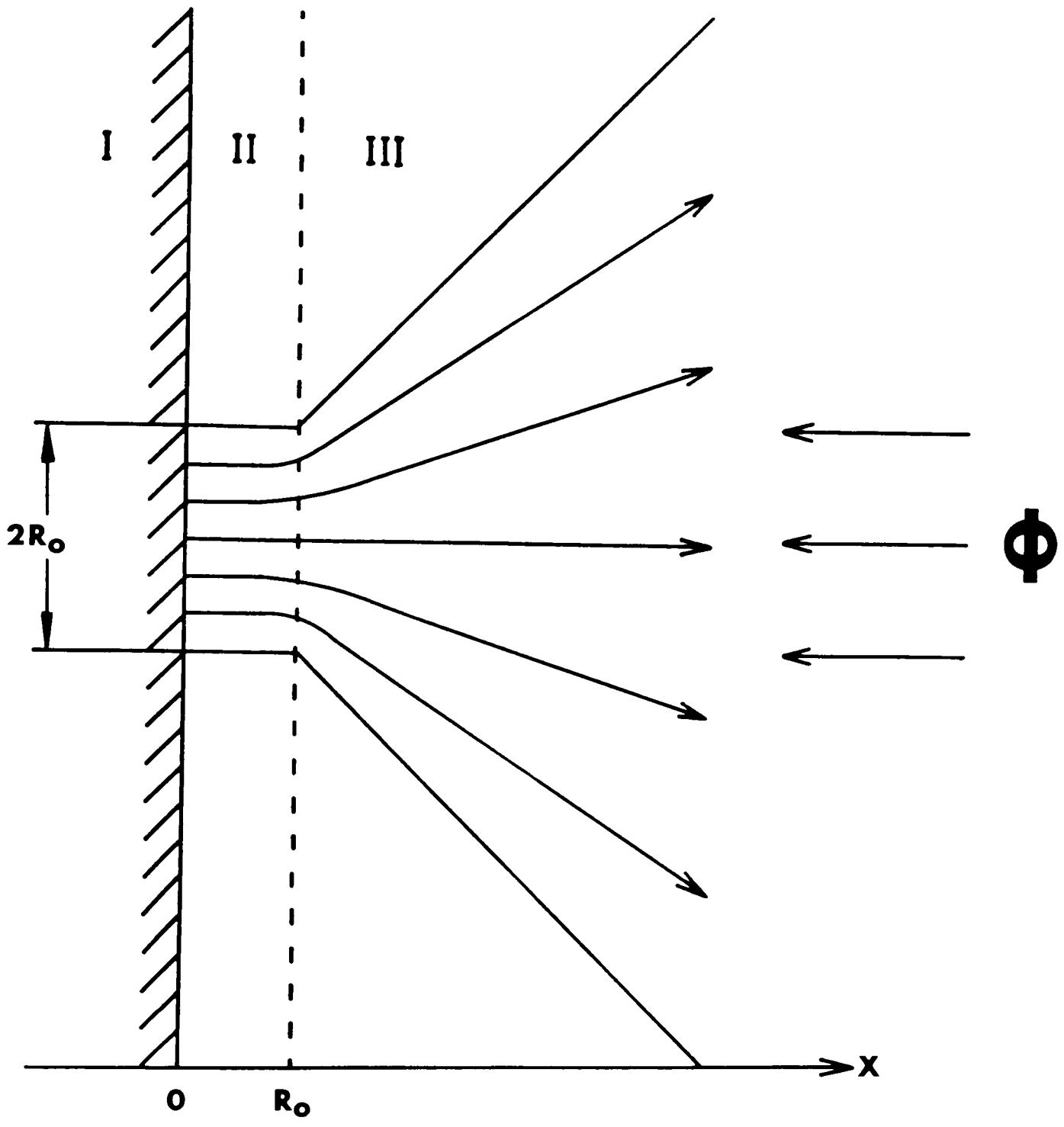

Fig. 1.1. Schematic drawing of the Plasma flow (after Puell 1970).

I Undisturbed target

II One-dimensional flow

III Three-dimensional flow.

shock wave advancing into region I can be neglected as the plasma density is very much less than the target density.

ii) A steady-state situation has been obtained. This is true if the ions and electrons are in the heating zone for periods less than the laser pulse duration. For nanosecond pulses this situation is achieved, as shown in the discussion on the model's validity.

iii) The absorption coefficient, K, given by Dawson and Oberman[12] is used for the case $n_e < n_{ec}$ sothat the term $(1 - n_e/n_{ec})^{-1/2}$ may be neglected :-

$$K = \frac{32\,\pi^3\,Z^2\,n_e\,n_i\,e^6\,\ln\Lambda}{3\,c\,\omega^2\,(2\pi\,m_e\,k\,T_e)^{3/2}}\,(1 - n_e/n_{ec})^{-1/2} \qquad n_e < n_{ec}$$

$$\simeq \frac{C\,Z\,n_e^2}{(k\,T_e)^{3/2}}\,(1 - n_e/n_{ec})^{-1/2}$$

$$\simeq \frac{C\,Z\,n_e^2}{(k\,T_e)^{3/2}} \qquad \text{.....(1.1a)}$$

$$\text{and } K = (2\omega/c)\,(n_e/n_{ec} - 1)^{1/2} \qquad n_e > n_{ec} \qquad \text{.....(1.1b)}$$

where n_e, $k\,T_e$, and m_e are the density, temperature, and mass of the electrons, n_i and Z are the density and charge of the ions, c is the velocity of light, C is a constant given from the above, n_{ec} is the critical electron density given by the plasma frequency, $\omega = (4\pi\,e^2\,n_{ec}/m_e)^{1/2}$ equalling the radiation frequency, and Λ is the

Spitzer coefficient[14]. For $n_e > n_{ec}$ K becomes very large.

iv) Thermal conduction and radiation losses in the plasma are neglected, as is the plasma ionization energy.

The continuity condition at the boundary II/III in the steady-state gives us that the radiation flux crossing the boundary must equal the plasma energy flow in the reverse direction. The energy of a single particle is the sum of its enthalpy h and kinetic energy $\frac{1}{2}mu^2$ sothat the continuity equation becomes :-

$$\phi_1 = n_{e1}\, u_{e1}\, (h_{e1} + \tfrac{1}{2}m_e\, u_{e1}^2) + n_{i1}\, u_{i1}\, (h_{i1} + \tfrac{1}{2}m_i\, u_{i1}^2) \quad .....(1.2)$$

where ϕ is the flux and 1 indicates the boundary II/III.

For an ideal, monatomic gas, kinetic theory gives us that the internal energy, U = (3/2) kT and pV = kT, (N = 1), sothat h = U + pV = (5/2) kT. As the plasma is neutral, $u_e = u_i = u$ and $n_e = Zn_i = n$. Also, $m_e << m_i$ sothat (1.2) becomes :-

$$\phi_1 = n_1\, u_1\, (h_{e1} + h_{i1}/Z + \tfrac{1}{2}u_1^2\, m_i/Z) \quad .....(1.3)$$

The ion temperature must lie between 0 and T_e, thus (1.3) can be written :-

$$\phi_1 = n_1\, u_1\, (5\alpha\, kT_1/2 + m_i\, u_1^2/2Z) \quad .....(1.4)$$

where α is between 1 and (1 + 1/Z).

1.7.2. Electron Temperature

The mass density = $n_i\, m_i = \rho$, as $m_e << m_i$.
Ideal gas equation, pV = N k T gives :-

$$p = (n_i + Z\, n_i)\, k\, T \quad \text{as } n_e = n_i$$

$$= Z\, \alpha\, n_i\, k\, T$$

but u_s, the adiabatic sound velocity, is given by :-

$$u_s^2 = \gamma\left(\frac{\partial p}{\partial \rho}\right)_T \qquad .....(1.5)$$

For a monatomic gas $\gamma = 5/3$, therefore,

$$u_s = \{ (5\ \alpha\ Z\ k\ T_1) / (3\ m_i) \}^{1/2} \qquad .....(1.6)$$

The plasma velocity in region II is subsonic. The expansion into the vacuum results in a supersonic flow. At the boundary we can take $u_1 = u_s$.

The absorption coefficient, K, as given in (1.1a) is not constant as radiation moves from the boundary towards the target. At any point x in region II we therefore have :-

$$\phi_x = \phi_1 \exp - \int_x^{r_o} K\ dx \qquad .....(1.7)$$

using the continuity equation :-

$$n\ u = n_1\ u_1 = n_x\ u_x = \text{constant} \qquad .....(1.8)$$

we get, $n^2 = n_1^2\ u_1^2\ u^{-2}$

so, $$\phi_x = \phi_1 \exp \{ - \int_x^{r_o} n_1^2\ u_1^2\ C\ Z\ (kT)^{-3/2}\ u^{-2}\ dx \} \qquad .....(1.9a)$$

$$= n_1\ u_1\ \tfrac{1}{2}(5\ \alpha\ k\ T_x + m_i\ u_x^2\ Z^{-1}) \qquad .....(1.9b)$$

from (1.4).

In order to obtain an expression for n_1 the approximation is taken that in region II $u = u_s$. Puell explains that although the flow velocity is overestimated, resulting in less energy being

available for the thermal contribution, the density is also underestimated by the equation of continuity, (1.8). K is proportional to $n_e^2 (k\ T_e)^{-3/2}$, thus these effects tend to cancel.

From (1.6) :-

$$u_s^2 = u_1^2 = (5\ \alpha\ Z\ k\ T_1)/(3\ m_i) \qquad .....(1.10a)$$

$$u^2 = (5\ \alpha\ Z\ k\ T)/(3\ m_i) \qquad .....(1.10b)$$

$$u_x^2 = (5\ \alpha\ Z\ k\ T_x)/(3\ m_i) \qquad .....(1.10c)$$

$$\frac{u_1^2}{u^2} = \frac{T_1}{T} \qquad .....(1.11)$$

Therefore, (1.9a) may be rewritten as :-

$$\phi_x = \phi_1 \exp \{ - \int_x^{r_o} n_1^2\ C\ Z\ k\ T_1\ (k\ T)^{-5/2} \quad dx \qquad .....(1.12)$$

Substituting for ϕ_x and ϕ from (1.9b) and (1.4) :-

$$n_1\ u_1\ \tfrac{1}{2}(5\ \alpha\ k\ T_x + m_i\ u_x^2/Z) = n_1\ u_1\ \tfrac{1}{2}(5\ \alpha\ k\ T_1 + m_i\ u_1^2/Z)$$

$$\exp \{ - \int_x^{r_o} n_1^2\ C\ Z\ k\ T_1\ (k\ T)^{-5/2}\ dx \}$$

$$.....(1.13)$$

Substituting for u_1 and u_x from (1.10a), (1.10c) and simplifying we obtain :-

$$k\ T_x = k\ T_1 \exp \{ - \int_x^{r_o} n_1^2\ C\ Z\ k\ T_1\ (k\ T)^{-5/2}\ dx \} \qquad .....(1.14)$$

On differentiating this expression with respect to x and using the boundary conditions :-

$$k\ T_x = 0, \qquad x = 0$$

$$k\ T_x = k\ T_1, \quad x = r_o$$

we get,

$$\frac{d\ (k\ T_x)}{dx} = k\ T_x\ n_1^2\ C\ Z\ k\ T_1\ (k\ T)^{-5/2}$$

$$= n_1^2\ C\ Z\ k\ T_1\ (k\ T)^{-3/2} \qquad .....(1.15)$$

$$\text{therefore,} \quad \frac{2}{5}\ (k\ T)^{5/2} = n_1^2\ C\ Z\ k\ T_1\ x \qquad .....(1.16)$$

$$\frac{2}{5}\ (k\ T_1)^{3/2} = n_1^2\ C\ Z\ r_o \qquad .....(1.17)$$

$$n_1 = (k\ T_1)^{3/4}\ (2/5\ C\ Z\ r_o)^{1/2} \qquad .....(1.18)$$

Considering region III, the plasma density is decreasing into the plasma by an inverse square law to a good approximation :-

$$n = n_1\ (r_o/x)^2 \qquad .....(1.19)$$

(The radius of the plasma is x at a distance x from target).

For an ideal gas, $P_1 V_1 / T_1 = P_2 V_2 / T_2$
For a reversible adiabatic expansion, $P_1 V_1^{\gamma} = P_2 V_2^{\gamma}$
combining :-
$T_1 / T_2 = (V_2 / V_1)^{\gamma-1}$
sothat the electron temperature is given by :-

$$(k T) / (k T_1) = (n / n_1)^{2/3} \qquad .....(1.20)$$

Substituting from (1.20) into (1.1a) and using (1.19) :-

$$K = C Z n_1^2 (r_o / x)^2 (k T_1)^{3/2} \qquad .....(1.21)$$

Expressing ϕ_1 in terms of the incident flux ϕ_o :-

$$\phi_1 = \phi_o \exp - \int_{r_o}^{\infty} C Z n_1^2 (r_o/x)^2 (k T_1)^{-3/2} \quad dx$$

$$= \phi_o \exp \{ - C Z n_1^2 r_o (k T_1)^{-3/2} \} \qquad .....(1.22)$$

Substituting (1.18) :-

$$\phi_1 = \phi_o \exp | - C Z r_o (k T_1)^{-3/2} \{ (k T_1)^{3/4} 2^{1/2} (5C Z r_o)^{-1/2} \}^2 |$$

$$= \phi_o \exp (-2/5)$$

therefore, $\phi_1 = 0.67 \phi_o$ .....(1.23)

Puell points out that although a significant fraction of the radiation is absorbed in region III, this occurs over a large distance compared with r_o, sothat it is reasonable to consider an adiabatic expansion.

Substituting the expressions for u_1, n_1 and ϕ_1 (1.6), (1.18), (1.23) into (1.4) we get :-

$$\frac{2}{3}\phi_o = (k\,T_1)^{3/4}\,\{\,2/(5C\,Z\,r_o)\,\}^{1/2}\,\{\,5\alpha\,Z\,k\,T_1\,(3\,m_i)\,\}^{1/2}$$

$$\{\,5\alpha\,k\,T_1\,/\,2\;+\;(m_i\,5\alpha\,Z\,k\,T_1)\,/\,(2Z\,3m_i)\,\} \qquad .....(1.24)$$

simplifying :-

$$k\,T_1 = \alpha^{-2/3}\,(3m_i\,C\,r_o\,/\,50)^{2/9}\,\phi_o^{4/9} \qquad .....(1.25a)$$

This final expression for the maximum electron temperature is in agreement with results obtained by other authors[14,15]. From (1.1a), $C \propto \omega^{-2}$ i.e.

$$k\,T_1 \propto \lambda^{4/9} \qquad .....(1.25b)$$

1.7.3. Ion Temperature

Shkarofsky et al[16] give an expression for the equipartition time, t_{ei}, for the ions in the plasma to achieve the electron temperature. For equipartition to occur, the ions must stay in the heating zone for a period at least equal to this time. Equating these two we can define the limiting case :-

$$t_{ei} \lesssim r_o / u_1$$

Substituting for n_e and u_1 we obtain :-

$$k\ T_{th} \leq 5 \times 10^{-19} \{ r_o\ Z\ (Z + 1)\ /\ (C\ A) \}^{2/5} \quad eV \qquad .....(1.26a)$$

$$so, \quad \phi_{th} < 5 \times 10^{-56} \{ r_o^2\ (Z + 1)^{12}\ /\ (Z^3\ A^7\ C^7) \}^{1/5} \qquad .....(1.26b)$$

where, T_{th} and ϕ_{th} are the limiting temperature and radiant flux ($W.cm^{-2}$), and A is the atomic mass of the ions.

1.7.4. Total Number of Particles

If N is the total number of particles produced, the particle flux is given by :-

$$\frac{dN}{dt} = n_1\ u_1\ (\pi\ r_o^2)$$

From (1.6), (1.18), (1.25) we obtain :-

$$\frac{1}{\pi\ r_o^2}\ \frac{dN}{dt} = n_1\ u_1 = \alpha^{-1/3} \{ 2/(3m_i\ C\ r_o) \}^{2/9}\ (\phi_o/5)^{5/9} \qquad .....(1.27)$$

Assuming a Gaussian laser pulse of peak intensity $\hat{\phi}_o$ and FWHM of 2τ Puell integrates this expression to obtain :-

$$N = \pi\ r_o^2\ \alpha^{-1/3}\ \tau\ \{ 9\pi/(20\ ln2) \}^{1/2}\ \{ 2/(3m_i\ C\ r_o) \}^{2/9}\ (\hat{\phi}_o/5)^{5/9}$$

$$.....(1.28)$$

This reduces to :-

$$N = 1.6768\ (m_i\ C)^{-2/9}\ r_o^{16/9}\ \alpha^{-1/3}\ \tau\ \phi_o^{5/9} \qquad .....(1.29a)$$

and from (1.1a),

$$N \propto \lambda^{-4/9} \qquad .....(1.29b)$$

1.7.5. Expansion Energy

At large distances from the target the ions carry all of the energy that was absorbed by the particles during the heating phase. Here we are neglecting the mass of the electrons and assuming a steady-state situation. Thus, the ion expansion energy,

$$E_{ion} = \phi_o\ /\ (n_i\ u),$$

where, $n_i\ u$ is the ion flux leaving the target.
As $n = n_e = Z\ n_i$ and $n\ u = n_1\ u_1$:-

$$E_{ion} = Z\ \phi_o\ /\ (n_1\ u_1) \qquad .....(1.30)$$

Substituting (1.25) and (1.27) into (1.30) :-

$$E_{ion} = 5\ \alpha\ Z\ k\ T_1 = 5\ Z\ \alpha^{1/3}\ (3\ m_i\ C\ r_o/50)^{2/9}\ \phi_o^{4/9} \qquad .....(1.31a)$$

from (1.1a), $E_{ion} \sim \lambda^{2/9}$ .....(1.31b)

therefore, $V \sim \lambda^{1/9}$ .....(1.31c)

1.7.6. Discussion on the Validity of this Model

a) Steady-State

The steady-state approximation will be valid if the laser pulse duration τ is large compared with the heating time t'. Using (1.6) and (1.25) :-

$$\tau > t' \simeq r_o^{8/9} \alpha^{-1/6} (3 m_i / 5 Z)^{1/2} (50 / (3 m_i C))^{1/9} \phi_o^{-2/9} \quad .....(1.32)$$

For typical values this limits the validity to pulses longer than about 1ns.

b) The Absorption Coefficient

The expression for K that was used is valid for $n_e < n_{ec}$. In this limiting case, from (1.18) and (1.25) the limiting value for the flux, ϕ_o' , is given by :-

$$\phi_o < \phi_o' = n_{ec}^3 \, 25 \, C \, r_o \{ 5 \alpha^3 Z^3 / (12 m_i) \}^{1/2} \quad .....(1.33)$$

Care must be taken, especially for CO_2 laser-produced plasmas, that this condition is met.

The above calculations assume that the thermal conduction length is negligible compared with the absorption length for the radiation. This situation is termed a thin thermal conduction zone. For a thick thermal conduction zone the thermal absorption length is comparable with the absorption length. The scaling laws are modified to give :-

$$T_e \propto p^{1/6} A^{-1/6} Z^{-1/2} \alpha^{1/4} \lambda^{1/3} \quad .....(1.34a)$$

$$\rho \propto p^{-1/12} A^{7/12} Z^{-3/4} \alpha^{1/8} \lambda^{-11/6} \quad .....(1.34b)$$

where, p is the laser power and ρ the plasma density.

The thermal conduction length, L, is the distance over which the conduction energy flux is comparable with the convection flux[17].

$$L = 2.07 \times 10^{15} A^{1/2} T_e^2 (\alpha Z)^{-3/2} (n_{ec} \ln\Lambda)^{-1} \quad .....(1.35)$$

where, T_e is in eV.

Absorption is important over lengths, ℓ, such that :-

$$Q / \ell \sim \mu I \quad .....(1.36)$$

where, Q = total energy flux, μ = absorption coefficient, I = laser intensity. In the steady state the outgoing energy flux equals the incoming laser flux, i.e. $Q \sim I$. Therefore,

$$\ell \sim 1 / \mu \quad .....(1.37)$$

The thick self-regulating regime is not realised in the experiments presented here, and so will not be further considered. The only possible exception to this statement is with lead, irradiated with CO_2 laser radiation. However, in this extreme situation the simple model is likely to break down anyway; for heavy targets the failure to include the ionization energy is a serious omission.

1.8. The Deflagration Wave Model

1.8.1. General Principles

If the target irradiance is increased beyond the self-regulating situation, the rapidly expanding plasma becomes transparent to the laser radiation. The heating zone moves into the target as a deflagration wave (D-W) preceded by a shock front. This regime was initially investigated by Fauquignon and Floux[18], and Bobin[19]. These authors developed a one-dimensional continuum hydrodynamic theory, which has been extended by Pert[20] to include three-dimensional flow.

1.8.2. Detonation Wave Theory

Consider a laser-driven shock-wave in an ideal gas, moving with velocity U in the laboratory reference frame. For convenience, it is conventional to use the U = 0 frame of reference, Fig.1.2.

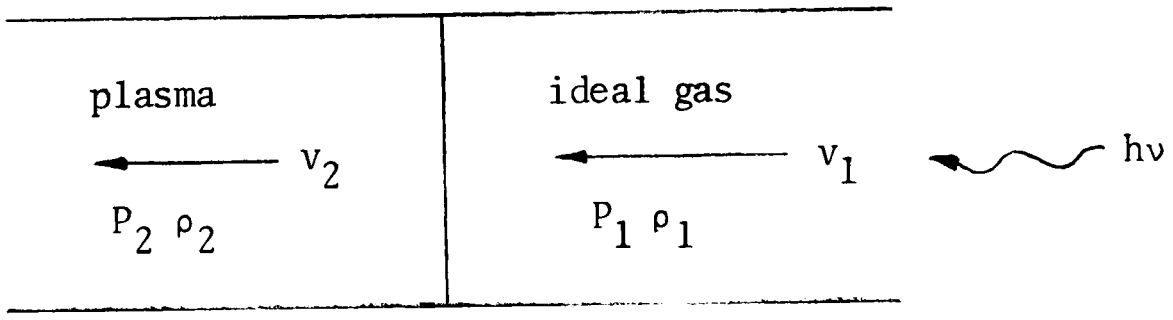

Fig.1.2. Notation for a laser-driven shock wave in an ideal gas.

Thus, the velocity of the ideal undisturbed gas $v_1 = -U$.

The equation of state and boundary conservation laws can be combined[21] to give the Hugoniot detonation equation :-

$$\frac{P_2}{P_1} = \frac{\frac{(\gamma + 1)}{(\gamma - 1)} - \frac{\rho_1}{\rho_2} + 2Q\frac{\rho_1}{P_1}}{\frac{(\gamma + 1)}{(\gamma - 1)}\frac{\rho_1}{\rho_2} - 1} \qquad \text{.....(1.38)}$$

where Q is the energy supplied to unit mass of gas on traversing the front. This equation can be plotted, Fig.1.3., as (P_2/P_1) vs. (ρ_1/ρ_2) for Q constant.

The continuity conditions lead to an expression for the slope of v_1 :-

$$v_1^2 = \frac{(P_2/P_1) - 1}{1 - (\rho_1/\rho_2)} (P_1/\rho_1) \qquad .....(1.39)$$

therefore,

$$\frac{d(P_2/P_1)}{d(\rho_1/\rho_2)} = - \frac{\rho_1 v_1^2}{P_1} \qquad .....(1.40)$$

Thus, a given value of the shock front is indicated in Fig.1.3. by a line passing through 1,1 (the undisturbed gas) with slope given by (1.40). In general there are two solutions. A unique situation occurs at the tangent to the Hugoniot detonation curve. This is termed the Chapman-Jouguet solution. Jouguet showed that at this point the velocity of the detonation wave relative to the heated matter behind the wave coincides with the local velocity of sound $(\gamma P_1 / \rho_2)^{1/2}$. It can also be shown that the Chapman-Jouguet condition is necessary for the steady-state[22].

1.8.3. Deflagration Wave Situation

For the detonation wave $(P_2 / P_1) > 1$. For the deflagration wave the reverse is true; the relevant Hugoniot curve is shown in Fig.1.4. The Chapman-Jouguet point is the maximum deflagration velocity in the frame of reference in which the solid is at rest (this takes into account the preceding shock wave).

Bobin[19] shows that the condition for maximum heating of a

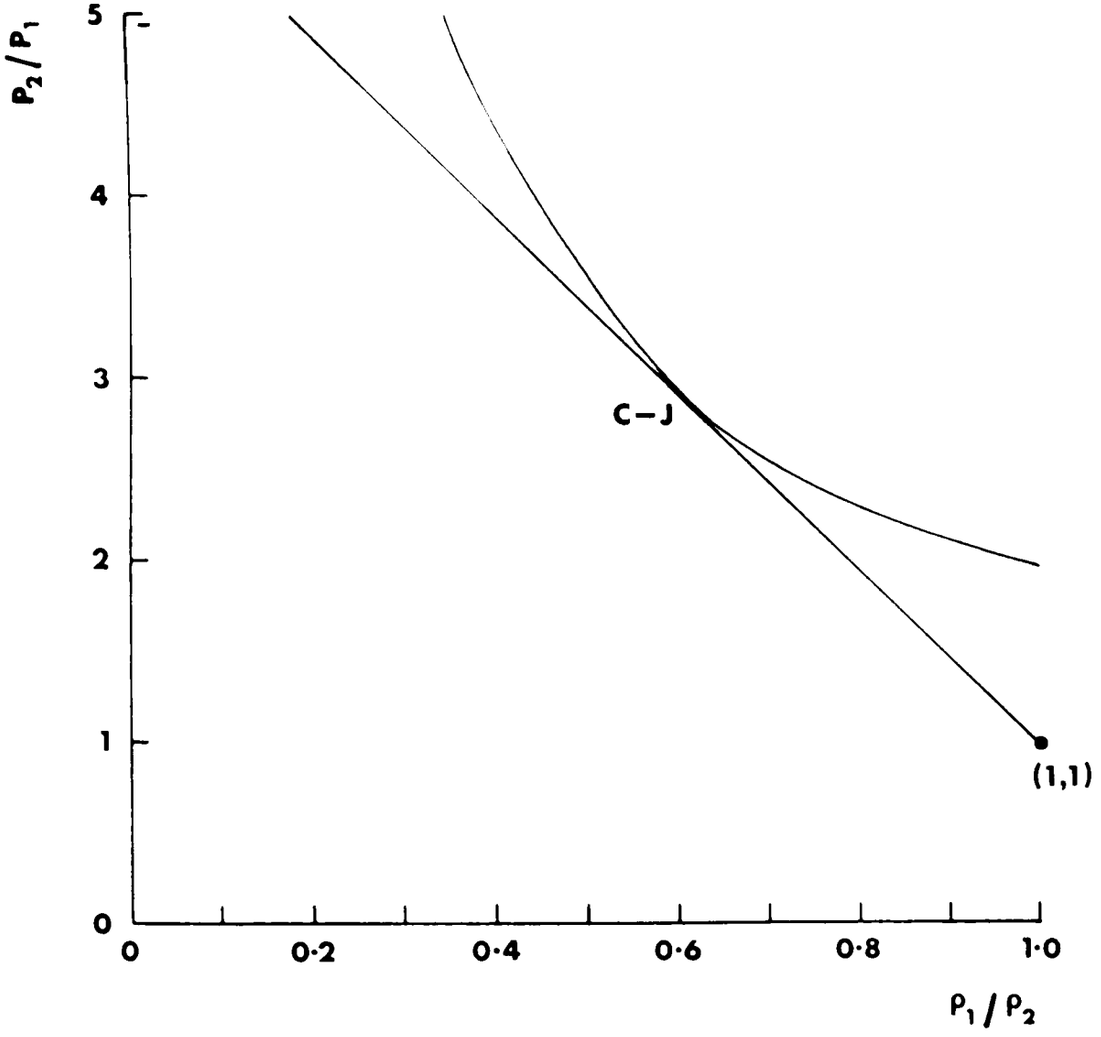

Fig. 1.3. Hugoniot detonation curve (Q = constant), indicating the Chapman – Jouguet point.

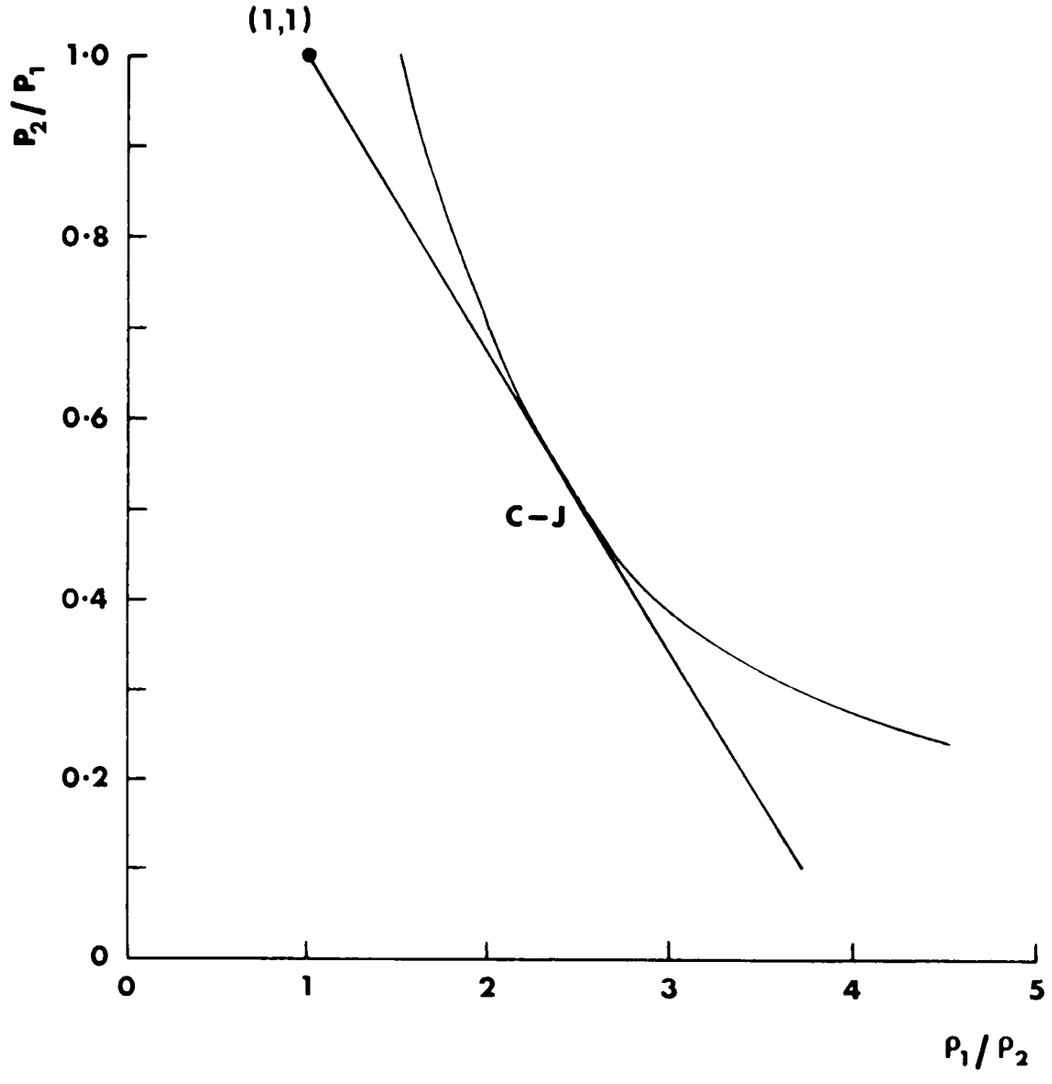

Fig. 1.4. Hugoniot deflagration curve, indicating the Chapman – Jouguet point.

freely expanding plasma by linear absorption of laser radiation occurs in the region of the cut-off density. For this situation, he derived, from an extension of self-regulating equations, that the peak temperature,

$$T \propto (m_i / 3k)\ (\phi\ \nu^2)^{2/3} \qquad .....(1.41)$$

He develops the model, taking the boundary conservation laws for mass, momentum and energy. Viscosity and thermal conduction corrections are applied, the former being fairly insignificant.

For the expanding isothermal plasma, the scaling laws given by Fauquignon and Floux are unchanged when the flow is considered in three dimensions :-

$$T_e \propto \alpha^{-1}\ Z^{-1/3}\ A^{1/3}\ \lambda^{4/3}\ \phi^{2/3} \qquad (\rho \simeq \rho_c) \qquad .....(1.42)$$

where, $\alpha = 1 + T_i/ZT_e \simeq 1 + 1/Z \qquad (Z > 3).$

$$V \propto (\lambda^2\ \phi)^{1/3} \qquad .....(1.43)$$

When thermal conduction is considered, these laws are only valid if the conduction length is much smaller than the focal spot radius :- $L << r_o$. This situation is termed a thin thermal conduction zone. For a thick thermal conduction zone $L >> r_o$, and thermal diffusion will dominate[17]. Bobin's relations may be modified to give :-

$$T_e \propto P^{2/11}\ A^{-7/11}\ Z\ \alpha^{3/11}\ \lambda^{-4/11} \qquad (\rho \simeq \rho_c,\ L >> r_o) \qquad .....(1.44)$$

where P is the total laser power.

1.8.4. Validity of the Deflagration-Wave Model

Bobin obtains an expression for the minimum pulse duration required if the deflagration-wave approach is to be valid :-

$$\tau_D = (4/5)\ \{(\gamma - 1)/(5\gamma - 1)\}\ (m_i/k)^2\ B^*\ (T_2^{3/2})/\rho_c \qquad .....(1.45)$$

where,

$$B^* = 1.98 \times 10^{-7}\ (Z\ /\ \nu^2\ m_i^2)\ (3k\ /\ m_i)^{3/2}$$

Z = mean plasma ion charge,
m_i = ion mass,
ν = laser frequency.

For the relatively long pulses encountered in the CO_2 and HF experiments presented here this condition is fulfilled.

1.9. Anomalous Heating of a Laser-Produced Plasma

1.9.1. Introduction

Anomalous absorption is a term applied to the absorption of radiation by instability and non-linear processes[23]. In the electron-ion decay instability, the e-m wave decays into a Langmuir (high frequency electron) wave and an ion-acoustic wave :-

photon → plasmon + ion-acoustic phonon.

If only two Langmuir waves are produced, the decay is termed the electron-electron instability :-

photon → plasmon + plasmon.

In both these processes, wave vectors and energies must be conserved. The plasma waves are initially produced by non-linear forces. Collisional and Landau damping converts these plasma wave energies into heat.

Anomalous backscatter of radiation typically occurs by creating a Langmuir or an ion-acoustic wave. These processes are termed stimulated Raman or stimulated Brillouin scattering (SRS or SBS) respectively. Very little heating results.

The instability threshold, growth rate and saturation point are important factors which vary with the radiation frequency. Non-linear coupling of Langmuir and ion-acoustic waves may also occur if their amplitudes are large enough.

Nishikawa[25] predicts two types of instability that occur when the radiation frequency is in the region of the plasma frequency. These are the oscillating two-stream and the parametric decay instabilities.

1.9.2. The Oscillating Two-Stream Instability

This occurs when the radiation frequency is less than the Bohm-Gross frequency[2] :-

$$\omega_o < \omega_{BG} \qquad \text{.....(1.46)}$$

where, $\omega_{BG} = \omega_{pe} (1 + 3K^2 \lambda_D^2)^{1/2}$

and, $\lambda_D = \{ (k T_e \varepsilon_o) / (n_e e^2) \}^{1/2}$

$\omega_{pe} = (n_e e^2) / (m_e \varepsilon_o)$

k = Boltzmann's constant
K = wavenumber
ε_o = permittivity of free space
λ_D = Debye length
ω_{pe} = electron plasma wave frequency.

n_i and n_e distributions are usually directly coupled. However, in the electric field of the laser radiation the electron is given a high frequency component about the ion distribution. When the ion frequency is zero we have the oscillating two-stream instability.

1.9.3. The Parametric Decay Instability

This occurs when the radiation frequency is greater than the Bohm-Gross frequency :-

$$\omega_o > \omega_{BG} \qquad .....(1.47)$$

A plasmon and an ion-acoustic phonon are produced from the decay of the pump photon.

1.9.4. Thresholds

Yamanaka[24] estimates the thresholds at 1.06μm of the parametric and oscillating two-stream instabilities in the case of a deuterium plasma. Threshold equations are given by Nishikawa[25]. Dyer[26] indicates the thresholds for 10.6μm, together with the transitions from self-regulating to deflagration-wave at both these wavelengths (deuterium target, r_o = 100μm). For $10 \lesssim T \lesssim 10^3$ eV the 10.6μm threshold is $\sim 10^{10} - 10^{11}$ W.cm^{-2}. By comparison, at 1.06μm and $T \sim 10^2$ eV the threshold is $\sim 10^{14}$ W.cm^{-2}. Dick and Pepin[27] plot the parametric decay instability thresholds for Al and $(CH_2)_n$ at 10.6μm. It can be seen that for low ($\lesssim 10^2$ eV) T_e the threshold increases with Z, but at high ($\gtrsim 10^2$ eV) T_e the reverse is true. They observed enhanced parametric absorption with Al ($> 3 \times 10^{10}$ W.cm^{-2}) and $(CH_2)_n$ ($> 10^{11}$ W.cm^{-2}). This was deduced, for example, from the low reflectivity, ion-velocity scaling, electron temperatures and a high energy x-ray component. High energy ions from a CO_2 laser-produced plasma were observed by Ehler[28] using a $(CH_2)_n$ target at a threshold of 5×10^{12} W.cm^{-2}. The origin of these fast

ions was considered to be a steep electron-density gradient. The ion energy scaling was $\sim \phi^{2/3}$, in agreement with theory, in contrast to the $\sim \phi^{4/9}$ scaling from a thermalized plasma. These suprathermal ions were resolved into their charge species with the time of flight detector. The ion angular distribution was also non-typical of a thermalized plasma. Fabre et al[29], also using a CO_2 laser, observed anomalous processes. They observed the onset of the parametric decay instability. In addition, the analysis of the backscattered radiation indicated SBS and other weaker non-linear processes.

1.10. Wavelength Scaling

1.10.1. Introduction

In this section we are concerned with the variation of relevant parameters with incident laser wavelength. These parameters include the focal spot size, flow regime, plasma temperature, ion expansion velocity, total ion number, the absorption coefficient and electron energy distribution. The instability thresholds are given in the previous section. If all of the parameters are to be included in a single theory, the resulting complexity requires the use of computer modelling.

1.10.2. The Focal Spot Size

In the case of diffraction-limited operation, the sine of the focal-spot angular radius, θ, is directly proportional to λ/D, where D is the aperture diameter. Thus, to maximise target irradiance for a given output power, a low wavelength and a large diameter beam is required. Gas lasers tend to have a large value of D, although the CO_2 laser also has a relatively large wavelength.

1.10.3. The Regime Diagram

The boundaries between the flow regimes discused in the previous sections are given in Fig.1.5. The figure indicates the transitions corresponding to Nd:glass, HF and CO_2 laser radiation with a hydrogen

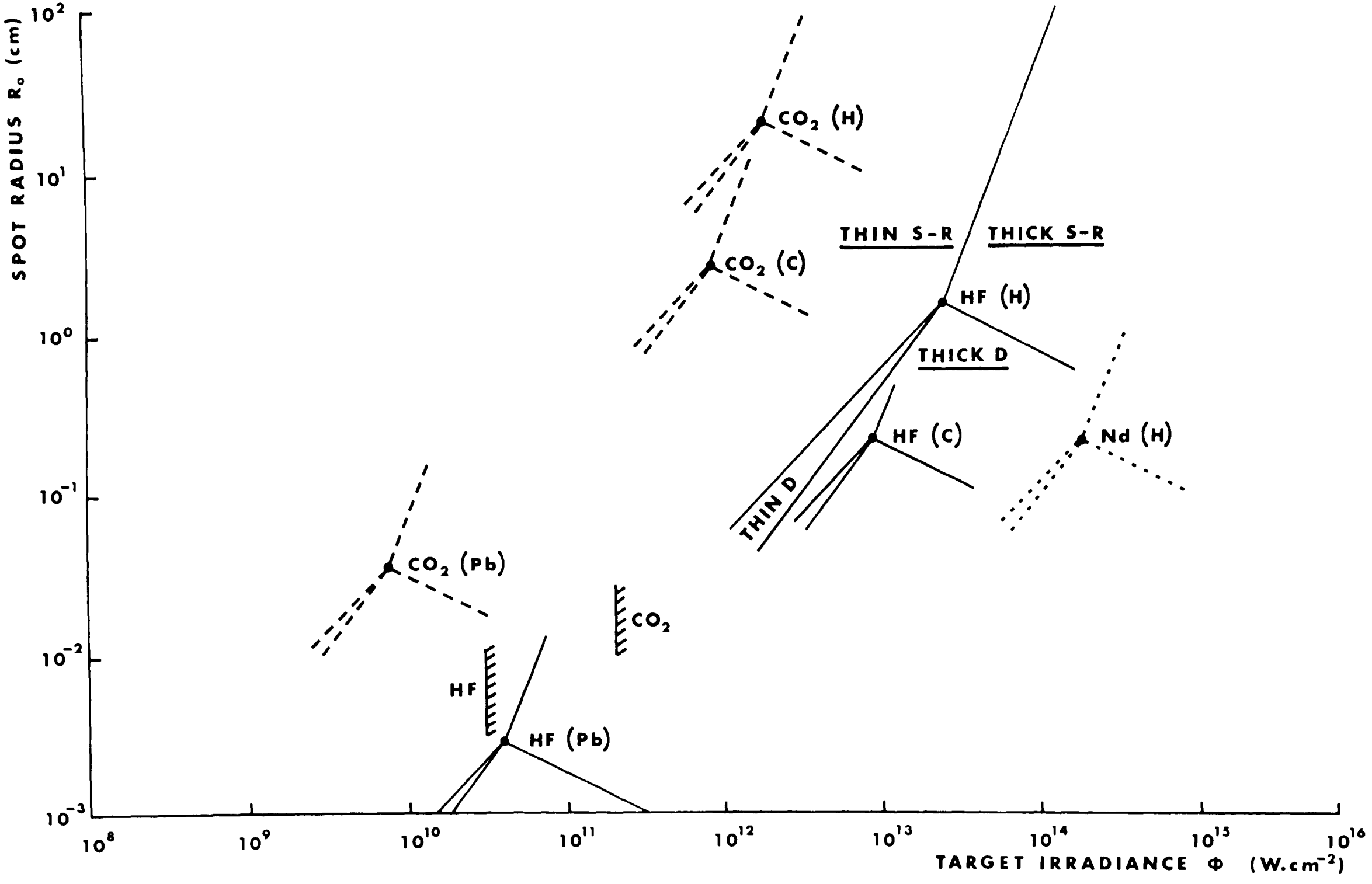

Fig.1.5. Regime diagram calculated assuming $\ln\Lambda = 5$ and for Nd:glass: $\bar{Z}, \alpha = 1$, HF: $\Phi = 3 \times 10^{10}$ W.cm^{-2}, CO_2: $\Phi = 8 \times 10^{10}$ W.cm^{-2}

target, HF and CO_2 with carbon and lead targets. The regime diagram is calculated assuming $\ln\Lambda = 5$. As $\bar{z}$ and α for HF and CO_2 were evaluated at the given irradiances, the diagram is only accurate for this situation, which corresponds to typical high irradiance results presented here. At higher irradiances, the positions change slightly due to the increase in $\bar{z}$ and decrease in α. The limits indicated approximately correspond to the spot sizes and maximum irradiances obtained in the present experiments. The scaling laws are :-

Self-Regulating (thin)

$$T_e \sim \lambda^{4/9} \qquad \text{.....(1.25b)}$$

$$N \sim \lambda^{-4/9} \qquad \text{.....(1.29b)}$$

$$V \sim \lambda^{1/9} \qquad \text{.....(1.31b)}$$

$$n_e \sim \lambda^{-2/3} \qquad \text{.....from (1.20), (1.25b)}$$

Self-Regulating (thick)

$$T_e \sim \lambda^{1/3} \qquad \text{.....(1.34a)}$$

$$\rho \sim \lambda^{-11/6} \qquad \text{.....(1.34b)}$$

Deflagration-Wave (thin)

$$T_e \sim \lambda^{4/3} \qquad \text{.....(1.42)}$$

$$V \sim \lambda^{2/3} \qquad \text{.....(1.43)}$$

Deflagration-Wave (thick)

$$T_e \sim \lambda^{-4/11} \qquad \text{.....(1.44)}$$

$$V \sim \lambda^{-2/11} \qquad \text{.....(1.44)}$$

1.10.4. The Absorption Length, ℓ

If the electron velocity distribution is Maxwellian, the inverse bremsstrahlung absorption coefficient, μ, is given by[30] :-

$$\mu = \frac{n_e\, n_i\, Z^2\, e^6 \{ 1 - \exp(-\hbar\omega/kT_e) \}}{\mu'\, 6\, \varepsilon_o^3\, c\, \hbar\, \omega^3\, m_e^2} \{ m_e/(2\pi\, kT_e) \}^{1/2}\, \bar{g}/(3)^{1/2} \qquad .....(1.48)$$

where,

$\mu' = \{ 1 - \omega_{pe}^2 / \omega^2 \}^{1/2}$ is the real refractive index of the plasma,

ω_{pe} = electron plasma frequency

$\bar{g}$ = averaged Gaunt factor

ε_o = permittivity of free space (8.854×10^{-12} $F.m^{-1}$)

ω = angular frequency of the radiation.

This expression strictly only considers free-free absorption by binary processes. However, this is reasonably accurate for wavelengths well below the electron plasma wavelength.

If we make the approximation $h\omega << kT_e$ (i.e. the incident radiation is weak compared with the plasma temperature), and put $n_i = n_e = n$, this expression is simplified to :-

$$\mu = \frac{n^2\, Z^2\, e^6\, \bar{g}}{\mu'\, 6\, \varepsilon_o^3\, c\, \omega^2\, (m_e\, k\, T_e)^{3/2}\, (6\pi)^{1/2}} \qquad .....(1.49)$$

Thus, the absorption coefficient, $\mu \sim \omega^{-2}, n^2$

$\sim \lambda^2, n^2$

and the absorption length, $\ell \sim \lambda^{-2}, n^{-2}$

For rapid spatial absorption, n and λ must be maximised. The critical electron density, $n_{ec} = 1.09 \times 10^{13} \lambda^{-2}$ cm^{-3} (λ in cm). Therefore, if the radiation is to penetrate into the plasma :-

$$\lambda^2 n < 1.09 \times 10^{13} \qquad .....(1.50)$$

Applying this constraint to (1.49) we obtain $\ell \sim \lambda^2$.

1.11. Gaseous Environment

1.11.1. Thermal Coupling

The surface absorption coefficient, as already discused for the vacuum environment, is not usually the most significant factor for high irradiance interaction in a gas. A surface plasma, or plasmotron, is usually produced at an irradiance threshold of $\sim 10^7$ W.cm^{-2} for HF laser radiation in atmospheric air. If this is optically dense, much of the radiation energy is absorbed by the plasma. Subsequently, the hot plasma relays much of this energy to the target, over an extended area, by electron conduction or U.V. radiation[31-33]; a process with increased overall efficiency for metals with much higher absorptance in the ultra-violet than in the infra-red. The enhanced coupling within the focal spot may be an order of magnitude larger than in the plasma-free situation. It is immediately apparent that the enhancement efficiency will increase with focal spot size, as, for very small spots, most of the retransmitted energy will be recieved outside of the region of interest.

As the irradiance is increased beyond $\sim 10^8$ W.cm^{-2} a laser supported detonation (LSD) wave may be initiated[34]. This is an optically dense plasma that moves back towards the laser at super-

sonic velocities, being continually fed by the absorption of radiation. The LSD wave decouples the radiation from the target surface, and results in a steady decrease in thermal coupling with time and also with LSD wave velocity, i.e. with laser fluence. The optimum thermal enhancement occurs at, or just below, the LSD wave threshold [35,36]. The LSD wave causes air ionization by shock compression[37], as described by the laser-induced Chapman-Jouguet detonation process. The radiation is effectively absorbed by the ionized gas, and this is the origin of the effective decoupling.

As the LSD wave moves towards the laser, it undergoes lateral spreading, according to the beam cone-angle. The rate of spread depends upon the beam fluence, gas pressure, temporal shape of pulse, laser wavelength, and the cone-angle. For rapid spread, or long pulse duration, recoupling is possible; in extreme cases, multiple recoupling can occur.

If the irradiance is increased by about a couple of orders of magnitude beyond the LSD wave threshold, air breakdown will occur. This is also highly absorbing, but the situation will be discused separately.

1.11.2. Laser Supported Detonation Waves

The initial LSD wave velocity, V, is given by[34]:-

$$V = \{ 2(\gamma^2 - 1)\ \phi / \rho_o \}^{1/2} \qquad .....(1.51)$$

where, γ is the specific heat ratio for air behind the absorption wave (AW) front ($\sim$1.24), ϕ the target irradiance, ρ_o the ambient air density.

The threshold irradiance has been derived by Allingham and Bishop[38] using the absorption length given by Raizer[39]:-

$$\phi_{min} = \{ (\gamma^2 - 1)^{1/3} (\gamma + 1) \, 2.76 \times 10^5 \, (2^{2/3} \gamma)^{-1} (\rho_o/\rho)^{0.12} \}^{3/2}$$

$$\times (T_{min}^{9/4} \rho_o/10^7) \quad (1 + \ell/r_o) \; W.cm^{-2} \qquad .....(1.52)$$

where,

$\rho / \rho_o = (\gamma + 1) / \gamma$

Here,

$\gamma \sim 1.24$

ℓ = absorption length at relevant laser wavelength

r_o = spot or beam radius

ρ_o = ambient gas density

ρ = gas density behind the AW front

T_{min} = minimum temperature behind the AW front to sustain the LSD wave.

$$\ell^{-1} = 0.14 \times \zeta \, P^2 \, (P_e/P)^2 \, (e^{h\nu/kT_{min}} - 1) \, (T_{min}/10^4)^{-3/2} \, (h\nu)^{-3}$$

.....(1.53)

where,

$P = \rho \, R \, T$

R = the gas constant per unit mass

P_e/P = the molecular electron fraction given by the Saha equation :-

$$(P_e/P)^2 \{ 1 - 2(P_e/P) \}^{-1} = 6.7 \times 10^3 \, G \, (T_{min}/10^4)^{3/2} \, P^{-1} \, e^{-I/kT_{min}}$$

.....(1.54)

Using averaged values adopted by Raizer, G = 1.9, I = 14.4 eV, ζ = 0.7.

ℓ and ϕ_{min} have conveniently been plotted at various laser wavelengths for values of r_o, T, P, and ρ_o [38].

The above approach considers the minimum irradiance required to maintain an undamped AW.

Smith [40] has used an alternative approach that includes the pulse duration. He calculates the generated vapour density at the target surface, and then evaluates the cascade ionisation threshold. The density is given by :-

$$N = (1 - R) \{ 1 - \exp(r_o/r_k) \} \phi t_c \{ 1 + (r_o/vt_c)^2 \}^{1/2} (q r)^{-1} \quad \text{.....(1.55)}$$

where,

v = vapour velocity from the surface
r_o = beam radius
$t_c = t_p/40$
t_p = laser pulse duration
q = latent heat of vaporisation
ϕ = irradiance at wavelength λ
r_k = surface defect dimension
R = reflection coefficient of the target surface.

The breakdown irradiance, ϕ_b, is given by :-

$$0.11 \nu_c \phi_b (3.5 \times 10^{22} \lambda^{-2} + \nu_c^2)^{-1}$$

$$= (40 I/t_p) + 4.6 \times 10^{-18} (D/r_o^2), \qquad r_o/v < t_c \text{.....(1.56)}$$

$$= (40 I/t_p) + 8.8 \times 10^{-22} \nu_c/M, \qquad r_o/v > t_c \text{.....(1.57)}$$

where,

ν_c = electron-atom collision frequency = 1.6×10^{-7} N
I = ionisation potential
D = diffusion coefficient
M = atomic mass

Using t_p = 325ns, $r_o = 5 \times 10^{-2}$cm, $v = 10^5 cm.s^{-1}$, $r_k = 10^{-3}$cm, $q = 4.75 \times 10^{-19} J.atom^{-1}$, R = 0.95, λ = 2.8μm, we obtain for aluminium :-

$N \simeq 1.05 \times 10^{12} I$
$\phi_b \simeq 6 \times 10^7 W.cm^{-2}$

Allingham[41] has plotted the breakdown threshold for CO_2 and Nd:glass lasers. Using the $1/\lambda$ threshold scaling a threshold of $\sim 5.3 \times 10^7 W.cm^{-2}$ is obtained for aluminium at 2.8μm. The two models are thus in agreement.

1.11.3. Gas Breakdown

Gas breakdown thresholds in air and argon at the HF and DF wavelengths are given by Deka et al[42] using a similar laser and resonator as employed in the experiments presented in chapter 5. In atmospheric air, the breakdown threshold, ϕ_t, was found to be $\sim 6 \times 10^{10} W.cm^{-2}$. Over the pressure range 300-3400 torr the breakdown threshold scaled as $\phi_T \sim P^{-0.6}$. With pure argon at 760 torr the threshold was found to be $1.6 \times 10^{10} W.cm^{-2}$. A scaling of $\phi_T \sim P^{-0.95}$ was deduced. The results were compared with measurements at 1.06μm[43] and 10.6μm[44] wavelengths to obtain a λ^{-2} scaling with peak on-axis breakdown intensity.

Hill et al[45] have also carried out threshold measurements at the 10.6μm wavelength using rare and molecular gases.

Deka[46] measures at 10.6μm :-

$$\phi_T \sim (P\ \tau)^{-0.65} \qquad .....(1.58)$$

where,

P = ambient pressure
τ = pulse length.

The breakdown time τ_b scales as :-

$$\tau_b \sim P^{-0.4} \qquad \text{.....(1.59)}$$

If the leading edge of the pulse is in the form of a ramp, then τ_b is also the transmitted pulse width, assuming :-

a) breakdown occurs on the leading edge,
b) the plasma is instantly optically dense.

1.12. References

1) Libenson M.N., Romanov G.S. and Imas Ya.A. Sov. Phys. Tech. Phys., 13, 925-8, 1969.
2) Hughes T.P. "Plasmas and Laser Light". Adam Hilger, 1975.
3) Weingartshofer A., Clarke E.M., Holmes J.K. and Jung Ch. Phys. Rev. A. 19, 2371-6, 1979.
4) Schlesinger L. and Wright J. Phys. Rev. A. 20, 1934-44, 1979.
5) Caruso A. and Gratton R. Plasma Phys. 10, 867-77, 1968.
6) Caruso A., Bertotti B. and Giupponi P. Nuovo Cimento 45B, 176-88, 1966.
7) Afanas'ev Yu.V., Krokhin O.N. and Sklizkov G.V. IEEE. J. Quant. Elect., QE-2, 483-5, 1966.
8) Afanas'ev Yu.V., Krol V.M., Krokhin O.N. and Nemchinov I.V. Appl. Math. and Mech., 30, 1218-25, 1966.
9) Afanas'ev Yu.V. and Krokhin O.N. Sov. Phys. JETP, 25, 639-45, 1967.
10) Krokhin O.N. "Physics of High Energy Density". ed. Caldirola P. and Knoepfel H. New York, Academic Press. 278-305, 1971.
11) Puell H.Z. Naturf. 25a, 1807-1815, 1970.
12) Dawson J. and Oberman C. Phys. Fluids, 5, 517-524, 1962.
13) Spitzer L. Jr., "Physics of Fully Ionized Gases". Intersci. Publ., New York, 128, 1962.
14) Basov N.G., Gribkov A., Krokhin O.N. and Sklizkov. Sov. Phys. JETP. 27, 575-582, 1968.
15) Mulser P.Z. Naturf. 25a, 282-295, 1970.
16) Shkarofsky I.P., Johnston T.W. and Bachynski M.P. "Particle Kinetics" Addison Wesley Publ. Co., 1966.
17) Dyer P.E., James D.J., Pert G.J., Ramsden S.A. and Skipper M.A. "Laser Interactions and Related Plasma Phenomena. vol. 3", Plenum Press, 191-212, 1974.
18) Fauquignon C. and Floux F. Phys. Fluids, 13, 386-391, 1970.
19) Bobin J.L. Phys. Fluids, 14, 2341-54, 1971.
20) Pert G.J. Plasma Phys., 16, 1019-1033, see also 1035-49, 1974.
21) see for example Hughes T.P. "Plasmas and Laser Light". Adam Hilger, 1975.

22) Shchelkin K.I. and Troshin Ya.K. "Gas Dynamics of Combustion". Transl. Kuvshinoff B.W. and Holtschlag L. Baltimore, Mono Book Corp., 1965.

23) Hora H. (ed) "Laser Plasmas and Nuclear Energy". Plenum Press, New York, 1975.

24) Yamanaka C., Yamanaka T., Sasaki T., Yoshida K., Waki M. and Kang H.B. Phys. Rev. A6, 2335-42, 1972.

25) Nishikawa K. J. Phys. Soc. Jap., 24, 916, 1152, 1968.

26) Dyer P.E. Ph.D. Thesis. University of Hull, 1974.

27) Dick K. and Pepin H. Optics Commun., 13, 289-93, 1975.

28) Ehler A.W. J. Appl. Phys. 46, 2464-7, 1975.

29) Fabre E., Popovics and Stenz C. VIII European Conference on Laser Plasma Interactions, Rynia, Warsaw, Poland, May, 1975.

30) see, for example, Hughes T.P. "Plasmas and Laser Light" Adam Hilger, 44, 1975.

31) Jumper E.J. and Jackson J.P. Air Force Weapons Lab. Report No. AFWL-TR-74-344, 1975.

32) Boni A.A., Su F.Y., Thomas P.D. and Musal H.M. Science Applications Inc. Report No. 77-567LJ, 1977.

33) Pirri A.N., Root R.G. and Wu P.K.S. AIAAJ., 16, 1296, 1978.

34) Ramsden S.A. and Savic P. Nature, 203, 1217-19, 1964.

35) Hettche L.R., Tucker T.R., Schriempf J.T., Stegman R.L. and Metz S.A. J. Appl. Phys., 47, 1415-1421, 1976.

36) Maher W.E. and Hall R.B. J. Appl. Phys., 49, 2254-2261, 1978.

37) Raizer Yu.P. Zh. Eksp. i. Teor. Fiz., 48, 1508-19, 1965. Transl: Sov. Phys. JETP, 21, 1009-17, 1965.

38) Allingham C.O. and Bishop H.V.H. Awre report LDPN/12/77.

39) Raizer Yu, P. Zh. Eksp. Teor. Fiz., 58, 2127-38, 1970. Transl: Sov. Phys. JETP, 31, 1148-54, 1970.

40) Smith D.C. J. Appl. Phys., 48, 2217-25, 1977.

41) Allingham C.O. AWRE report LDPN/13/77.

42) Deka B.K., Dyer P.E., James D.J. and Ramsden S.A. Optics Commun., 19, 292-6, 1976.

43) Lencioni D.E., Appl. Phys. Lett., 25, 15-17, 1974.

44) Lencioni D.E., Appl. Phys. Lett., 23, 12-14, 1973.

45) Hill G.A., James D.J. and Ramsden S.A., J. Phys. D: Appl. Phys., 5, L97-9, 1972.

46) Deka B.K., Ph.D. Thesis, University of Hull, 1977.

CHAPTER 2

PULSED HF LASER DEVELOPMENT

2.1. Introduction

This chapter reviews the principal milestones in the development of the pulsed HF laser. Since T.F. Deutsch[1] first reported lasing action for this chemical laser in 1967, various excitation schemes have been sucessfully employed. The different techniques and their corresponding parameters are considered here, although detailed design data has only been given where relevant, as it can be obtained from the references cited. No attempt has been made to provide a fully comprehensive list of publications relating to the use of the HF laser, in view of the large number available and their lack of direct relevance to the work presented in this thesis.

2.2. Deutsch's Laser

The pioneering work of Deutsch established a variety of possible reactants. Using H_2 , D_2 , CH_4 and CH_3Cl as anion sources he achieved lasing action with the freons CF_4 , $CBrF_3$, $CClF_3$ and CCl_2F_2. Deutsch carefully recorded the broad-band spectral wavelengths for HF and DF radiation, although regretably the information on the laser itself was very limited. A water-cooled tube 2m long and with an I.D. of 32mm was utilized - the gas discharge being excited by 50 - 200A current pulses of about 1μs duration and 2 - 10Hz repetition. The output energy was not given, but presumeably it would have been a few mJ at best.

2.3. Dumanchin Type Construction

Wenzel and Arnold of Los Alamos[2] built a Dumanchin[3] type construction of a double-discharge HF laser. In this laser, the pre-ionization required for glow discharge is achieved with a low energy discharge between glass-insulated trigger wires and adjacent cathode blades. This produces uniform ionization in the vicinity of

the cathode sothat the ensuing main breakdown is homogeneous. Initially, a maximum output energy of 102.5mJ was obtained by employing a gas mixture of SF_6 + C_4H_{10}. A marginally lower energy resulted from replacing the butane with hydrogen. As the discharge dimensions were 50.8cm x 2.5cm across a gap of 2.4cm, the energy density was 336mJ/l. It was fairly important that the slotted electrode was made the anode; a reduction in output energy resulted from polarity reversal. The optimum discharge potential was 80KV using two 0.01μF capacitors in a two-stage Marx bank. At a later date, a five-stage Marx bank was constructed giving 125J discharges. When operated at 250KV the maximum output energy became 560mJ. Arc formation was found to degrade the output. A 3sec gas change was employed at a total pressure of 50torr (with butane) or 8torr (with hydrogen) for optimum performance, the gas ratios r being 21:1 and 16:1 respectively. Wenzel and Arnold tried adding helium to the mixture, but this was found to decrease the output energy. The electrical and chemical efficiencies were 0.6% and 0.25% when pumped by a 16J pulse.

A year later, Arnold and Wenzel[4] discused improvements to this system. They found that chemically blackening the cathode and roughening of the chamber walls suppressed spurious reflections. Using a discharge volume of 0.33l and a low inductance (0.13μH) two-stage Marx bank, they were able to extract 3.5J pulses with a peak power of 35MW and electrical efficiency of 1.8%. The energy density was 10.6J/l. With a slightly slower circuit and output energies about 1.4J, they achieved an electrical efficiency of 3.1%.

2.4. Pin Construction

In 1972, Pummer and Kompa[5] reported their construction of a pin HF laser. They utilized a dilute aqueous copper sulphate electrolyte to ballast 1000 brass pins feeding a discharge volume of 2m x 3cm x 3cm. With a gas mixture of SF_6 + H_2 at a total pressure of 62.5torr and ratio 24:1, they achieved 1.2J of photon energy and a peak power of 3MW. The electrical efficiency was

about 0.8% and the energy density was 700mJ/l. No mention was made of the pin life-time in the publication, although we understand that pin corrosion rapidly occured. In agreement with Wenzel and Arnold, they found He to be detrimental to output energy.

Pummer et al[6] increased the discharge volume to 3m x 5cm x 4cm gap. Using a 3-stage Marx bank (∿40KV per stage) they achieved an 11J output. The pulse duration was observed to be pressure dependent (as explained in 2.10.), being 5μs below 20torr and ∿20ns above 250torr. Considerable pulse-shortening was observed when this laser was used as an amplifier. It was considered likely that subnanosecond pulses could be obtained in this manner. The electrical efficiency for an 11J output was calculated to be 3.8%.

2.5. Lamberton-Pearson Type Construction

In 1974, Voignier and Gastaud[7] employed the Lamberton-Pearson trigger-wire laser with high pressure (400-600torr) $SF_6 + H_2 + He$. Rogowski profiled electrodes were used with a 1.5cm gap and active volume of $60cm^3$. The optimum gas ratio was found to be 12:1:14. Helium or Argon was found necessary to prevent arcing. The addition of trace amounts of C_2H_6 increased discharge uniformity. This is to be expected as C_2H_6 has a lower ionization potential than hydrogen and a much higher photoionization cross-section. At the optimum total gas pressure of 550torr a 1J, 17MW output was attained with a 4% electrical efficiency and 16.5J/l. Considering the small active volume and high energy density this was a significant achievement.

2.6. U.V. Pre-ionization Construction

Attempts have been made with most laser systems to scale their dimensions and parameters to much larger values. Higher output powers can be achieved, for example, by increasing the discharge volume and optical gain coefficient or by decreasing the pulse duration.

2.6.1. Sliding-Spark Method

One step towards achieving this goal was made by Wlodarczyk in

1978[9]. Previous attempts at increasing the discharge cross-section had failed for high-pressure, continuous electrode HF lasers because of arc formation. The problem centers on the electrophilic behavour of SF_6 which depletes the free electrons needed for uniform glow discharge. Wlodarczyk utilized a sliding UV pre-ionization atmospheric laser, similar to various CO_2 lasers[10]. Atmospheric lasers have the great advantage of not requiring vacuum equipment and so tend to be compact, as well as being simple to construct and operate. UV pre-ionization has successfully been employed to condition large CO_2 laser discharge volumes, and in spite of the added problems with SF_6 it was expected to be useful with HF. In this prototype system a 3 x $3cm^2$ glow discharge was achieved using significantly more UV radiation than in a similar CO_2 discharge. The aluminium Rogowski electrode was shot-blasted to increase the photoemission and ion absorption area (as well as to decrease the parasitic output). This technique was reported by Karasikov and Shamir[11]. The increase in pressure to atmospheric also has the beneficial effect of increasing the gain coefficient, although of course the parasitic problems are also increased. A brown deposit was observed on electrode surfaces after operation; removal of this coating proved to be detrimental to the discharge. One of the advantages of UV pre-ionization is in the good beam uniformity resulting from the homogenous glow discharge. This is important in situations where the beam is focused to produce maximum or known irradiances, although in laser-chemistry the beam quality is often not critical. With this UV pre-ionized laser Wlodarczyk achieved a maximum output energy of 425mJ and a peak power of 15.7MW using a charging voltage of 40KV and a discharge length of 26cm. The gas mixture employed was He (3-9 1/min), SF_6 ($150cm^3$/min), and C_3H_8 ($10cm^3$/min) giving an efficiency of 2% and 1.8J/l.

2.6.2. Flash-Lamp Method

Nichols et al[12], in 1976, used a flash-lamp photoinitiated $F_2 + H_2/D_2$ laser to achieve good performance. Other experimenters,

for example see ref. 2.13, 2.14, had employed flashlamp initiation; however, the results of Nichols et al represented the largest energies and efficiencies. Using an active volume of 12.8 l at atmospheric pressure they achieved 292J, 8.1% chemical efficiency and 29% electrical efficiency for HF. With DF the energy attained was 144J with 14% electrical efficiency. The optimum electrical efficiencies were achieved using a Teflon covered laser wall. The high UV reflectivity of Teflon compared, for example, with aluminium gave significant improvement. The fluorine gas was diluted with nitrogen or argon before being added to the hydrogen. Oxygen was also added to the mixture to inhibit pre-ignition. Argon was found preferential to nitrogen as the higher temperatures attained with the monatomic diluent lead to a greater electrical efficiency. This factor of two improvement did not lead to a larger energy output, however, as the oxygen content had to be increased.

2.7. Electron-Beam Excitation

2.7.1. Hydrogen - Fluorine Reactants

Hydrogen and fluorine are used directly in many situations involving sophisticated gas handling. Most of these giant lasers are beyond the financial scope of small establishments and so they tend to be found in government research laboratories such as Los Alamos. Parher and Stephens[15] report an electrical efficiency for F_2/H_2 of 50-100 times that for SF_6/H_2. There are a number of contributory reasons for this result. For a start, the dissociation energy of F_2 (1.6eV) is less than that of SF_6 (3.4eV). Energy is released in the additional reaction :-

$$H + F_2 \rightarrow HF^* + F_2 \qquad .....(2.1)$$

The reactions :-

$$F_2 + e \rightarrow F^- + F + KE \qquad .....(2.2)$$

$$F^- + e \rightarrow F + e + e - 3.45eV \qquad .....(2.3)$$

produce a maximum yield of 1.81×10^{18} F atoms/J, which is to be compared with a maximum 3.9×10^{18} F atoms/J calculated from the molecular disociation energy. Other reactions producing F atoms, for example :-

$$F_2 + e \rightarrow F_2\ (^1\pi_u) + e \rightarrow F + F + e$$

may also occur.

2.7.2. Electron-Beam Excitation

Greiner et al[16] describe a 0.2GW system that produces 60ns, 12J pulses from an atmospheric H_2/F_2 e-beam initiated laser. The chemical efficiency was 0.25% and the electrical efficiency ~100%. Oxygen was added to the gas mixture to aid stability, and SF_6 or Xe added to help e-beam energy deposition.

A 50J, 50MW laser is described by Aprahamian et al[17]. The active volume was ~4.2l and the electrical efficiency was only 6%.

Bashkin et al[18] have used a 200keV, 0.7-1.0kA, 35ns electron beam in a $H_2:F_2:O_2$:He mixture at 1.3 atmospheres to achieve 100J/l. The electrical efficiency was about 900% and the chemical efficiency about 4%. However, the active volume was fairly small (0.665l) sothat the output energy was only 66J.

e-beam initiated HF lasers have a large number of advantages over the other excitation schemes : these lasers are scaleable. They do not suffer from the filamentation, inhomogeneities and parasitic oscillations of TEA lasers or the low electrical efficiencies of UV pre-ionized lasers (due to low UV photon absorption cross-sections). For these reasons even larger amplifier chain e-beam HF lasers are being studied at Los Alamos and elsewhere, but such work is outside the scope of this review. It is interesting to note, however, that in 1975 G. Schott of Los Alamos considered the $H_2 + F_2$ e-beam HF laser to be scaleable to $\gtrsim 10^4$J and ~TW per litre[19]. To what extent this has been realised must, unfortunately, be subject to conjecture.

2.8. Nuclear Pumped Lasers

Lasing action has been successfully achieved by utilizing the technique of nuclear pumping. The limitation on scaling conventional lasers to large diameters is the constraint of uniform energy deposition in the pumping phase. Even electron-beam excitation is limited by the electron mean free path. The potential importance of nuclear pumping is that far larger sizes are possible.

One technique that has been employed involves coating the walls of the laser chamber with a fissile or nuclear material. If the chamber is in the vicinity of a nuclear reactor, thermal neutrons can be used in the $^{1}n(^{10}B,\alpha)^{7}Li$ and $^{1}n(^{235}U,FF)FF$ reactions[20-24]. This technique is not suitable for large systems as the fission energy is not uniformly deposited[25].

Another technique uses a fissile gas mixed with the lasing gas. The reaction $^{3}He(n,p)^{3}H$ has been employed[26-28]. Although this aproach can be scaled to very large dimensions, the lasing gas is heavily diluted.

Kushner[29] has presented a more direct system which can be applied to the HF chemical laser. A mixture of $^{235}UF_6$ and H_2 is used together with the fission reaction $^{1}n(^{235}U,FF)FF$. Fission fragments dissociate UF_6 to produce fluorine atoms which in turn react with the hydrogen to form HF. Kushner has used a computer model to predict peak gains $\gtrsim$ 50%/m. In addition this system has a low neutron flux threshold ($<10^{14}$ neutrons cm^{-2} s^{-1}) and can be scaled to extremely large dimentions.

2.9. CO_2 Laser Pumped HF Lasers

HF lasers have been directly pumped using 10.6μm laser radiation[30-32]. One technique involves employing resonantly absorbing fluorine donors such as SF_6 or N_2F_4. Initiation of an HF laser has also been achieved with a CO_2 laser-produced plasma. Wood and Silfvast[33] obtained an output power of 500W by cylindrically focusing the 10.6μm radiation onto an aluminium target surrounded by CF_4 and H_2.

2.10. Short Pulse Generation

The production of nanosecond pulses from the HF laser has been actively pursued at Los Alamos. One technique involves four essential elements :-

i) A pin-discharge 10mJ multiline oscillator constrained by apertures to operate on TEM_{oo}. The output pulse is long and diffraction limited.

ii) An electro-optic switch to transmit a 1ns segment.

iii) Intermediate amplifier.

iv) High pressure electron-beam amplifier.

Spacial filtering is employed and the laser windows are made of saphire.

Details of a possible switching technique are given by Getzinger et al[34]. Using auxiliary switched laser beams they were able to deplete the optical gain of the pre-amplifier on either side of the switched ns pulse, thus achieving minimum pedestal. This technique, not possible with CO_2 lasers, can be utilized as the HF gain can be rapidly re-established.

It is possible, however, to produce short pulses without use of any electro-optic switch. To achieve this, the electrical discharge should have a rapid rise and decay time. In addition, a high-loss resonator is desireable. To understand these points it is worth noting that the population inversion is attained when fluorine atoms react with hydrogen molecules. A fast electrical rise-time, therefore, produces fluorine atoms rapidly which in turn gives a rapid inversion. Rapid depopulation requires a cessation of the production of HF*, as well as its active removal by collisional and other methods. In particular, the inversion is destroyed by stimulated emission. A high gain medium (i.e. high pressure gas) and high F concentration resulting from high field strengths are therefore required. High-loss resonators require higher inversion thresholds. The pulse length is therefore reduced as the time above threshold is decreased.

3ns pulses have been achieved in this manner by Schilling and

Decker[35] who employed a transversely excited Blumlein laser at a maximum pressure of 200torr and field strength of 19KV/cm. The low power ∿MW pulses were considered suitable for further amplification.

Yet another method commonly used to achieve short pulses involves mode-locking. This was first achieved with the HF laser by Simonis[36] who utilized a diffraction grating to obtain single line action. An unstable optical cavity, together with an inter-cavity saturable absorber, were used to passively mode-lock, resulting in a train of multikilowatt pulses separated by the cavity round-trip time or simple multiples of this period. The saturable absorber was HF gas itself at a pressure of ∿1torr. Even without the HF cell mode-locking tended to occur. Shortest pulse durations were ∿5ns and these occured in trains of ∿1μs. Although ns interaction experiments with a mode-locked train are not completely excluded, it is possible to switch out single pulses.

2.11. 16μm Emission

Gürs et al[37] have developed a TE HF laser giving emission lines of wavelengths 12.7 to 17μm originating from pure rotational transitions. Concentrating on a 16.02μm line they presented a parameter study optimising on a gas composition of He,SF_6 and butane at pressures between 20 and 150mbar. Hydrogen was not a suitable H donor, as it tended to eliminate rotational transitions (as did D_2, HCl, CO and N_2). The 16.02μm line had a pulse energy of about 5μJ. This is of potential importance in the laser isotope separation of uranium from UF_6.

2.12. Compact Lasers

One of the major problems in developing compact powerful HF lasers is the restriction that the system has to be operated at low partial pressures. This limitation is imposed by the strong electronegative nature of the fluorine donor.

Brink and Hasson[38] have partially overcome this problem, achieving compact atmospheric operation of a helium-free mixture.

The attachment losses are reduced by using corona (high field) UV pre-ionization with nanosecond delay before the main discharge. The corona and discharge electrodes are actually connected in parallel sothat pre-ionization occurs on the rising edge of the voltage pulse. Using an active volume $\sim 10^3 mm^3$ an output energy of 20×10^{-3}mJ has been obtained for a 20ns pulse.

Deutsch[39], using Rogowski electrodes in SF_6:H_2:He mixtures, was able to achieve glow discharge without pre-ionization. This was accomplished by using resistive graphite as the electrode material. Gibson[40] used a 500Ωmm germanium cathode, together with a brass anode, to obtain the same result. Resistive material tends to limit transverse currents in the electrodes and thus the probability of arc formation. Hatch[41] has developed the theme by employing germanium for both electrodes. With an active volume of 42×10^3 mm^3 a maximum multiline output of 167mJ and 2MW was achieved for a gas flow rate of 1 l min^{-1}.

2.13. References

1) Deutsch, T.F. Appl. Phys. Lett. 10, 234-6, 1967.

2) Wenzel, R.G. and Arnold, G.P. IEEE J. Quant. Elect. QE-8, 26-7, 1972.

3) Dumanchin R., Farey J.C., Michon M. and Rocca-Serra J. "High power density pulsed molecular laser". International Quantum Electronics Conference, Kyoto, 1970; a description of the device also appears in Laser Focus, June, 1971.

4) Arnold G.J. and Wenzel R.G. IEEE J. Quant. Elect. QE-9, 491-3, 1973.

5) Pummer H. and Kompa K.L. Appl. Phys. Lett. 20, 356-7, 1972.

6) Pummer H., Breitfeld W., Wedler H., Klement G., and Kompa K.L. Appl. Phys. Lett. 22, 319-20, 1973.

7) Voignier F. and Gastaud M. Appl. Phys. Lett. 25, 649-50, 1974.

8) Lamberton H.M. and Pearson P.R. Elect. Lett. 7, 141-2, 1971.

9) Wlodarczyk G. IEEE J. Quant. Elect. QE-14, 768-771, 1978.

10) Wood O.R., "High pressure pulsed molecular lasers", Proc. IEEE, 62, 355-397, 1974.

11) Karasikov N. and Shamir J., "Operation of TEA CO_2 lasers with rough surface electrodes", IEEE J. Quant. Elect. QE-12, 257, 1974.

12) Nichols D.B., Hall R.B. and Mc Clure J.D. J. Appl. Phys. 47, 4026-30, 1976.

13) Chen H.L., Taylor R.L., Wilson J., Lewis P. and Fyfe W. J. Chem. Phys. 61, 306, 1974.

14) Batovskii O.M. and Gur'ev V.I. Sov. J. Quant. Elect. 4, 801-4, 1974.

15) Parher J.V. and Stephens R.R. Appl. Phys. Lett. 22, 450-2, 1973.

16) Greiner N.R., Blair L.S. and Bird P.F. IEEE J. Quant. Elect. QE-10, 646-7, 1974.

17) Aprahamian R., Wang J.H.S., Betts J.A. and Barth R.W. Appl. Phys. Lett. 24, 239-42, 1974.

18) Bashkin A.S., Konoshenko A.F., Oraevskii A.N., Tomashov V.N. and Yuryshev N.N. Sov. J. Quant. Elect. 9, 1270-5, 1979.

19) Schott G.L. "Pulsed hydrogen fluoride laser oscillator amplifier experiments". Soc. of Photo-optical Instrumentation Engineers Seminar on Optical Methods in Energy Conversion, June,1975, Rochester, N.Y.

20) Akerman M.A., Miley G.H. and McArthur D.A. Appl. Phys. Lett. 30, 409-12, 1977.

21) De Young R.J., Wells W.E., Miley G.H. and Verdeyen J.T. Appl. Phys. Lett., 28, 519-21, 1976.

22) Prelas M.A., Akerman M.A., Boady F.P. and Miley G.H. Appl. Phys. Lett. 31, 428-30, 1977.

23) McArthur D.A. and Tollefsud P.B. Appl. Phys. Lett. 26, 187-190, 1975.

24) Helmik H.H., Fuller J.L. and Schneider R.T. Appl. Phys. Lett., 26, 327-8, 1975.

25) Guyot J.C., Miley G.H. and Verdeyen J.T. Nucl. Sci. Eng. 48, 373-86, 1972.

26) De Young R.J., Wells W.E. and Miley G.H. Appl. Phys. Lett. 28, 194-7, 1976.

27) Jalufka N.W., De Young R.J., Hohl F. and Williams M.D. Appl. Phys. Lett. 29, 188-90, 1976.

28) De Young R.J., Jalufka N.W. and Hohl F. Appl. Phys. Lett. 30, 19-21, 1977.

29) Kushner M.J. J. Appl. Phys. 51, 2421-8, 1980.

30) Lyman J.L. and Jensen R.J. J. Phys. Chem. 77, 883-8, 1973.

31) Akinfiev N.N., Basov N.G., Galochkin V.T., Zavorotnyi S.I., Markin E.P., Oraevskii A.N. and Panktratov A.V. JETP Lett. 19, 383-4, 1974.

32) Belotserkovets A.V., Kirillov G.A., Kormer S.B., Kochemasov G.G., Kiratov Yu.V., Mashendzhinov V.I., Savin Yu.V., Stankeev E.A. and Urlin V.D. Sov. J. Quant. Elect. 5, 1313-5, 1975.

33) Wood II O.R. and Silfvast W.T. IEEE J. Quant. Elect. QE-15, 1323-5, 1979.

34) Getzinger R.W., Ware K.D., Carpenter J.P. and Schott G.L. IEEE J. Quant. Elect. QE-13, 97-100, 1977.

35) Schilling P. and Decker G. Infra-red Phys. 16, 103-107, 1976.

36) Simonis G.J. Appl. Phys. Lett. 29, 42-4, 1976.

37) Gürs K., Hofmann H. and Schäfer. Opt. Commun. 33, 197-202. 1980.

38) Brink D.J. and Hasson V. J. Phys. E : Sci. Inst. 13, 553-6, 1980.

39) Deutsch T.F. IEEE J. Quant. Elect. 10, 84-6, 1974.

40) Gibson A.F., Hall T.A. and Hatch C.B. IEEE J. Quant. Elect. 13, 801-3, 1977.

41) Hatch C.B. J. Phys. E : Sci. Inst. 13, 589-591, 1980.

CHAPTER 3

HF LASER DESIGN AND PARAMETER STUDIES

3.1. Introduction

The development of a pulsed transversely excited HF laser, together with a parametric study of the lasing medium and discharge voltage, is presented. This laser was used in certain target interaction experiments presented in chapter 4.

3.2. First Design

A 10J TE pin laser system, built at Garching[1], was used as a basis for the first design. Our discharge chamber consisted of two 80cm modules with active cross-sections 4.5 x 4.5cm^2. Both modules had 1000 Ni plated pins serving as the cathode, resistively coupled by a saturated copper sulphate solution. An oil emersed voltage doubling circuit was employed, as shown in Fig.3.1.

With the cavity shown in Fig.3.2., chosen for ease of alignment, the output characteristics were obtained by sampling energy (with a Lumonics 20D pyroelectric joulemeter) and pulse shape (with a fast gold-doped Ge detector), back-reflected from a NaCl beam-splitter. Parameters varied to obtain optimum output included the charging voltage, V_c, hydrogen donating gas, HX, total gas pressure, P_{tot}, and relative composition of gases, $r = SF_6/HX$.

H_2, CH_4, C_2H_6, C_3H_8, C_4H_{10} were substituted for HX, V_c was varied up to 70KV and P_{tot} up to 100torr. In the case of $V_c \gtrsim 60$KV a trace of SF_6 was required to hold the spark-gap from self-triggering. It was ascertained that H_2 and C_3H_8 gave the highest output powers, with energies up to 7J. However, it was apparent that a good fraction of this was parasitic - as might be expected in view of the high optical gain of HF lasers[2,3]. It is possible that diffuse parasitics[4] were partly responsible for the parasitic output.

Measurements at far-field were hampered by atmospheric attenuation of the HF laser beam. This attenuation is largely due to water

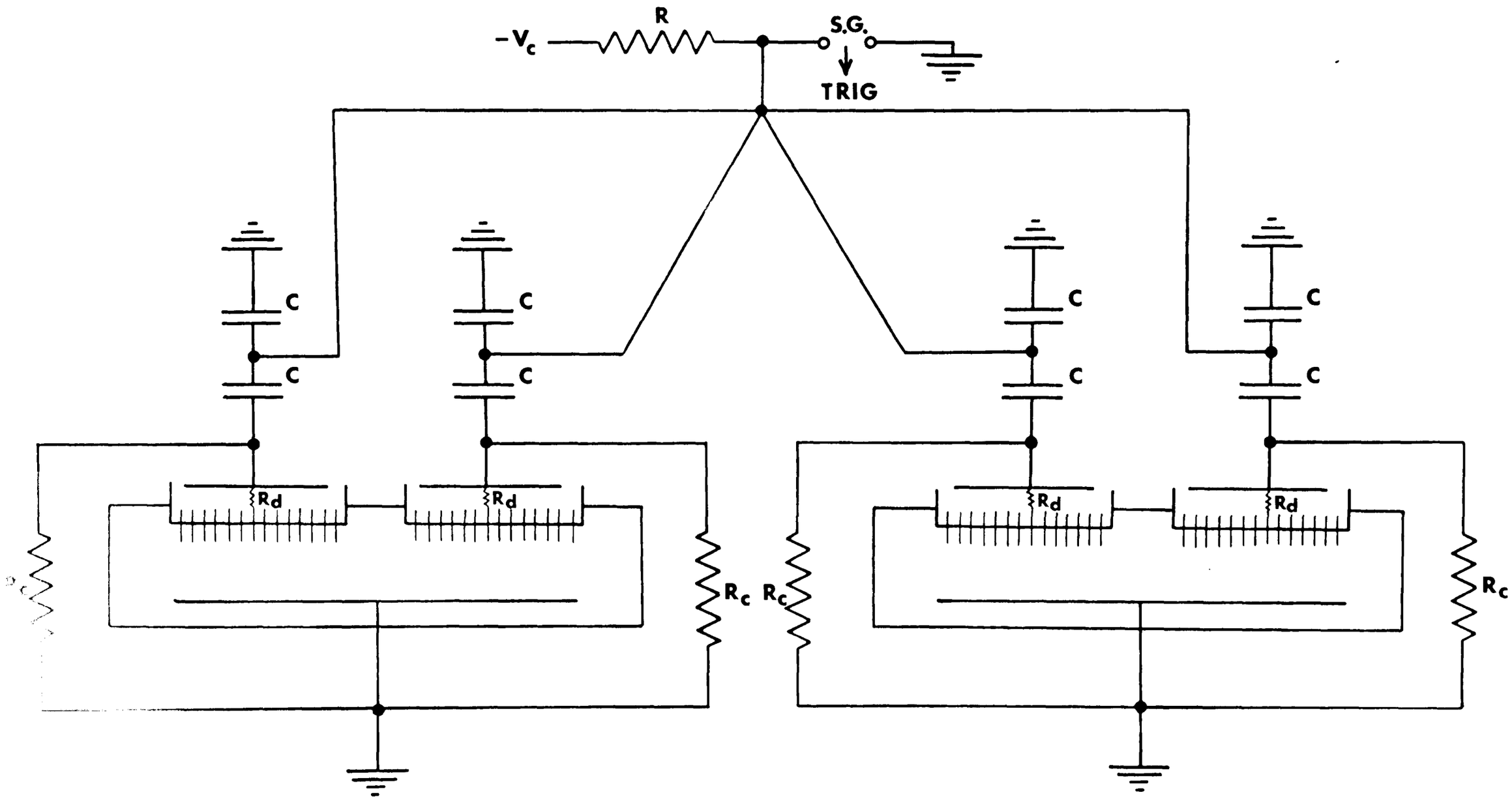

$C = 0{\cdot}04\ \mu F$ 100 KV. $R_d = CuSO_4$ resistor. R_c = charging resistor.

Fig.3.1. Oil emersed voltage doubling circuit.

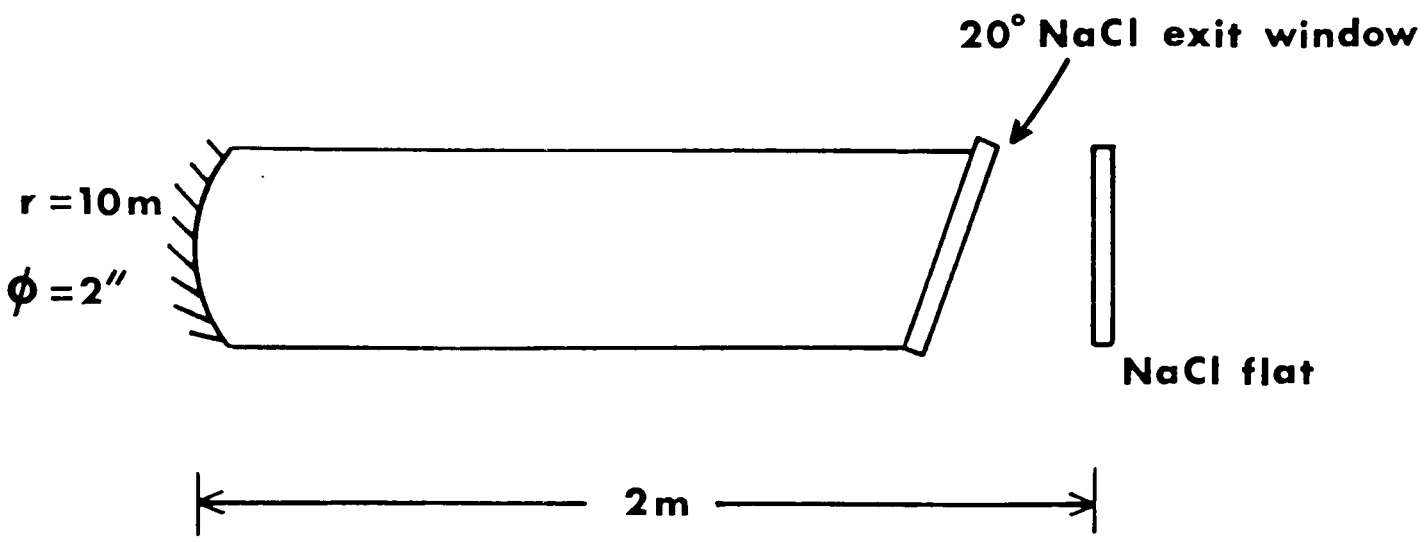

Fig.3.2. Semi-confocal stable resonator.

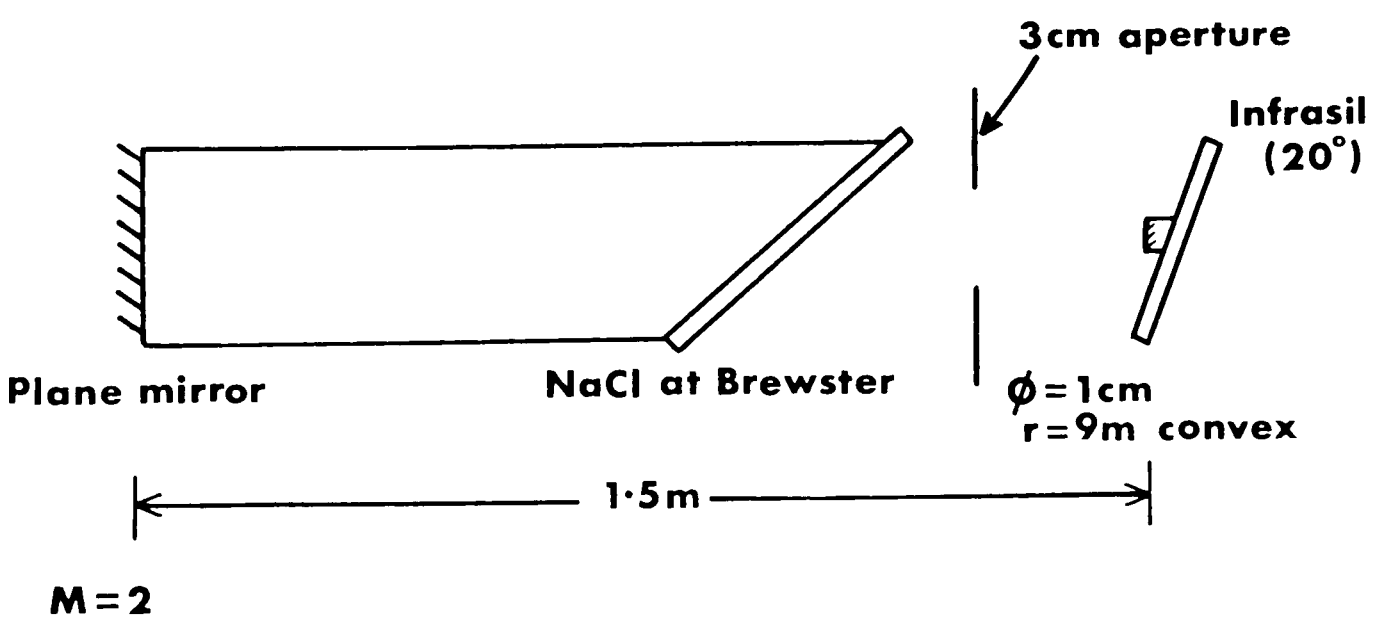

Fig.3.3. Semi-confocal unstable resonator.

vapour, and to a lesser extent to carbon-dioxide. A dry-nitrogen cell was used to determine an absorption coefficient, κ, of the order 0.1/m : $E_{out} = E_{in}\, e^{-\kappa x}$, dependent upon atmospheric conditions. As the windows of such cells were likely to introduce aberrations, the beam was piped over silica gel.

It is worth noting that the production of fluorine in the chamber is likely to damage the gold mirror and salt output window. For this reason, the waste gas is removed from the centre of the chamber and the optical element positioned well away from the discharge volume. The waste gas is highly toxic, especially if water from the $CuSO_4$ resistor has leaked into the chamber, and appropriate safety precautions must be taken. When SF_6 is used in spark-gaps a highly toxic gas is also produced and such gaps should be well flushed out before opening.

The chamber was extensivly modified to overcome pin corrosion (from the resistive solution), parasitics and electrical tracking down the sides of the chamber wall.

3.3 Second Design

3.3.1. Discharge Chamber

A plastic tube of i.d. $4\frac{1}{4}$" was used as the basis for the new chamber. 300 x 330Ω/2W solid carbon resistors were used in a random array to give a discharge cross-section of 5cm x 5cm and length 70cm. Solid resistors suffer from the disadvantage that they occasionally explode or breakdown. Reliable resistors are very expensive. In this design cheap(Radio-Spares) resistors were chosen, sothat component failure was experienced every few weeks. Liquid resistors are self-healing. However, the pins and electrolytes, as used above, caused serious corrosion problems. Subsequent to the present construction, it was found that hard-drawn stainless steel and either ammonium sulphate or potassium carbonate aqueous solutions would have proved suitable for the pins and electrolyte. This new combination is worth serious consideration for any future design. An aluminium electrode 5cm x 71cm, with rounded corners, was

engraved to remove the specular surface. Six electrical connections were soldered onto the lower surface. These were fed through the tube, to present a vacuum seal. The inside of the tube was covered in two layers of fibre-glass and the end-plates were sprayed with Nextel optical matt-black paint.

3.3.2. Electrical Circuit

The electrical circuit was identical with the half of the previous circuit that fed one module.

3.3.3. Optical Resonator

Initially, the resonator shown in Fig.3.3.,which was designed for component convenience, was tried. On focusing the output, using a 4m radius mirror, rings were obtained, although there was still a small parasitic background originating from the aperture edges. The output energy was also low (1.2J) and it is clear that a large fraction of the active volume is not included in this cavity. The use of infrasil has the advantages of higher optical quality and is less susceptable to damage, but is more expensive than salt.

In order to decrease aberrations the Brewster output window was replaced by the cavity mirror, as shown in Fig.3.4. The energy was also increased by use of the confocal unstable resonator shown in the same figure. A typical output burn is given in Fig.3.5. The output energy was found to be in excess of 2J and highly stable.

3.3.4. Operating Parameters

The optimum value for r was found to be 10 for hydrogen and 30 for propane. A marginally higher energy and power were obtained at $V_C \gtrsim$ 60KV for propane. The reverse was found to be true for lower charging voltages. The energy and power outputs for these two gases at optimum value of r, using the resonator shown in Fig.3.3., is given in Fig.3.6.,3.7.

3.4. HF Parameter Studies

A parametric study of the HF chemical laser described above was

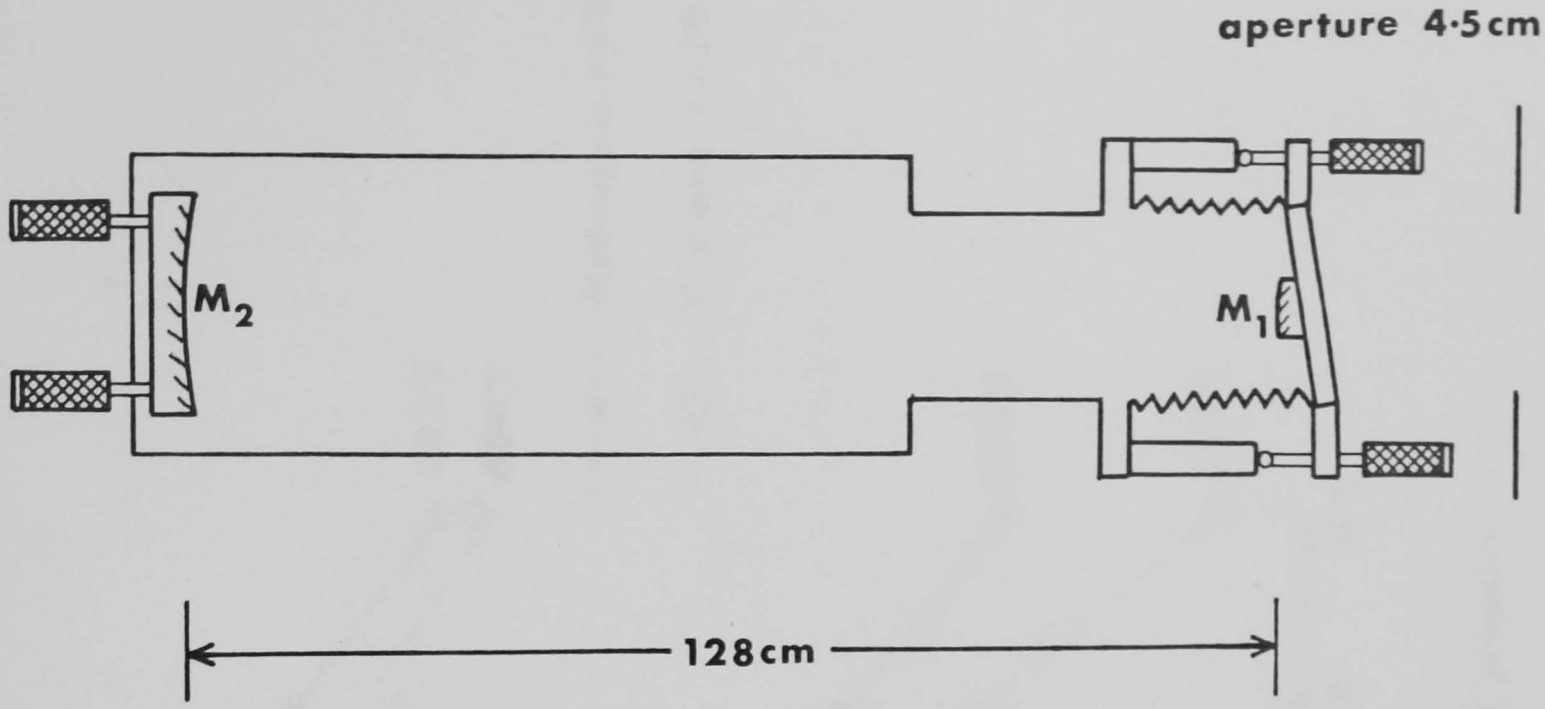

M_1 = 2 cm DIA 10 m rad convex Au on NaCl flat at 15°

M_2 = 2″ DIA 20 m rad concave Au

Fig.3.4. Confocal unstable resonator.

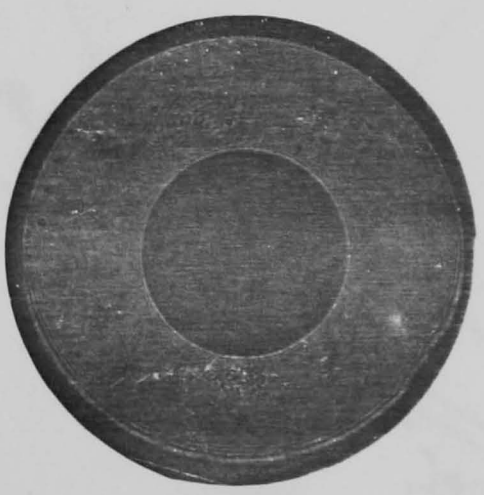

Fig.3.5. Output burn from HF laser using the above resonator.

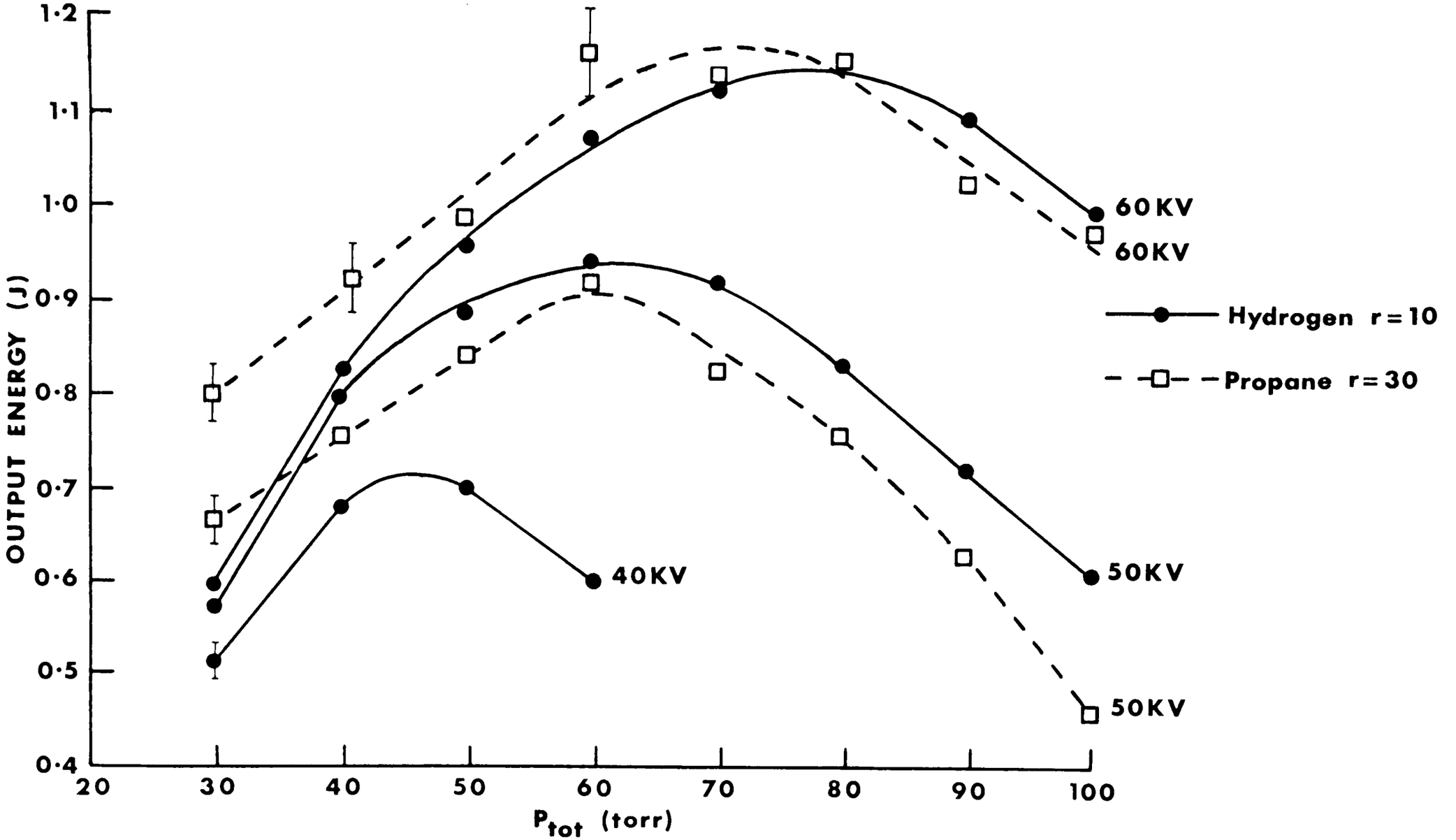

Fig.3.6. Output energy versus total gas pressure for hydrogen and propane.

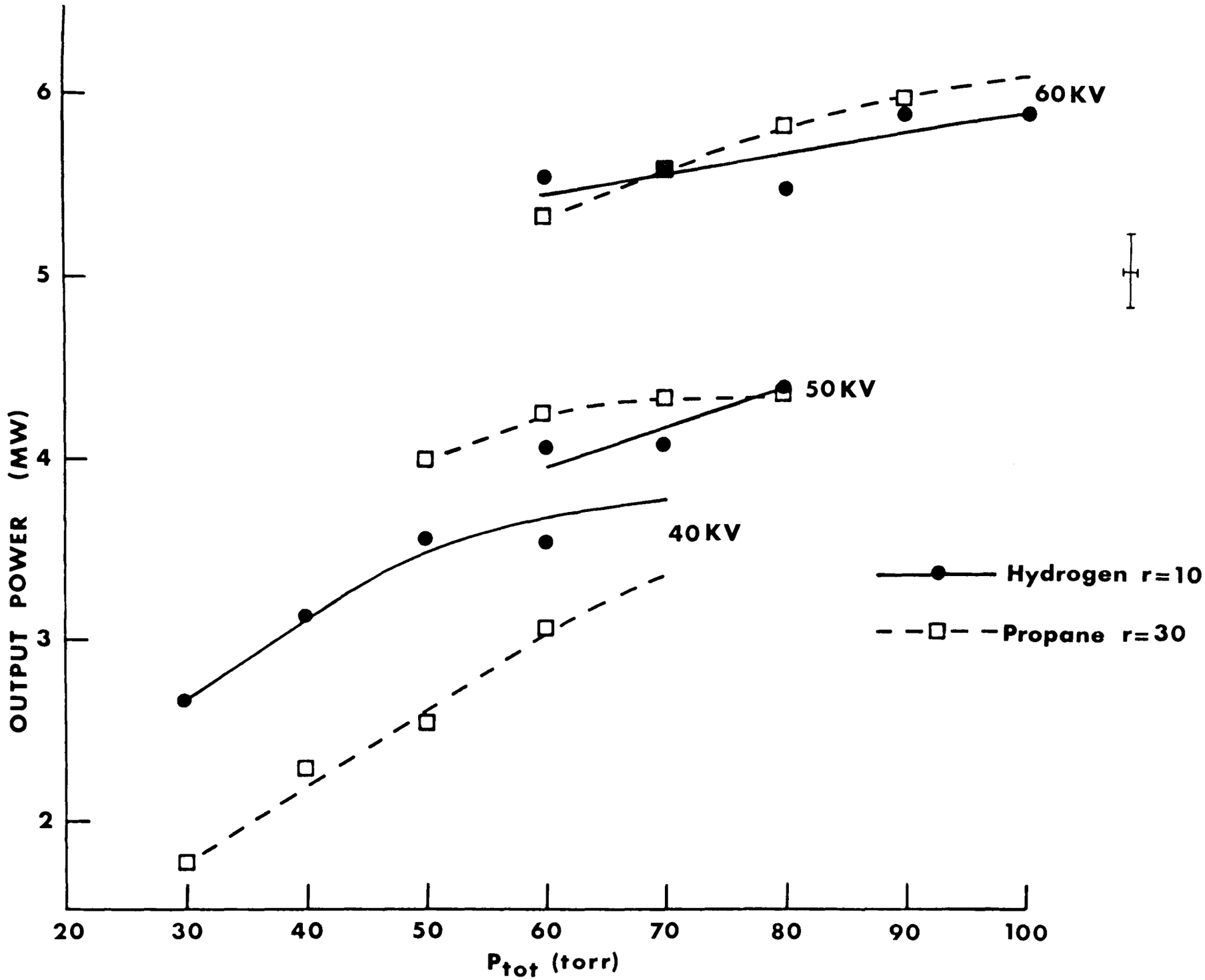

Fig.3.7. Output power versus total gas pressure for hydrogen and propane.

carried out at room temperature using hydrogen, propane or butane as the hydrogen donor. Obara and Fujioka[5] give the following as the main reactions :-

$$SF_6 + e^- \rightarrow F + SF_5 + e^- - 71.4 \text{ to } 75.9 \text{ Kcal.mole}^{-1}$$

$$F + HX \rightarrow HF(V) + X + \text{energy (chemical pumping reaction)}$$

$$HF(V) + M \rightarrow HF(V-1) + M$$

where, HF(V) = vibrationally excited HF
HX = hydrogen donor
M = collisional deactivators of HF(V)
with H_2 and CH_4 $V \leq 3$, for C_4H_{10} $V \leq 4$.

In these studies we define :-

r = partial pressure SF_6/partial pressure hydrocarbon
γ = partial pressure hydrocarbon/pressure (hydrocarbon + SF_6)
P_{tot} = total pressure
V_c = charging voltage
V_d = discharge voltage
E_{out} = output energy
P_{out} = output power
d = inter-electrode gap spacing
p_{SF_6} = partial pressure of SF_6

In order to determine the optimum value of r, E_{out} was measured, using a Lumonics 20D pyroelectric joulemeter, as a function of r, keeping P_{tot} and V_c constant. An example for hydrogen, using the confocal unstable resonator, is shown in Fig.3.8. indicating an optimum value of r ≃ 10 under the stated conditions. The variation of r with V_c is indicated for butane in Fig.3.9. The peak of these

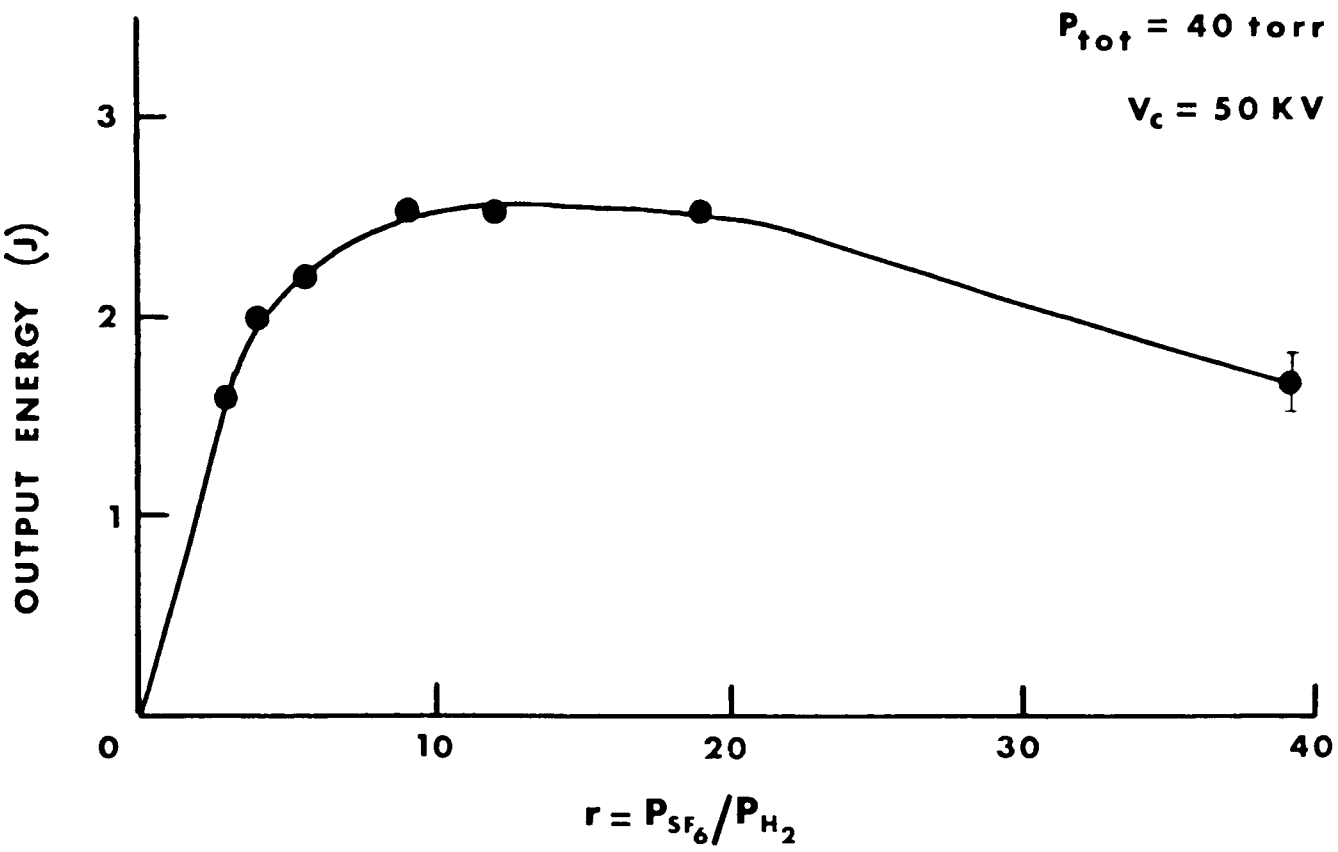

Fig.3.8. Output energy versus r (Hydrogen) using the confocal unstable resonator.

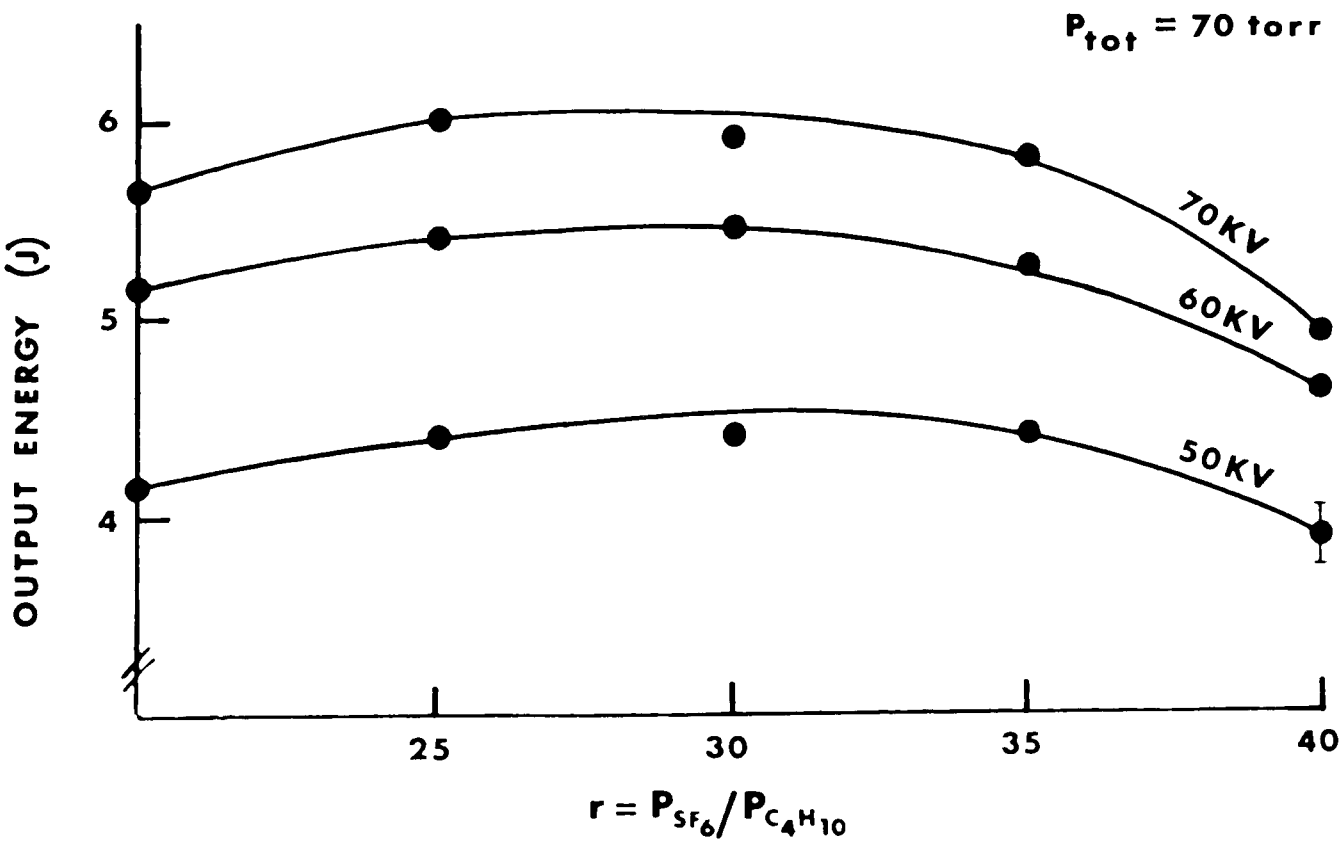

Fig.3.9. Output energy versus r (Butane) using the confocal unstable resonator.

curves is relatively insensitive to V_c and also P_{tot}, and thus we can justify the detailed investigations at r = 10 for hydrogen and r = 30 for propane and butane. E_{out} and P_{out} for various V_c are given as a function of P_{tot} in Fig.3.6.,3.7. It has been shown by Obara and Fujioka[5] that a similar plot of peak power versus P_{tot} for various V_d gives a constant value for the ratio V_d/P_{tot}. $V_d/(p_{SF_6}.d)$ is therefore also a constant, indicating that the mean electron - SF_6 collision energy is approximately constant for the maximum peak powers. As the mean free path (m.f.p.) of electrons in SF_6 gas is $(\pi r^2 n)^{-1}$, where πr^2 is the collision cross-section for neutral SF_6 and n is the SF_6 gas density (which can be estimated from Loschmidt's number for a perfect gas), Obara and Fujioka obtain the mean electron collision energy to be slightly less than the disociation energy $SF_6 \rightarrow SF_5 + F$. This result has also been verified by Deka and Dyer[6].

The variation of E_{out} with P_{tot} and V_d for C_3H_8 and H_2 are given in Fig.3.10.-3.13. The variation of peak power with P_{tot} and V_d is given in Fig.3.14.,3.15. for hydrogen, using the pulse lengths shown in Fig.3.16.,3.17. As expected, the maximum peak power increases with V_c. The output energy depends upon the number of SF_6 disociations, whereas the output power depends upon the rate of disociation. At low pressures the electron mean free path is large, giving efficient disociation. E_{out} is therefore proportional to p_{SF_6}. At high pressures, the short electron mean free path reduces the number of electrons with the disociation energy, and so E_{out} is inversely proportional to p_{SF_6}. The increase in peak power with V_d gives a small dependance for the low pressures, in agreement with the results of Obara and Fujioka, and they explain this as being due to the high mean electron collision energy. It can be seen that, under conditions of optimum r, the highest power outputs are achieved at high V_d and P_{tot}.

The variation of output energy with γ for various P_{tot} is given in Fig.3.18. for propane. The peak output energy occurs at smaller γ as P_{tot} is increased up to a limit of 70 torr. Above this pressure

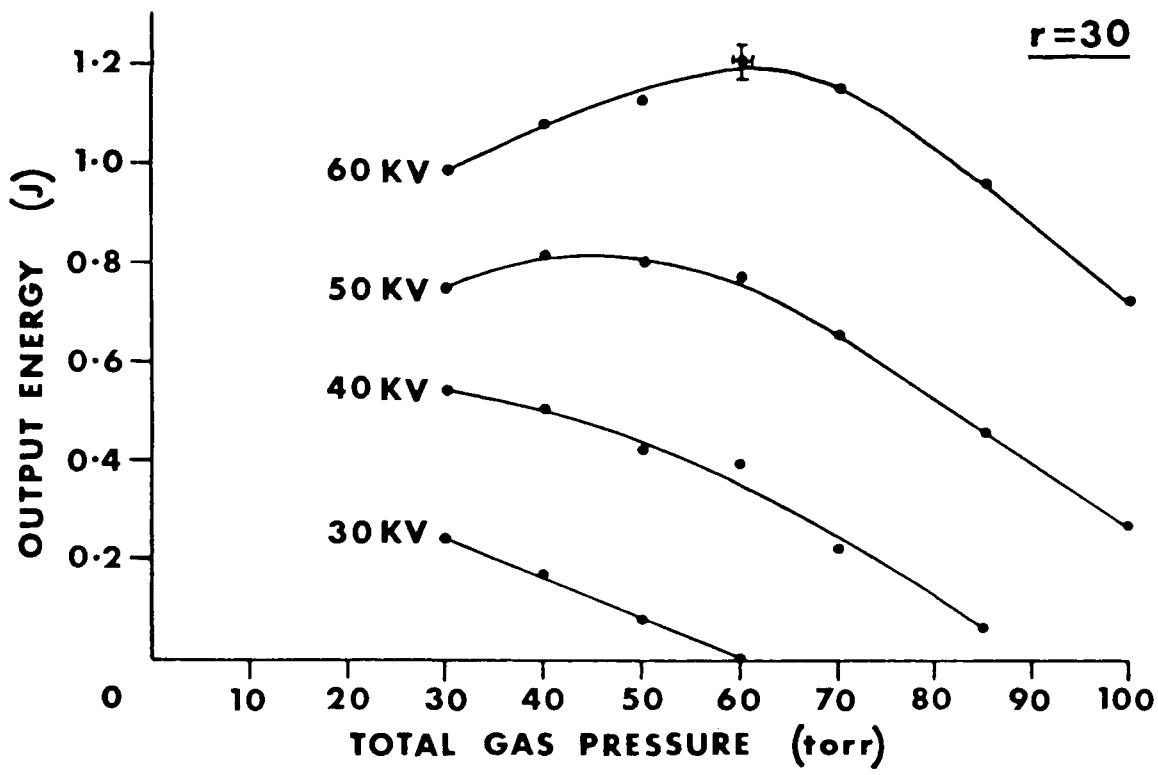

Fig.3.10. Output energy versus total gas pressure for propane (Semi-confocal unstable resonator).

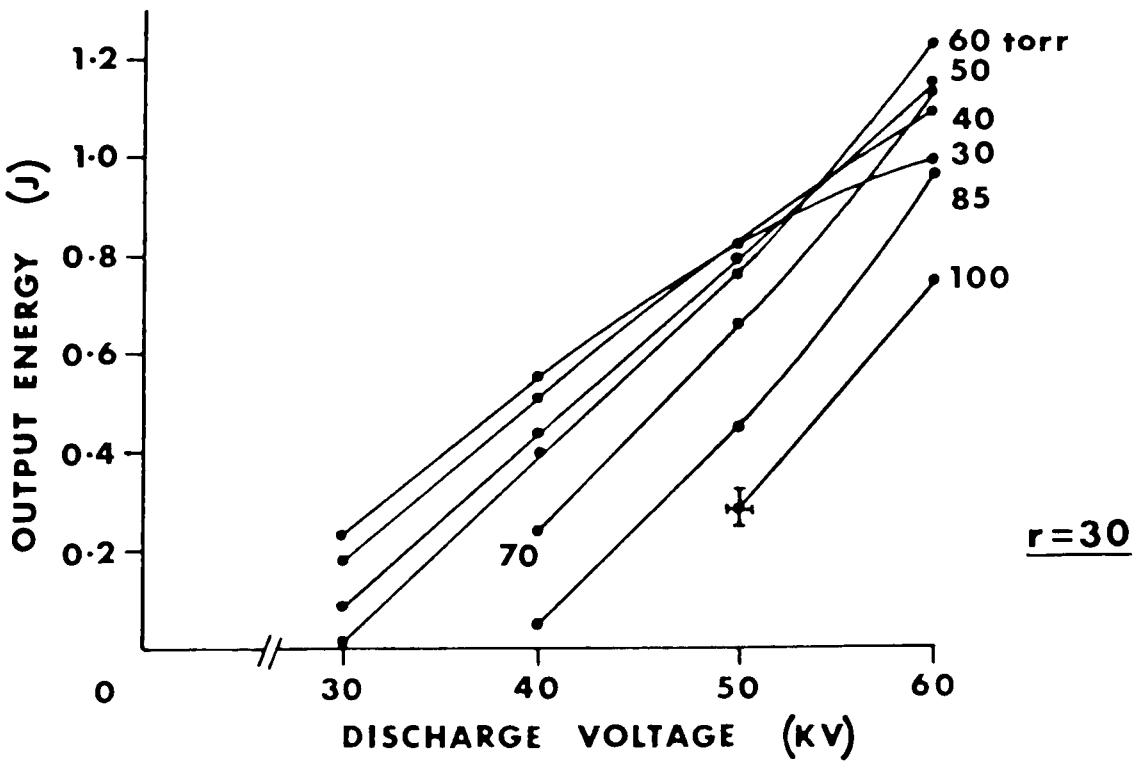

Fig.3.11. Output energy versus discharge voltage for propane (Semi-confocal unstable resonator).

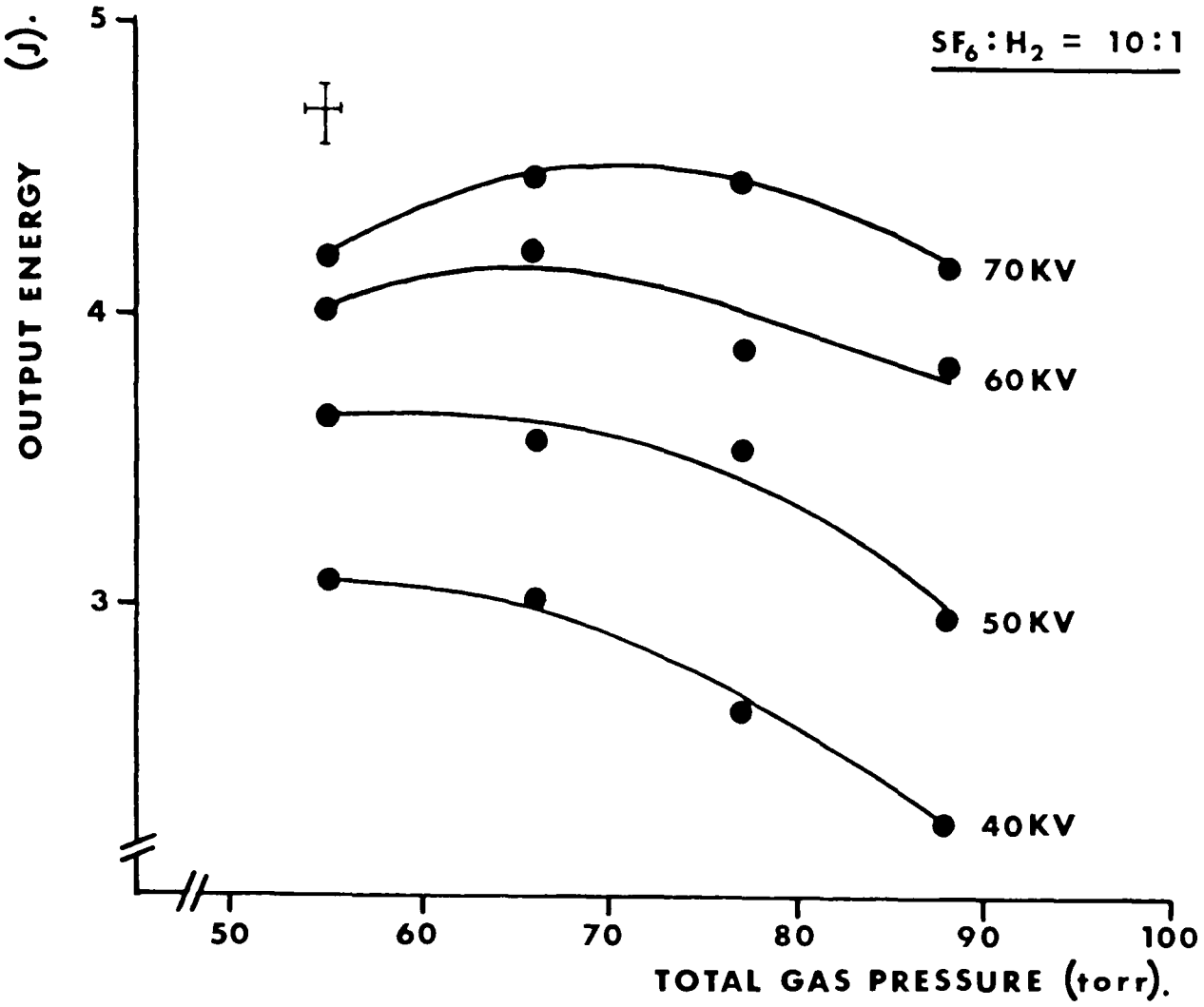

Fig.3.12. Output energy versus total gas pressure at various discharge voltages for hydrogen (Confocal unstable resonator).

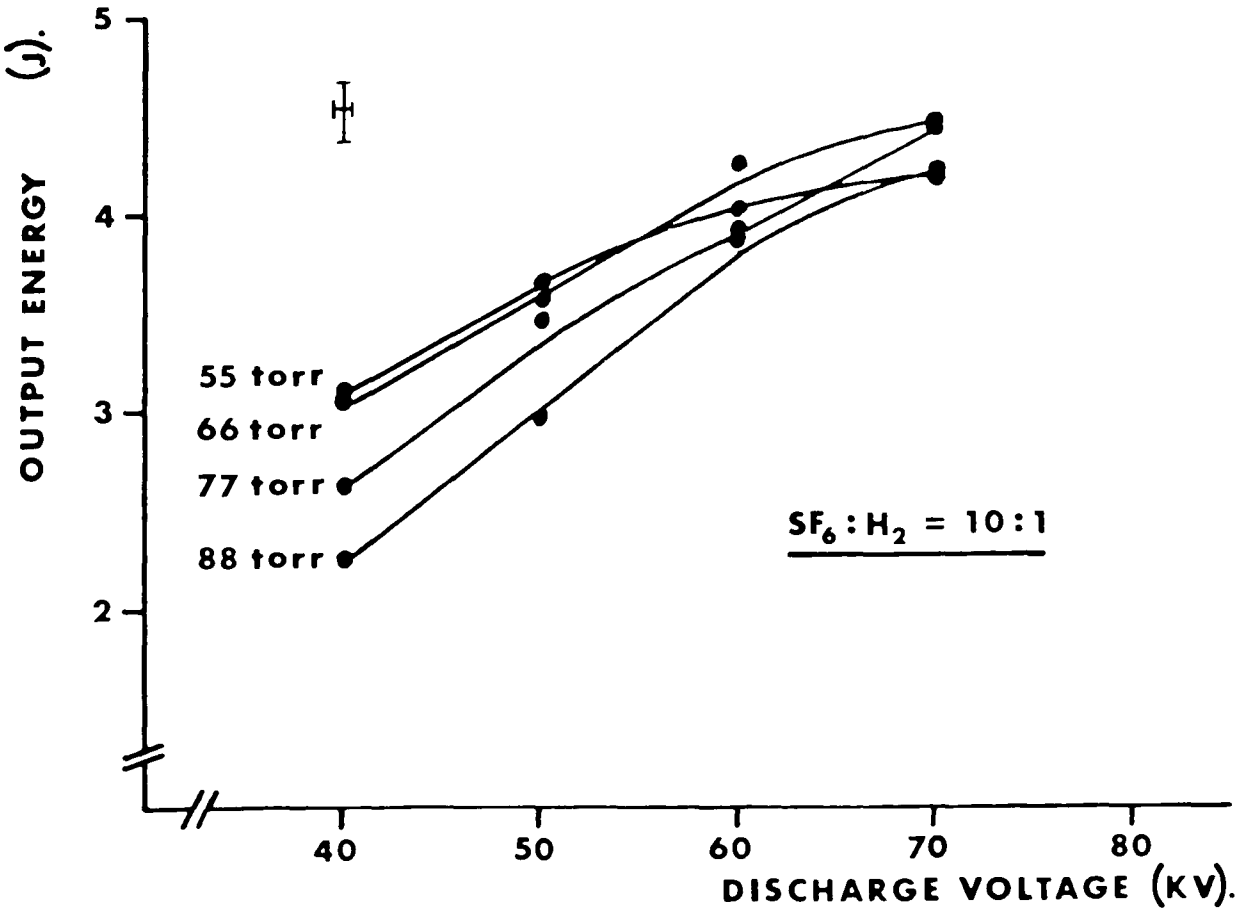

Fig.3.13. Output energy versus discharge voltage, at various total gas pressures, for hydrogen (Confocal unstable resonator).

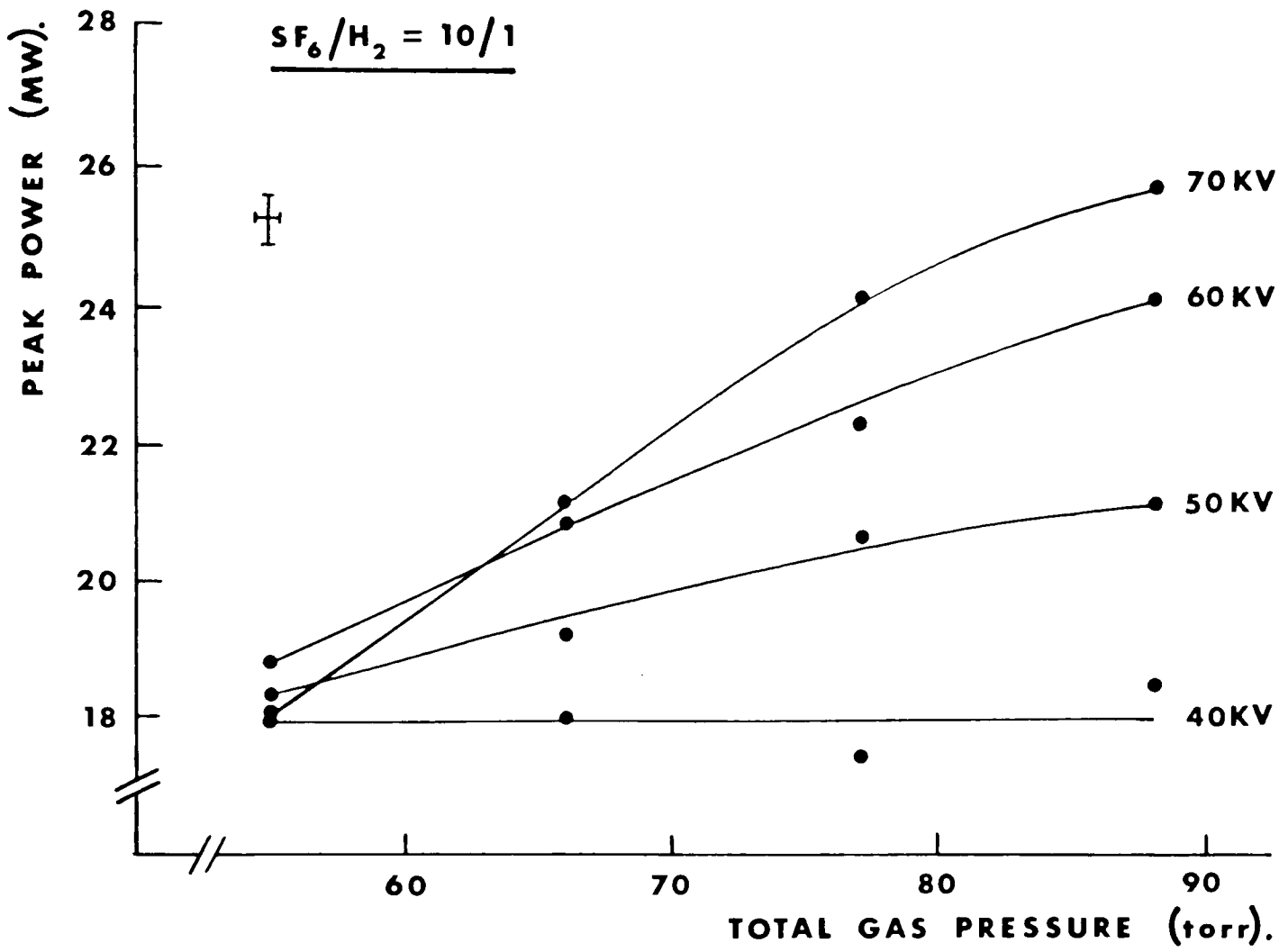

Fig.3.14. Peak power versus total gas pressure for hydrogen (Confocal unstable resonator).

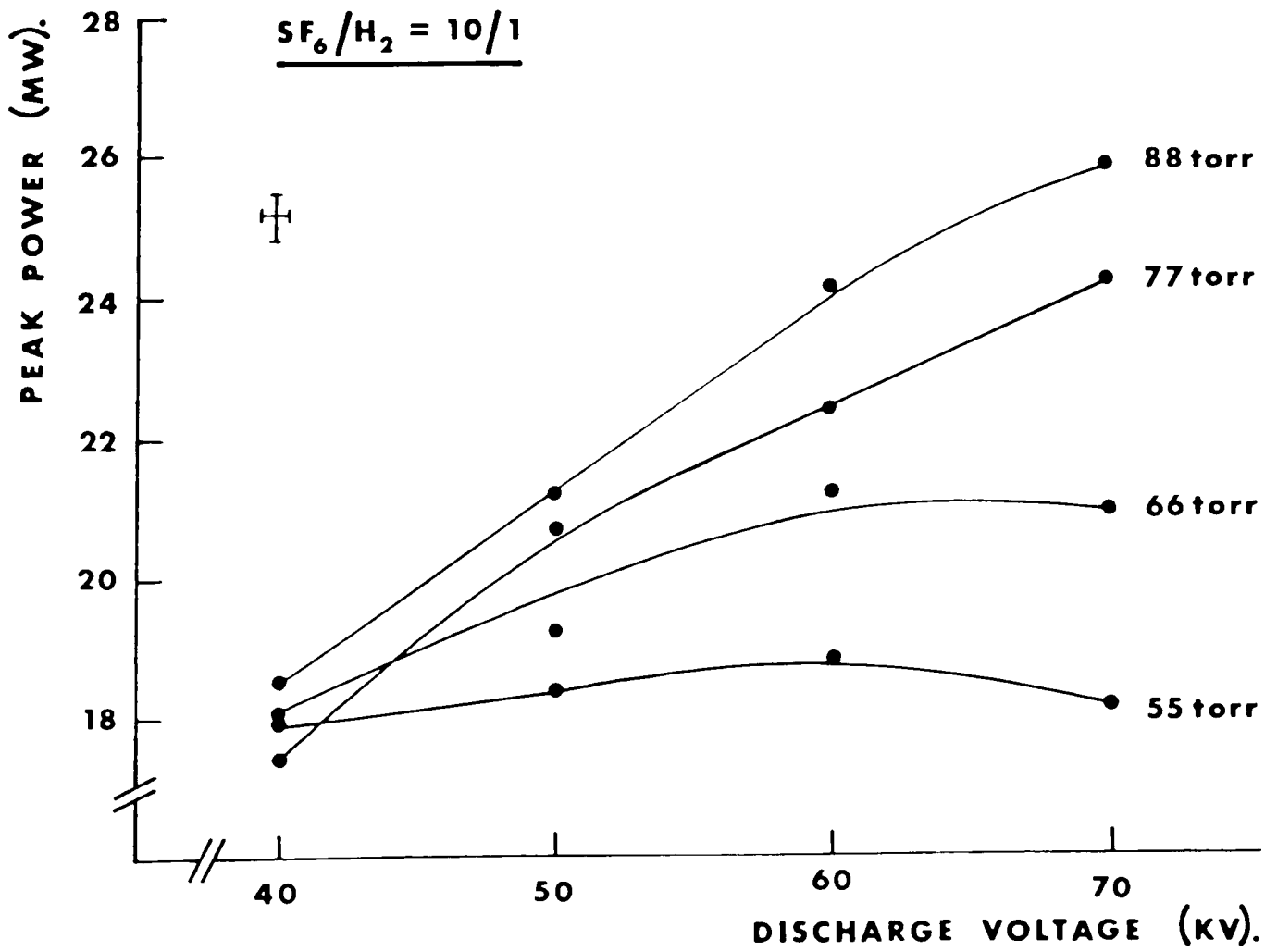

Fig.3.15. Peak power versus discharge voltage for hydrogen (Confocal unstable resonator).

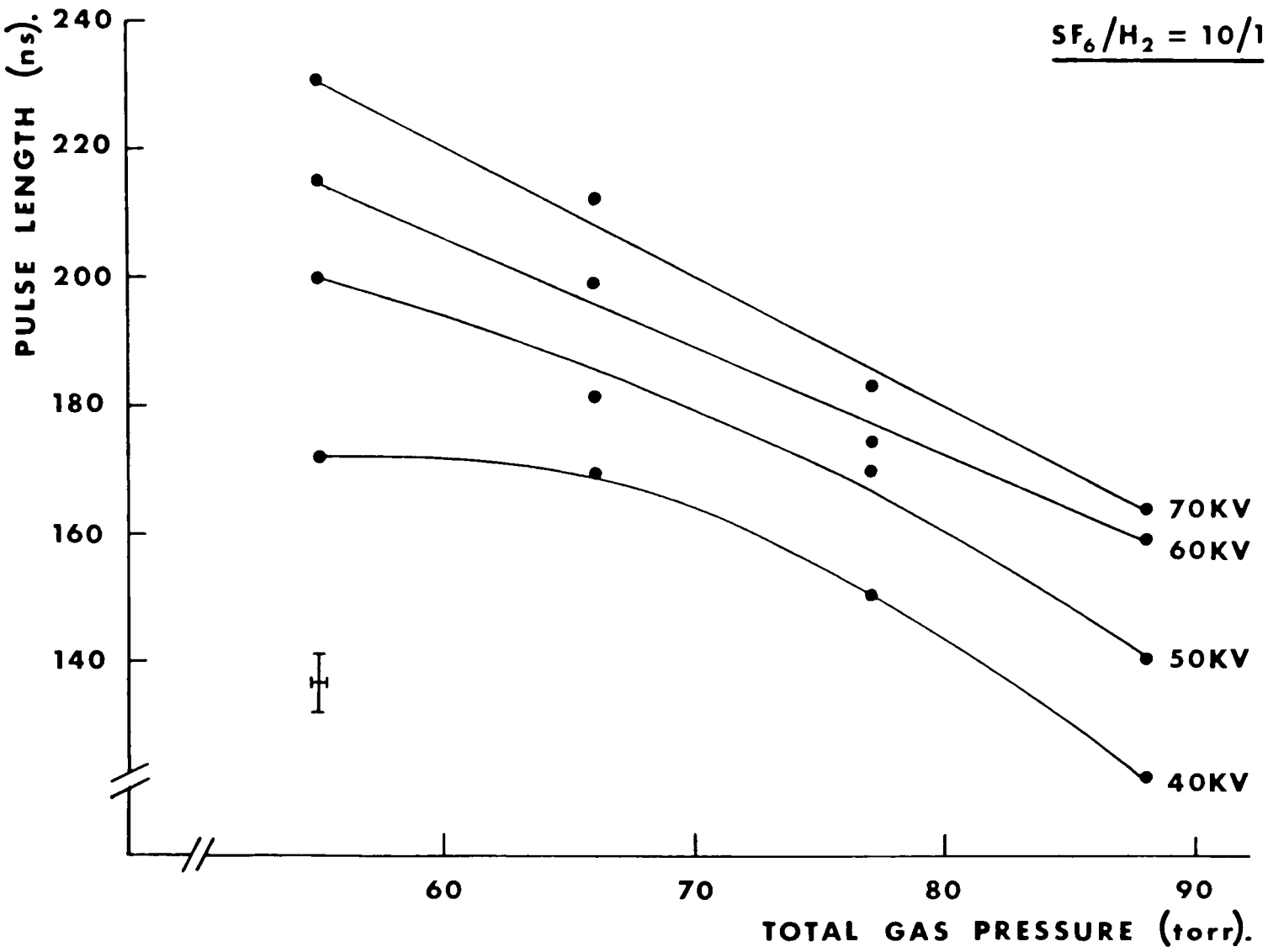

Fig.3.16. Pulse length versus total gas pressure for hydrogen (Confocal unstable resonator).

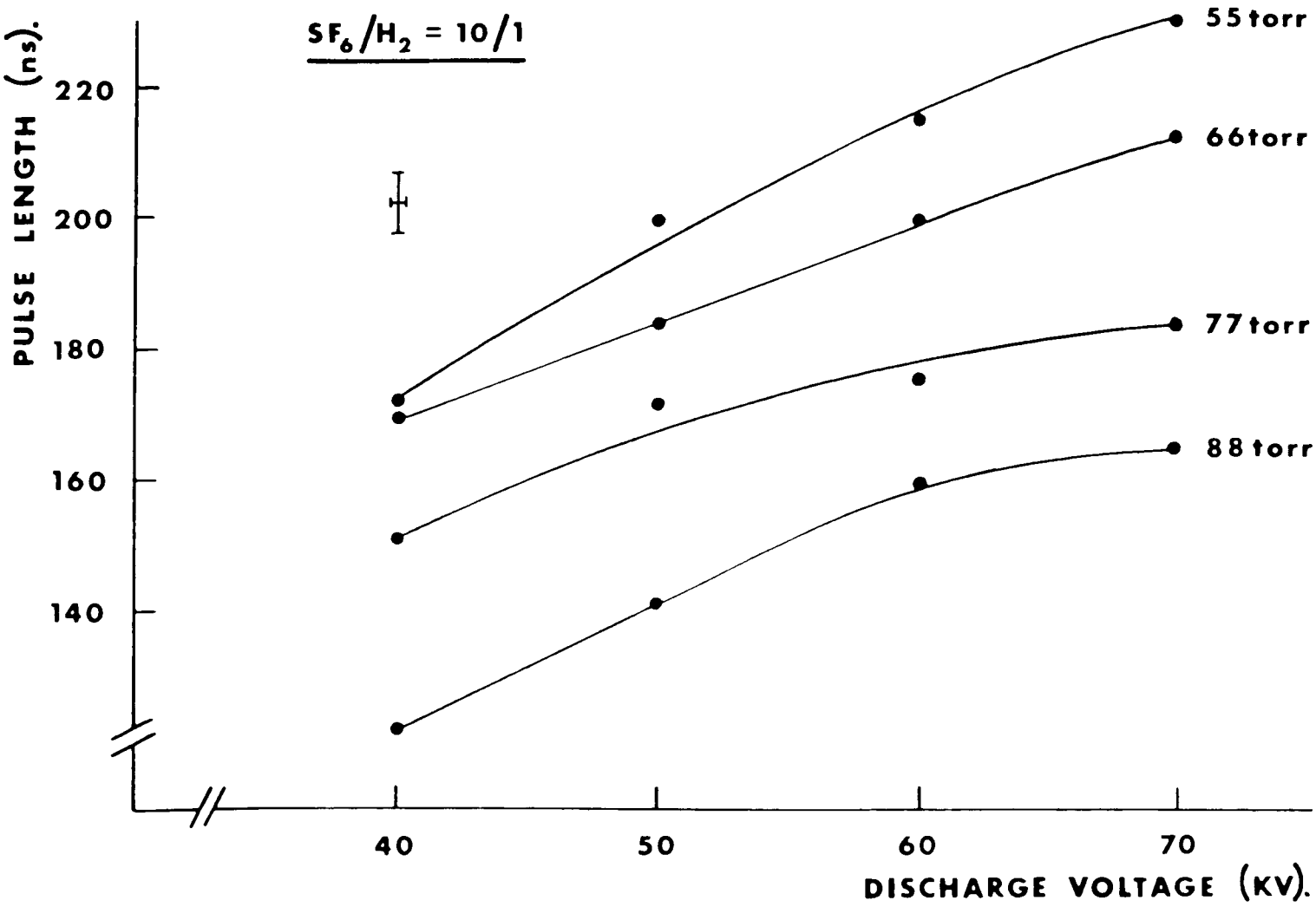

Fig.3.17. Pulse length versus discharge voltage for hydrogen (Confocal unstable resonator).

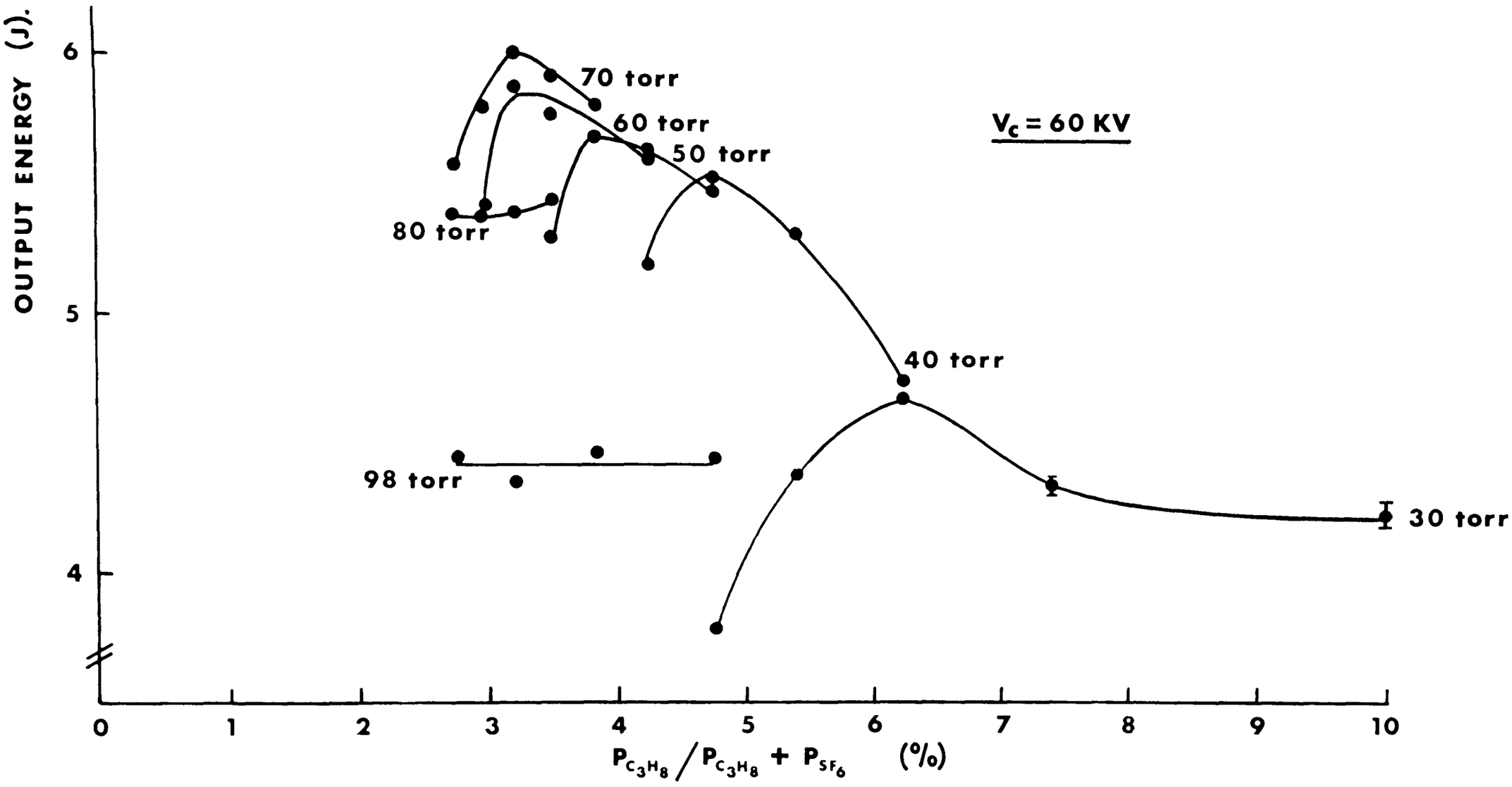

Fig.3.18. Output energy versus γ for propane at various total pressures (Confocal unstable resonator).

the output energy fell, and did not peak in the region investigated. As P_{tot} is increased, the increase in the SF_6 partial pressure increases the amount of disociation, and thus the output energy. A low γ means a lack of the hydrogen donor, and therefore an incomplete chemical pumping process. At high γ, the excess of the hydrogen donor deactivates HF(1) and thus decreases output[5]. The optimum γ for energy was found to occur at lower values than for power, in agreement with Deka and Dyer[6] - the expla/nation being that although the HF production rate decreases, vibrational relaxation of HF by the hydrogen donor is reduced, leading to longer duration pulses.

3.5. References

1) Pummer H., Breitfeld W., Wedler H., Klement G. and Kompa K.L. Appl. Phys. Lett. 22, 301-2, 1973.

2) Marcus S. and Carbone R.J. IEEE J. Quant. Elect. (corresp.) QE-7, 493-4, 1971.

3) Jones C.R. Appl. Phys. Lett. 22, 653-655, 1973.

4) Chester A.N. Appl. Optics 12, 2139-46, 1973.

5) Obara M. and Fujioka T. Jap. J. Appl. Phys. 13, 995-1000, 1974.

6) Deka B.K. and Dyer P.E. IEEE J. Quant. Elect. QE-14, 661-73, 1978.

CHAPTER 4

HF LASER-TARGET INTERACTION STUDIES (VACUUM ENVIRONMENT)

4.1. Introduction

There is an absence of data available on the interaction of high-power HF laser radiation with solid targets in a vacuum. This is to be regretted, as, for this laser, the critical plasma density is intermediate to that obtained using CO_2 and Nd:glass lasers :-

LASER	WAVELENGTH (μm)	CRITICAL ELECTRON DENSITY n_{ec} (cm^{-3})
Ruby	0.6943	2.313×10^{21}
Neodymium:glass	1.06	9.92×10^{20}
Hydrogen Fluoride*	~2.87	$\sim 1.36 \times 10^{20}$
Deuterium Fluoride*	~3.8	$\sim 7.73 \times 10^{19}$
Carbon Dioxide	10.6	9.92×10^{18}

* HF and DF lasers are broad-band, the wavelength given corresponds to the line with maximum energy[1].

TABLE 4.1.

The use of the HF laser thus allows plasma production to be investigated in a new and potentially interesting regime. It is hoped that the high power and efficiency of modern HF lasers[2] might lead to the possibility of producing very high target irradiances. This work demonstrates that good beam quality can be extracted from modest systems and useful irradiances achieved. In addition, characteristics of plasmas produced by a pulsed unstable-resonator HF laser are presented and scaling laws for the interaction established. Soft x-ray emission from an HF plasma is reported for

the first time, permitting a determination of the plasma temperature.

4.2. Laser Applications

The 2.2J laser system, described on p48, was used primarily to study specular reflection from tilted plane polished targets, and to provide ion-velocity scaling data at $\leq 2 \times 10^{10} W.cm^{-2}$ for a range of targets.

A $\sim$ 0.7J, 5MW high-radiance, unstable resonator HF laser[1] was employed to irradiate aluminium and carbon targets in a vacuum ($<10^{-4}$torr), using the experimental configuration shown schematically in Fig.4.1. This system was used primarily for x-ray and ion-velocity scaling measurements at $\lesssim 7 \times 10^{10} W.cm^{-2}$. It is to be noted that the lower energy laser gave the highest power on target. To a large extent this was a direct consequence of the focal-spot radius.

4.3. Focusing

4.3.1. Low Power System (A)

The laser output, Fig.4.2., was directed by a 45° turning mirror onto a 4" diameter 22" focal length plano-convex lens. The appearance of the beam at this stage is shown in Fig.4.3. The beam was now focused onto the target via a vacuum NaCl entry window of high optical quality. It is worth pointing out here that the diffraction limited spot size is $\sim$ 70μm (diameter of the first dark ring), and spherical aberration blurr diameter is $\sim$ 40μm. This gives a total theoretical diameter of $\sim$ 80μm, which is to be compared with the 200μm actually measured according to the Polaroid burn spot (which is likely to give an over estimate) and $\sim$ 120μm calculated from an extrapolation of diagnostic results from the high power system (where the spot size was more accurately determined).

4.3.2. High Power System (B)

Fig.4.1. shows how a 25cm focal length mirror at an effective aperture ratio of $\sim$ 6.5 was used to focus the beam in this system. The calculated diameter of the central lobe of the focused unstable

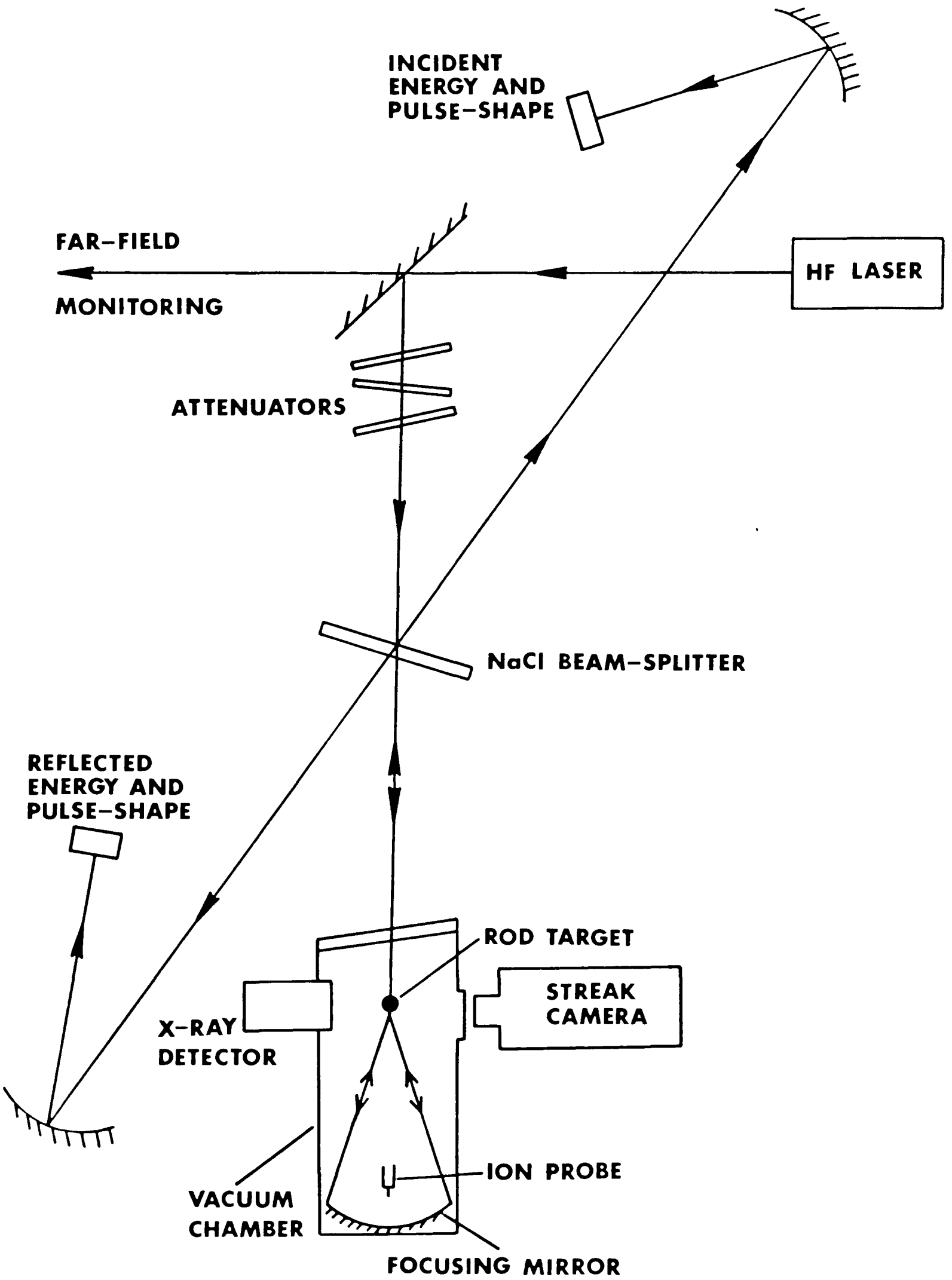

Fig.4.1. Schematic experimental configuration.

Fig.4.2. Output burn on exposed Polaroid, system A.

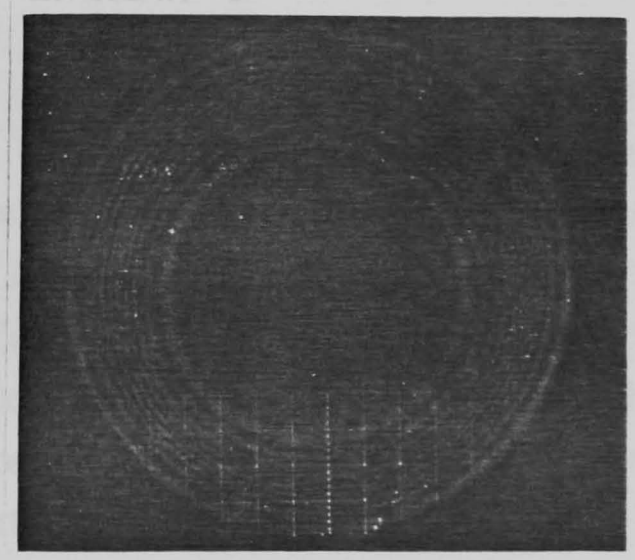

Fig.4.3. Burn on exposed Polaroid incident on focusing lens 1·5m from output, system A.

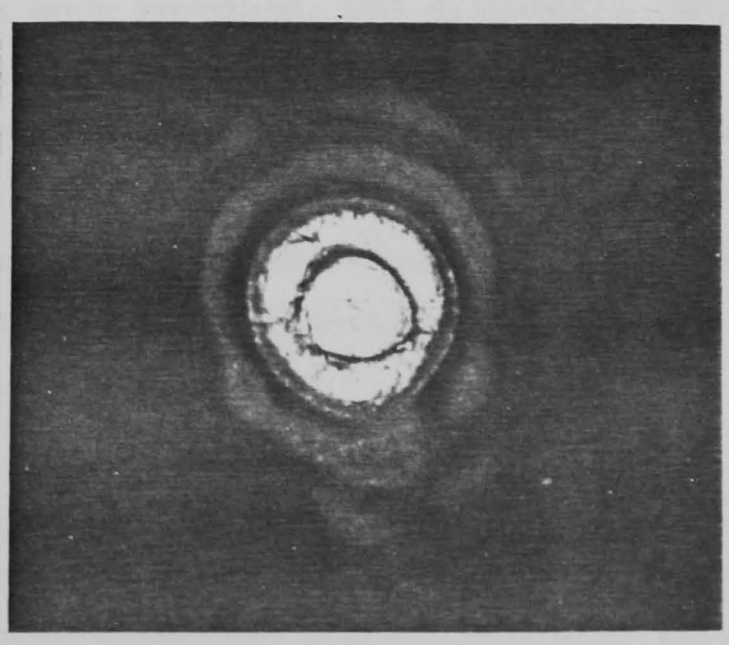

Fig.4.4. Magnified far–field distribution, system B.

resonator beam was $\sim$ 40μm and, based on the known energy distribution in the focal plane[1], the average irradiance, ϕ_p, over the central lobe was estimated to be $7 \times 10^{10} W.cm^{-2}$. The appearance of the output beam burnt on exposed Polaroid 410 film was uniform, but only just visible. The far-field distribution of the laser was monitored using auxiliary focusing optics, as shown in Fig.4.1., sothat any misalignment of the resonator could be observed and corrected as necessary during the experiments. The distribution is given in Fig.4.4.

4.4. Target Chambers

4.4.1. Low Power System

A photograph of the target chamber is given in Fig.4.5. An ultimate vacuum of 10^{-6}torr is achieved by use of a rotary/diffusion pump combination without a cold-trap. Clement et al[3] have shown that higher pressures influence ion measurements by the process of charge exchange. A fast cycle time (better than 20min to 10^{-5}torr) for a clean system aided experiments that involved change of targets etc. The vacuum system was built "fail-safe" sothat it could be kept running over-night.

The chamber itself was of internal diameter 60cm and had a number of side ports which could be used to hold windows, diagnostics etc. The base of the chamber was designed to take magnetic clamps. The whole system was made moveable, and diagnostic cables were triaxially piped into a doubly-screened room to lessen noise pick-up. The salt entry window was protected by a resistive heater that gave uniform heating. It also had the advantage of involving no lighting and of a dust cover. The window was found to suffer far less damage from the atmosphere than other NaCl optics protected with a lamp or plastic cover.

4.4.2. High Power System

A compact chamber employing high quality optics was used, enabling a large solid angle for x-ray and streak detection to be achieved.

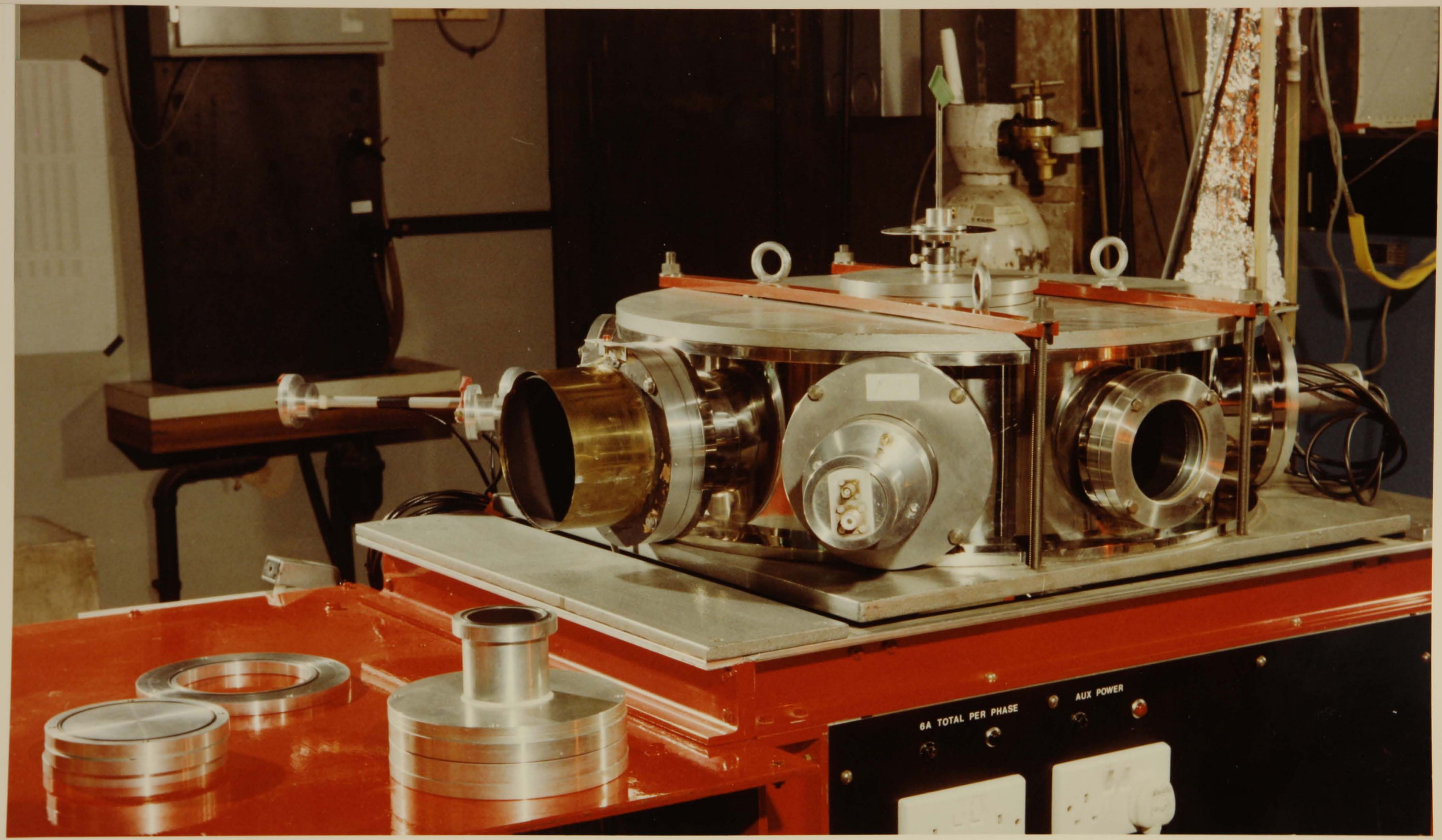

Fig.4.5. Photograph of the target chamber.

An ultimate vacuum of 10^{-5}torr was achieved using a low capacity rotary/diffusion pump combination.

4.5. Results

4.5.1. Low Power System

a) Ion Measurements

Faraday-cup charge-collecting probes were positioned in the target chamber and biased at -70V to collect positive ions. A typical bias characteristic curve is given in Fig.4.6. As the ion-signal at large distances was small, especially for low target irradiances, the laser pulse itself was used as a time-marker in the determination of the asymptotic ion expansion velocity. Fig.4.7., 4.8. shows typical ion-probe signals from polyethylene and copper. Photoelectric signals were not seen under these conditions. The incident energy was monitored using a Lumonics 20D pyroelectric joulemeter and the laser pulse-shape obtained with a high-speed, liquid-nitrogen cooled, gold-doped germanium detector. A typical pulse-shape is given in Fig.4.9.

The ion-velocity was measured as a function of target irradiance, material and azimuth - the target itself being inclined at 10° to prevent specular feedback to the laser system. The target irradiance was varied from 5×10^{10} to 3.5×10^{8}W.cm^{-2} by use of Inconel on Infrasil substrate attenuators[4,5]. These give an approximately wavelength independent attenuation. Target materials used were: polyethylene, carbon, aluminium, copper, silver and lead. These were in the form of 'Specpure' rods, which were freshly machined, polished and cleaned prior to use.

Results showing the ion-velocity scaling for the six targets at 15° and 40° from the beam axis, and in the horizontal plane, are shown in Fig.4.10.-21. 2/9 scaling, as predicted by the self regulating model, was obtained at 15° for polyethylene, carbon, aluminium, copper (approximately) and at 40° for polyethylene and lead. In other cases, a lower scaling was achieved. The higher Z materials tended to give multiple ion species, the predominant ones being included in the previous graphs.

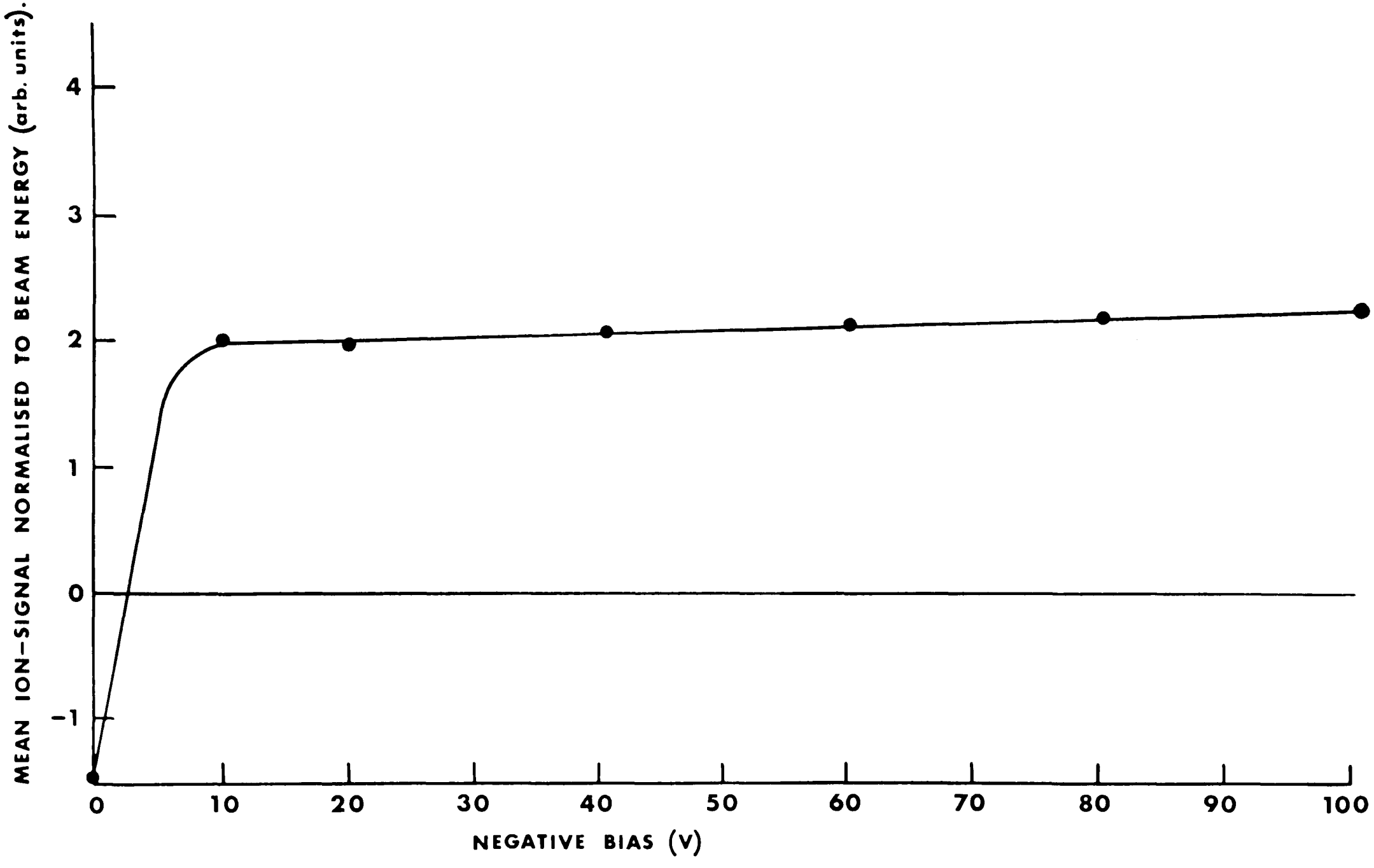

Fig.4.6. Typical bias characteristic curve.

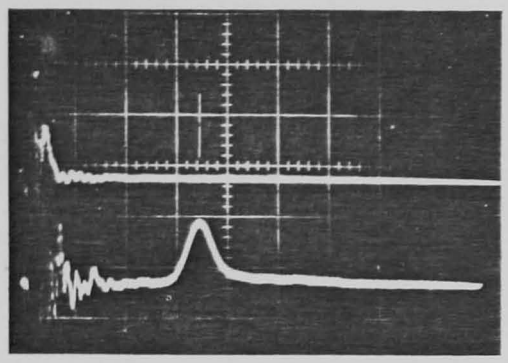

top: laser pulse time marker.

bottom: ion signal.

Fig.4.7. Polyethylene ion time of flight oscilloscope trace.

$\Phi = 1{\cdot}6 \times 10^{9}$ W.cm.$^{-2}$ 1μs/div.

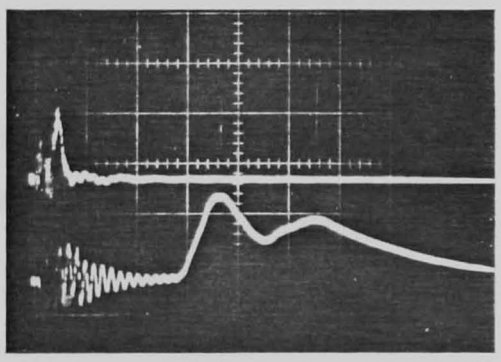

top: laser pulse time marker.

bottom: ion signal.

Fig.4.8. Copper ion time of flight oscilloscope trace.

$\Phi = 5{\cdot}4 \times 10^{9}$ W.cm.$^{-2}$ 1μs/div.

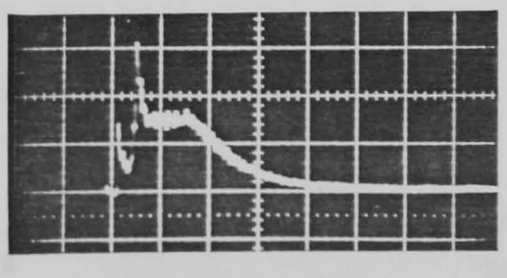

Fig.4.9. Laser pulse shape. 100 ns/div.

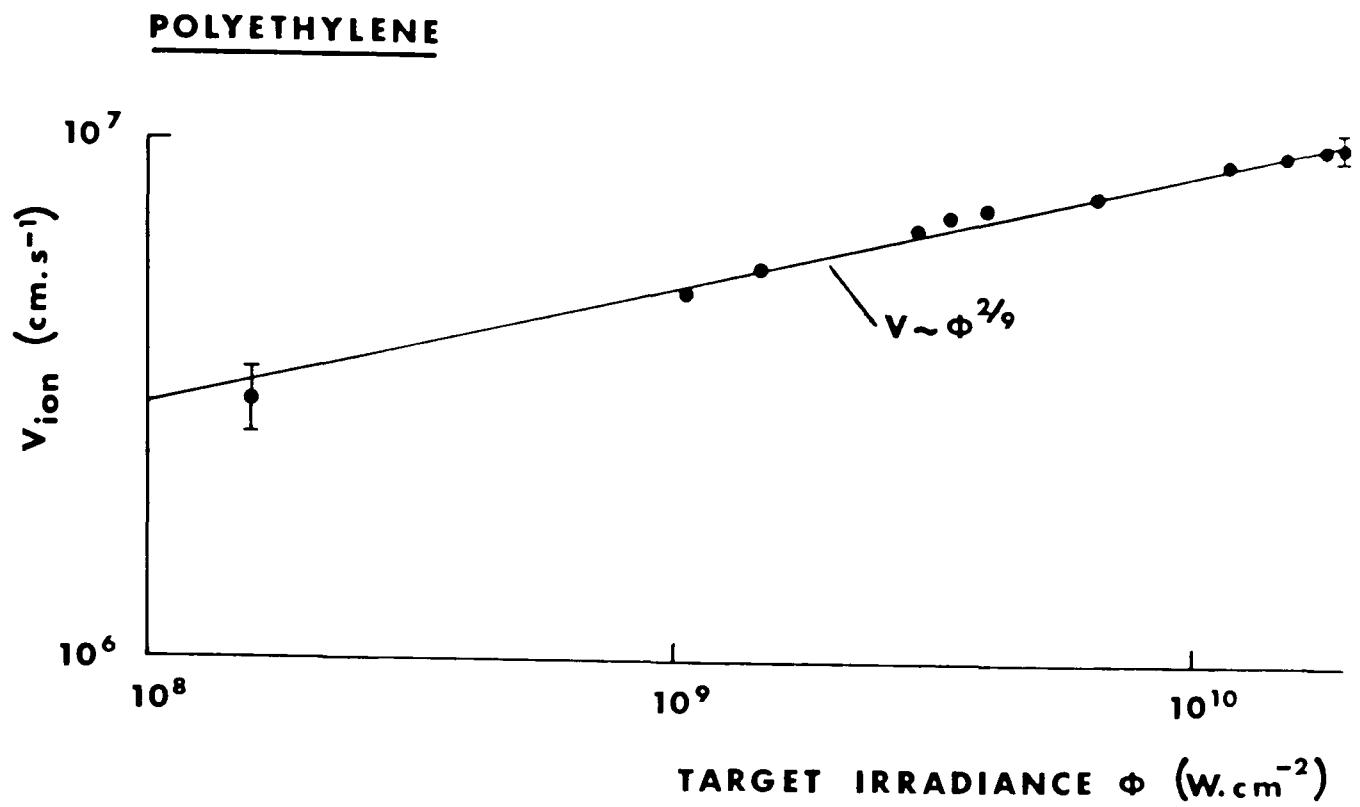

Fig.4.10. Asymptotic ion expansion velocity (15°) versus target irradiance (polyethylene).

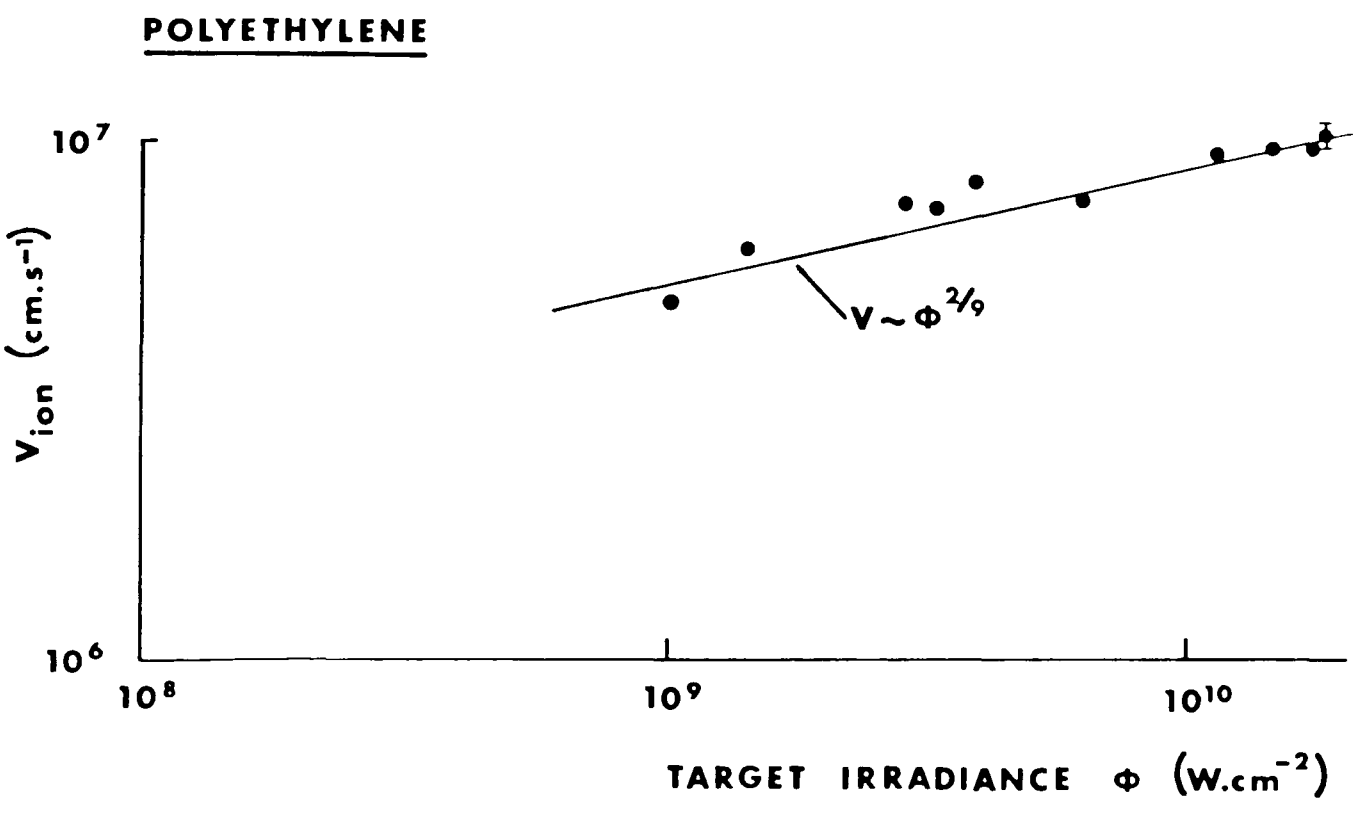

Fig.4.11. Asymptotic ion expansion velocity (40°) versus target irradiance (polyethylene).

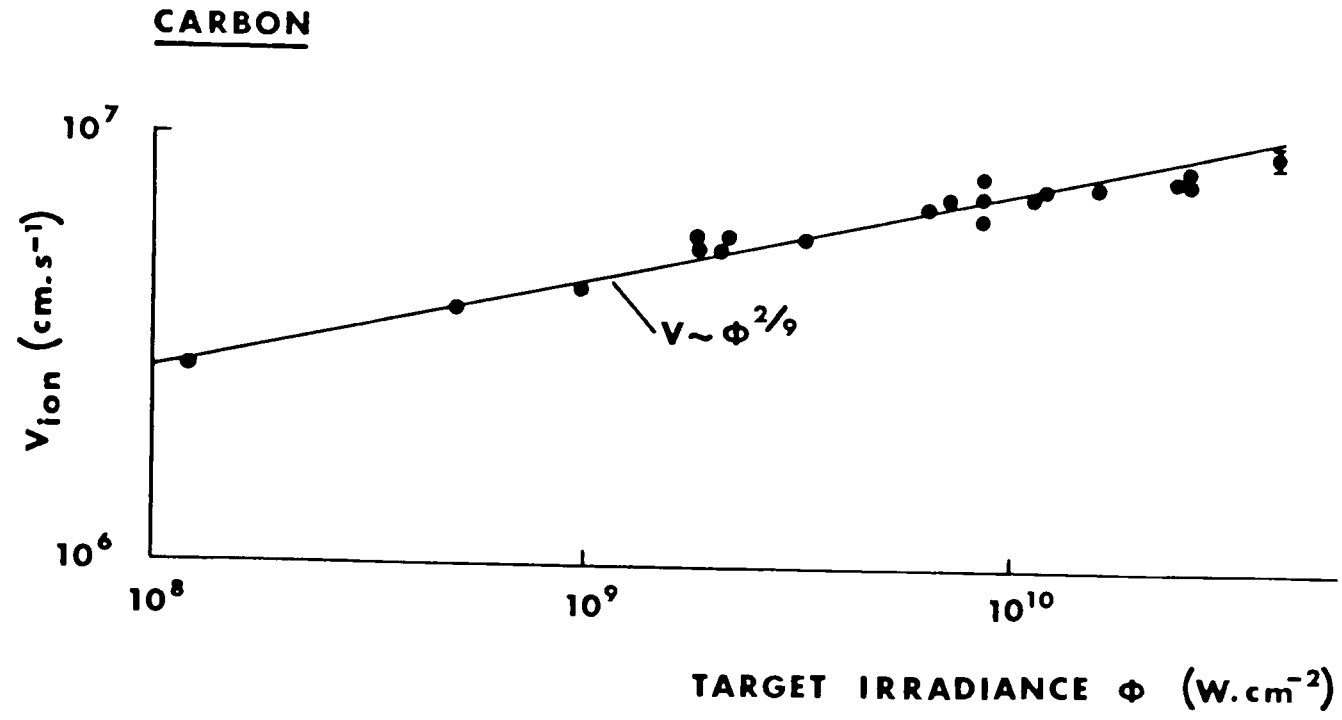

Fig.4.12. Asymptotic ion expansion velocity (15°) versus target irradiance (carbon).

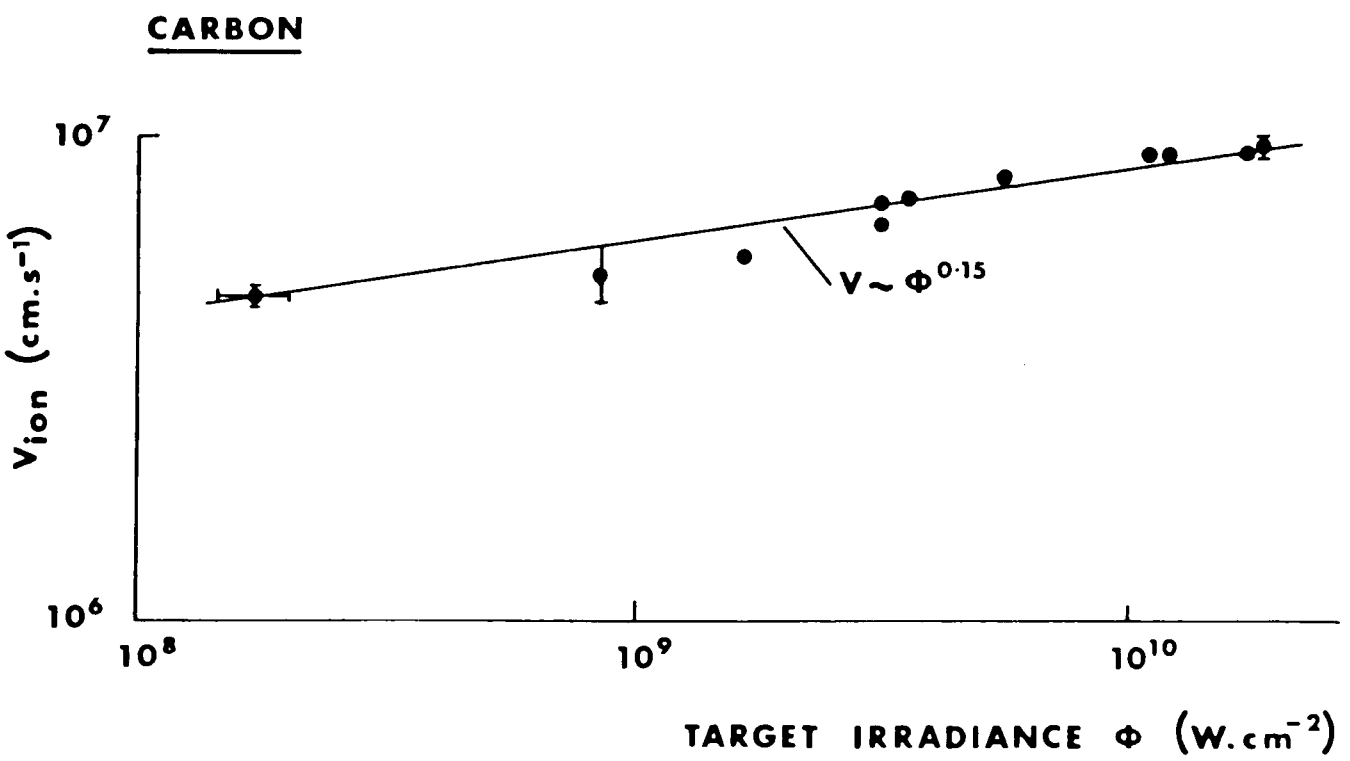

Fig.4.13. Asymptotic ion expansion velocity (40°) versus target irradiance (carbon).

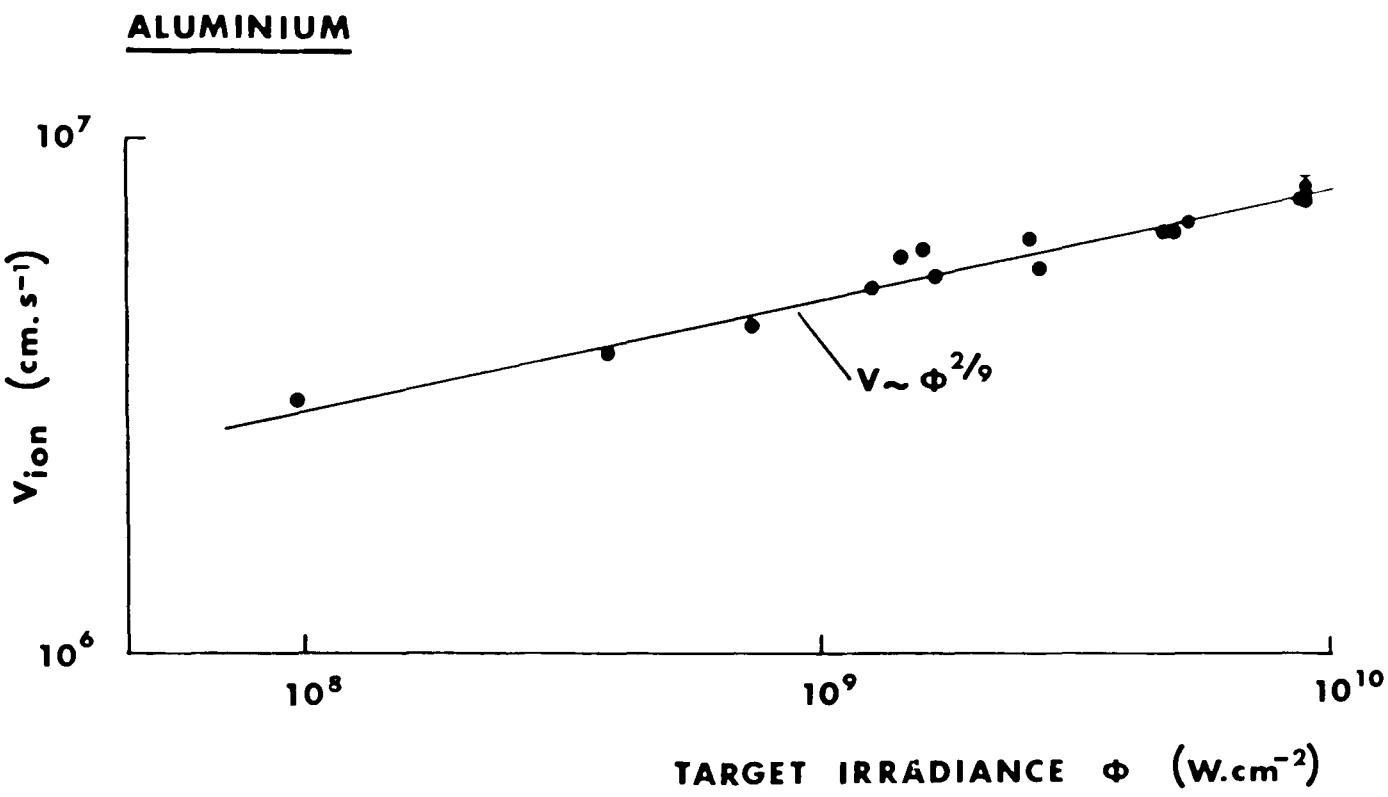

Fig.4.14. Asymptotic ion expansion velocity (15°) versus target irradiance (aluminium).

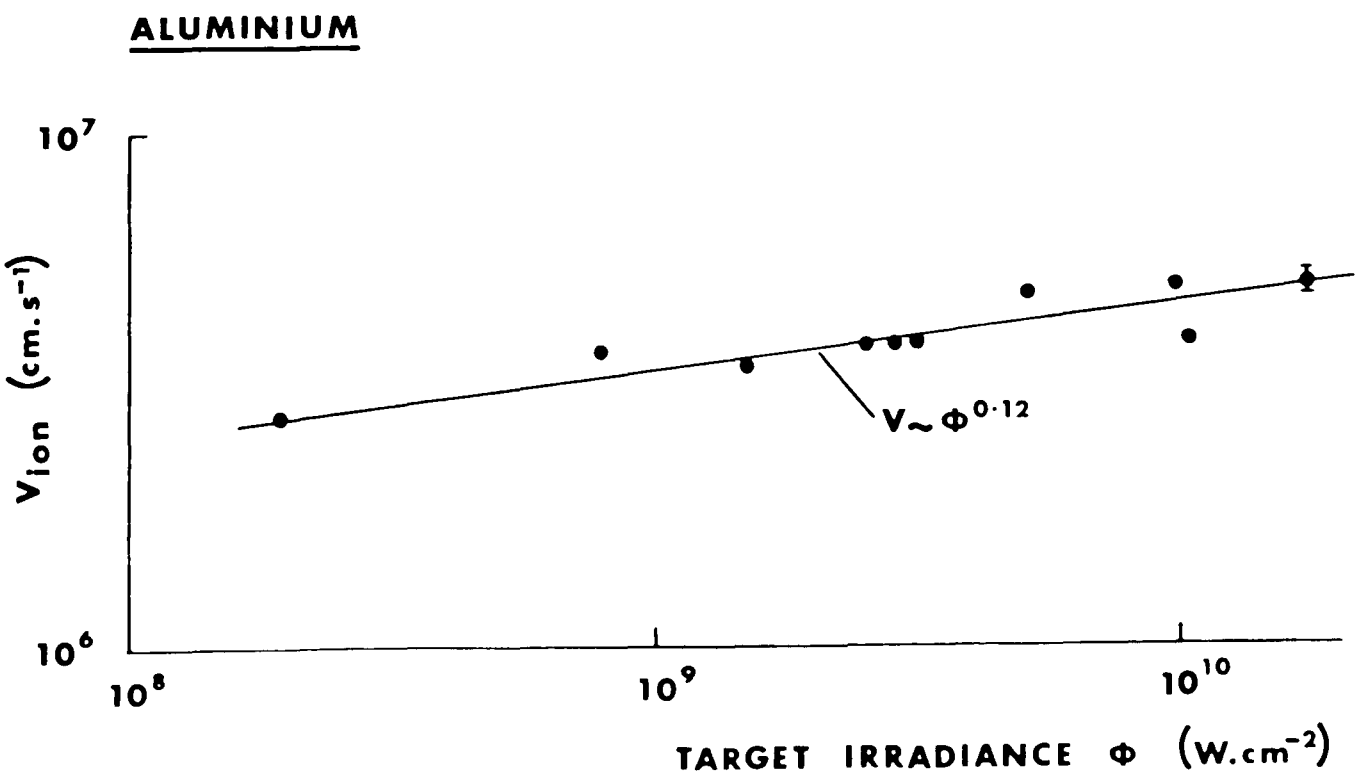

Fig.4.15. Asymptotic ion expansion velocity (40°) versus target irradiance (aluminium).

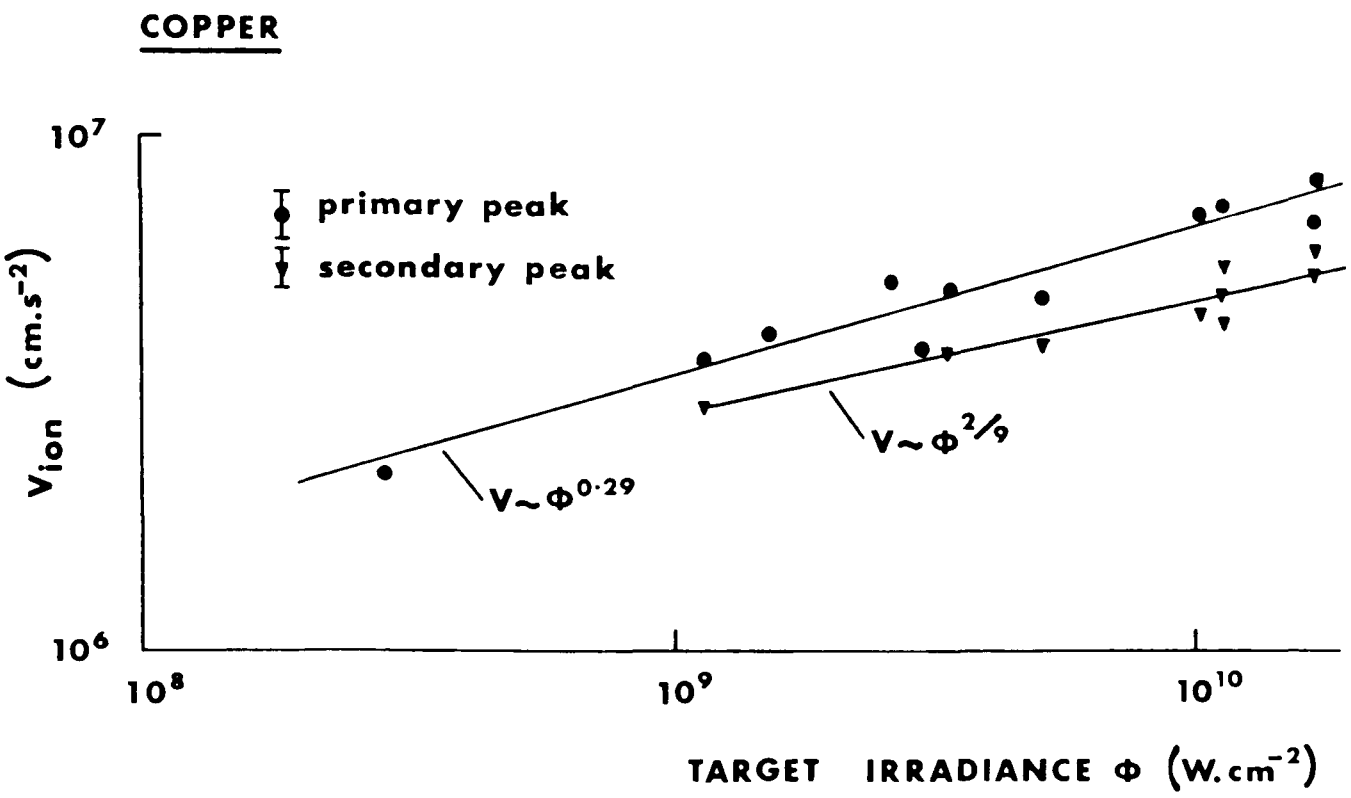

Fig.4.16. Asymptotic ion expansion velocity (15°) versus target irradiance (copper).

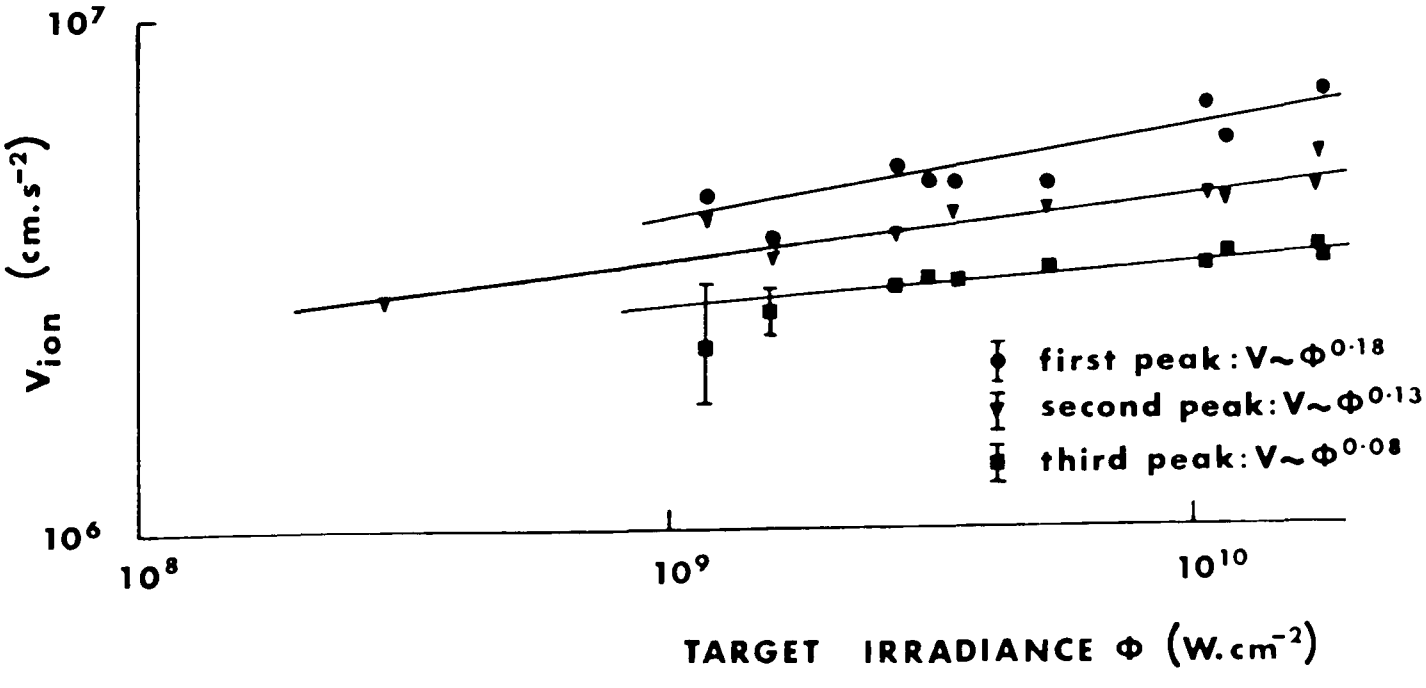

Fig.4.17. Asymptotic ion expansion velocity (40°) versus target irradiance (copper).

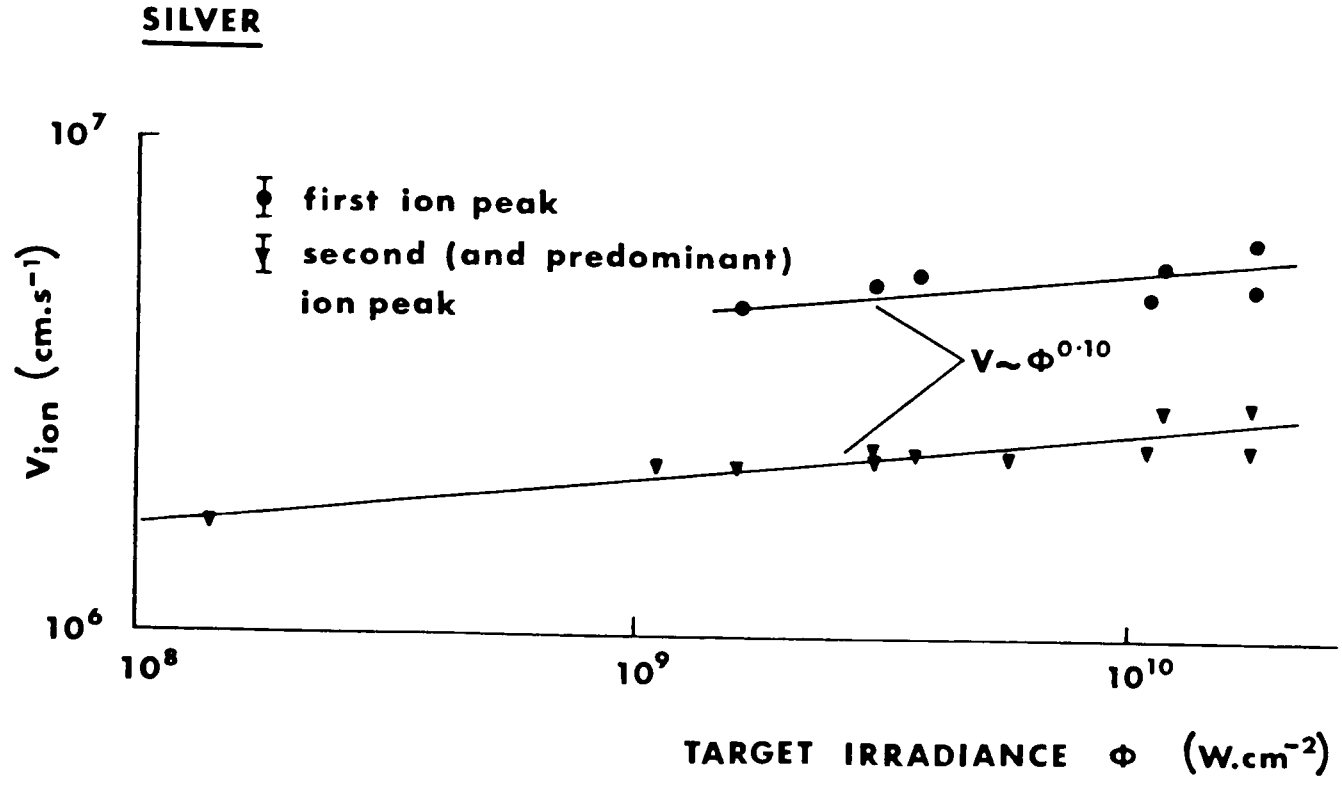

Fig.4.18. Asymptotic ion expansion velocity (15°) versus target irradiance (silver).

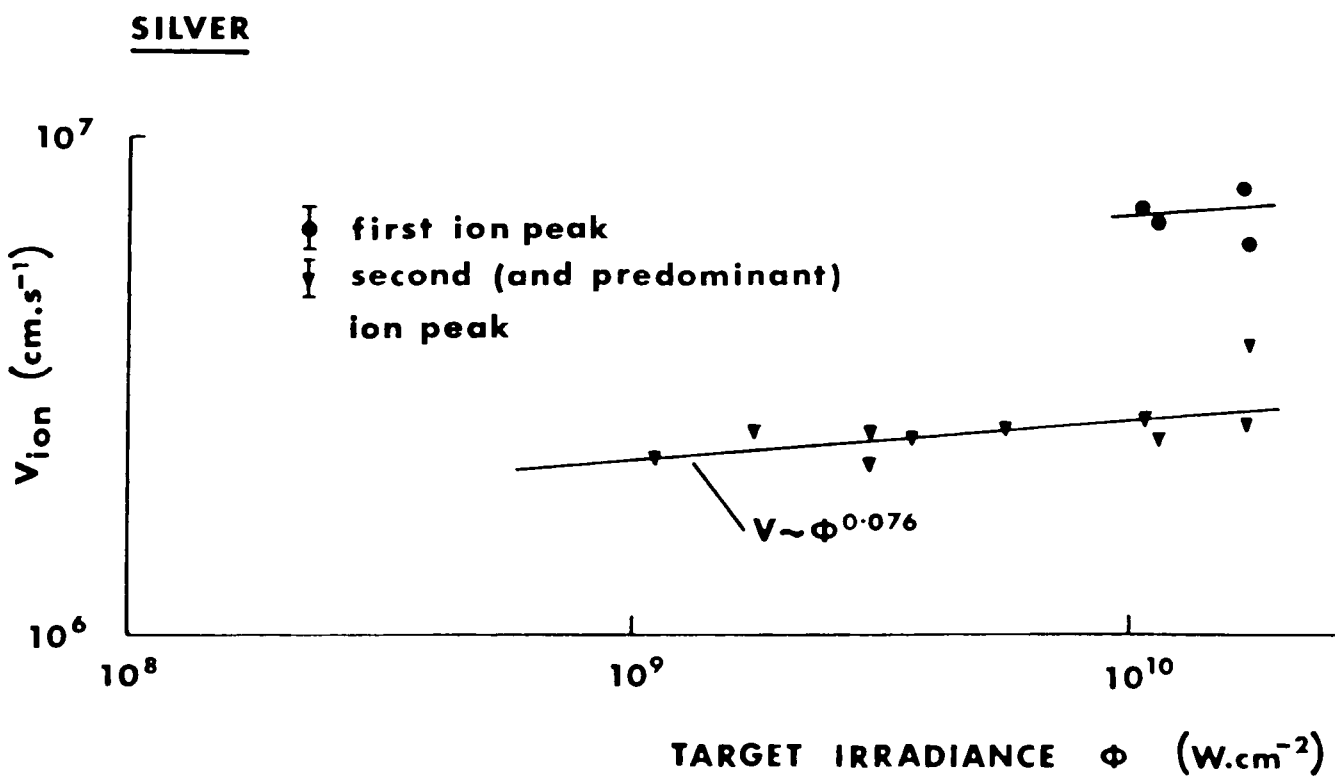

Fig.4.19. Asymptotic ion expansion velocity (40°) versus target irradiance (silver).

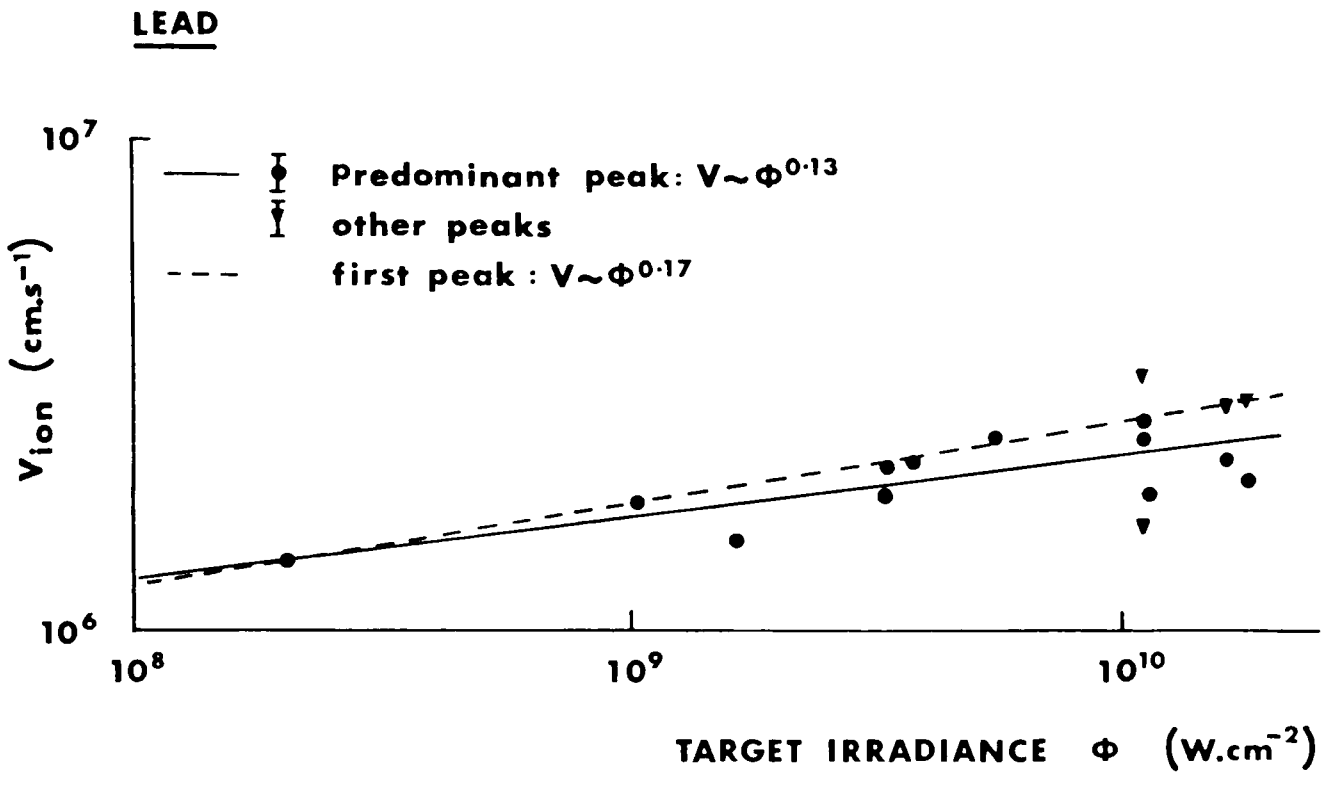

Fig.4.20. Asymptotic ion expansion velocity (15°) versus target irradiance (lead).

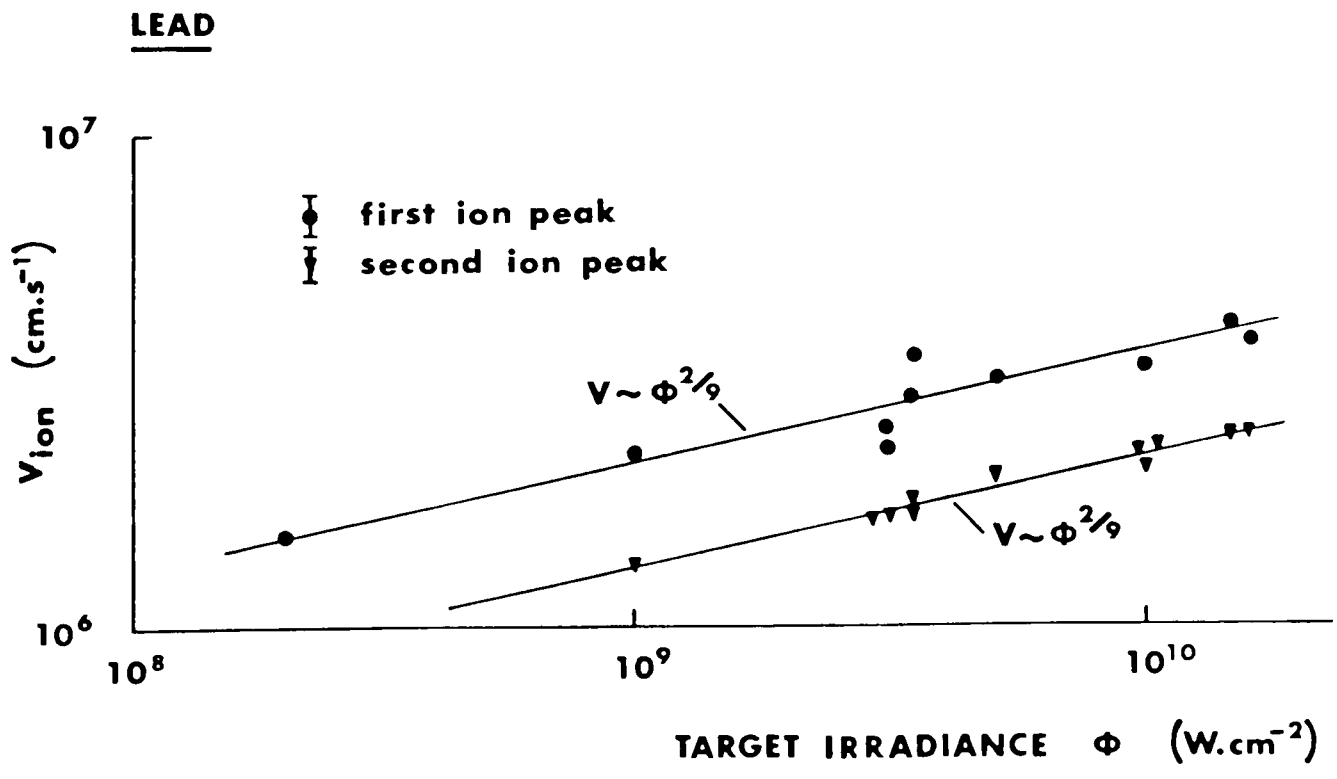

Fig.4.21. Asymptotic ion expansion velocity (40°) versus target irradiance (lead).

Fig.4.22. shows a polar plot of ion-velocity for carbon: it is seen to peak in the forward direction as found by Bykovskii et al[6] at 1.06μm. A polar plot of total number of ions collected per unit solid angle ($dn/d\Omega$) is shown in Fig.4.23.

The ion number was obtained by manually integrating the ion signals. This gives $n\bar{Z}$, where $\bar{Z}$ is the mean charge. $\bar{Z}$ was estimated using the following expression for a coronal ionization equilibrium (Dick et al[7], Shearer and Barnes[8]) :-

$$\bar{Z} = 26 \{(10^{-3} T_e) / (1 + 10^{-3} T_e (26/Z_n))\}^{1/2} \quad .....(4.1)$$

where, Z_n is the nuclear charge of the element and T_e is the electron temperature in eV. T_e was obtained using Puell's energy balance expression[9,10] :-

$$E_{ion} = 5(\bar{Z} + 1) T_e \quad .....(4.2)$$

where, E_{ion} is the ion expansion energy.

Graphs incorporating these expressions for the six targets have been plotted ; the one for carbon is shown in Fig.4.24.

Ion number scaling for polyethylene, carbon and aluminium at 15°, and also carbon at 40°, are shown in Fig.4.25.-28. The complex structure of the signals from high Z materials makes interpretation of number difficult. It can be seen that a change in slope was generally observed. The self regulating model predicts a 5/9 scaling for total ion number. From the results for carbon at 15° and 40°, a much higher scaling was observed - the scaling possibly tending to 5/9 at fluxes slightly higher than those used.

Plots of ion expansion energy versus target atomic weight are shown for the two angles in Fig.4.29,30. at a target irradiance of $2 \times 10^{10} W.cm^{-2}$. These are seen in general to rise to a maximum about atomic weights $\sim$ 100.

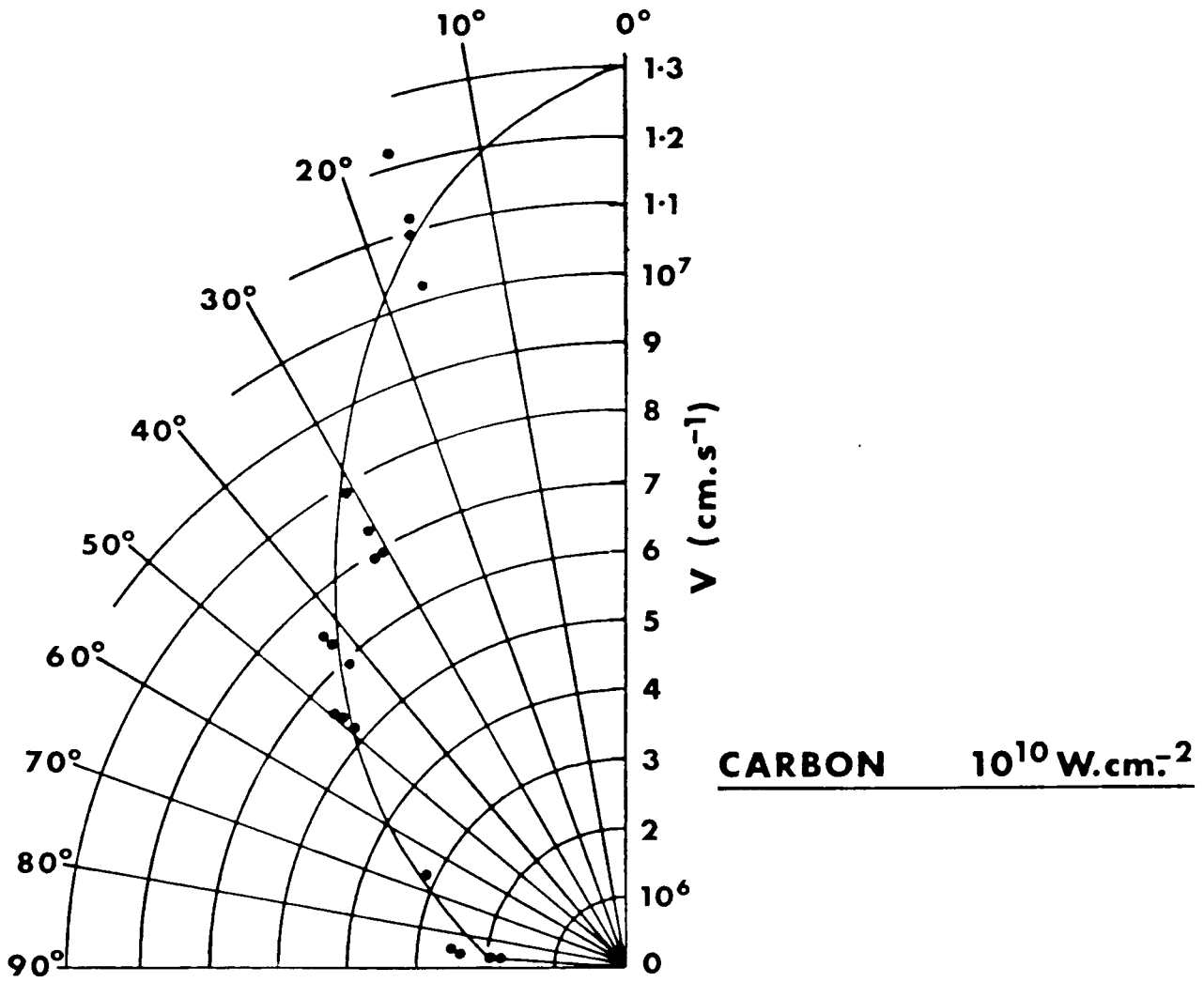

Fig.4.22. Polar plot of ion velocity.

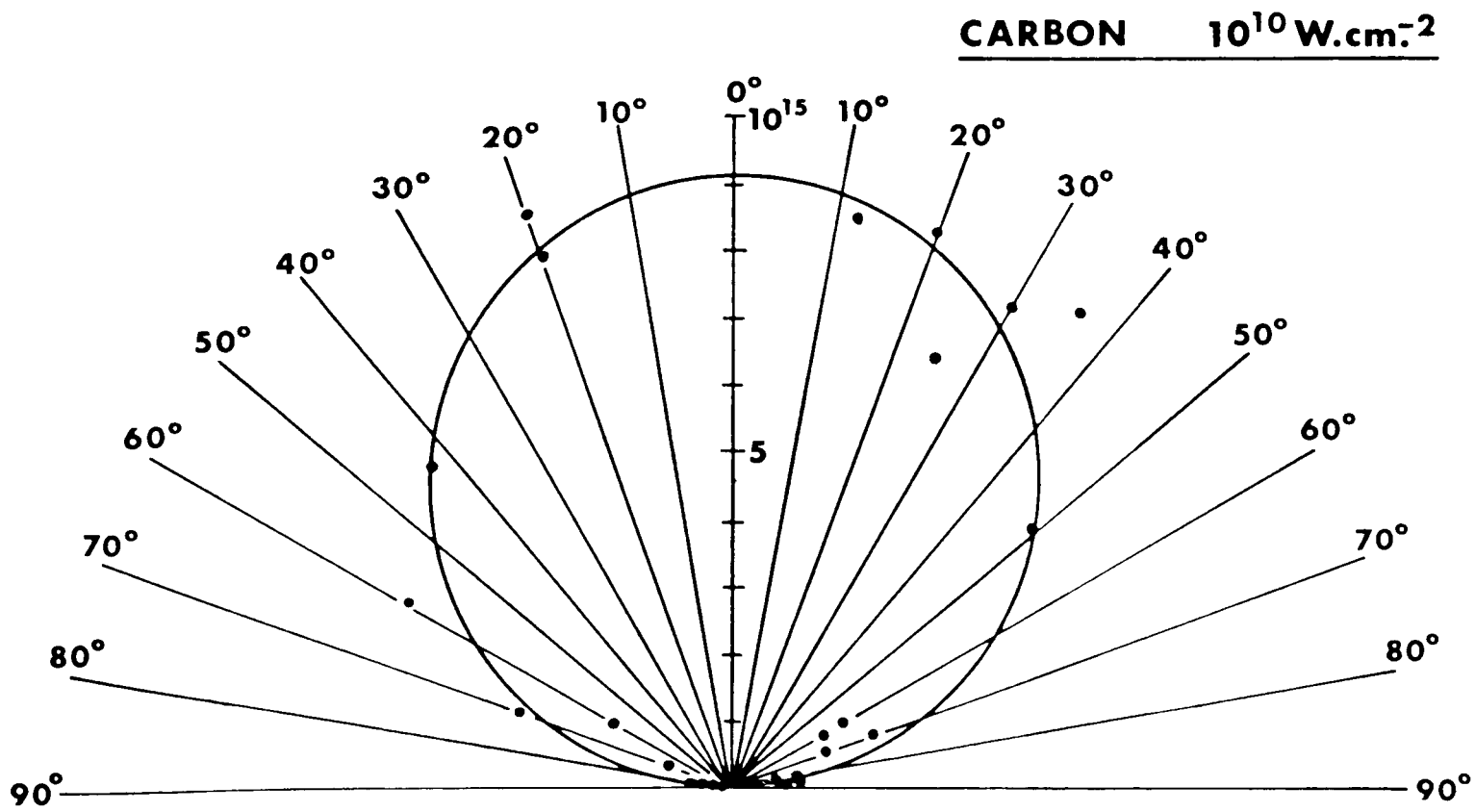

Fig.4.23. Polar plot of ion number, $\frac{dn}{d\Omega}$ (st^{-1}).

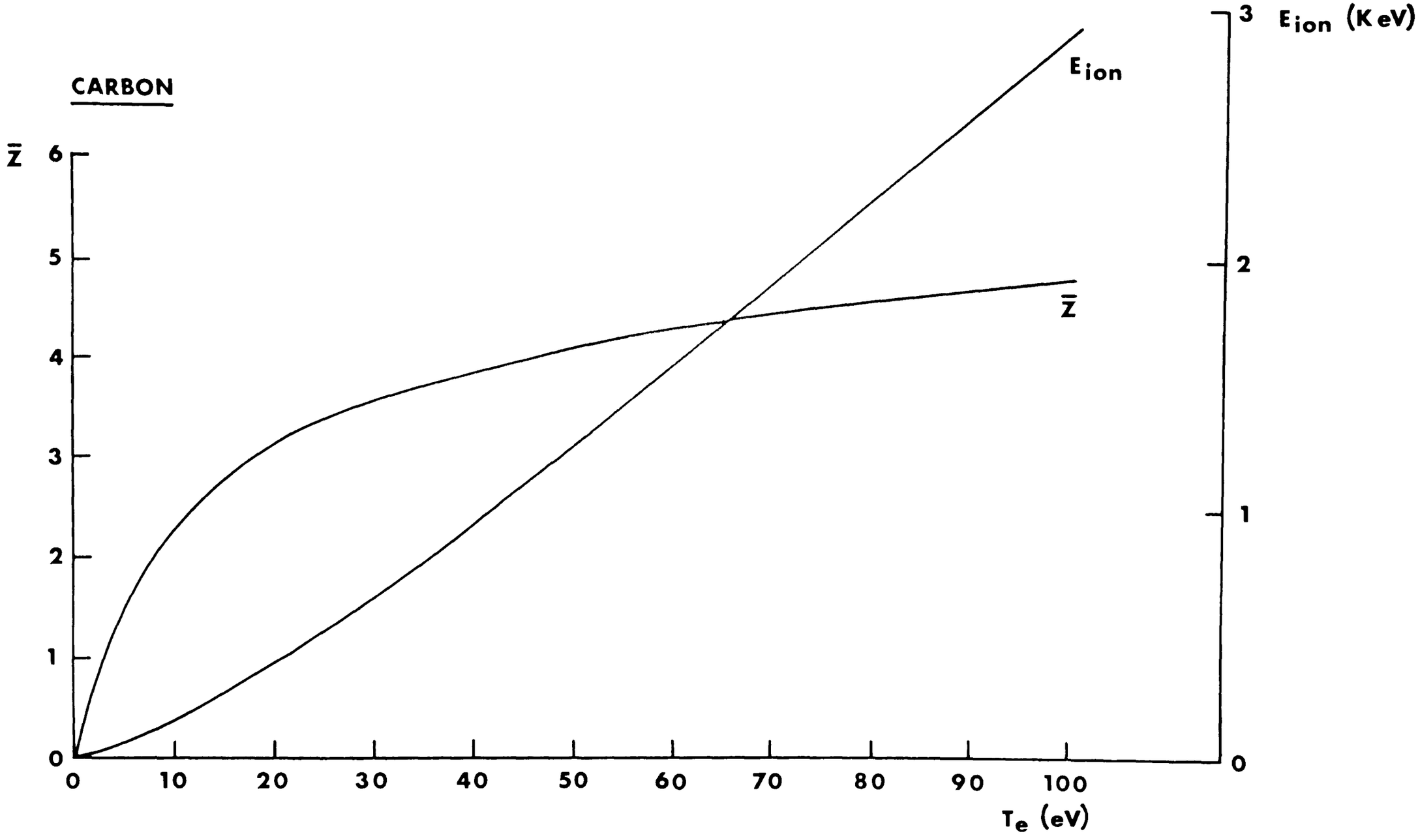

Fig.4.24. Mean ion charge and ion expansion energy versus electron temperature, as derived from Puell's expressions (carbon).

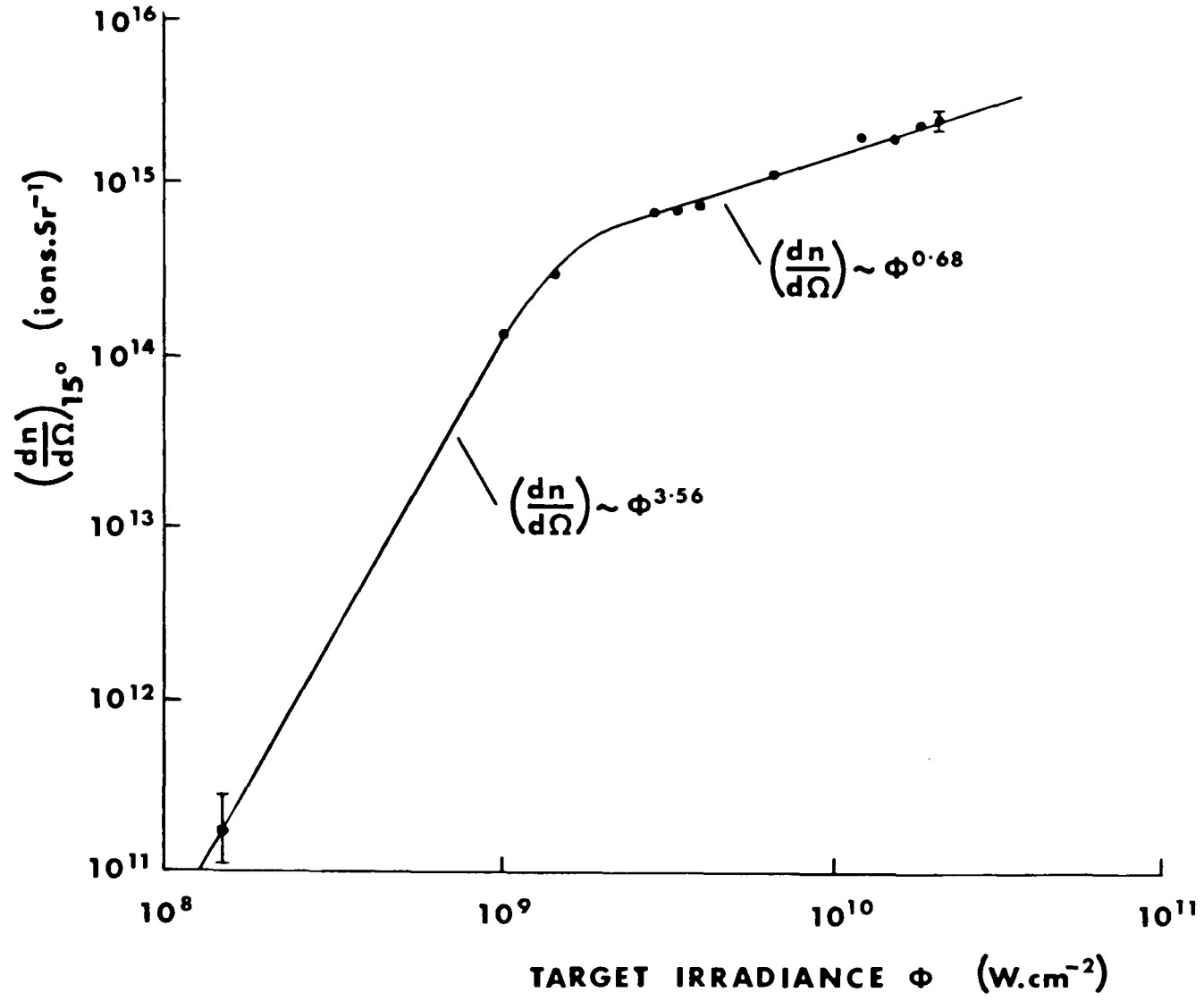

Fig.4.25. Ion number (15°) versus target irradiance (polyethylene).

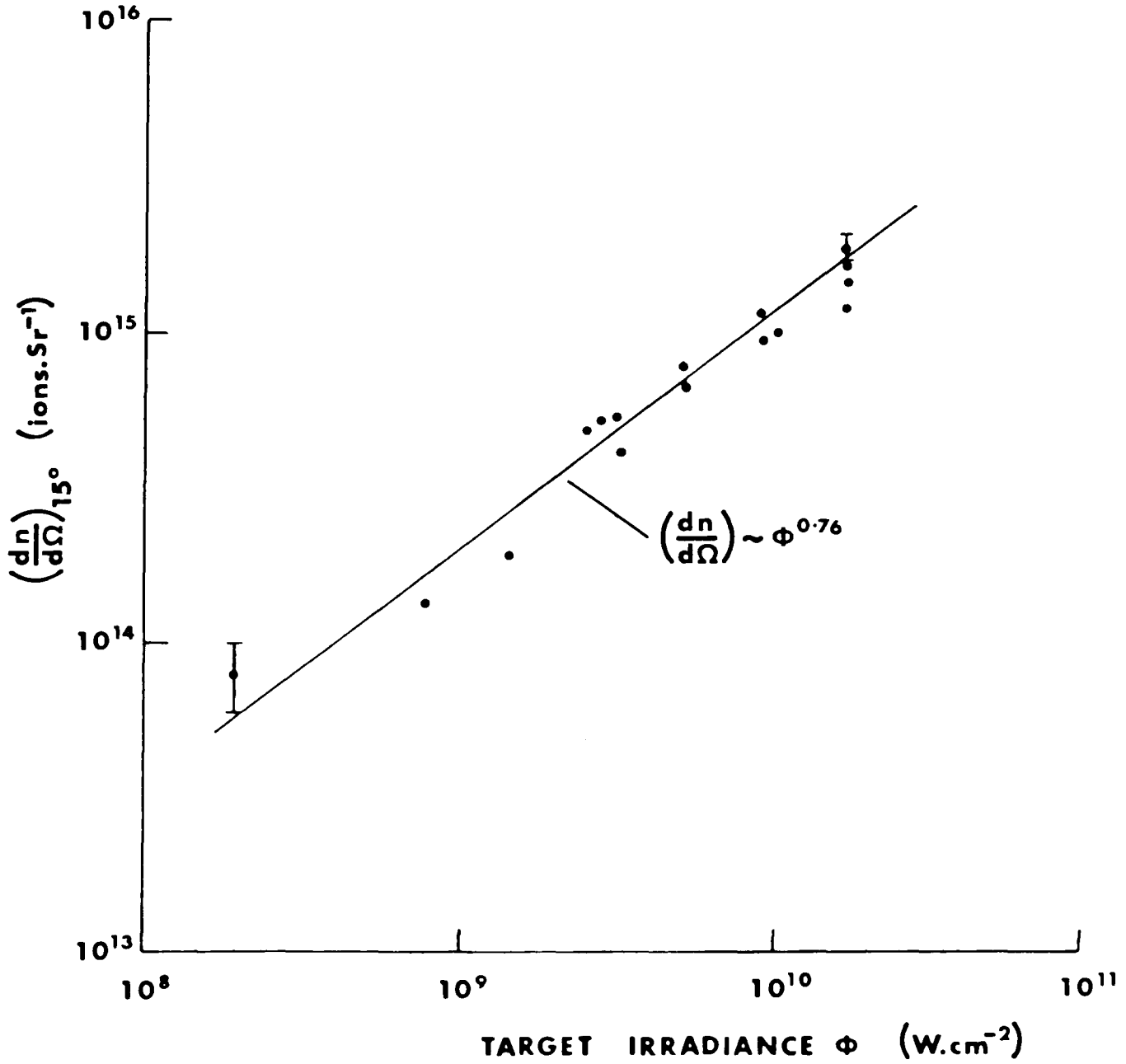

Fig.4.26. Ion number (15°) versus target irradiance (aluminium).

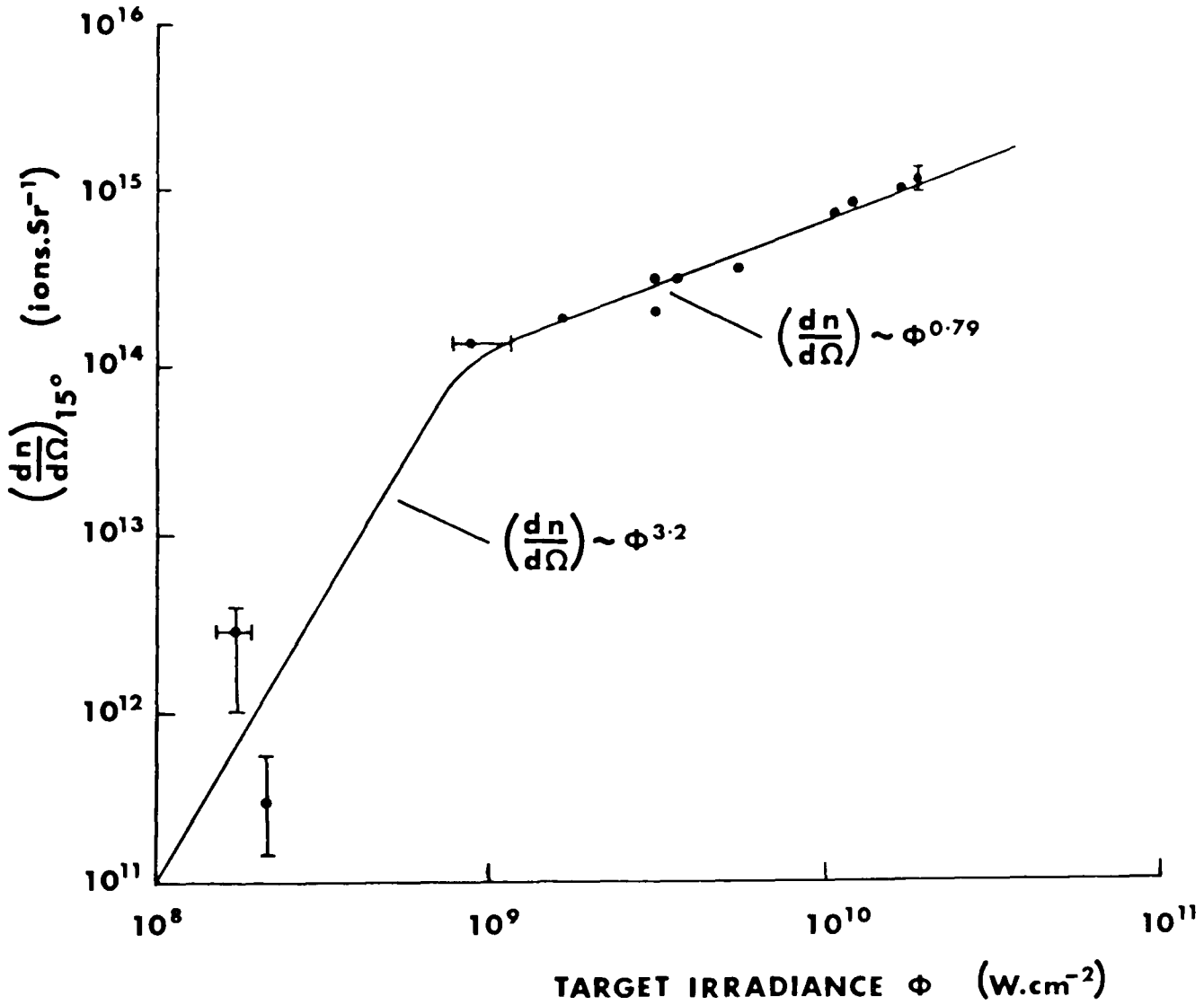

Fig.4.27. Ion number (15°) versus target irradiance (carbon).

Fig.4.28. Ion number 40° versus target irradiance (carbon).

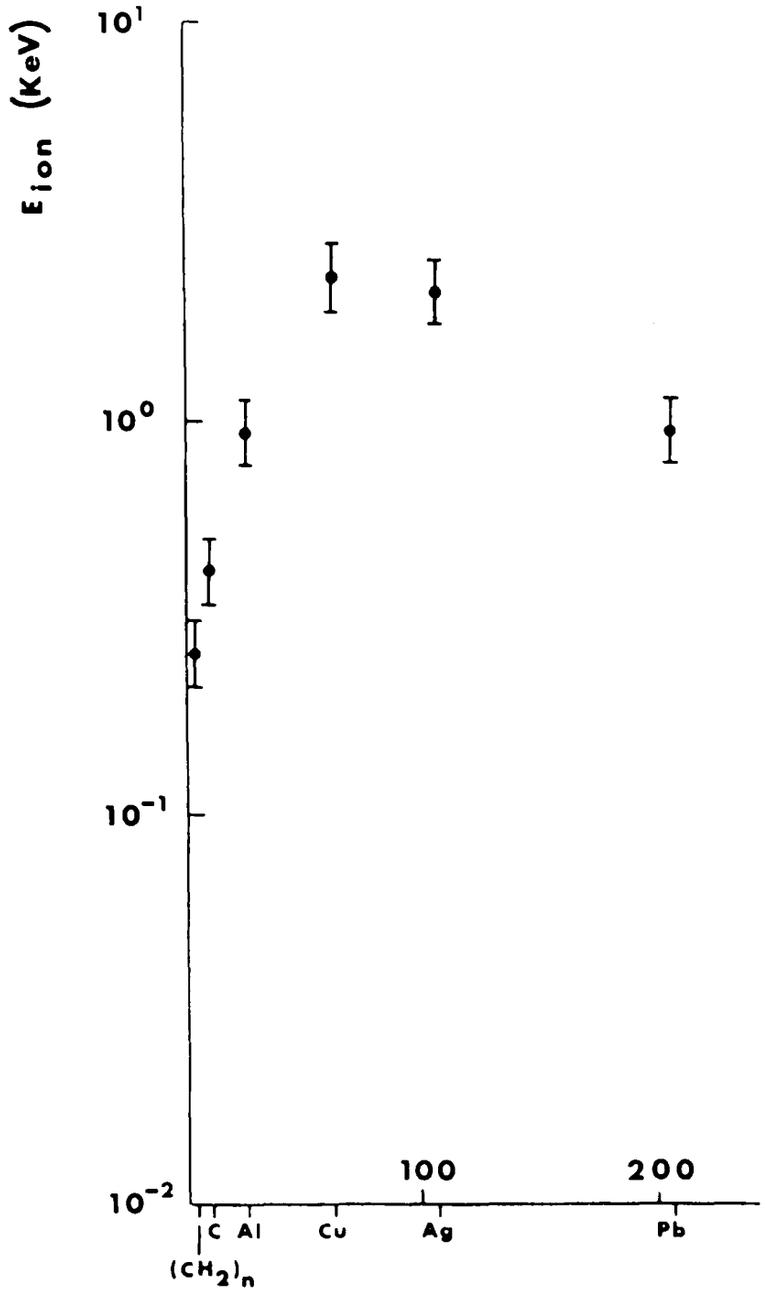

Fig.4.29. Ion energy (15°) versus atomic weight for target irradiance = 2×10^{10} W.cm^{-2}

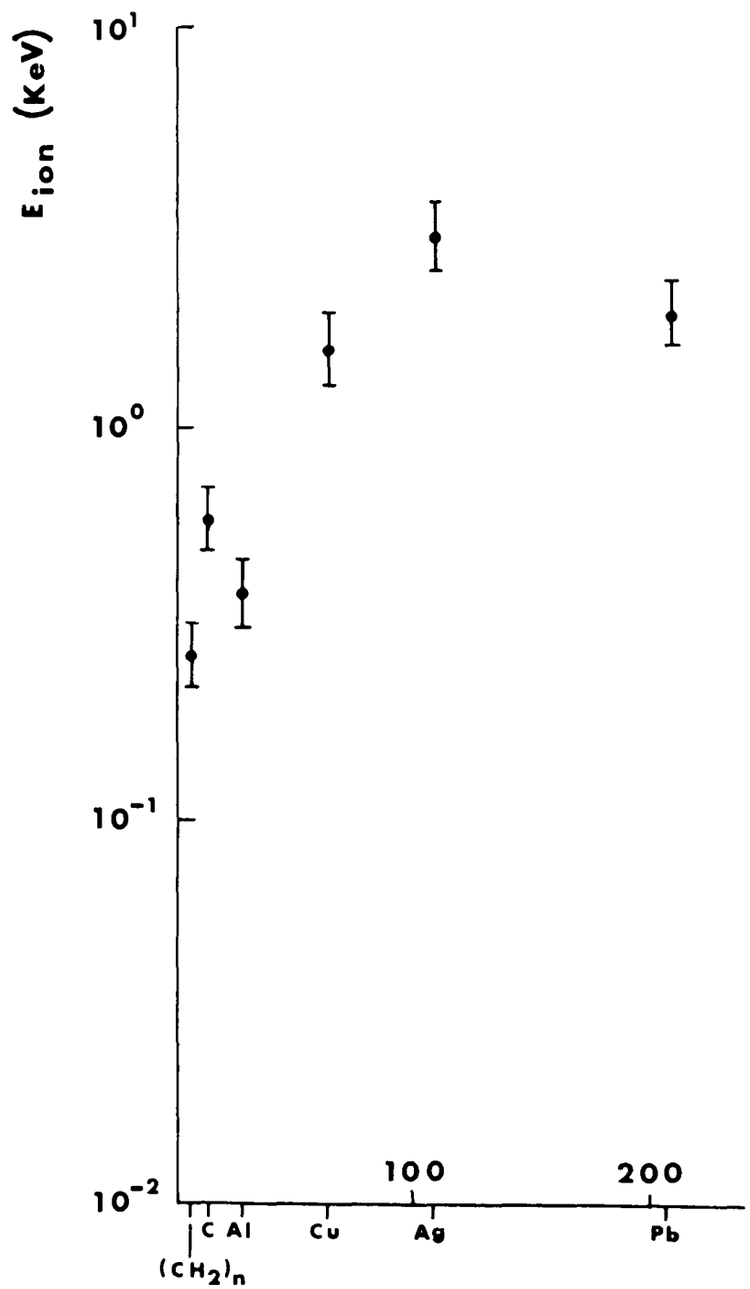

Fig.4.30. Ion energy (40°) versus atomic weight for target irradiance = 2×10^{10} W.cm^{-2}

A summary of estimated electron temperatures and target irradiance scaling from these measurements is presented in Table 4.2.

b) Optical Streak Photography

A John Hadland (P.I.) Ltd. Imacon streak camera fitted with a type P856 image converter tube (English Electric Valve Co.) was used to obtain optical streak photographs of the laser-produced-plasma (l.p.p.) A 100A/V current probe was connected round one of the two laser voltage lead-throughs to obtain a positive 60V trigger signal for streak plug-in type MS146. This plug-in was capable of speeds : 1,2,5,10ns/mm of film. The camera was fitted with a 300μm slit and placed on its side to be normal to the target. Focusing was carried out using a fine metallic rule. This also gave the magnification.

Streak photographs were taken for carbon and aluminium targets. The measured expansion velocity was found to depend upon the camera aperture, i.e. exposure and depth of field. In general, the velocities measured were smaller than those obtained using the ion-collectors, although the maximum velocities obtained are in agreement. This result is not surprising, as the ions are being emitted into 2π steradians sothat the projected velocity along the imaged slit will in general be less than its true velocity. In the optical system used, the depth of field was fairly large, enabling such ions to be seen. The angular velocity and number distribution will also affect the exposure for a given velocity. In addition, the ions are in the acceleration phase and so have not achieved the asymptotic value. Boland et al[11] have also observed that ions in the lower ionization states are more copious emitters of visible photons.

c) Specular Reflectivity

Specular reflection measurements for the six targets oriented at 20° to the incident beam are given in Fig.4.31-34. For the metals the reflectivity is high at low irradiance levels, due, presumably, to direct reflection from the target surface[12]. This is reinforced

TARGET	ELECTRON TEMPERATURE (eV)	DERIVED TEMPERATURE IRRADIANCE SCALING
$(CH_2)_n$	16†	$T_e \sim \phi^{0.39}$
C	21	$\phi^{0.35}$
Al	34	$\phi^{0.32}$
Cu	63	$\phi^{0.43}$
Ag	60	$\phi^{\sim 0.16}$
Pb	$\sim$ 32	$\phi^{0.32}$

† Using average nuclear charge and mass for $(CH_2)_n$

Summary of estimated electron temperature and target irradiance scaling from charge-collector probe measurements at $3 \times 10^{10} W.cm^{-2}$ (HF).

TABLE 4.2.

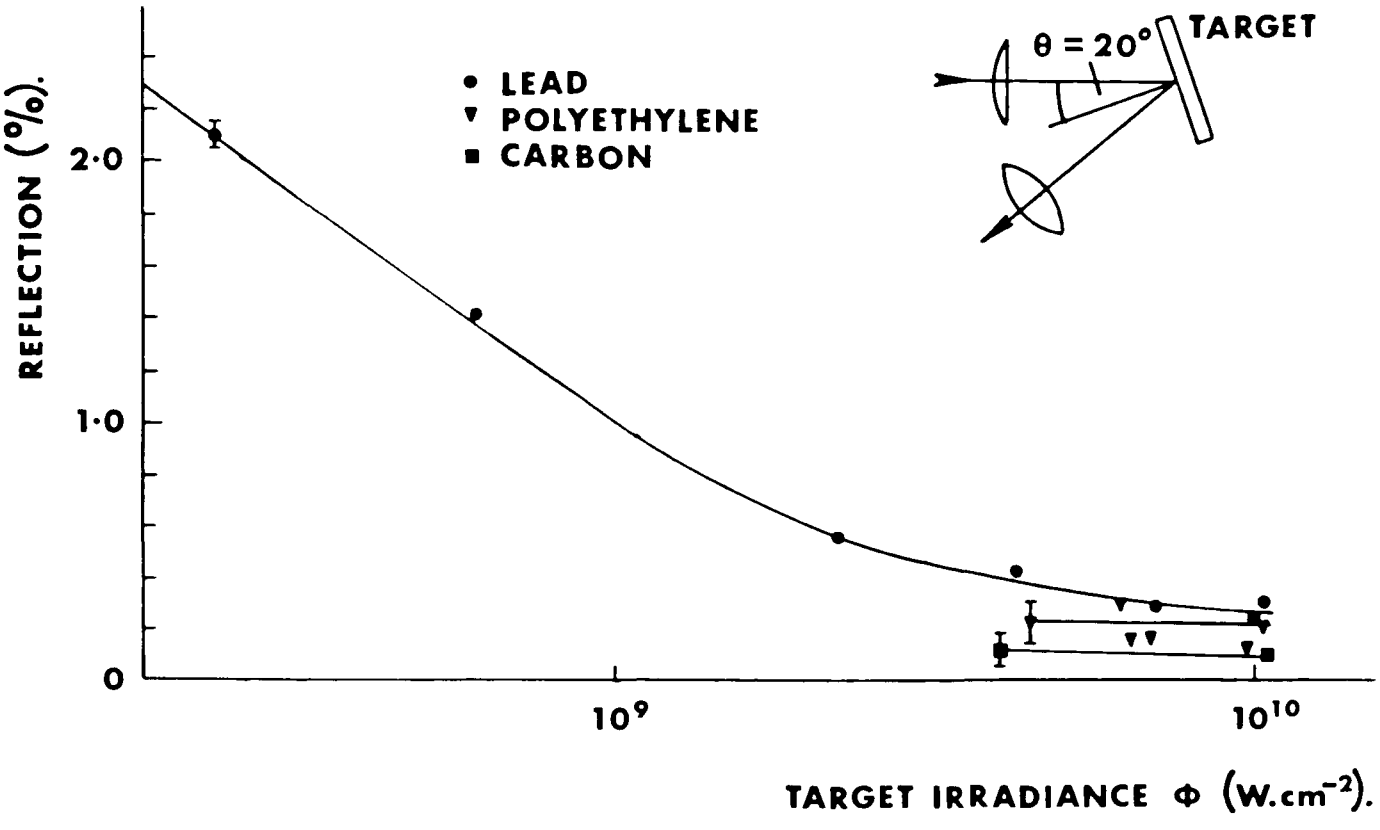

Fig.4.31. Reflectivity of HF laser produced lead, polyethylene and carbon plasmas.

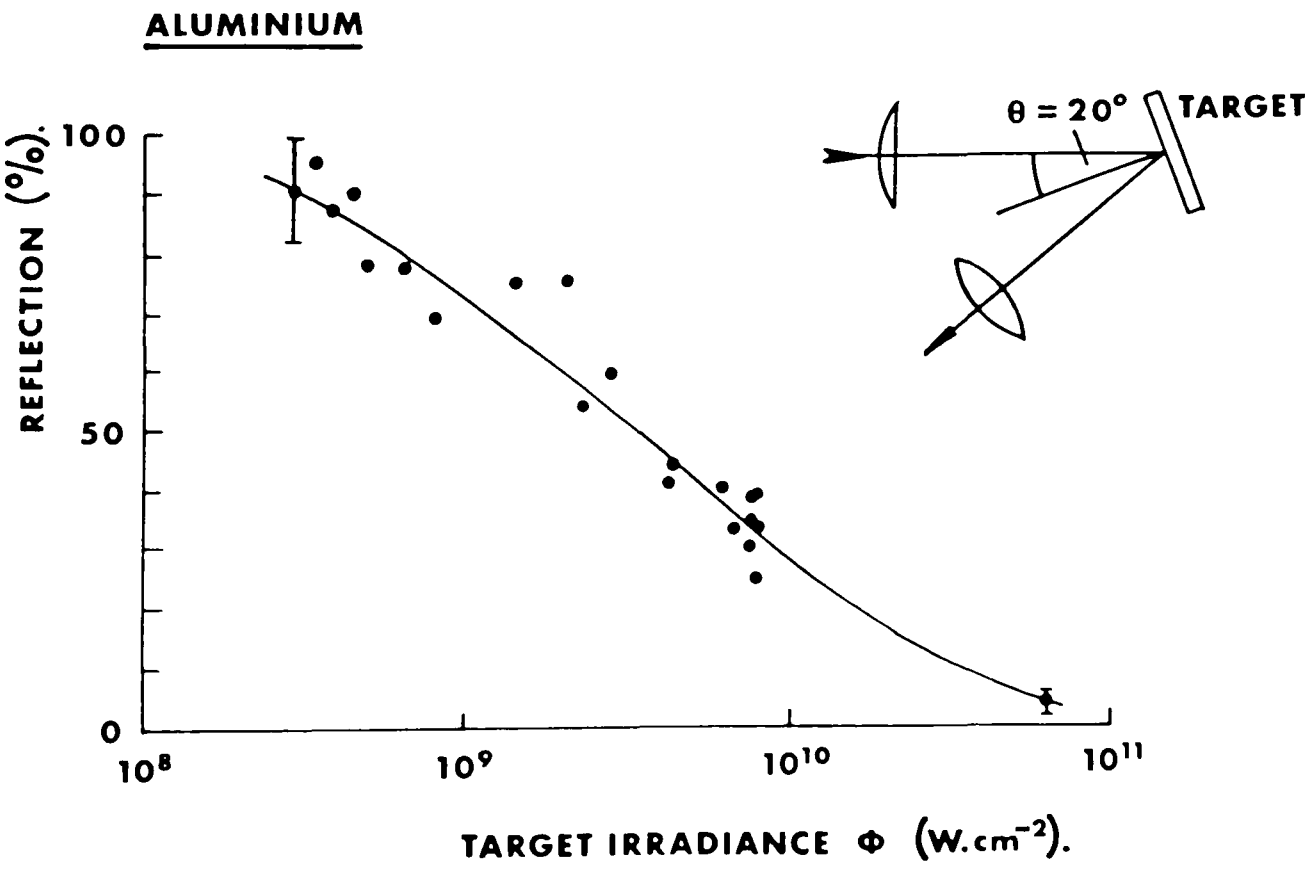

Fig.4.32. Reflectivity of HF laser produced aluminium plasma.

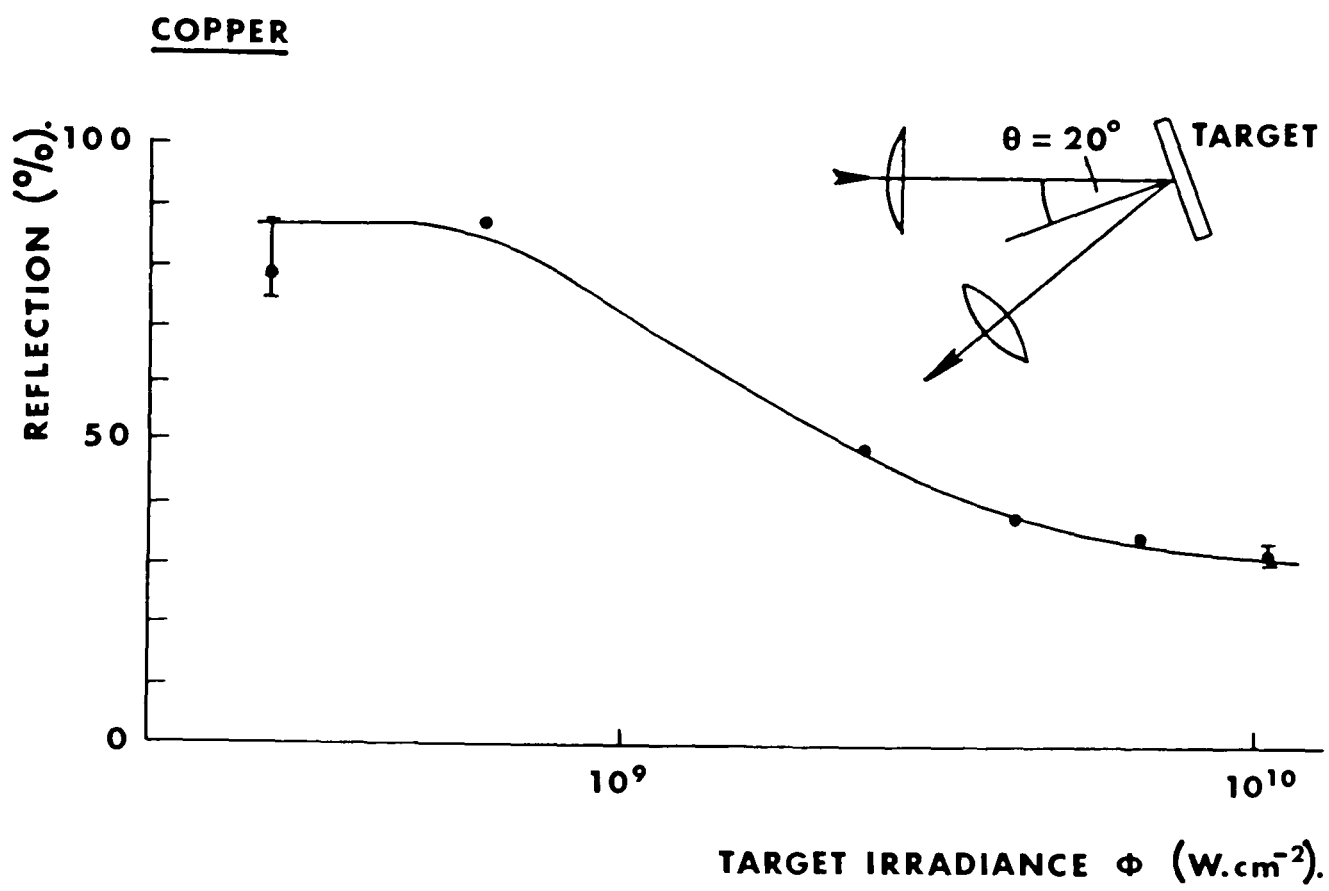

Fig.4.33. Reflectivity of HF laser produced copper plasma.

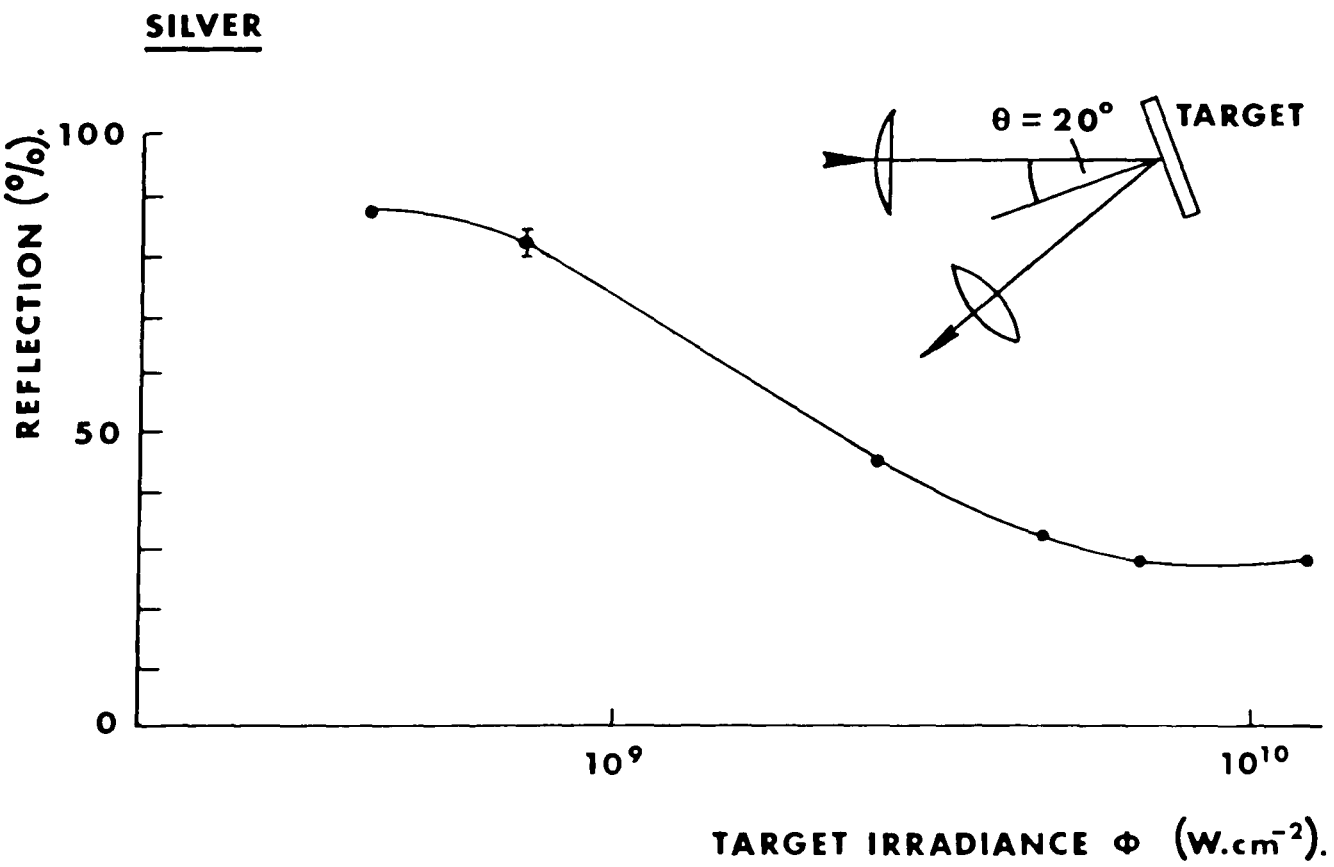

Fig.4.34. Reflectivity of HF laser produced silver plasma.

by the observation of the spatial distribution on reflection, which was not fundamentally changed, although some aberration was observed. The reflectivity decreases steadily as ϕ is increased. Under high irradiance conditions the reflected and incident laser pulse shapes were observed to have similar time histories.

4.5.2. High Power System

a) X-ray Continuum Emission

Elton[13] has extended calculations of the total integrated bremsstrahlung radiation passing through absorbing foils, including beryllium, for a plasma energy range of about 50eV to 100KeV. Using his calculations, together with ion-velocity measurements, calculations showed that x-rays could only be observed using thin foils ($\lesssim 5 mg/cm^2$). Even under these conditions the detection of x-rays was predicted to be uncertain. Considerable care was therefore used to obtain optimum target irradiances by using a high quality beam. The x-ray detector was set at a very high gain, and signals were collected over a large solid angle. Electrical noise was reduced by careful screening.

Using an EMI 9813KB photomultiplier, operated at an EHT of 2.6KV, together with an NE 104 plastic scintillator, x-ray signals were obtained. Be foils of mass per unit area 4.50 and 2.06 $mg.cm^{-2}$, and of areas 0.567 and 0.722 cm^2, were employed 6.9cm from the plasmas to limit the range of x-ray wavelengths detected, and to remove optical detection. The immunity of the system to stray light was confirmed by using a laser produced gas break-down spark[5] as an intense light source at the laser focus.

The signals were obviously subject to statistics but otherwise reproducible. They were displayed on a Tektronix 7844 oscilloscope, time synchronised with the laser pulse. The shot-to-shot fluctuations were reduced by using a 20MHz bandwidth amplifier to provide some integration. The strongest emission was obtained with aluminium, in agreement with results using a CO_2 laser as presented in chapter 7. With both aluminium and carbon the emission

intensity decreased rapidly as the target irradiance was decreased, as predicted from Elton's calculations[13]. Fig.4.35. shows typical x-ray signals for optimum conditions, together with the incident laser pulse shapes. The emission durations for Al and C were found to be $\sim$ 60ns and $\sim$ 40ns (FWHM) respectively; after allowing for the transit delays, the emission was found to begin concurrent with the main spike of the laser pulse.

Approximate electron temperatures were obtainable using the two-foil absorber ratio technique[14]. However, a more accurate determination results from a technique based on the absolute sensitivity of the detector[15]. This method has significant advantages over the absorber ratio technique, when low temperatures (<100eV) and weak emission signals are encountered, because of the high sensitivity of the signal to T_e variations[15]. To estimate the temperature, the radiating plasma volume, V, was assumed to be $V = \frac{1}{2} \pi r_o^3$, with $r_o = 20\mu m$, and the average electron density, $\bar{n}_e$, within this volume, half the critical density ($\bar{n}_e \approx 5 \times 10^{19} cm^{-3}$). Contributions from free-free and free-bound transitions were considered when calculating the radiated power, with a coronal equilibrium model being used to determine the density of different ionization stages in the Al and C plasmas[16]. The T_e deduced from these measurements are given in Table 4.3. The limits on temperature given correspond to a factor of $\sim$ 10 error in the term $n_e^2 V$ used to calculate the power emitted by the plasma, and indicate that the temperature is insensitive to the precise value of this parameter.

b) Ion Emission

A negatively biased charge collector probe mounted axially in the vacuum chamber, and located 15cm from the target surface, Fig.4.1., was used to determine the asymptotic ion expansion velocity.

For both Al and C targets, ion probe signals consisting of a single, temporally smooth, pulse were obtained, similar to those reported previously for ruby[17] and gain-switched CO_2[10] laser-solid target experiments. Under sensitive conditions a photoelectric

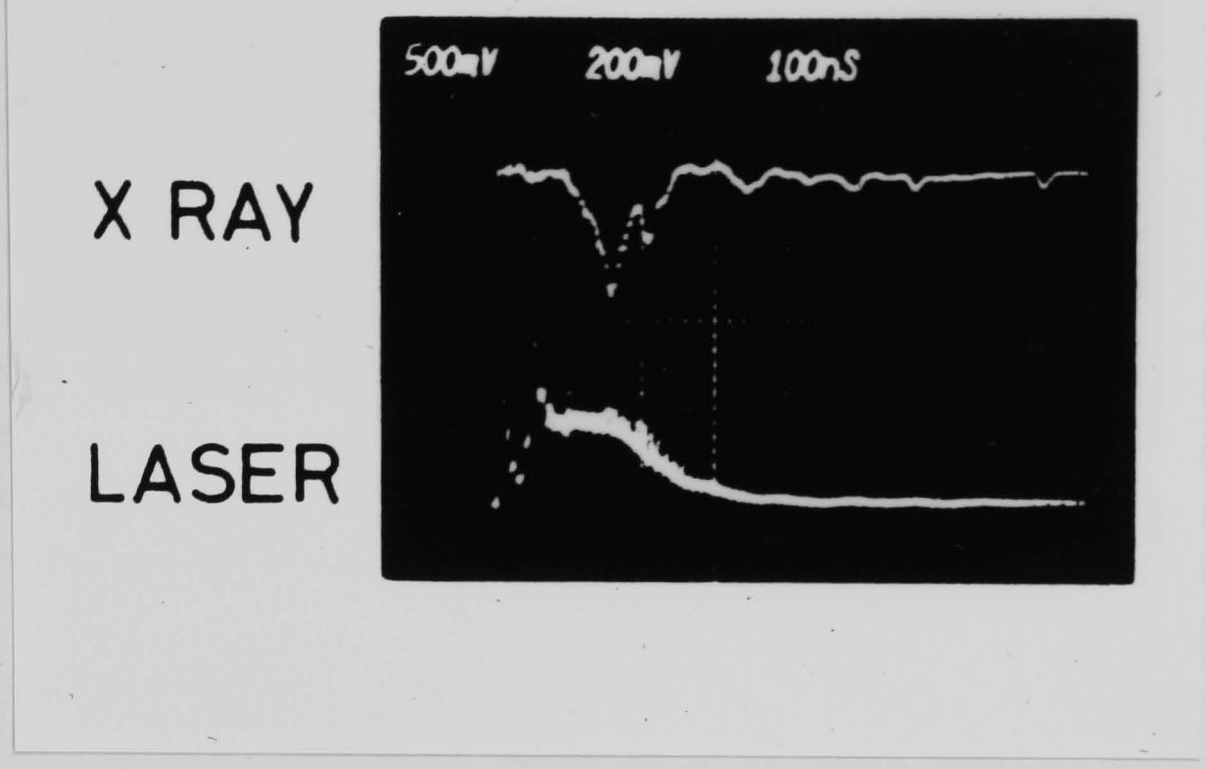

Fig.4.35. Typical x-ray signals for optimum conditions, together with incident laser pulse shape. 2·06 mg cm^{-2} Be foil, polished Al target.

signal was clearly obtained, Fig.4.36. The time delay between the peak of the laser pulse and the peak of the ion pulse was used to derive the asymptotic ion expansion velocity, V_p; results of V_p versus the target irradiance, ϕ_p, are included in Fig.4.11,13. for C and Al targets. In both cases, a $V_p \propto \phi_p^{2/9}$ scaling law gave a reasonably good description of the experimental data. An estimate of the plasma electron temperature, T_e, was obtained from the asymptotic ion expansion energy, E_{ion}, using the energy balance relationship as before. Electron temperatures derived in this manner are given in Table 4.3. for $\phi_p = 7 \times 10^{10} W.cm^{-2}$, and are seen to be approximately a factor of two lower than those derived from the x-ray measurements.

c) Streak Camera Measurements

In Fig.4.37. the laser pulse shape is shown together with a time synchronised streak photograph of the plasma produced from a carbon target at $7 \times 10^{10} W.cm^{-2}$. The temporal structure exhibited by the laser pulse was reproducible and resulted from J-line switching and vibrational cascading in the multiline HF laser[18]. The streak photograph shows that plasma production is initiated by the first, fast rising, low amplitude, component of the pulse, with a small step in the luminous front occurring upon the arrival of the main 'spike' on the pulse. During the latter stages of the interaction ($\gtrsim$ 100ns), when the laser intensity is approximately constant, the luminous plasma boundary appears to be stationary and extends to $\sim$ 1mm from the target surface. The overall laser pulse width and the period of luminous emission are seen to be comparable ($\sim$400ns).

d) Beam Quality

The presence of the target and focussing optics did not significantly change the beam properties from those determined off target. For example, no noticeable difference in either the laser pulse delay time or pulse-shape was observed with the target present, indicating low reflective laser-target coupling. Optical and electron-microscope

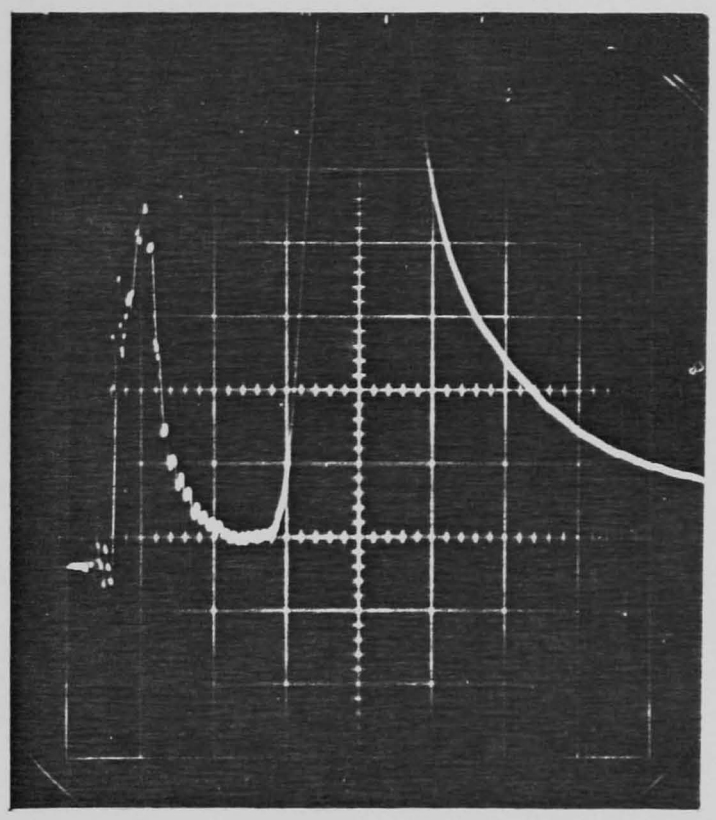

Fig.4.36. Photoelectric signal preceding main carbon ion pulse. 500 ns/div, 0·2 V/div.

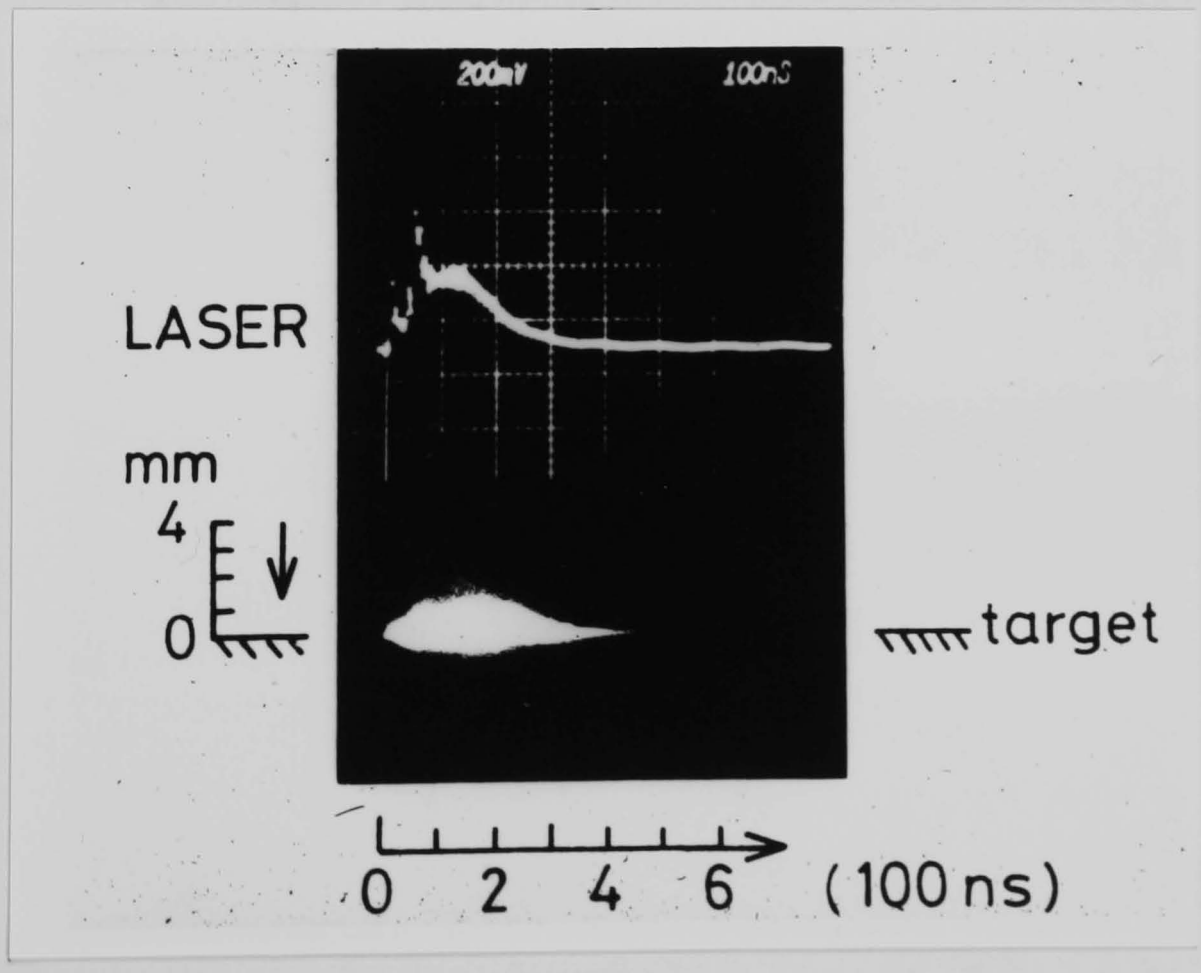

Fig.4.37. Laser pulse shape time synchronised with a streak photograph of the plasma produced from a carbon target at an irradiance of 7×10^{10} W.cm^{-2}

TARGET	EXPERIMENTAL TEMPERATURE (eV) $\phi = 7 \times 10^{10} W.cm^{-2}$		CALCULATED TEMPERATURE (eV) $\phi = 7 \times 10^{10} W.cm^{-2}$	
	Ion Probe	X-Ray	ϕ	$< \phi >$
C	30	$65 \pm \begin{matrix} 20 \\ 12 \end{matrix}$	72	34
Al	38	$75 \pm \begin{matrix} 25 \\ 17 \end{matrix}$	87	40

Experimental and calculated electron temperatures (HF).

Table 4.3.

inspection of the laser damage sites on the Al targets showed the presence of deep central craters of ∿ 40μm diameter with peripheral damage out to diameters of ∿ 110μm, Fig.4.38,39., which was consistent with diffraction limited performance of the unstable resonator[1].

4.6. Discusion of the Results from Both Systems

4.6.1. The Interaction

For the irradiance levels and pulse lengths used, the steady-state self-regulating model[9,19,ch1], should provide a good description of the interaction. This model assumes that laser radiation is absorbed primarily in the under-dense plasma zone, an assumption which can be shown to be valid providing $\phi_p \lesssim \phi_o$, where[9]:-

$$\phi_o \gtrsim 1.2 \times 10^{11}\ r_o\ Z^{3/2}\ A^{-1/2}\ \lambda^{-4}\ W.cm^{-2} \qquad .....(4.3)$$

Here, λ (μm) is the laser wavelength, r_o (μm) is the characteristic focal spot radius, and A the atomic weight of the target material. For the HF laser, with λ = 2.8μm and r_o = 20μm, equation 4.3. gives $\phi_o \gtrsim 10^{11} W.cm^{-2}$ for Al and C targets, which is somewhat higher than the maximum irradiance levels employed. Under steady-state conditions, the dependences of the electron temperature, T_e, and the ion velocity, V, on r_o, λ and ϕ can be shown to be[19]:-

$$T_e = a\ r_o^{2/9}\ \lambda^{4/9}\ \phi^{4/9} \qquad .....(4.4)$$

$$V_p = b\ r_o^{1/9}\ \lambda^{2/9}\ \phi^{2/9} \qquad .....(4.5)$$

where a and b are coefficients depending upon Z and A, which can be derived from Puell's analysis[9]. It should be noted that the applicability of these scaling laws to our results is supported by the ion velocity measurements which show good agreement with the $V_p \propto \phi^{2/9}$ dependence predicted by equation 4.5.

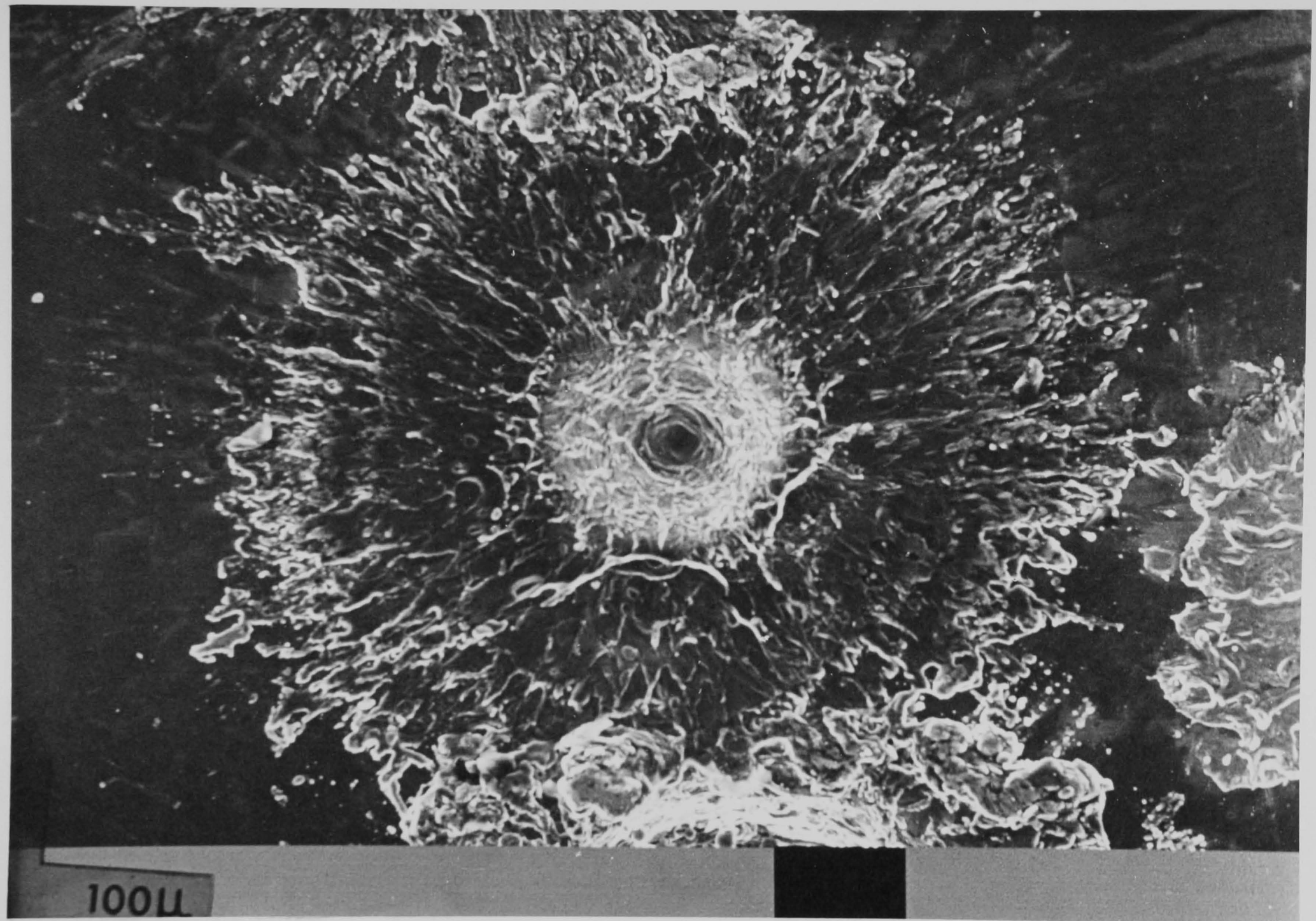

Fig.4.38. Electron microscope photograph of the laser damage site on an aluminium target ($\sim 10^{10} W.cm^{-2}$)

Fig.4.39. Electron microscope photograph of the laser damage site on an aluminium target ($\sim 10^{10} W.cm^{-2}$)

4.6.2. Comparison with Theory

In Table 4.3., temperatures calculated using equation 4.5. are given for Al and C targets with $\phi = \phi_p = 7 \times 10^{10} W.cm^{-2}$, $2r_o = 40\mu m$ and $\lambda = 2.8\mu m$. It can be seen that the temperatures predicted using the maximum irradiance, ϕ_p, are consistently higher than those derived experimentally from the ion probe data, but are in broad agreement with the x-ray measurements. Since the x-ray detection technique provides a measurement of the highest temperature[17] achieved (in both space and time) during the laser pulse, it is reasonable to suppose that this temperature relates to localised heating produced by the main lobe of the focused unstable resonator beam, which is characterised by ϕ_p. In contrast, since the ion probe detectors yield space and time averaged values for T_e, it is more appropriate in this case to compare the results with predictions based on an average value for the irradiance, $\langle\phi\rangle$. This is done in Table 4.3., where T_e values are given for $\phi = 7 \times 10^{9} W.cm^{-2}$, which corresponds to a spot-size of $2r_o = 110\mu m$, as determined experimentally from the overall damage crater diameter, and a time averaged (rather than peak) value for the incident laser power. T_e values calculated in this way agree well with the ion probe measurements.

A comparison of the reflectivity measurements with predictions based on the optical thickness of the underdense plasma[20,21] shows, Table 4.1. that the experimental results are much higher than would be expected. Thus, it is likely that reflection from the target surface dominates the results over the entire range studied; this explanation would also account for the significant difference in reflection observed for Al and C targets.

TARGET	R (%)	
	$\Phi = 10^{9}$ W.cm^{-2}	$\Phi = 10^{10}$ W.cm^{-2}
$(CH_2)_n$	< 1.88	0.29
C	0.01	0.13
Al	0.04	0.61
Cu	0.05	1.28
Ag	0.60	1.59
Pb	0.02	0.11

Total reflection coefficient calculated[21] assuming an isothermal plasma with a linear density gradient.

Table 4.4.

4.7. References

1) Deka B.K., Dyer P.E. and James D.J. Optics Commun. 18, 462-465, 1976.

2) Gerber R.A. and Patterson E.L. J. Appl. Phys. 47, 3524-9, 1976.

3) Clement R.M., Davies R.A., Miles H.T. and Sethuraman. J. Phys. D. Appl. Phys., 13, 1643-8, 1980.

4) Jones C.R. Appl. Phys. Lett. 22, 653-5, 1973.

5) Deka B.K., Dyer P.E., James D.J. and Ramsden S.A. Optics Commun. 19, 292-6, 1976.

6) Bykovskii Yu.A., Degtyarenko N.N., Elesin V.F., Kozyrev Yu.P. and Sil'nov S.M. Zh. Eksp. Teor. Fiz. 60, 1306-19, 1971. Transl. Sov. Phys. JETP 33, 706-12, 1971.

7) Dick K., Pepin H., Martineau J., Parbhakar K. and Thibaideau A. J. Appl. Phys. 44, 3284-93, 1973.

8) Shearer J.W. and Barnes W.S. Laser Interactions and Related Plasma Phenomena vol.1. ed. Schwarz H.J. and Hora H. (New York: Phenum), 1971.

9) Puell H. Z. Naturf. 25a, 1807-15, 1970.

10) Dyer P.E., Ramsden S.A., Sayers J.A. and Skipper M.A. J. Phys. D: Appl. Phys. 9, 373-382, 1181, 1976.

11) Boland B.C., Irons F.E., McWhirter R.W.P. J. Phys. B. 1, 1180-91, 1968.

12) Dick K. and Pepin H. Optics Commun. 13, 289-293, 1975.

13) Elton R.C. NRL report 6738, 1968.

14) Jahoda F.C., Little E.M., Quinn W.E., Sawyer G.A. and Stratton T.F. Phys. Rev. 119, 843-856, 1960.

15) Ahmad N. and Key M.H. J. Phys. B: Atom. Molec. Phys. 5, 866-877, 1972.

16) McWhirter R.W.P. Plasma Diagnostic Techniques, ed. Huddlestone R. and Leonard S. Academic Press (London), 1965.

17) Puell H., Neusser H.J. and Kaiser W. Z. Naturf. 25a, 1815-22, 1970.

18) Hough J.J.T. and Kerber R.L. Appl. Optics 14, 2960-70, 1975.

19) Caruso A. and Gratton R. Plasma Phys. 10, 867-77, 1968.

20) Kiddier R.E. Physics of High Energy Density, ed. Caldirola P. and Knoepfel H. Academic Press (London), 1971.

21) Dyer P.E., James D.J., Ramsden S.A. and Skipper M.A. Phys. Lett. 48a, 311-312, 1974.

CHAPTER 5

HF LASER-TARGET INTERACTION STUDIES (GASEOUS ENVIRONMENT).

5.1. Introduction

The interaction of HF laser radiation, with certain solid targets in a gaseous environment, is briefly studied. Platinum, stainless steel and aluminium targets are used in air at atmospheric or reduced pressures. Measurements on thermal coupling, reflectance, plasmotron threshold, laser supported detonation wave threshold and velocity are presented, together with transmission studies through a laser-induced gas-breakdown plasma.

5.2. Thermal Coupling

5.2.1. Introduction

For many industrial and military applications, the optimum transfer of radiation energy to a surface, in a gaseous environment, is required. Typical conditions are :-

ambient pressure	0-760 torr.
ambient gas	air, sometimes argon
surface	(polished) metals, such as steel, titanium and aluminium alloys
laser	CO_2, DF, Nd:glass, ruby
focal spot diameter	$\lesssim$ 5mm

The coupling coefficient, α, is defined as the ratio of the thermal energy absorbed by the target to the radiation energy incident on it. α has been measured[1-4] at the CO_2 and Nd:glass wavelengths as functions of target material, ambient conditions, laser intensity and fluence (energy/spot area), pulse duration, and focal spot size. In this section, we present measurements at the HF wavelength, using polished platinum targets in air at an ambient pressure of 0-760 torr.

5.2.2. Experimental Procedure

The schematic layout for the thermal coupling measurements is shown in Fig.5.1. The ∿ 300ns HF laser radiation intensity was varied using the Inconel on Infrasil attenuators. Pulse-shapes and energy were measured using a liquid nitrogen cooled, Au doped Ge photoconductive detector and a calibrated Lumonics 20D pyroelectric joulemeter. Chromel-alumel thermocouples were symmetrically spot-weded on the rear surface of thin polished platinum discs. As 0.1°C absolute accuracy was not necessary in these experiments, known calibration data for these pure metals was assumed, and is shown in Fig.5.2. The output signal was monitored using a D83 Telequipment oscilloscope with a V3 high-gain amplifier. A typical signal is shown in Fig.5.3. The target and detection system were screened in a Faraday cage to remove radiative noise pick-up from the laser system. A time-averaged value of α was obtained using the relation-ship :-

$$\alpha = \frac{M \bar{C} \theta}{E} \qquad \ldots\ldots(5.1)$$

where, M is the target mass (interaction loss negligible), $\bar{C}$ the mean specific heat over the temperature variation, θ the temperature rise from room temperature, and E the incident laser energy. In the case of pre-fabricated targets, the mass was calculated using dimensions and target density. For some experiments, the target was positioned in an evacuable cell.

The spot size was defined as follows. The irradiance was decreased until the threshold burn condition on exposed, uncoated 410 Polaroid film was achieved. The irradiance was now increased by a factor of two, and the spot size accurately measured. Allowance was made for the thickness of the Polaroid film. The single crater sizes on the targets showed agreement with these values.

The incident energy was recorded for each thermocouple measure-

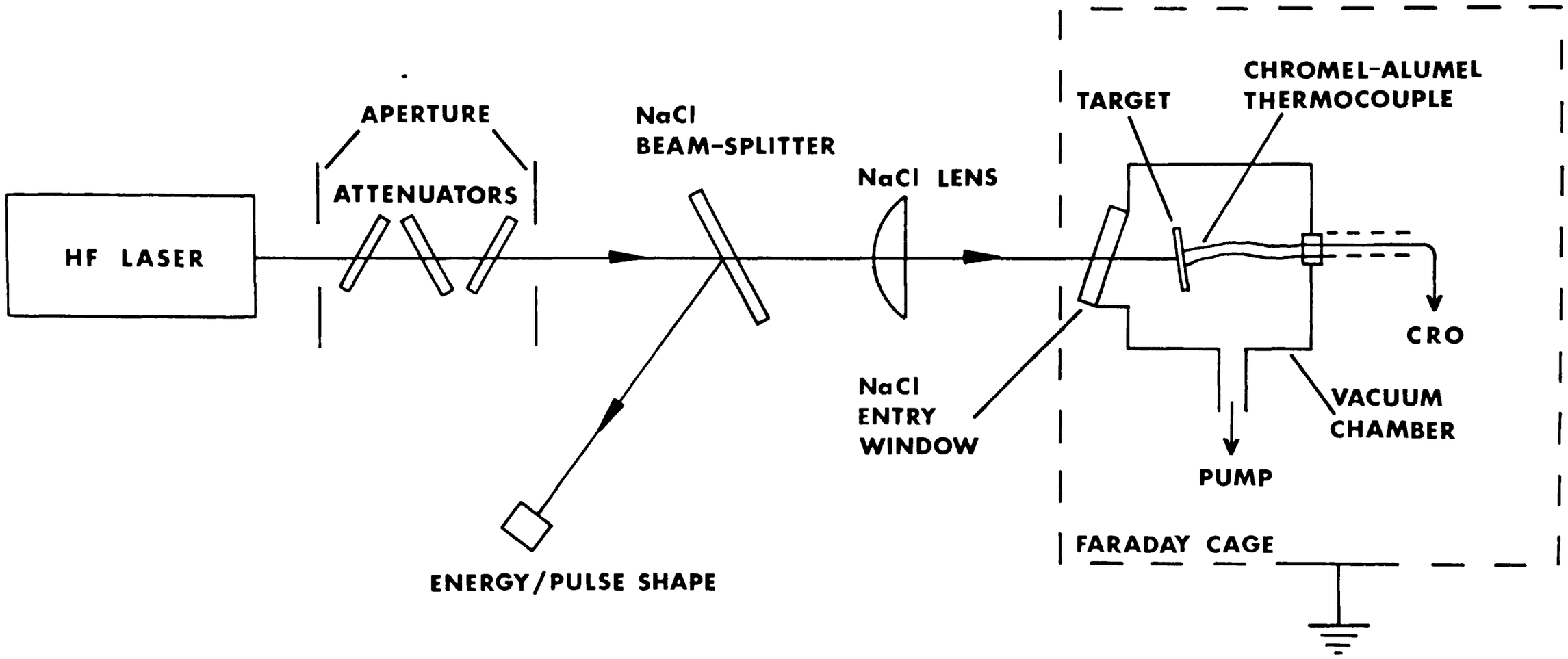

Fig. 5.1. Schematic configuration for thermal coupling measurements.

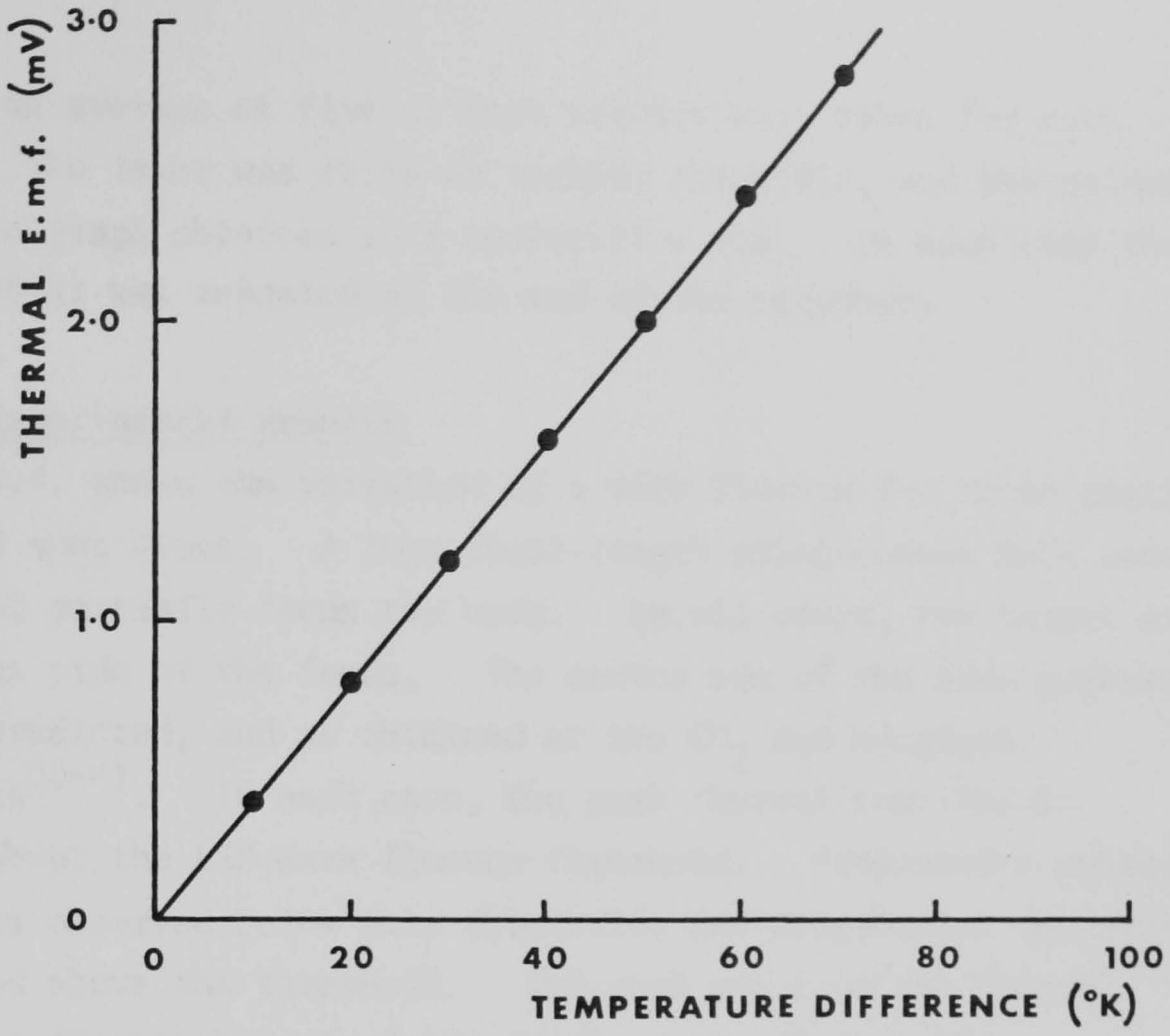

Fig.5.2. Chromel – alumel (T1 and T2) thermocouple calibration graph.

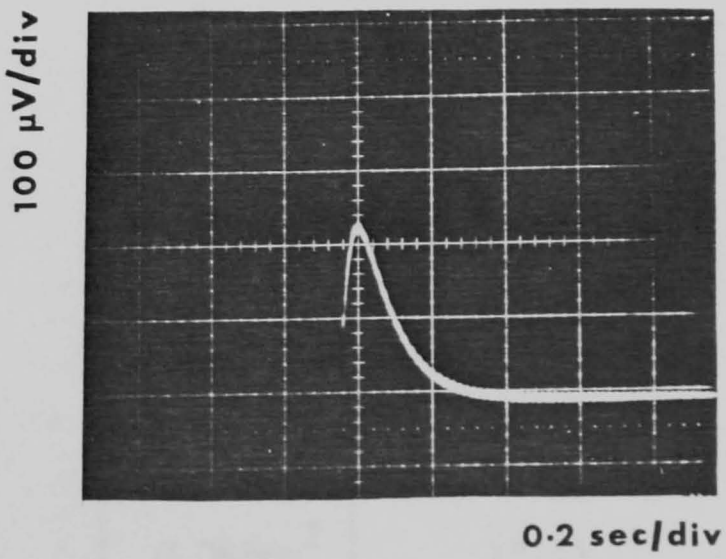

Fig.5.3. Thermocouple oscilloscope trace.

ment, and an average of five or more results was taken for each reading. The laser was fired at regular intervals, and the values for a given graph obtained in a consecutive run. In each case the initial result was repeated at the end of the sequence.

5.2.3. Experimental Results

Fig.5.4. shows the variation of α with fluence for three platinum target and spot sizes. A 20cm focal-length plano-convex NaCl lens was used to partially focus the beam. In all cases, the target was on the lens side of the focus. The curves are of the same general shape as predicted, and as obtained at the CO_2 and Nd:glass wavelengths[2-4]. In each case, the peak thermal coupling is obtained about the LSD wave fluence threshold. Progressive enhanced coupling is observed below this threshold, and progressive decoupling is observed above the threshold. The peak value of the thermal coupling coefficient obtained was in the range 10.5-16.5%.

Fig.5.5. shows results obtained using a 50cm focal-length, plano-convex NaCl lens. Consider the following table, which summarises these two graphs :-

TARGET DIA	FOCAL-LENGTH	SPOT AREA	SPOT/TARGET AREA	PEAK α
3.0mm	20cm	$0.010cm^2$	14.1%	16%
3.5mm	50cm	$0.032cm^2$	33.3%	11%
4.8mm	20cm	$0.024cm^2$	13.3%	10.5%
4.8mm	50cm	$0.036cm^2$	19.9%	14%
8.1mm	20cm	$0.066cm^2$	12.8%	12%
8.1mm	50cm	$0.088cm^2$	17.1%	19%

TABLE 5.1.

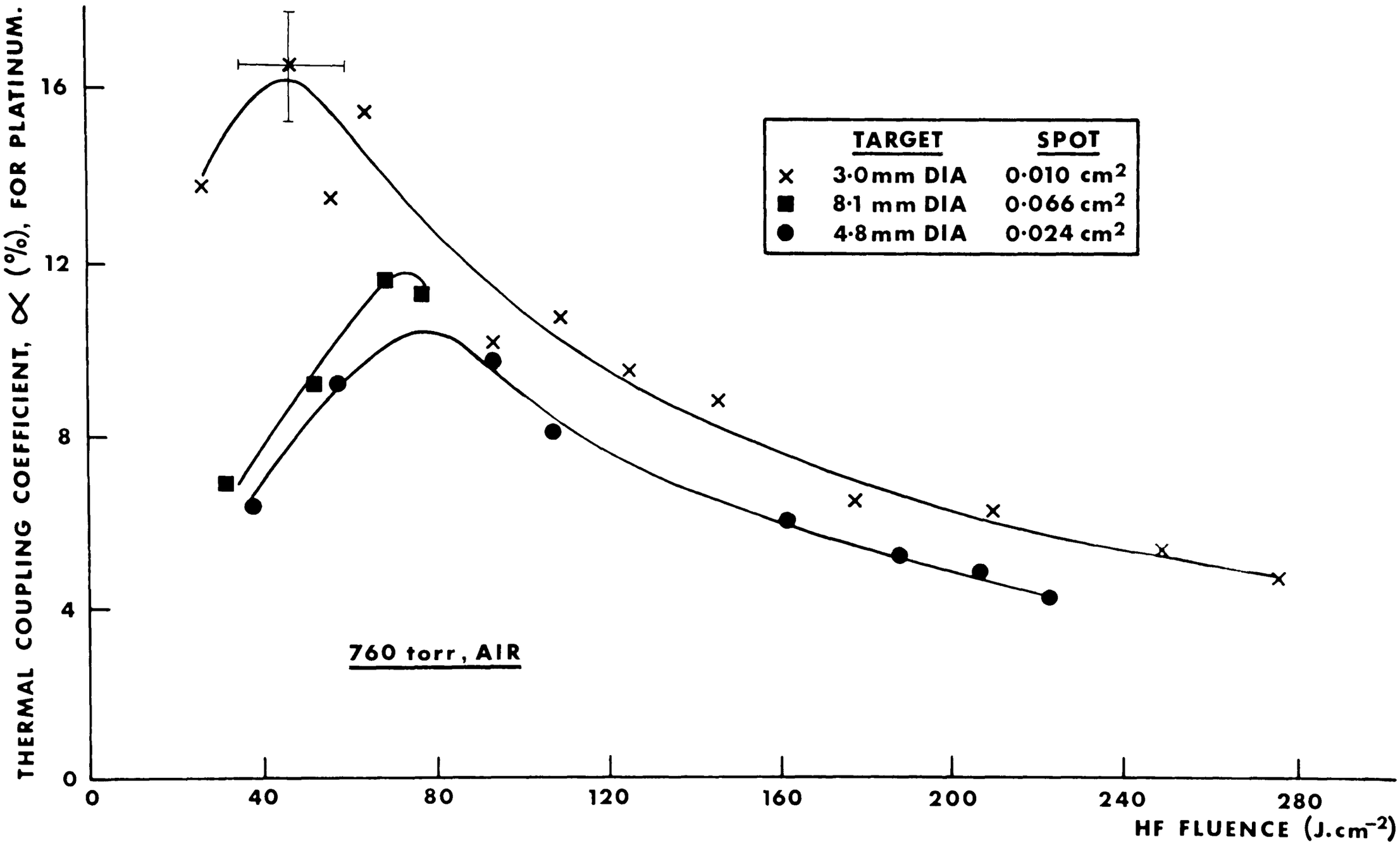

Fig.5.4. Variation of thermal coupling coefficient with fluence for platinum targets, using a 20cm focal length lens.

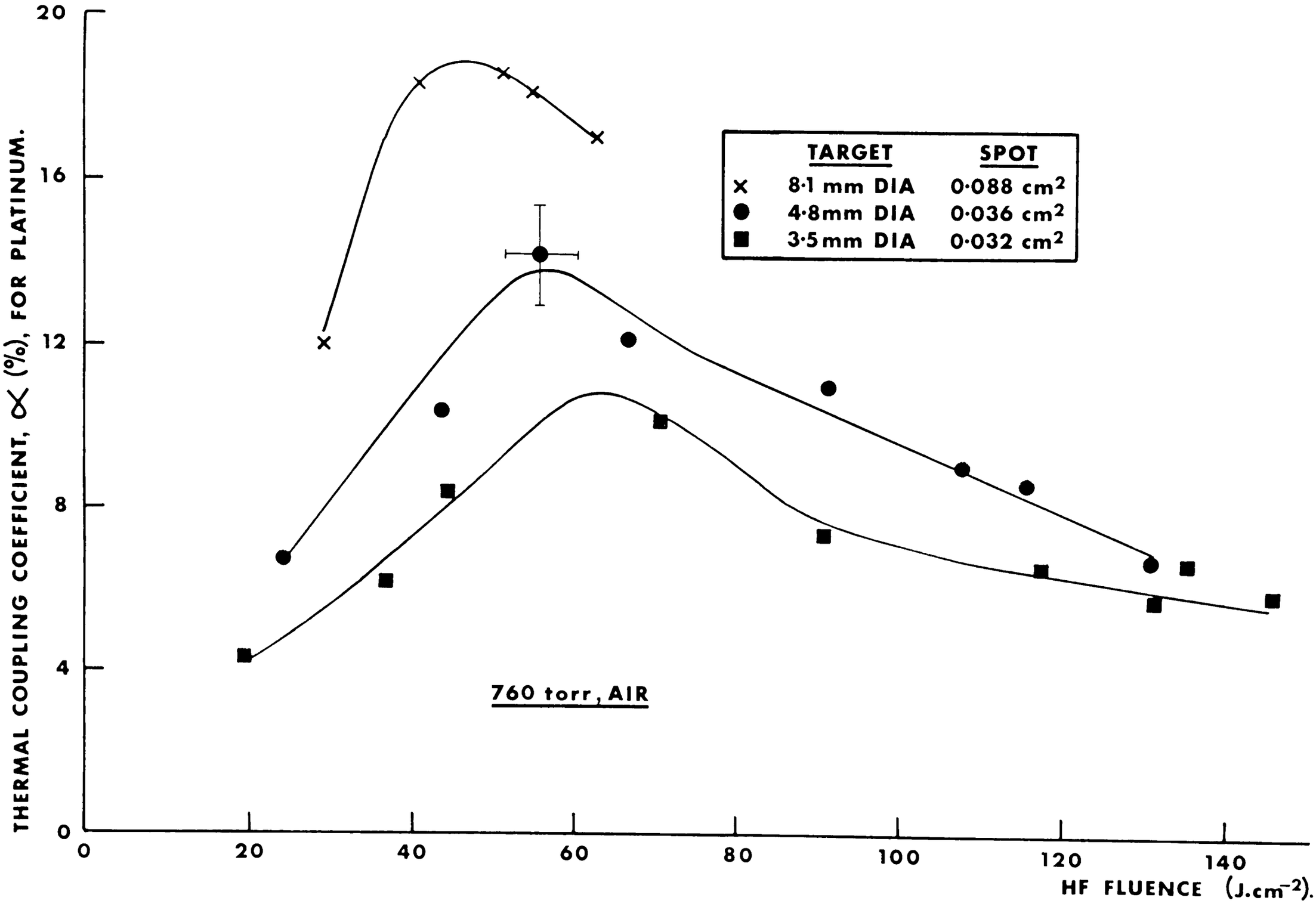

Fig.5.5. Variation of thermal coupling coefficient with fluence for platinum targets, using a 50cm focal length lens.

For the larger targets, an enhanced thermal coupling is to be noted with the longer focal-length lens. In both these cases, the focal spot also covers a larger fraction of the target. Thus, the enhancement cannot be due to plasma spread outside the spot. In contrast, the smaller targets indicate the reverse situation. This can be explained by assuming significant plasma spread beyond the target in the case of the 3.5mm diameter target. The explanation for the enhancement with the larger targets is not immediately apparent.

The peak coupling does not follow an obvious trend with spot size. Measurements at larger spot sizes were not possible, unfortunately, because of the available laser output energy. This would have been desirable to clarify the situation.

Conflicting results have been obtained at the CO_2 wavelength[2,4], as the spot size was increased, Marcus et al. observed a marginal enhancement, but Maher et al. observed the reverse.

The minimum beam intensity required to support an LSD wave is calculated in ref.5.5.,5.6. and plotted as a function of spot radius in Fig.5.6. Experimental peak coupling values are also indicated to show their equivalence. The LSD wave threshold for 0.5-1mm radius spots was found to be $\sim$ (2-3) x $10^8 W.cm^{-2}$.

The thermal coupling coefficient - fluence dependence was also measured at reduced air pressure. Fig.5.7. shows the dependence at 760 and 100 torr in the case of a 3mm diameter target and $\sim$ 1mm diameter spot. The two curves are similar, although the increased LSD wave velocity at 100 torr (see next section) is made apparent by the slightly reduced coupling. These results are in general agreement with measurements at the CO_2[2,4] and Nd:glass[3] wavelengths.

Peak coupling coefficients presented here at the HF wavelength for platinum targets, (12-18%), are relatively low when compared with values for other metals at the CO_2 wavelength, ($\sim$25-35%). This variation may be partly due to a target dependence, but the increased plasma absorption length at $\sim$ 2.8μm is likely to be significant. Breakdown plasma transmission experiments at the HF wavelength are described in section 5.4. and compared with CO_2 results.

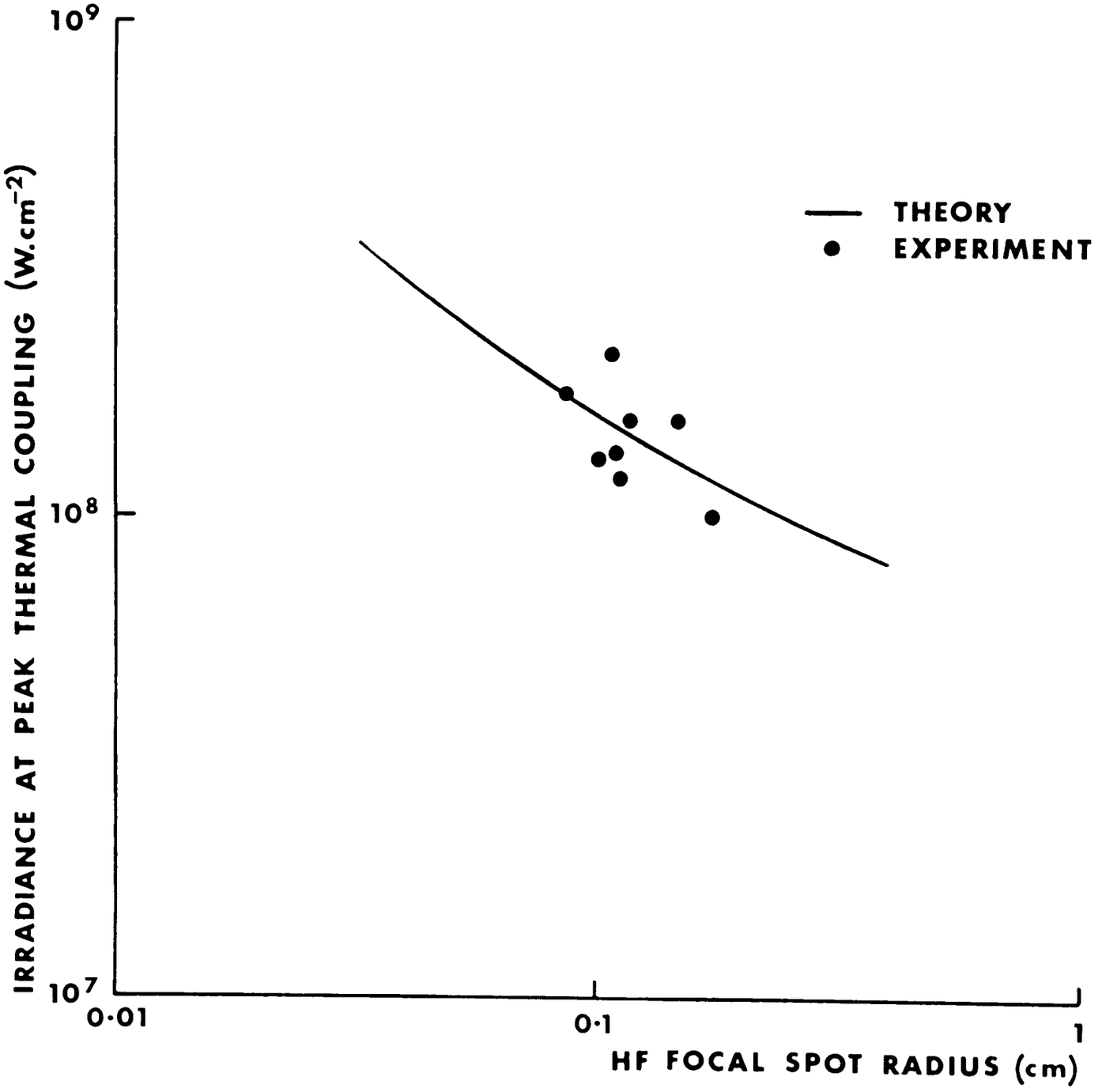

Fig.5.6. Theoretical minimum beam intensity, to support an LSD wave, versus focal spot radius. This is compared with experimental results of irradiance at peak thermal coupling.

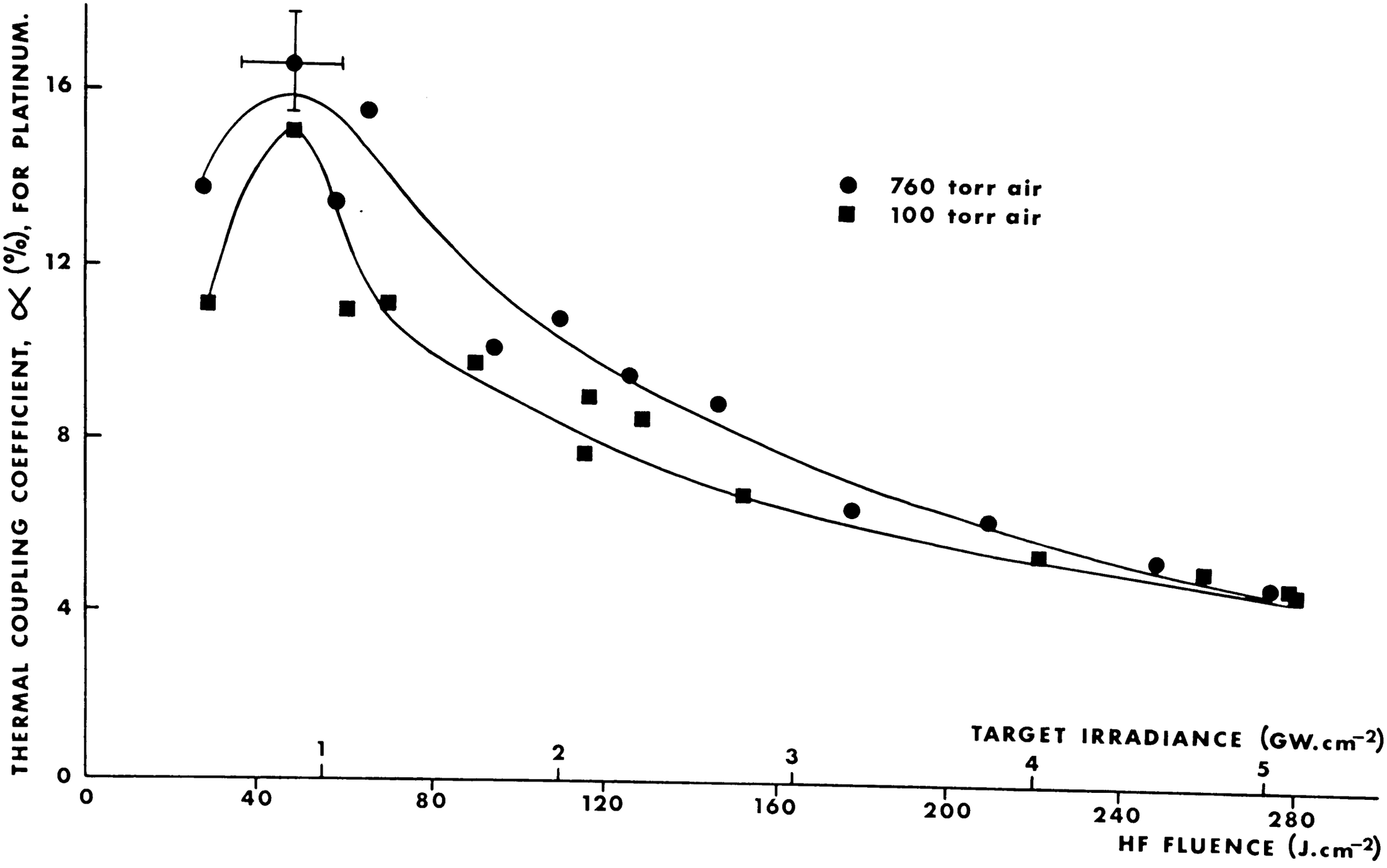

Fig.5.7. Variation of thermal coupling with fluence and irradiance, for 3mm DIA platinum target at 760 torr and 100 torr air pressures.

5.3. Ignition and Propagation of LSD Waves

5.3.1. Introduction

High speed (streak) photography has been employed to determine LSD wave velocity and threshold irradiance when HF laser radiation is focused onto metal targets in air. Targets used were polished stainless steel and aluminium, and unpolished platinum. Ambient pressure was varied from 10^{-3}torr to atmospheric. The reflection coefficient was measured on both sides of the LSD wave threshold irradiance in order to investigate the decoupling effects.

5.3.2. Experimental Procedure

A photograph of the experimental configuration is shown in Fig.5.8. This is similar to the configuration used for thermal coupling. Incident energy and pulse shape were monitored as before. In addition the specularly reflected radiation, from the tilted target, was collected and partially focused, with a concave mirror, onto another calibrated joulemeter. The Hadland streak camera, as previously described, was positioned to view luminous plasma that expanded back towards the laser. The tilting of the target ensured that specular 'blow-off' was insignificantly observed (because of the camera's depth of field) and reflective coupling, with the laser itself, was minimised. An observation NaCl side window was incorporated into the vacuum chamber, to enable the procurement of streak measurements at reduced pressure.

Both stable and unstable resonators were used in these experiments. For the latter situation, the laser output was regularly checked by observing the far-field distribution. The distribution also enabled an estimate of the target irradiance to be made. When operated in the multi-mode stable configuration, a maximum irradiance of $\sim 10^{9}$W.cm^{-2} was possible for spot sizes $\gtrsim$ 1mm. With the unstable resonator, the maximum irradiance was $\sim 10^{10}$W.cm^{-2} for a spot size of $\sim$ 100μm.

5.3.3. Experimental Results

a) Aluminium Target

Fig.5.9. shows a typical streak photograph at an irradiance of $\sim 9.6 \times 10^{7}$W.cm^{-2}. This clearly indicates a plasmotron situation, as

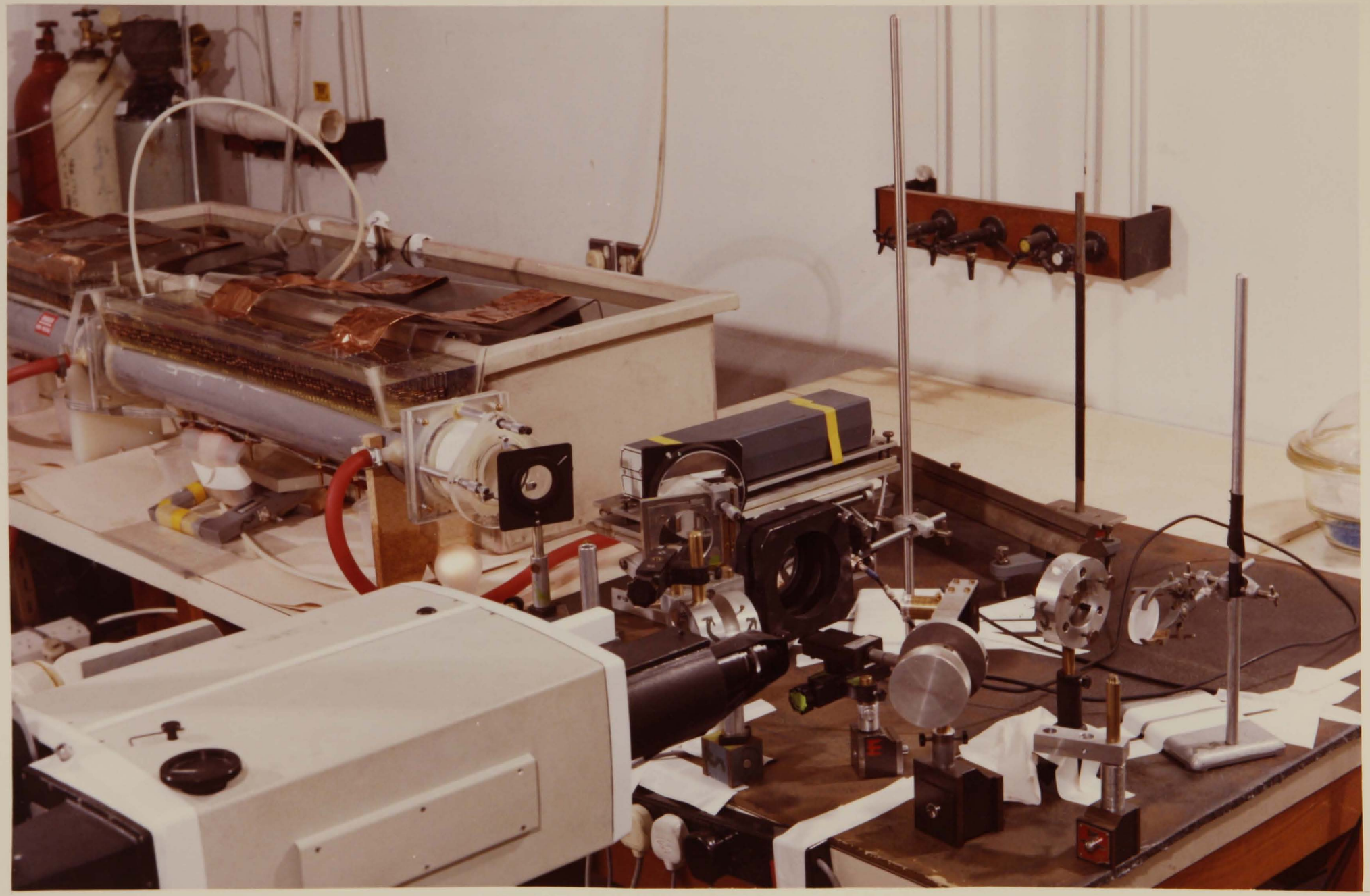

Fig.5.8. Photograph of the experimental configuration used for atmospheric high-speed photography.

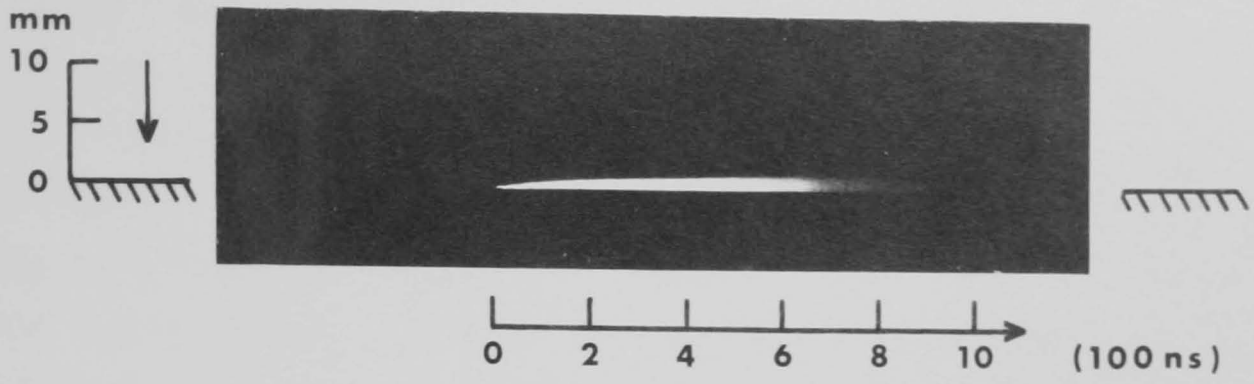

Fig.5.9. Streak photograph of an aluminium plasmotron in atmospheric air at an irradiance of $\sim 9{\cdot}6 \times 10^{7}$ W.cm^{-2} Camera aperture f/22.

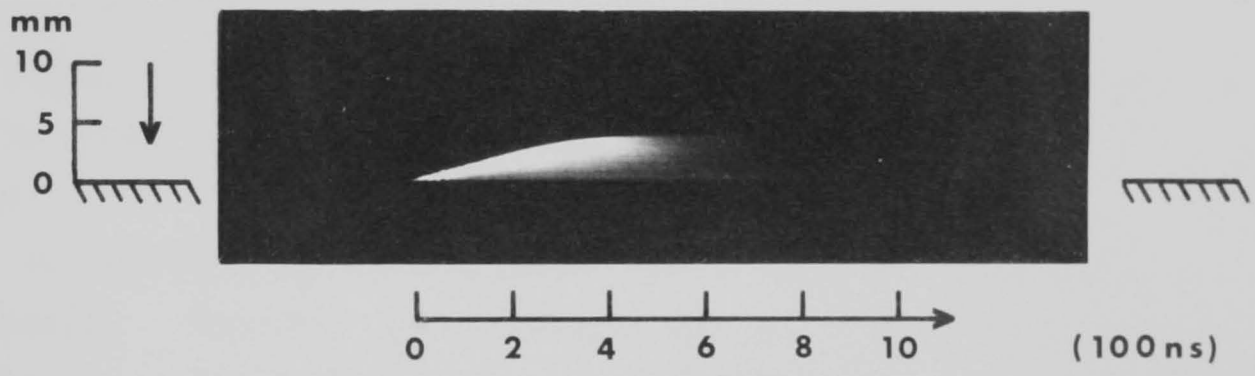

(a)

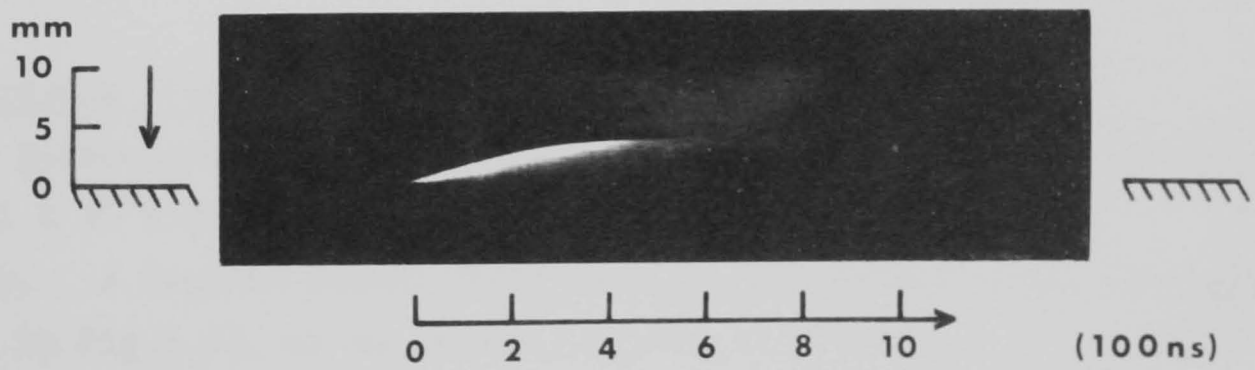

(b)

Fig.5.10. Streak photograph of an aluminium LSD wave in atmospheric air at an irradiance of $\sim 3{\cdot}5 \times 10^{8}$ W.cm^{-2}

(a) Camera aperture f/22, 10 dB neutral density filter.

(b) Camera aperture f/22, 12 dB neutral density filter.

also observed at the CO_2 wavelength. At a threshold of $\sim$ 1.6 - 2.0 x $10^8 W.cm^{-2}$ an LSD wave was observed. For the given spot size, this is in good agreement with the theoretical value given in ref.5.6.

Fig.5.10 shows a typical streak photograph at an irradiance of $\sim$ 3.5 x $10^8 W.cm^{-2}$. This is clearly an LSD wave situation without any recoupling apparent. The expansion velocity of $\sim$ 1.17 x $10^6 cm.sec^{-1}$ is in fair agreement with the predicted value, obtained from 5.2., of 1.46 x $10^6 cm.sec^{-1}$ (using ρ_o = 1.2047 x $10^{-3} g.cm^{-3}$ at 20°C and ϕ = 3.5 x $10^{15} erg.sec^{-1}cm^{-2}$). The difference can be explained by the decreased irradiance, at the absorption front, due to the cone angle. For example, at 1mm from the surface the irradiance has decreased by a factor of 1.465, resulting in a theoretical velocity of 1.29 x 10^6 $cm.sec^{-1}$. Under similar conditions, TEA CO_2 laser radiation produces recoupling, in contrast to these results.

In Fig.5.11. the initial plasma expansion velocity/irradiance scaling is shown to obey the one third law above the LSD wave threshold.

The reflection coefficient is given in Fig.5.12. as a function of irradiance. For very low irradiance values, the surface acts as a good mirror. As the irradiance is increased the reflectance falls steadily; above the LSD wave threshold $\lesssim$ 10% of the radiation was reflected.

b) Stainless Steel and Platinum Targets

The plasmotron threshold for polished stainless steel was found to be $\sim$ 1 x $10^8 W.cm^{-2}$. This is higher than the threshold for aluminium. A typical streak photograph of a stainless steel plasmotron is shown in Fig.5.13. at an irradiance of 1 x $10^8 W.cm^{-2}$.

LSD wave initiation for stainless steel occured at an irradiance of $\sim$ 2.3 x $10^8 W.cm^{-2}$, which is at a similar level to that of aluminium. Typical streak photographs at this threshold irradiance are shown in Fig.5.14a-b. The initial LSD wave expansion velocity again obeyed the $\phi^{1/3}$ dependence as given in Fig.5.11. The velocities for stainless steel and aluminium were very similar.

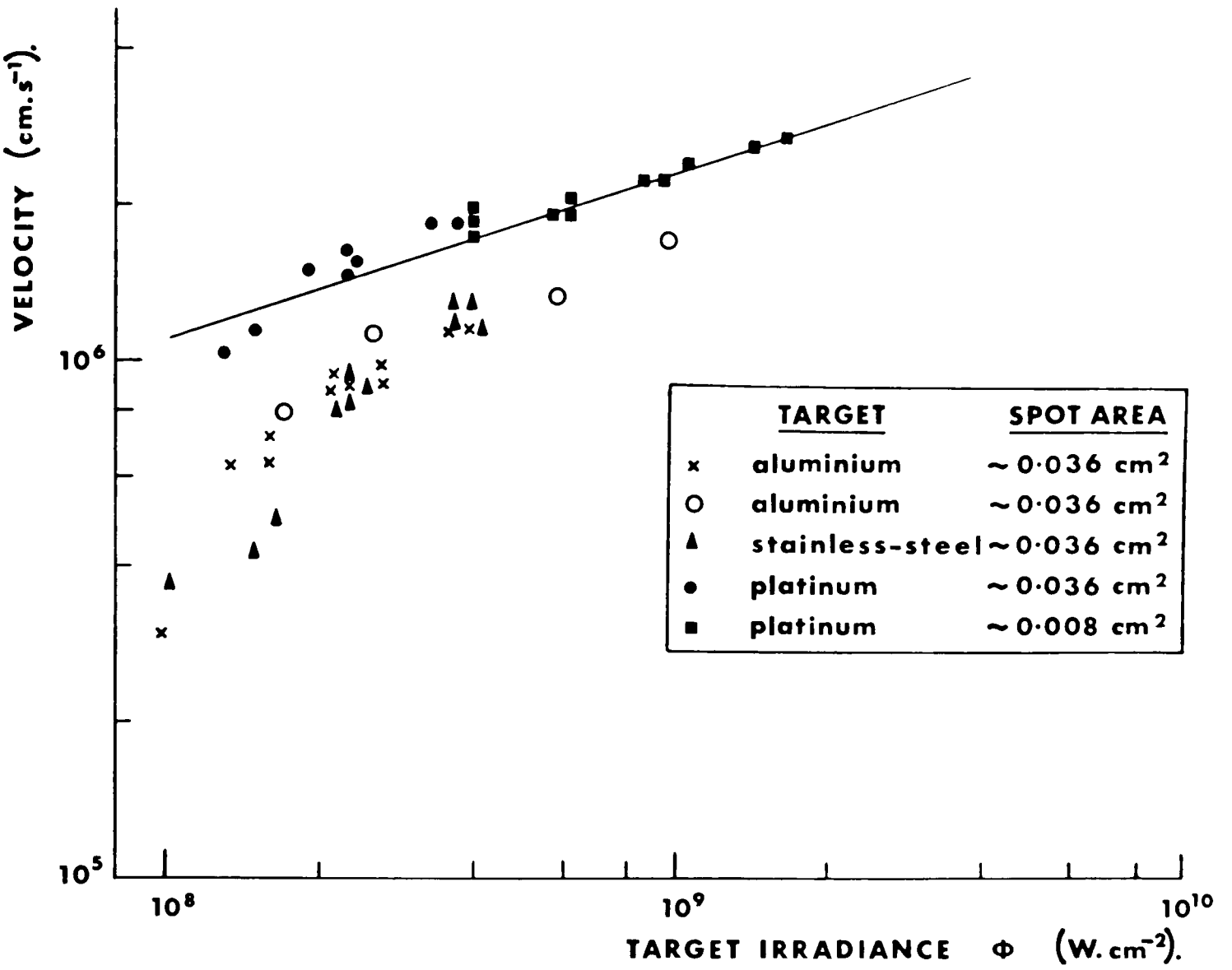

Fig. 5.11. Initial plasma expansion velocity versus target irradiance.

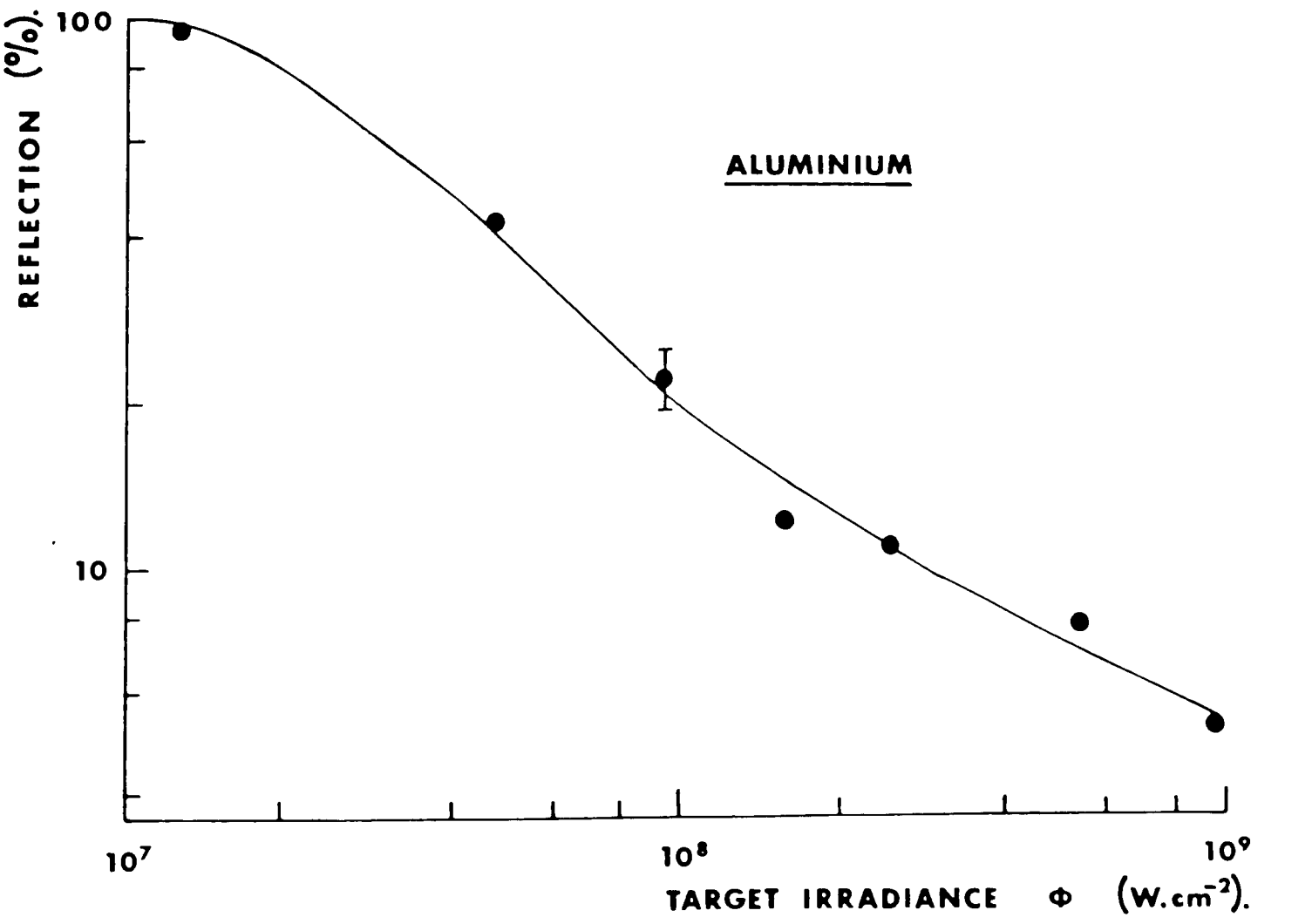

Fig. 5.12. Reflection from an aluminium target, in air, versus irradiance.

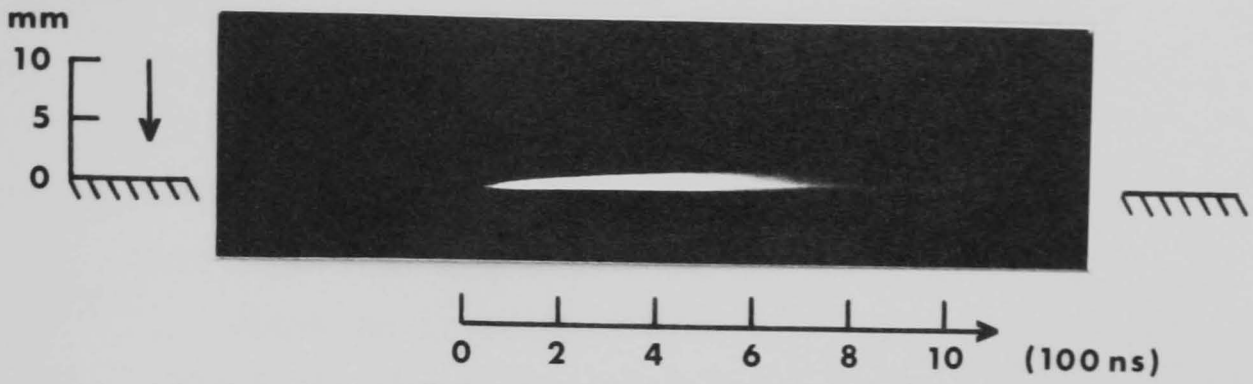

Fig.5.13. Streak photograph of a stainless steel plasmotron in atmospheric air at an irradiance of $\sim 1 \times 10^8$ W.cm^{-2} Camera aperture f/22.

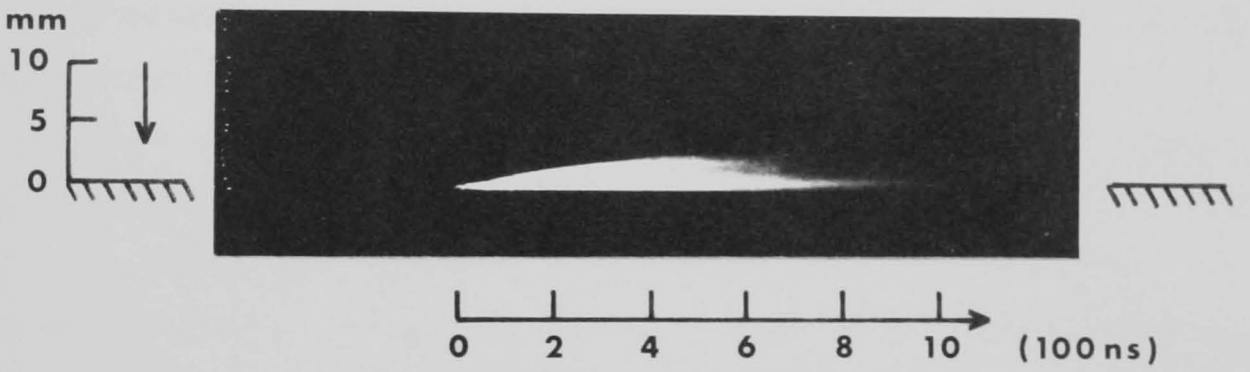

(a)

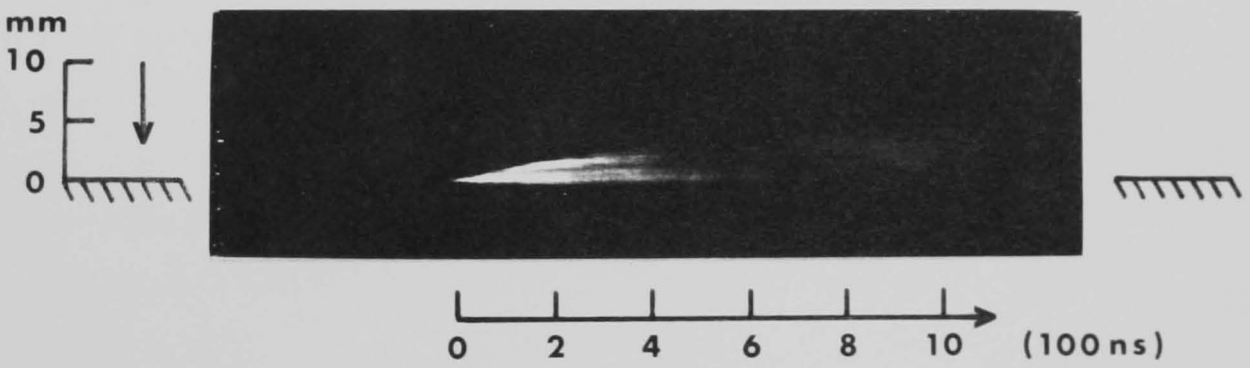

(b)

Fig.5.14. Streak photograph of a stainless steel plasma in atmospheric air at an irradiance of $\sim 2{\cdot}3 \times 10^8$ W.cm^{-2}

(a) Camera aperture f/22, 5 dB neutral density filter.

(b) Camera aperture f/22, 10 dB neutral density filter.

Using the unstable resonator configuration, high irradiances ($\lesssim 10^{10} W.cm^{-2}$) at small spot areas were available to study the plasma behaviour. Fig.5.15. shows a streak photograph taken at an irradiance of $\sim 4.6 \times 10^{8} W.cm^{-2}$. A rapid, strong decoupling is seen to be followed by a weaker recoupling $\sim$ 280ns from the initial LSD wave production. This behaviour has also been observed at the CO_2 laser wavelength[7,8]. Above an irradiance of $\sim 3 \times 10^{9} W.cm^{-2}$ no recoupling was observed. Fig.5.16. shows the initial expansion velocity scaling with irradiance. In this case a low ($\sim\phi^{0.15}$) scaling was observed. It is likely that radial losses are important for the small spot areas employed here. Thus, the lowered effective irradiance would decrease the scaling from the $\phi^{1/3}$ given by theory.

The plasmotron threshold was found to decrease slightly with ambient air pressure. For example, with stainless steel, the threshold was approximately constant at $1.1 \times 10^{8} W.cm^{-2}$ above 400 torr, but at 100 torr it was $\sim 7 \times 10^{7} W.cm^{-2}$. The LSD wave threshold was found to be approximately constant in the pressure range 20-760 torr.

Fig.5.17. shows the relationship between the initial plasma expansion velocity and ambient pressure. Three different irradiance levels are indicated; as expected the higher irradiance gives the higher expansion velocity. For low pressures the velocity is independent of pressure; above $\sim$ 100 torr the velocity was found to scale as $P^{-0.32}$ in good agreement with the $P^{-1/3}$ predicted by theory. Fig.5.18. shows the expansion velocity as a function of irradiance at ambient pressures of 20, 100 and 400 torr. For each pressure, a $\phi^{1/3}$ scaling was observed above the LSD wave threshold.

With platinum, the velocity dependence, as shown in Fig.5.11.,5.19., was found to be similar to those of stainless steel and aluminium. The platinum plasmotron threshold was found to be $\sim 1.2 \times 10^{8} W.cm^{-2}$. Fig.5.20., at $\sim 1.3 \times 10^{8} W.cm^{-2}$, shows a combined LSD wave and weak plasmotron. Above about $1.5 \times 10^{8} W.cm^{-2}$ only an LSD wave was observed, for example, as shown in Fig.5.21.

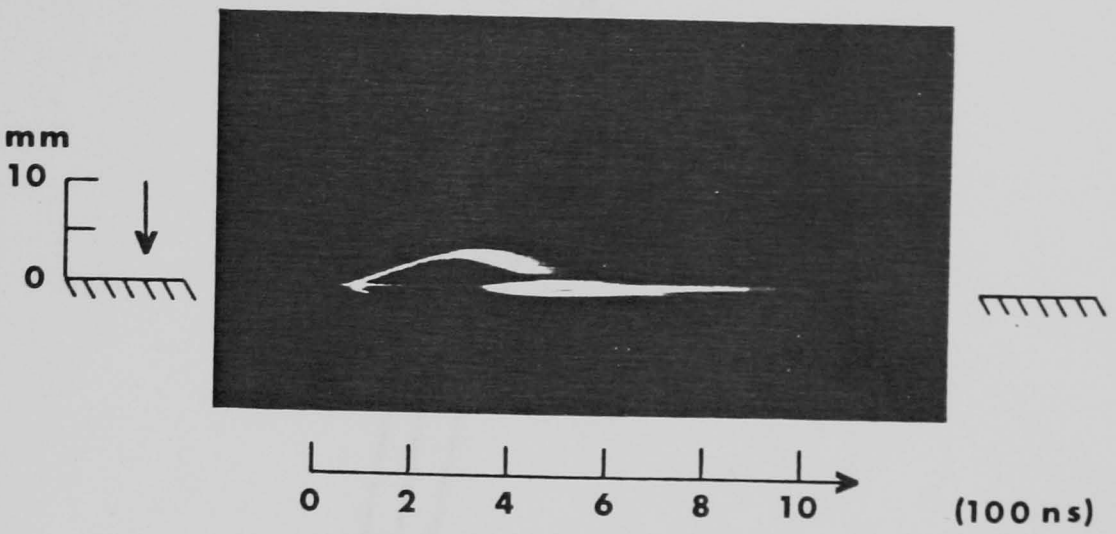

Fig.5.15. Streak photograph of plasma production from stainless steel in air at atmospheric pressure. Target irradiance ~ $4{\cdot}6 \times 10^{8}$ $W.cm^{-2}$ (unstable resonator configuration). Camera aperture f/2.

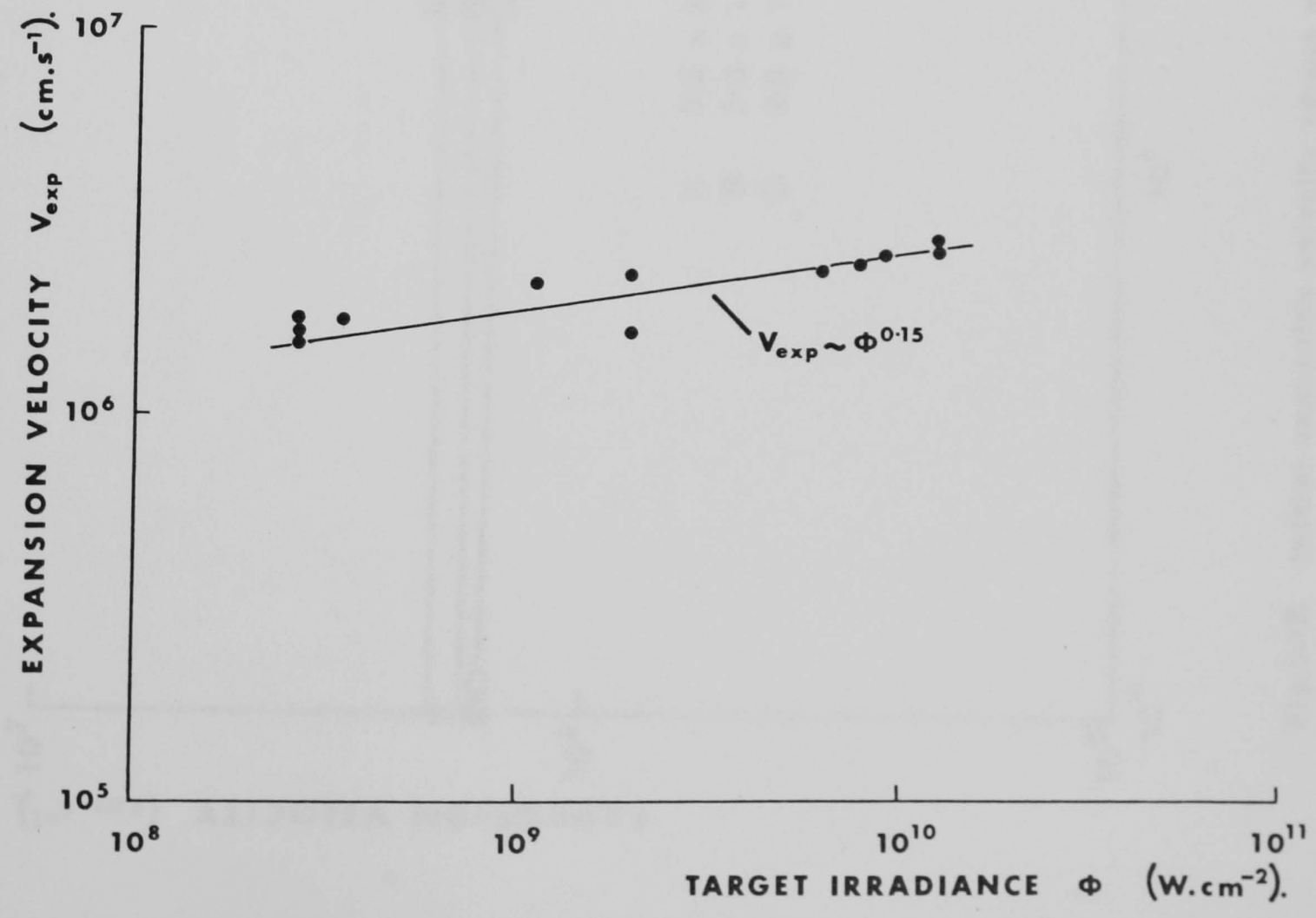

Fig.5.16. Initial plasma expansion velocity versus target irradiance for stainless steel.

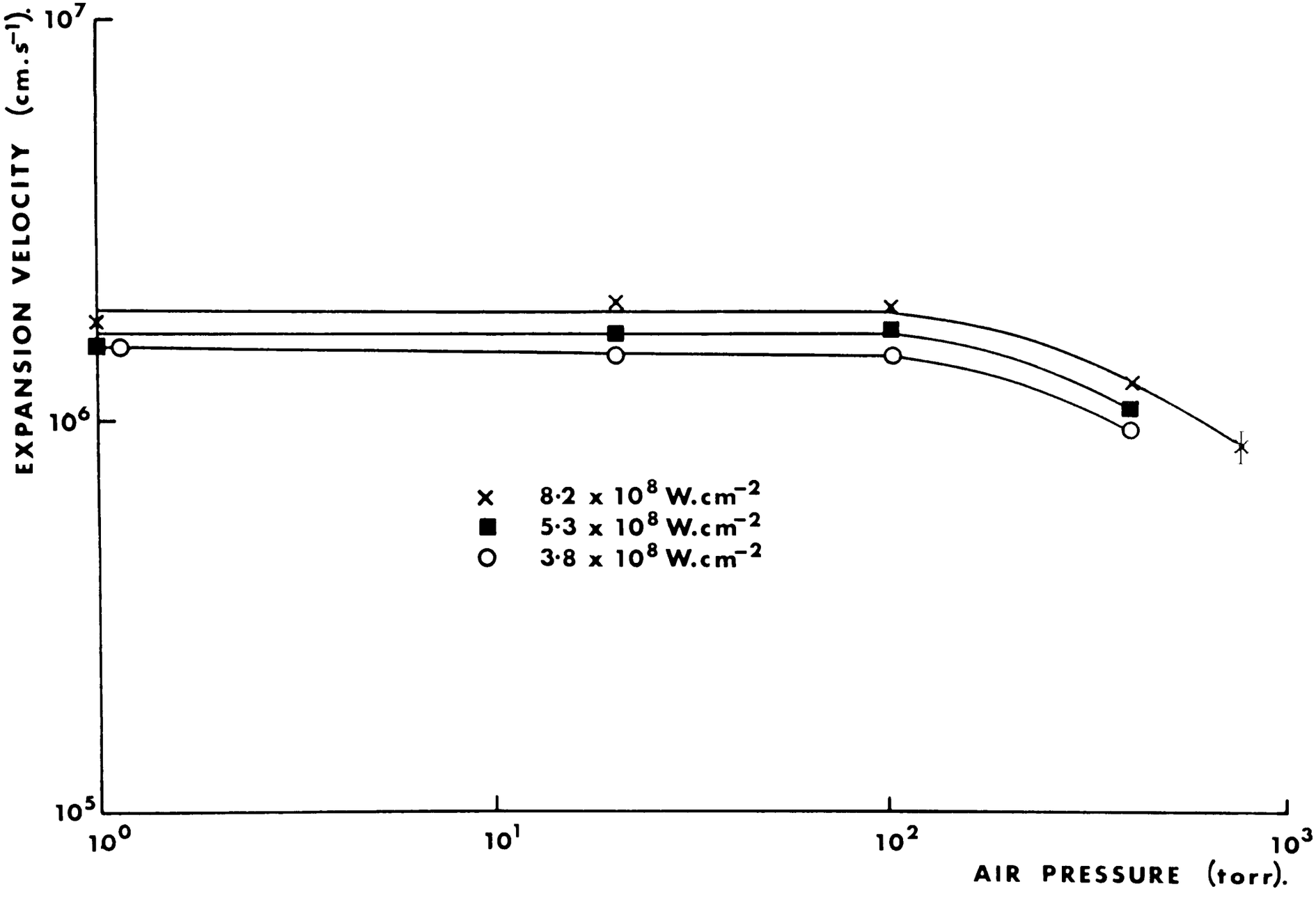

Fig. 5.17. Initial expansion velocity versus air pressure for constant irradiance.

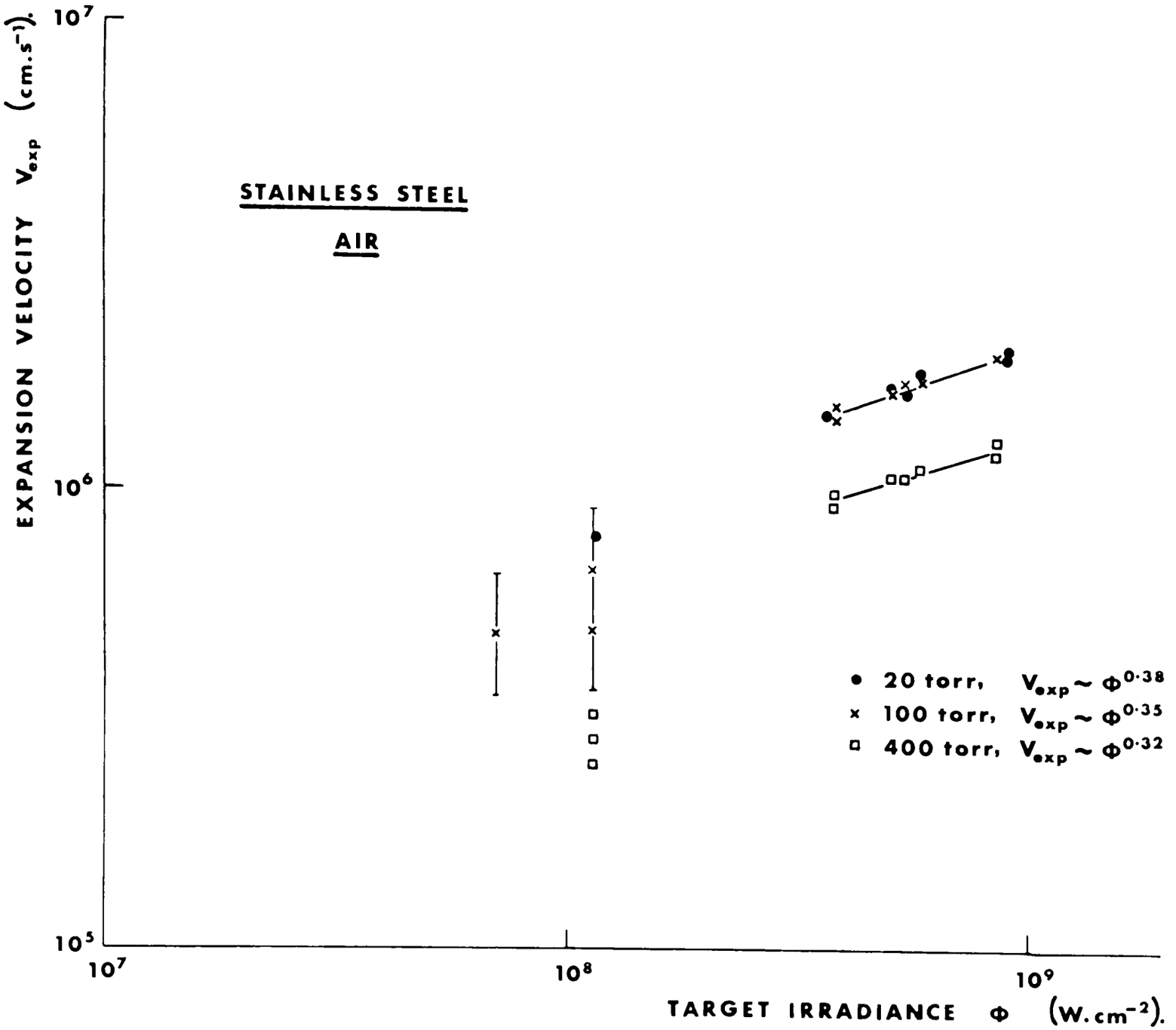

Fig. 5.18. Initial expansion velocity versus target irradiance, at pressures of 20, 100, and 400 torr.

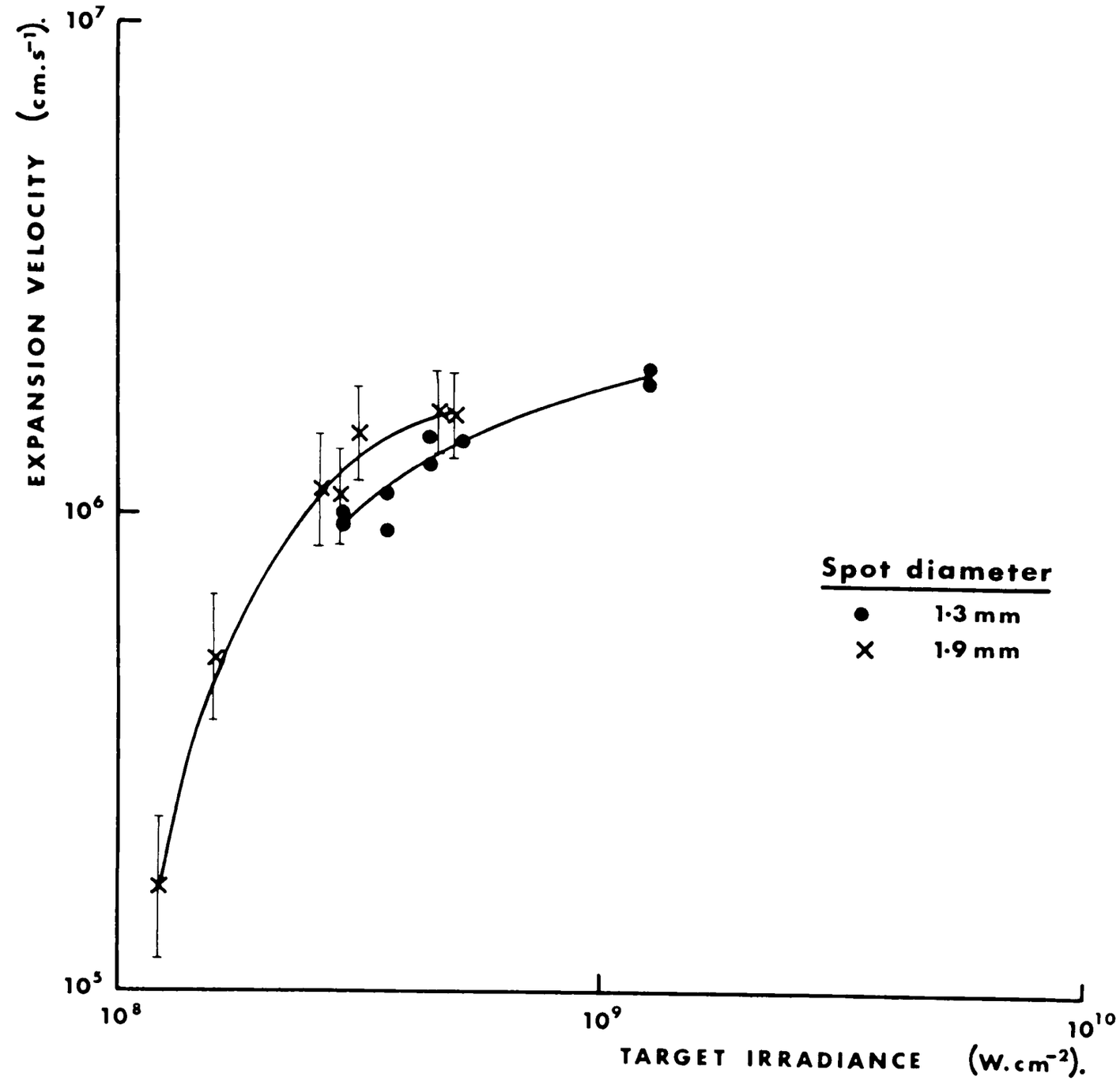

Fig.5.19. Initial plasma expansion velocity versus target irradiance, using a 50 cm lens and a platinum target in air.

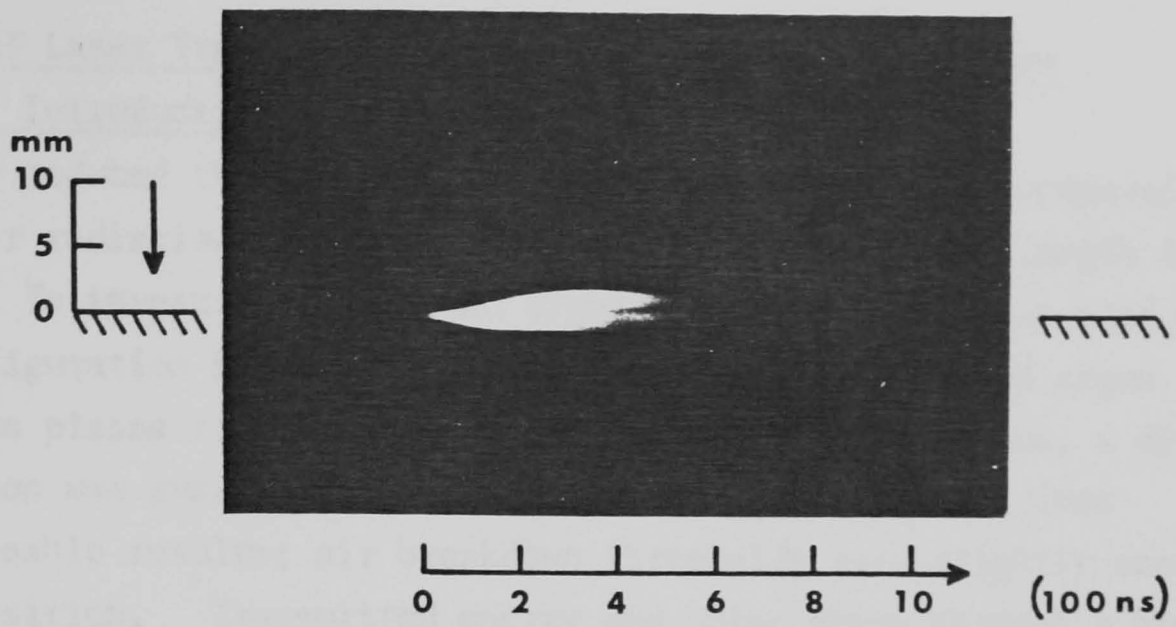

Fig.5.20. Streak photograph of plasma production from platinum in atmospheric air. Irradiance ~ $1{\cdot}3 \times 10^{8}$ W.cm.$^{-2}$ Camera aperture f/22, 20dB neutral density filter.

Fig.5.21. Streak photograph of plasma production from platinum in atmosperic air. Irradiance ~ $1{\cdot}5 \times 10^{8}$ W. cm.$^{-2}$ Camera aperture f/22, 25dB neutral density filter.

5.4. HF Laser Transmission Through a Gas Breakdown Plasma

5.4.1. Introduction

The reduced thermal coupling of HF laser radiation, compared with CO_2 laser radiation, suggests that the plasma absorption length is large. To investigate this, an argon breakdown plasma was used in the configuration shown in Fig.5.22. Deka[9] has studied argon breakdown plasma transmission at the CO_2 wavelength. Thus, a direct comparison was available. Pure argon was chosen, as it gives reproduceable results; air breakdown thresholds vary slightly according to composition. Transmitted energy and pulse shape through a breakdown plasma are studied as a function of argon pressure.

5.4.2. Experimental Procedure

The experimental configuration is shown in Fig.5.22. A $\sim$ 1J unstable resonator HF laser[10] giving $\sim$ 160ns FWHM pulses was focused using an f/10, 30cm NaCl lens into the high pressure argon cell. Transmitted radiation was collected and focused with a second f/10 lens over a H_2O- and CO_2-free path, produced using flowing dry nitrogen gas (H_2O and CO_2 are highly absorbing to HF radiation). The pulse shape was measured, using the liquid nitrogen cooled Au-doped Ge detector, for the radiation scattered from a ground NaCl plate. The transmitted energy was measured using a calibrated 'Gen-Tec.' pyroelectric joulemeter.

5.4.3. Experimental Results

In Fig.5.23. the transmitted energy and pulse duration (FWHM) are given as a function of gas pressure. The transmission coefficient is seen to steadily decrease with increasing pressure, falling from $\sim$ 1.0 below the breakdown threshold to $\sim$ 0.16 at 2460 torr. The corresponding decrease in pulse width is 160ns to $\sim$ 7ns. At atmospheric pressure the transmission was determined to be $\sim$ 35%, which is high when compared with $\lesssim$ 10% for air at 10.6μm wavelength.

The large absorption length for HF radiation is probably due to the breakdown plasma density being sub-critical. As the pressure is

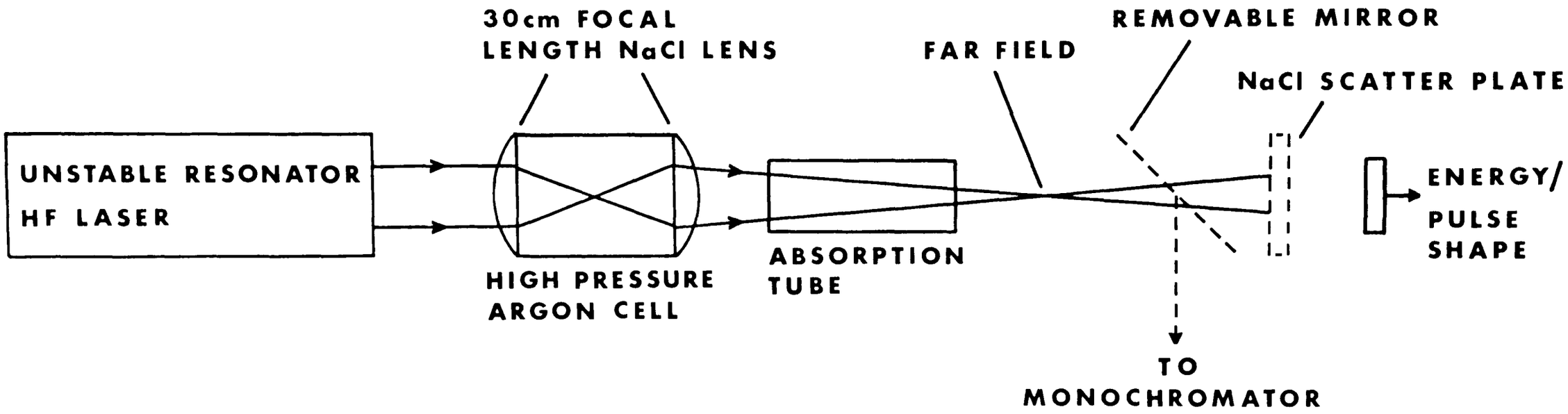

Fig.5.22. Experimental configuration for HF transmission measurements through a gas breakdown plasma.

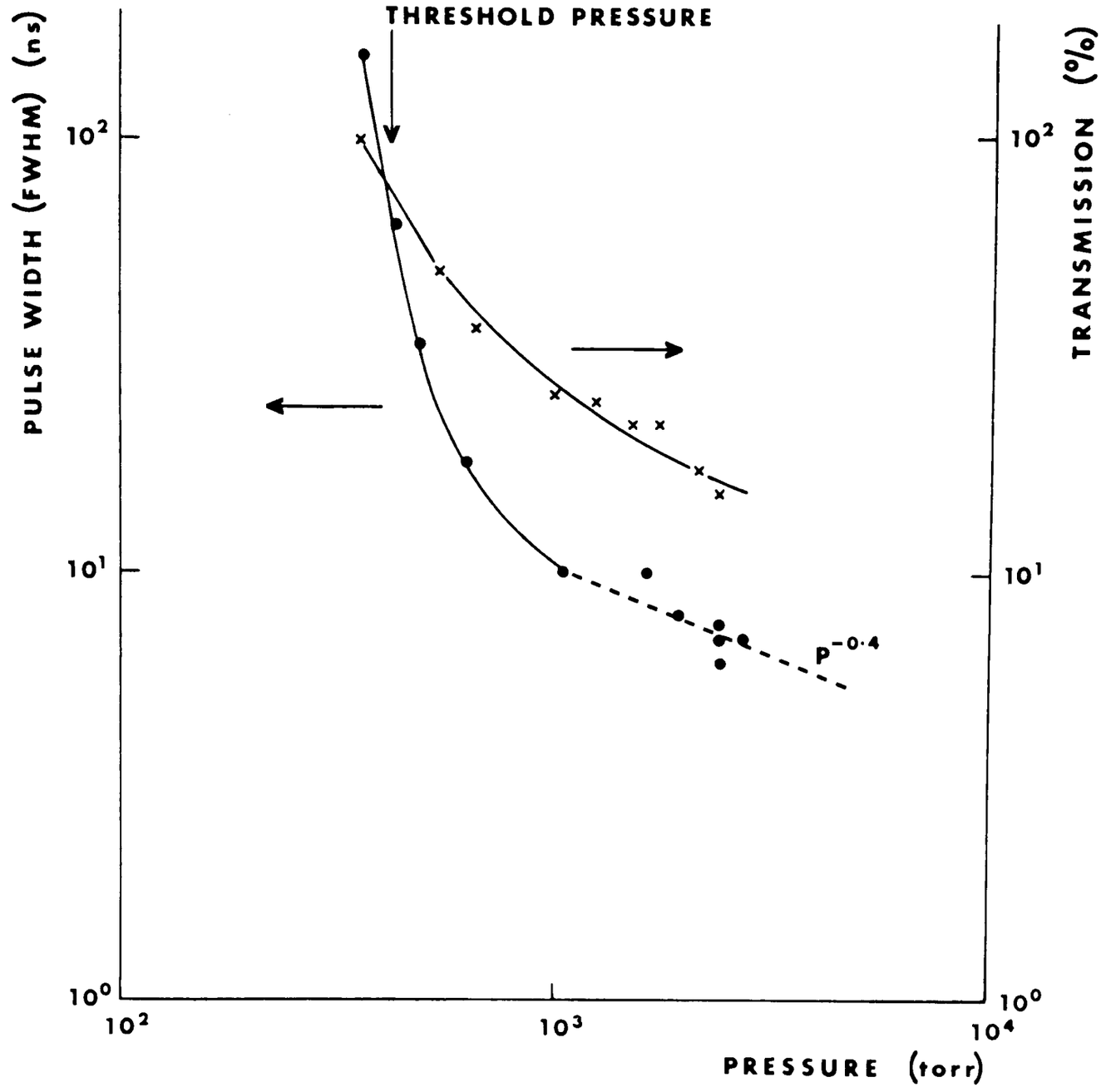

Fig. 5.23. Variation of pulse duration and transmitted energy, for breakdown in argon, as a function of gas pressure.

increased, the increased density increases absorption and decreases the breakdown time; both these factors decrease the transmission. For pressures $\geq$ 1000 torr, breakdown occurs on the rising edge of the incident pulse. Thus, the pulse width is given by 5.9. Indeed, Fig.5.23. shows experimental agreement with this theoretical scaling.

5.5. Conclusions

The coupling coefficient for platinum has been investigated as a function of target and spot size, cone angle, fluence and ambient pressure using HF laser radiation in air. The maximum coupling obtained was $\sim$ 15-18%. Peak coupling irradiance was found to be in the region of the LSD wave threshold in agreement with measurements at other wavelengths. There was no obvious thermal coupling trend as the spot size was varied. LSD wave thresholds and velocities for platinum, stainless steel and aluminium were found to agree with theory. The weak coupling at the HF wavelength for platinum is likely to be a direct result of inefficient energy transfer to a sub-critical density plasma. This is also indicated by the argon gas breakdown studies, where HF radiation was found to have a high transmittance compared with longer wavelength radiation. Further studies, using a target-induced breakdown and a transparent solid target would be desirable, although similar results are likely. The plasmotron thresholds for the three targets were determined. For irradiances above the LSD wave threshold, rapid thermal decoupling was obtained. In contrast to the case of CO_2 laser interaction, subsequent recoupling was not observed with the large spots irradiated with the multimode stable resonator. Recoupling was observed under certain conditions, however, for small spots using the unstable resonator. Large spot measurements, although desirable, were not carried out due to the unavailability of a suitable laser.

5.6. References

1) Marcus S., Lowder J.E., Manlief S. and Mooney D.L. IEEE J. Quant. Elect. QE-11, 49D, 1975.

2) Marcus S., Lowder J.E. and Mooney D.L. J. Appl. Phys. 47, 2966-68, 1976.

3) Hettche L.R., Tucker T.R., Schriempf J.T., Stegman R.L. and Metz S.A. J. Appl. Phys. 47, 1415-1421, 1976.

4) Maher W.E. and Hall R.B. J. Appl. Phys. 49, 2254-2261, 1978.

5) Raizer Yu.P. Zh. Eksp. i Teor. Fiz., Pis'ma 7, 73-6, 1968. Transl: Sov. Phys. JETP Lett. 7, 55-7, 1968.

6) Allingham C.O. and Bishop H.V.H. AWRE report LDPN/12/77.

7) Maher W.E., Hall R.B. and Johnson R.R. J. Appl. Phys. 45, 2138-45, 1974.

8) Barchukov A.I., Bunkin F.V., Konov V.I. and Lyubin A.A. Sov. Phys. JETP, 39, 469-77, 1974.

9) Deka B.K. PhD Thesis, University of Hull, 1977.

10) Deka B.K. and Dyer P.E. IEEE J. Quant. Elect., QE-14, 661-73, 1978.

CHAPTER 6

CO_2 LASER-TARGET INTERACTION STUDIES (VACUUM ENVIRONMENT)

6.1. Introduction

A gain-switched TEA CO_2 laser was used to irradiate various solid targets in a vacuum[1]. Target irradiances between 10^8 and 1.2×10^{11} $W.cm^{-2}$, with 60ns (FWHM) pulses, enabled ion and x-ray scaling laws to be deduced and the backscattered laser radiation to be measured. The results indicate the existence of a high energy electron component in the plasma and the onset of an instability heating mechanism at $\sim 2 \times 10^{10} W.cm^{-2}$.

6.2. Experimental Arrangement

6.2.1. Oscillator

A double-discharge TEA oscillator[2], comprising of eight 48cm modules with a cross-section of $5 \times 5cm^2$, was operated in two modes. In the first mode the molecular gas flow ratio $\gamma = CO_2/(CO_2 + N_2)$, with 80% helium, was optimised at 0.6 for power and 0.5 for energy[2,3]. This results in a low amplitude ($\sim$ 1μs) tail following the high intensity spike[4], Fig.6.1. In the second mode $\gamma = 1$. Although this reduced the energy to under a third of the optimum, the tail amplitude was considerably decreased, Fig.6.1.

An unstable resonator[5] was used to obtain single mode operation without significant energy loss compared with the multimode output.

6.2.2. Target Chamber

Pulses were focused using a bi-convex NaCl lens designed to minimimize coma and spherical aberration. The lens had a focal length of 25cm and was used at f/6. Calibrated CaF_2 flats were employed to attenuate the beam, as shown in Fig.6.2. The craters and burns formed at low irradiances indicated a focal spot radius of about 200μm. 'Spec-pure' target rods of polyethylene, carbon, aluminium, copper, silver and lead were polished and mounted at 80° to the beam axis to

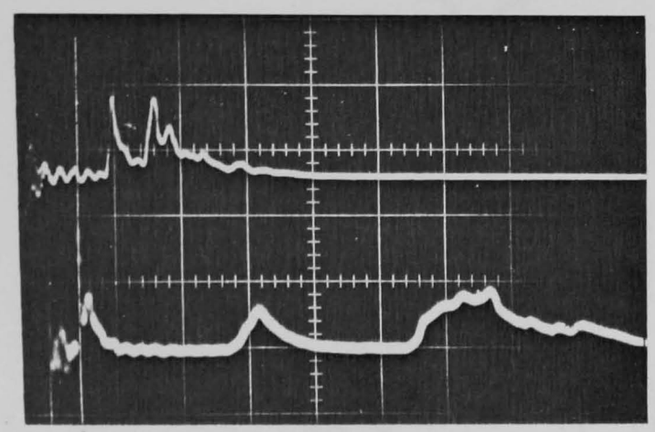

CHARGE COLLECTOR SIGNALS

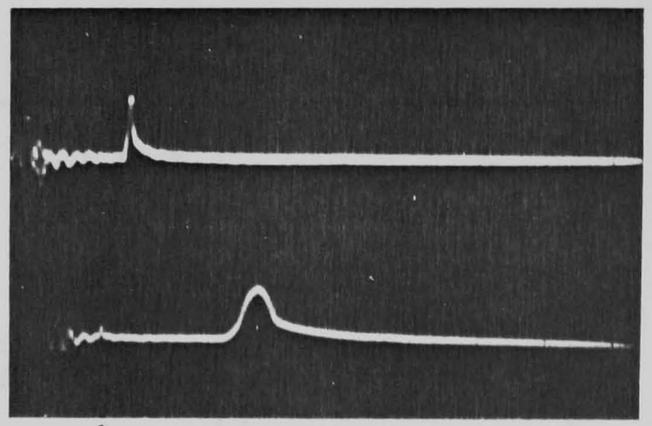

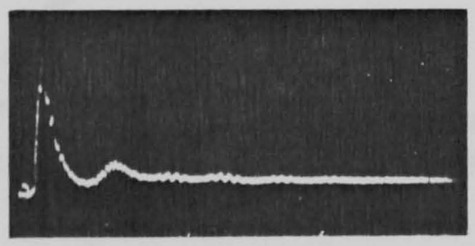

LASER PULSE SHAPE

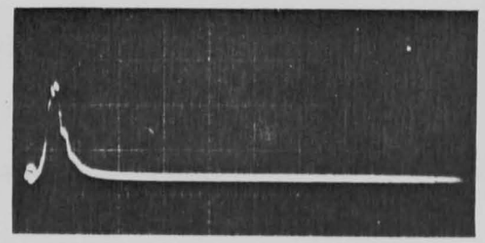

Fig.6.1. Charge collector signals for an aluminium target at an irradiance of $\sim 6 \times 10^9$ W.cm^{-2} pe = photoelectric signal. Left: laser pulse with tail. Right: single gain switched spike.

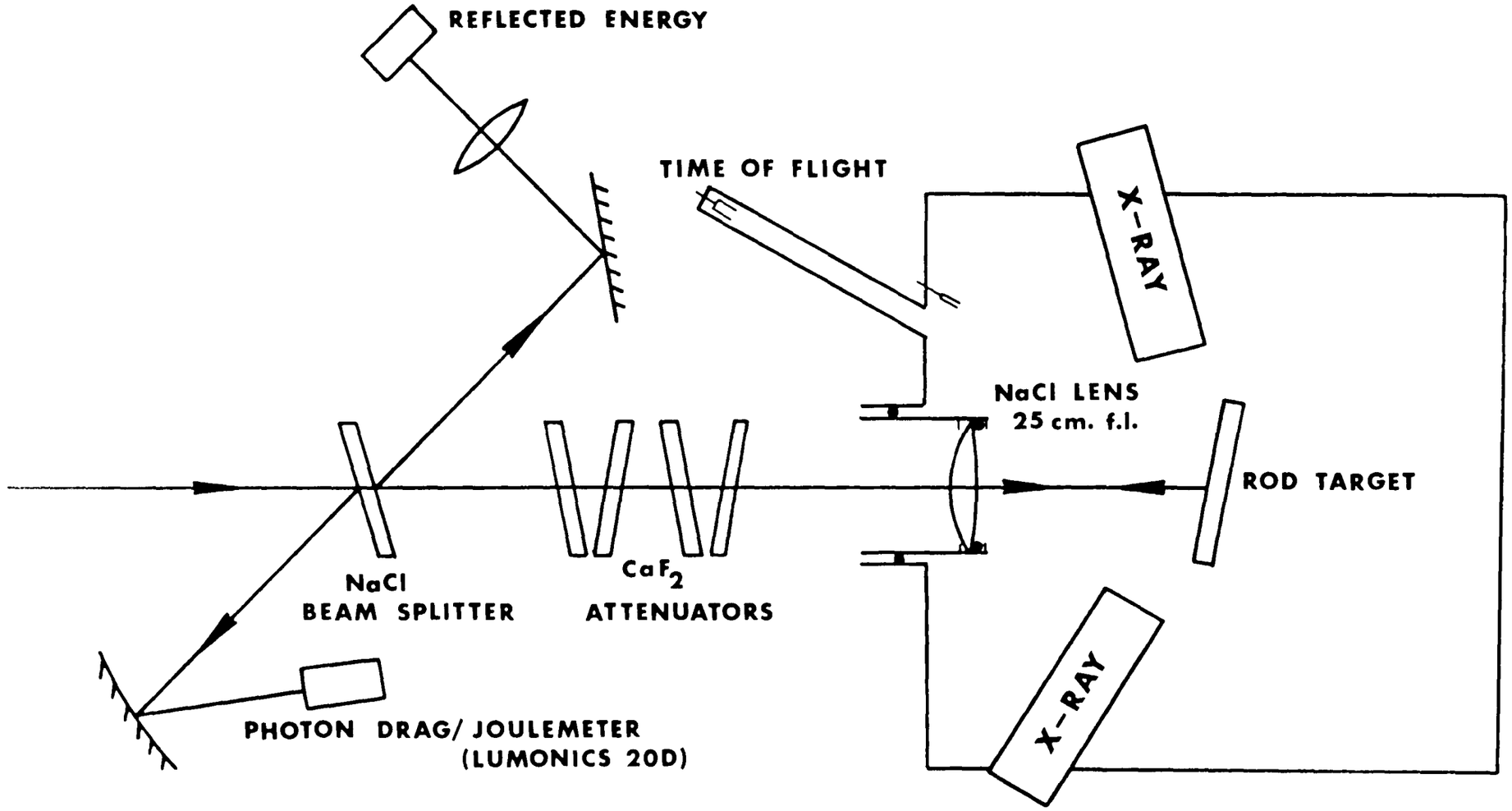

Fig.6.2. Schematic experimental arrangement.

prevent specular feedback to the oscillator. The chamber was evacuated to < 10^{-5} torr.

6.3. Diagnostics

6.3.1. Pulse Shape Measurements

The incident and reflected pulse shapes were measured using Rofin 7411 photon-drag detectors, as shown in the schematic diagram, Fig.6.2.

6.3.2. Charge-Collector Measurements

Ion velocities were obtained by the time of flight technique, as with the HF system. In this case, the probes were separated by 48.7 cm and mounted in the forward direction, inclined at 20° to the optical axis, sothat they were sighted along the direction of specular reflection. The solid angles presented by the two probes were made equal. Ion number was obtained by electronic integration of the ion pulse.

6.3.3. X-ray Continuum Measurements

The soft x-ray emission from the plasmas under these conditions is far more copious than with HF, enabling the two-foil ratio technique [6,7] to be employed. High and medium gain photomultipliers (EMI 9813KB and 9814KB) were used, together with a plastic scintillator (NE104), depending upon the x-ray intensity. The former combination resulted in a statistical spread of the signal amplitude, but had far greater sensitivity. The soft x-rays were filtered through foil combinations that included 25, 125 and 250μm thick light-tight beryllium. Signals were displayed on a Tektronix 7904 oscilloscope using a 20MHz limited amplifier to introduce some integration.

It has been pointed out[1] that line radiation was not significant in our situation in view of the relatively low plasma temperature deduced from probe measurements, and the probable failure to reach coronal ionization equilibrium in the plasma.

6.3.4. Backscatter Measurements

The laser radiation reflected and collected by the lens, a solid

angle of 0.06Sr, was directed onto the pyroelectric joulemeter, using a NaCl beam-splitter and lens as shown in Fig.6.2. This was normalized using a second joulemeter to monitor the incident energy.

6.4. Results

6.4.1. Charge-Collector

A strong photo-electric signal was obtained in the majority of measurements. This acted as a useful time-marker. Velocities were therefore obtained using this signal for the two probes in addition to timing between the probes. In the presence of the low amplitude tail to the laser pulse, the photoelectric signal overlapped with the fastest ion signals on the near probe. The tail also produced multiple ion species, especially for the heavier targets. This will, in part, be due to the tail interacting with a pre-conditioned plasma. The ion velocity scaling laws deduced using the initial ion pulse were the same in both modes of operation, although this was not true if the largest ion pulse was considered. In order to unambiguously interpret the scaling, N_2-free gas mixtures were employed. Typical ion signals for these two situations are shown in Fig.6.1., and presented in ref.6.1.

Fig.6.3-8. show the ion-velocity scaling for the six targets studied using a N_2-free gas mixture. Velocity measurements were taken representing the most abundant ion species. The effect of the residual tail in producing secondary peaks was established. In general, the scaling was lower than 2/9, except at $\lesssim 10^9 W.cm^{-2}$, with some further decrease at the higher target irradiances. Multiple peaks were observed with the heavier targets, in agreement with Beverly[8] (using low Z targets in two-beam experiments) and Ehler[9] (in high power, short-pulse experiments). The asymptotic ion-expansion energy at $8 \times 10^{10} W.cm^{-2}$ for the six targets is shown in Fig.6.9. Table 6.1. gives the electron temperature, calculated as with HF. The temperature-flux dependence, also given in Table 6.1., indicates a low scaling.

The ion-number scaling with irradiance for the six targets steadily changes from ~ 1 to ~ 0.5 as ϕ is increased. The self-regulating

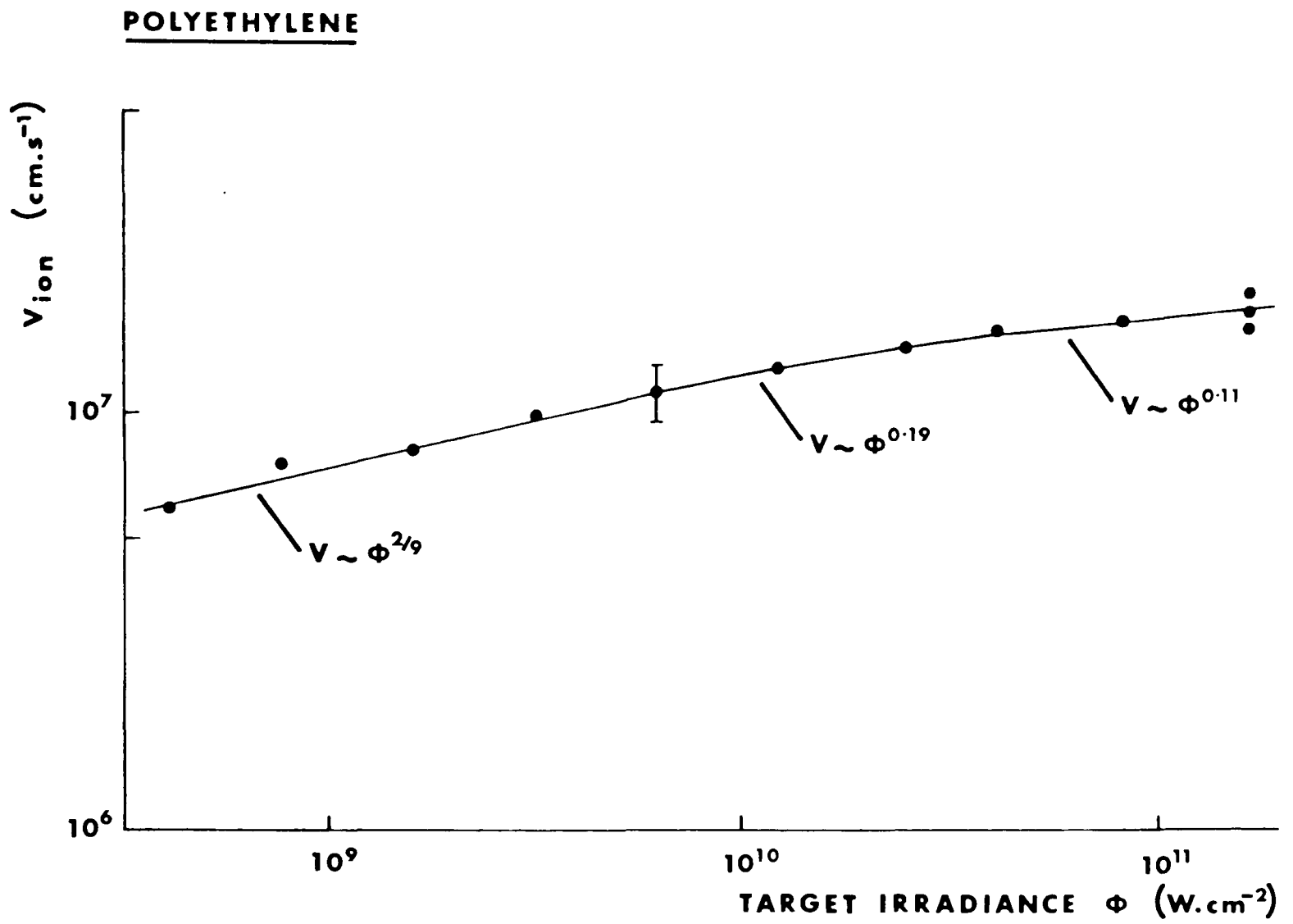

Fig.6.3. Asymptotic ion expansion velocity versus target irradiance (polyethylene).

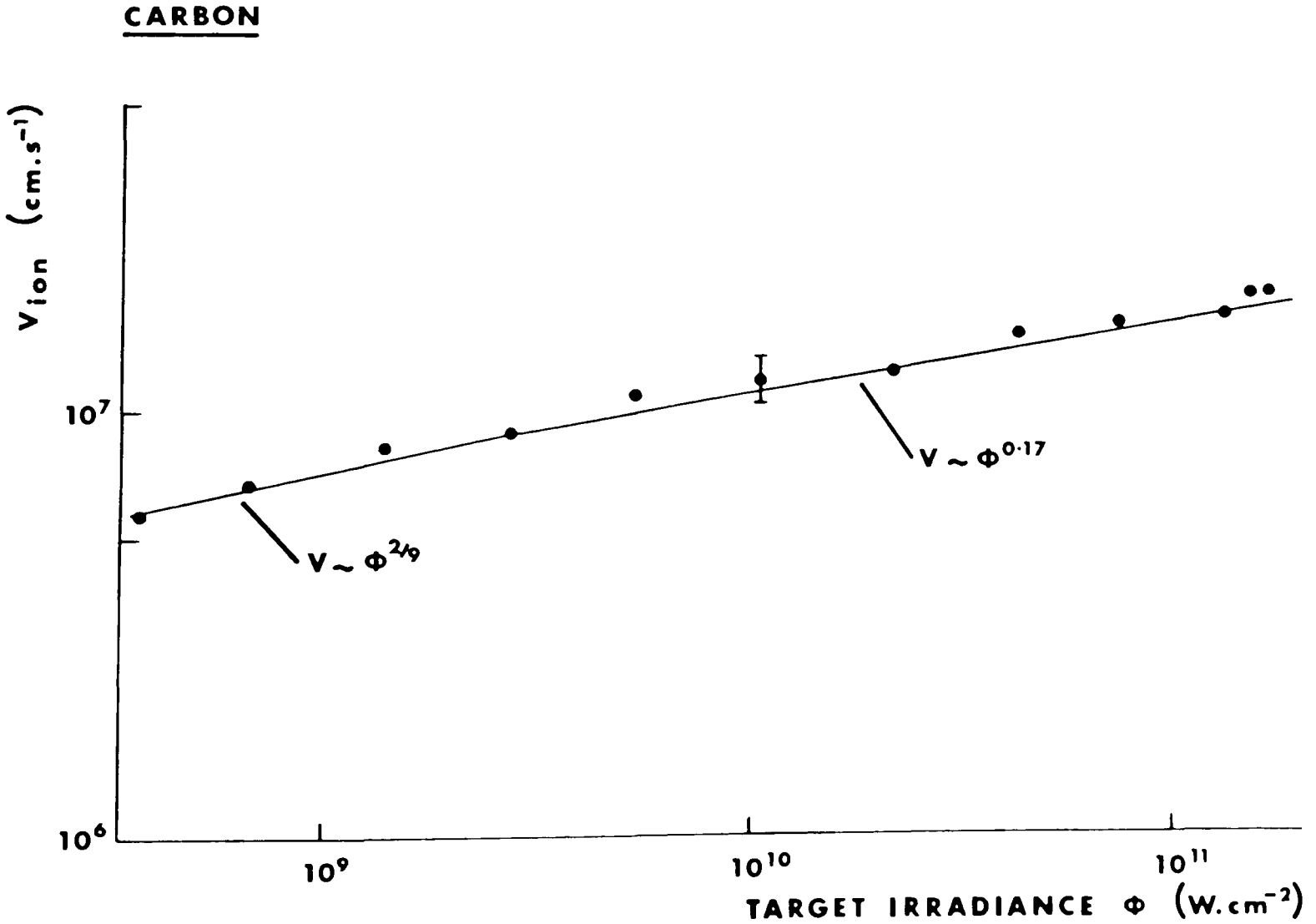

Fig.6.4. Asymptotic ion expansion velocity versus target irradiance (carbon).

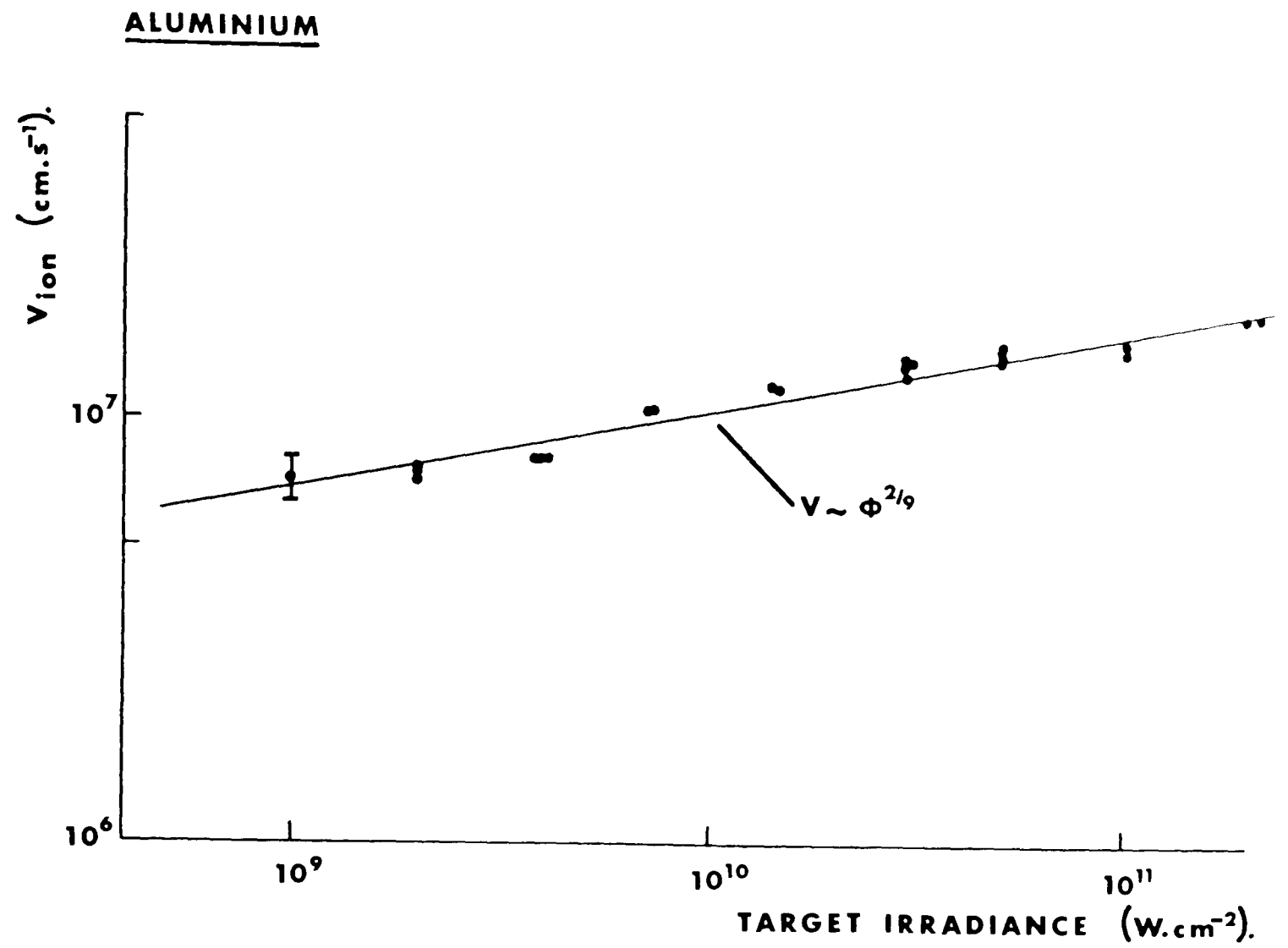

Fig.6.5. Asymptotic ion expansion velocity versus target irradiance (aluminium).

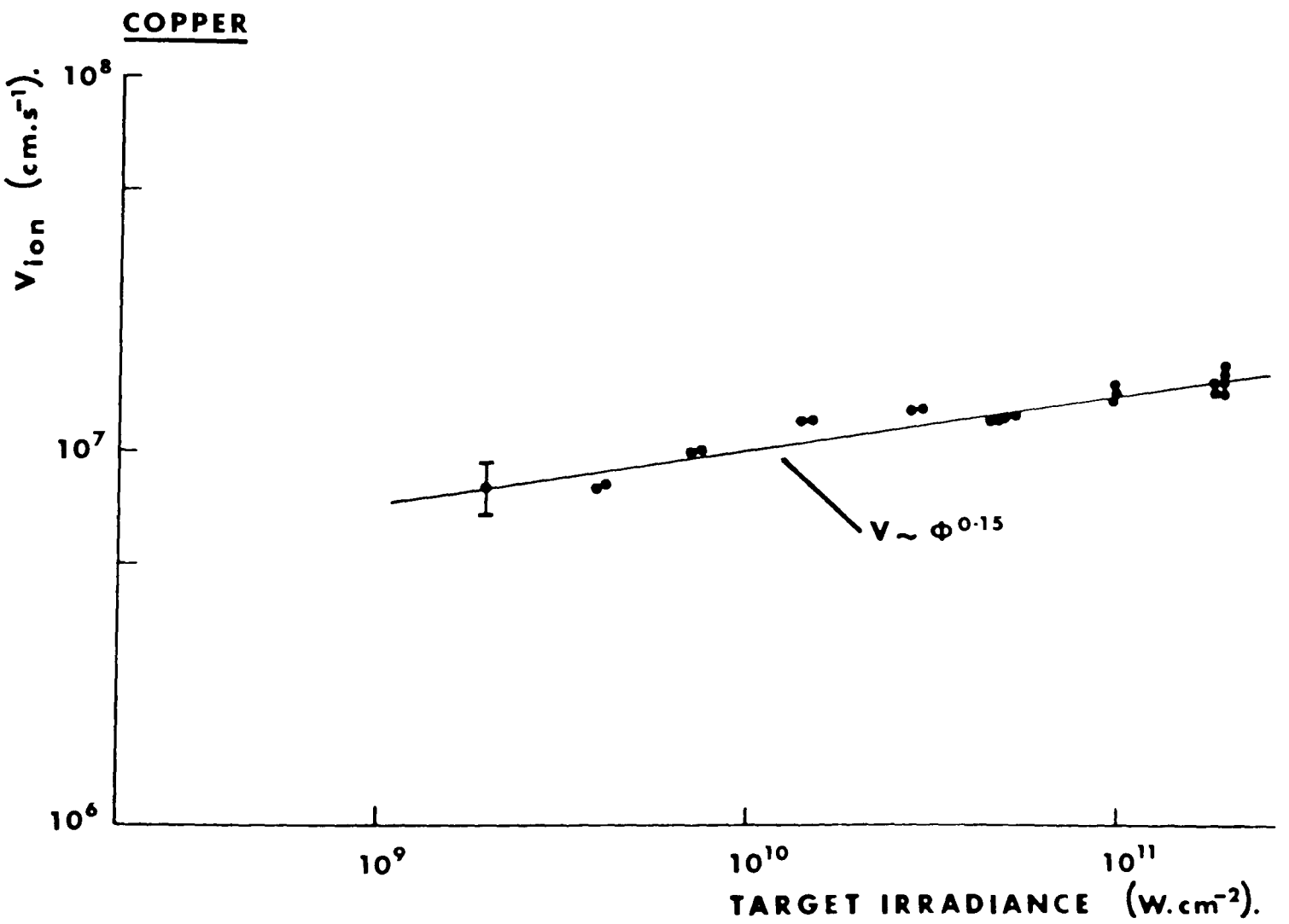

Fig.6.6. Asymptotic ion expansion velocity versus target irradiance (copper).

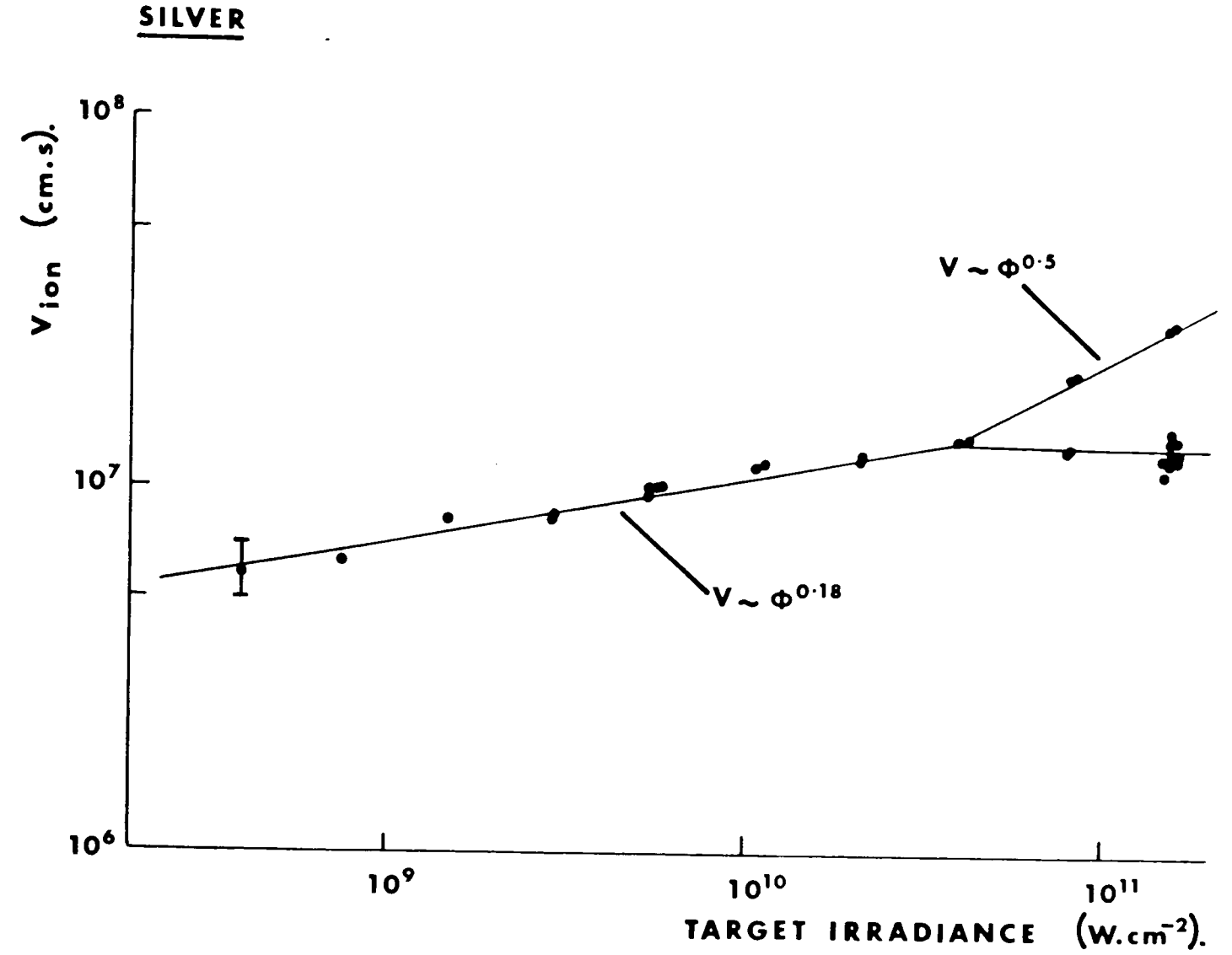

Fig.6.7. Asymptotic ion expansion velocity versus target irradiance (silver).

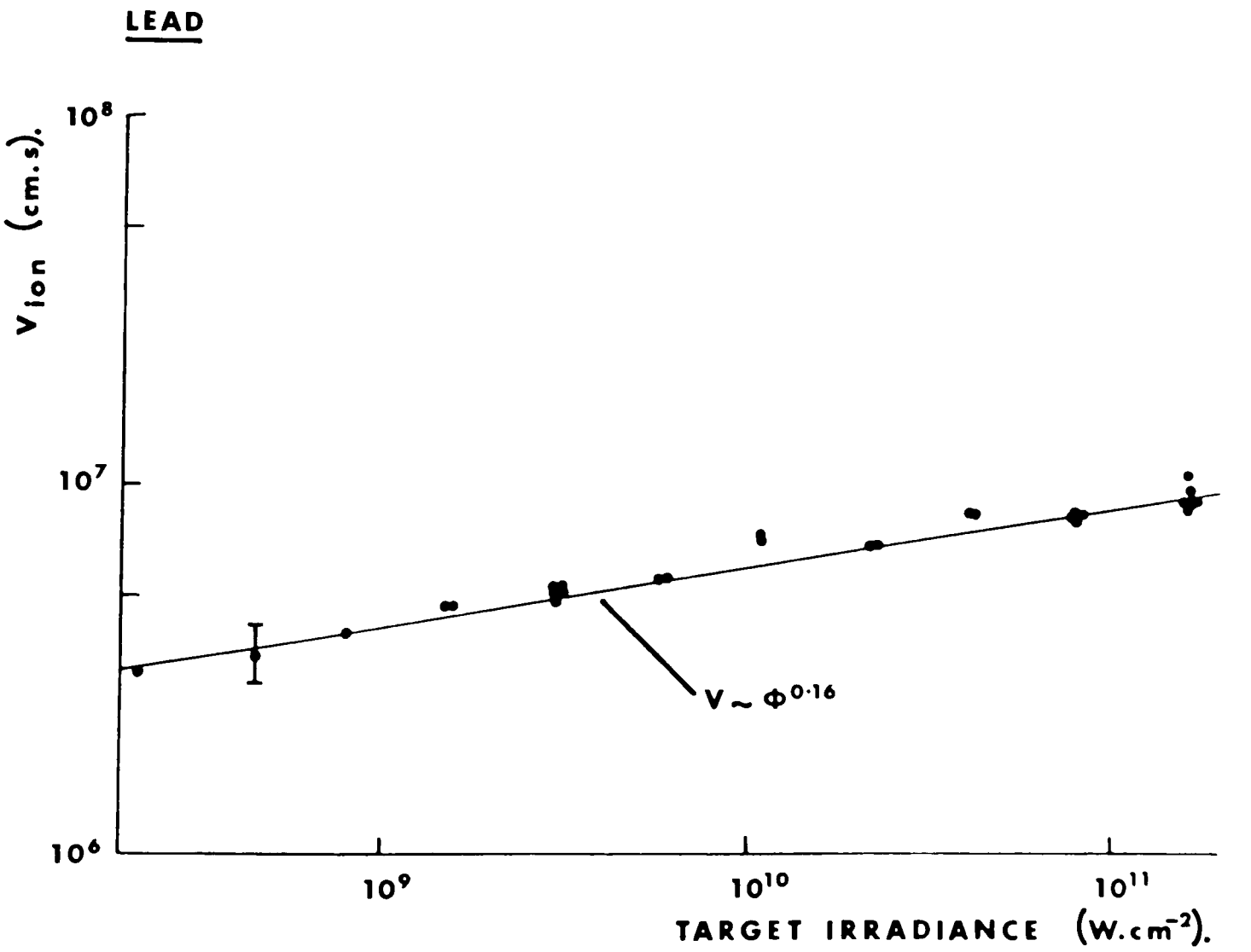

Fig.6.8. Asymptotic ion expansion velocity versus target irradiance (lead).

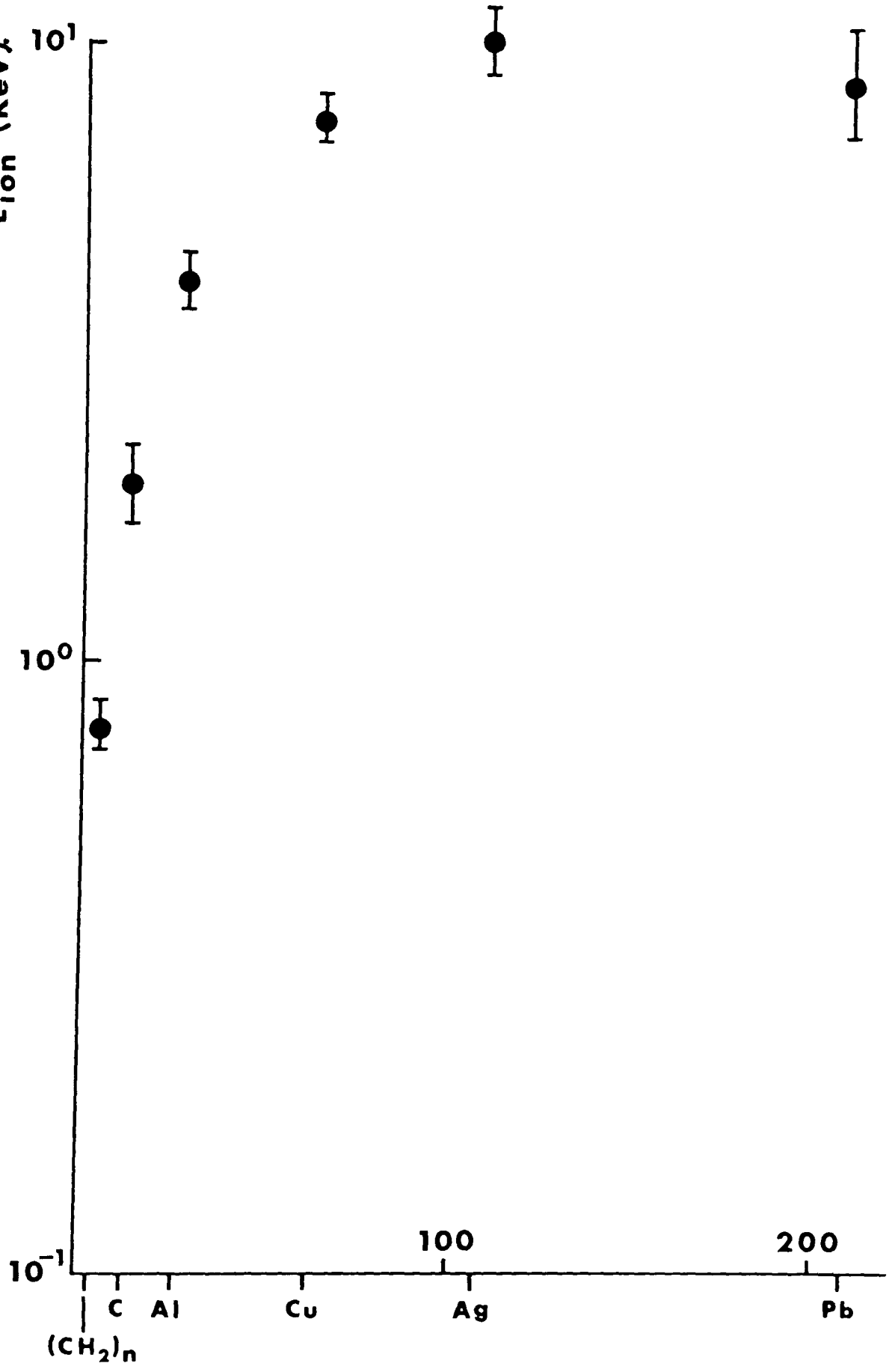

Fig.6.9. Asymptotic ion expansion energy versus atomic weight for a target irradiance of 8×10^{10} W.cm^{-2}

model predicts a scaling of 5/9 and thus this was only obtained at the higher fluxes, in agreement with results using the HF laser.

TARGET	ELECTRON TEMPERATURE (eV) $\phi = 8 \times 10^{10} W.cm^{-2}$	DERIVED TEMPERATURE IRRADIANCE SCALING, $2 \times 10^{8} < \phi < 1.2 \times 10^{11} W.cm^{-2}$
$(CH_2)_n$	50 †	$T_e \sim \phi^{0.37}$
C	70	$\phi^{0.30}$
Al	105	$\phi^{0.31}$
Cu	145	$\phi^{0.20}$
Ag	∿ 180	$\phi^{0.25}$ ††
Pb	∿ 160	$\phi^{0.21}$

† using average nuclear charge and mass for $(CH_2)_n$

†† over the range $2 \times 10^{8} \leq \phi \leq 2 \times 10^{10} W.cm^{-2}$.

Summary of estimated electron temperature and target irradiance scaling from charge-collector probe measurements (CO_2).

TABLE 6.1.

The ion number, N, was observed to decrease rapidly with increasing atomic weight at an irradiance of $10^{11} W.cm^{-2}$. For the lightest

elements, a scaling of $N \sim m_i$ was achieved at irradiances of 10^9 and 10^{11}W.cm^{-2}. This was also observed with HF radiation at 10^9W.cm^{-2}. For the intermediate mass elements, the scaling was in the order of $\sim m_i^{4/9}$. The self-regulating model predicts (1.29a) that $N \sim (m_i C)^{-2/9}$. As C is roughly proportional to m_i, an approximate -4/9 scaling is to be expected. Dyer et al[10] have, however, warned that the continuum fluid mechanics used is only valid for scale lengths much greater than the mean free path. For hydrogen, the thermal conduction length is only 4 λ_e, and possibly this accounts for the high scaling in the region of polyethylene. In the region of lead, at the lower irradiance only, a slightly lower scaling was obtained. This is possibly due to the neglect of the ionization energy dependence in the simple model. At the higher irradiance a -4/9 scaling was, however, achieved, in agreement with the model.

With nitrogen in the gas mixture, the ion data was complicated by the appearance of additional peaks due to the significant laser tail. Over the target irradiance range 2 x 10^8 to 2 x 10^{11}W.cm^{-2} the scaling laws are given in Table 6.2.

With the exception of copper and lead, the first-pulse scaling and the ion energies are comparable with the $\gamma = 1$ situation. It is possible that the high ion energies for copper and lead are a direct result of the tail interacting with a preconditioned plasma.

6.4.2. Soft X-ray

The soft x-ray continuum emission gave an electron temperature which was either considerably in excess of that determined from the ion-probe measurements or was strongly dependent upon the foil absorber combinations used to filter the x-rays.

Table 6.3. gives a summary of the results for the six targets at a target irradiance of 1.2 x 10^{11}W.cm^{-2}. The equivalent electron temperatures are in the kilovolt range, and are a function of the foil combinations. The electron temperature exhibits only a weak flux scaling; in contrast, the x-ray signal intensity is highly flux dependent, as shown in ref.6.1. The equivalent electron temperatures are

TARGET	ION PULSE	SCALING
$(CH_2)_n$	1st	$V \sim \phi^{0.22}$
	2nd	$\phi^{0.21}$
C	1st	$\phi^{0.24-0.16}$
	2nd	$\phi^{0.50-0.19}$
Al	1st	$\phi^{0.21}$
	2nd	$\phi^{0.24}$
Cu	1st	$\phi^{0.24}$
	2nd	$\phi^{0.13}$
Ag	1st	$\phi^{0.17}$ †
	2nd	$\phi^{0.21}$
Pb	1st	$\phi^{0.23}$
	dominant,	
	ϕ 2 x 10^8 - 5 x 10^{10}	$\phi^{0.07}$
	$\phi \gtrsim 5 \times 10^{10} W.cm^{-2}$	$\phi^{0.24}$

† plus a new 'hot' group $\gtrsim 10^{11} W.cm^{-2}$.

Ion velocity scaling for $2 \times 10^8 \leqq \phi \leqq 2 \times 10^{11} W.cm^{-2}$.

TABLE 6.2.

TARGET	Be FOILS 25μm/50μm	Be FOILS 25μm/125μm	Be FOILS 25μm/250μm
$(CH_2)_n$	∿ 0.5 KeV	∿ 1 KeV	∿ 1.5 KeV
C	∿ 1	∿ 1	∿ 3
Al	0.23	0.34	0.39
Cu	0.17	0.44	0.6
Ag	0.28	0.90	1.1
Pb	0.17	0.82	1.1

Electron temperature (KeV) from soft x-ray measurements using the three Be foil combinations indicated, at a target irradiance of $1.2 \times 10^{11} W.cm^{-2}$.

TABLE 6.3.

calculated assuming a bremsstrahlung plasma. Any variation in this temperature with foil combination indicates deviations from this distribution. Our results, therefore, indicate the presence of a non-thermal electron distribution at high irradiances.

Under most conditions, the x-ray emission from the plasma was found to be associated with the main pulse of the laser. However, at high irradiances ($\sim 10^{11} W.cm^{-2}$) there appeared to be considerable interaction between the target and laser, as shown in ref.6.1. The spiking in the tail appears to be due to induced mode-locking and may give significant x-ray production, as shown in the same reference.

The interaction between laser and plasma is particularly strong for some targets and seems to correlate with the fraction of energy back-scattered by the plasma. This plasma mirror effect has been observed using a Nd:glass laser[11].

The x-ray emission duration varied only slightly with atomic weight, being ∿ 50ns for all targets except lead, which was slightly longer (∿65ns). The x-ray signal amplitudes are given in ref.6.1. As with HF, aluminium gave a signal which was an order of magnitude higher than for carbon.

6.4.3. Backscatter

The backscattered laser radiation energy is shown in Fig.6.10. for the six targets using the two modes of laser operation. The significant difference for these two modes with silver and lead is to be correlated with the plasma mirror effect, which was particularly strong for these targets. The large amplitude spikes results in higher plasma reflectivity, which is consistent with the observation that the nonspecular backscattered radiation increases with target irradiance in the case of polyethylene[12].

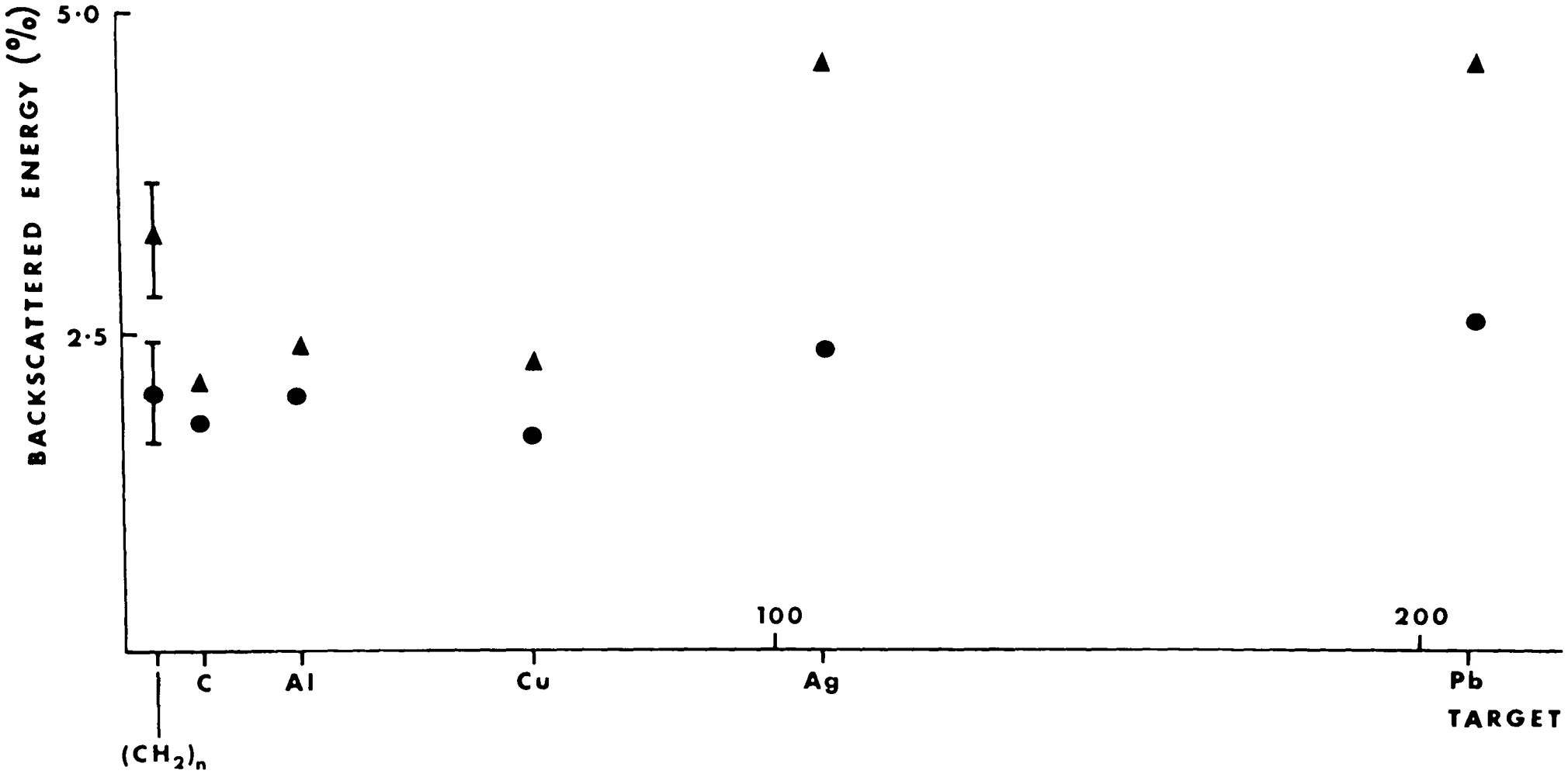

Fig.6.10. Backscattered laser energy versus atomic weight: ▲ laser pulse with tail. $\Phi = 10^{11}$ W cm^{-2}. ● - -

6.5. References

1) Dyer P.E., Ramsden S.A., Sayers J.A. and Skipper M.A. J. Phys. D: Appl. Phys. 9, 373-382, 1181, 1976.

2) Dyer P.E. PhD thesis, University of Hull, 1974.

3) Dyer P.E., James D.J. and Ramsden S.A. J. Phys. E: Scientific Inst. 5, 1162-4, 1972.

4) Johnson D.C. IEEE J. Quant. Elect. QE-7, 185-9, 1971.

5) Siegman A.E. Appl. Opt. 13, 353-67, 1974.

6) Johoda F.C., Little E.M., Quinn W.E., Sawyer G.A. and Stratton T.F. Phys. Rev. 119, 843-56, 1960.

7) Dyer P.E., James D.J., Ramsden S.A. and Skipper M.A. Appl. Phys. Lett. 24, 316-7, 1974.

8) Beverly R.E. Phys. Lett. 44a, 321-2, 1973.

9) Ehler A.W. J. Appl. Phys. 46, 2464-7, 1975.

10) Dyer P.E., James D.J., Pert G.J., Ramsden S.A. and Skipper M.A. Laser Interactions and Related Plasma Phenomena 3, 191-212, Phenum Press, 1974.

11) Batanov V.A., Gocheleshvili K.S., Ershov B.V., Malkov A.N., Kolisnichenko P.T., Prokhorov A.M. and Federov V.B. JETP Lett. 20, 185-7, 1974.

12) Dick K. and Pepin H. Opt. Commun. 13, 289-93, 1975.

CHAPTER 7

DISCUSSION

7.1. Target Interaction (Vacuum Environment)

7.1.1. Ion Measurements

Low Z targets were found to follow the self-regulating model scaling for both HF and CO_2 laser wavelengths in the relevant flow regime indicated in Fig.1.5. For high Z targets, a lower scaling is to be expected when the effects of ionization are included in the simple model. This expectation was confirmed in the case of silver and lead. Although the simple self-regulating (and indeed, the deflagration wave) model was primarily developed for Nd:glass laser-plasma interaction, this result is indicative of a more general validity. In agreement with Montes et al[1], even at the more extreme wavelength of the CO_2 laser (10.6μm) the simple self-regulating model was obeyed over the same irradiance band, although departures were observed from the deflagration wave model at higher irradiances[2,3]. This weaker scaling at high irradiances and long wavelength may be explained by including a correction term to take into account thermal conduction broadening of the plasma. This effect is insignificant for Nd:glass in the irradiance band considered here, and also for short pulse ($\gtrsim$ ns) CO_2 interactions[4,5] at the irradiance range considered in ref.7.2.,7.3.

It is of interest to compare the temperature scalings, as deduced from the ion measurements, given in Tables 4.2. and 6.1. Very similar scalings are achieved at these two wavelengths for the lighter targets, copper and lead give a much higher scaling with HF, whereas the reverse is true in the case of silver. Of special note is the low temperature achieved by lead with HF.

The low scaling at 10.6μm of electron temperature with target irradiance ($\sim \phi^{0.20\text{-}0.37}$) has been verified in part by Dick and Pepin[3]. The simple self-regulating model predicts a scaling of $T_e \sim \phi^{4/9}$, whereas the deflagration wave model predicts $T_e \sim \phi^{2/3}$. The latter

would not in any case be expected here, as shown by the regime diagram. For the heavier targets, good agreement is obtained with theory if thermal conduction broadening of the plasma is considered[6]. Thermal conduction broadening occurs when the conduction scale length approaches or exceeds the characteristic laser spot size. This occurs at about $T_e \sim$ 1KeV for Nd:glass[7] and $\sim$ 100eV for CO_2. In the limit where thermal conduction broadening dominates the heating process, simple steady state modelling[6] predicts a scaling of $T_e \sim \phi^{2/11}$. The simple model does not take into account ionization energy, which may be relevant for the heavier targets.

Measurements made by Skipper[4] (using 5ns pulses), and Ehler[5] (using 1.5ns pulses), with low Z materials irradiated at 10.6μm, gave a somewhat high ion irradiance scaling. This is consistent with a decreased importance of thermal conduction. Skipper has found that the energy carried by the total number of ions produced in the interaction accounts, within accuracy of measurement, for the laser pulse energy absorbed. No fast ions were observed in the measurements presented here, or by Skipper for 5ns pulses at an irradiance of $1.2 \times 10^{12} W.cm^{-2}$. Ehler, on the other hand, obtained a high energy ion current for irradiances above $5 \times 10^{12} W.cm^{-2}$. At $2 \times 10^{14} W.cm^{-2}$ 90% of the total ion energy was due to fast ions.

7.1.2. X-ray Measurements

X-ray emission at the HF wavelength was, as expected from Elton's calculations[8], less copious than with CO_2 laser radiation. Bleach and Nagel[9] have measured the x-ray emission versus atomic number using a Q-switched 20ns ruby laser at an irradiance of $\sim 10^{12} W.cm^{-2}$. Peaks in this plot were obtained for elements with atomic numbers such that shell ionization energies were 20-30 times the average electron energy in the plasma[10]. Bleach and Nagel argue that the lower critical density of CO_2 radiation compared with that of ruby and Nd:glass is partially offset by the higher temperature attainment with CO_2 for x-ray production. (There are less electrons available to carry the absorbed energy). The situation with HF radiation is, of course,

intermediate.

Thus, x-ray peaks are likely to be observed, although they may well be increasingly weaker as the laser wavelength is increased. Pepin et al[11] observed x-ray peaking at an irradiance of $7 \times 10^{12} W.cm^{-2}$ using 1ns CO_2 pulses. However, to achieve this, oxide-free targets were necessary. The x-ray yield was found to scale approximately as $\sim \phi^{2.5}$ for carbon, aluminium, iron, tin and lead. This is consistent with the approximately $\sim \phi^3$ scaling achieved in the previous chapter with 60ns pulses and a lower irradiance. Unfortunately, the available HF irradiance was too small to observe peaking or irradiance scaling. In view of the results at spanning wavelengths, it is, however, very probable that peaking occurs and that the x-ray signal amplitude remains strongly dependent upon the target irradiance at higher irradiances (as predicted by Elton's calculations). Nagel et al[12] showed that the x-ray peaks are due to transitions to the principal atomic shells. The results here are not inconsistent with those of Pepin, although, unfortunately, six points are not adequate to indicate the trend.

Above about $10^{12} W.cm^{-2}$ non-thermal x-ray and fast ion production, consistent with the onset of the parametric decay instability, are to be expected. Although our irradiances with HF were too low to observe this, the theoretical expectation is backed up by observations using Nd:glass[13] and CO_2[11 and for example 14,15] lasers.

The high-energy tail to the non-thermal electron distribution at high CO_2 irradiances is probably due to a laser-driven instability. The most likely instability is the parametric decay instability, which has a threshold above $10^{10} W.cm^{-2}$ for CO_2[16,17].

7.1.3. Backscatter Measurements

The specular reflectivities of the metal targets at the HF wavelength were shown in chapter 4 to fall from nearly 100% at low irradiances to a much lower value ($\sim$ 30%) at $10^{10} W.cm^{-2}$. Lead was an exception, however, falling from $\sim$ 2.5% at $10^8 W.cm^{-2}$ to $\sim$ 0.4% at $10^{10} W.cm^{-2}$. Both polyethylene and carbon had very low specular reflectivities, amounting to only a fraction of a percent, solely

measurable at the highest irradiances achieved. These results can be compared with those at the spanning wavelengths of CO_2 and Nd:glass Dyer et al[15] measured a higher coefficient for a CO_2 radiated carbon plasma which was fairly constant at the measured values between 10^8 and $10^{12}W.cm^{-2}$. Weak reflection has also been observed at all angles by Martineau et al[18] using a deuterium target and a 60ns, 300MW CO_2 TEA laser. Mitchell et al[19], using a slab polyethylene target irradiated at 10.6μm at the high irradiance range of 10^{13}-$10^{15}W.cm^{-2}$ obtained a backscatter of $\leq$ 5%. Slightly higher reflectivity has been observed at 1.06μm[20,21]. Ripin observed the reflectivities and angular distribution of radiation at the high irradiances of 10^{15}-$10^{16}W.cm^{-2}$ and found the process to be highly complex. Donaldson et al, using a 50ns CO_2 laser, have studied the reflectivity of a carbon target over the intensity range 10^{11}-$10^{13}W.cm^{-2}$. Total reflectivity was found to be $\lesssim$ 8%. In agreement with Dyer et al[2], the absolute reflectivity was found to be insensitive to target material and irradiance over the range 3×10^{11}-$10^{13}W.cm^{-2}$.

Yamanaka et al[20], using 10.6μm radiation, observed a 60% peak reflectance at $4 \times 10^{10}W.cm^{-2}$, and this has been verified by Hall and Negm[22]. This peak is interpreted as indicating the on-set of the parametric decay instability. As this instability occurs at higher irradiances as the laser wavelength is decreased, no reflection peak is to be expected for the HF measurements given here. This expectation has been verified.

Apart from instability indication, the reflection data is important in determination of radiation coupling to the target.

7.2. Target Interaction (Gaseous Environment)

7.2.1. Thermal Coupling

Thermal deposition experiments presented in 5.2. and in ref.7.23-26. were carried out at normal or near normal beam incidence. Mc Kay et al[27], using 10μs CO_2 laser pulses on sheet aluminium targets in air, measured the thermal coupling as a function of target angle, θ. They found that the plasma ignition was only dependent on the beam

intensity, I_o, whereas the coupling varied as $I_o \cos\theta$. Walters et al[28] explain plasma ignition as being due to the surface defects rapidly attaining thermionic emission temperatures. The thermionic electrons then gain energy by the process of inverse-bremsstrahlung. These two steps depend on the fluence and flux respectively. The above experimental results suggest that the second criterion dominates the overall process.

Mahler et al[29] have performed multiple-pulse thermal-coupling experiments in air using a photo-initiated DF laser. Aluminium targets were methonal cleaned and irradiated with a 1.9 x 1.9cm^2 focused beam at a fluence of 67J.cm^{-2}, the plasma ignition threshold being 31J.cm^{-2}. Under these conditions the absorbed fluence was a maximum of 5-7J.cm^{-2} for a first exposure, rising to a value of approximately 13.5J.cm^{-2} after multiple exposures. As the time between laser pulses was long, being several minutes, the target attained ambient temperature before subsequent exposures. This increase in thermal coupling has not yet been observed using higher wavelength lasers. It is believed that the effect is due to the increase in surface damage with multiple exposures. Such damage is expected to enhance both direct absorption and shorter-wavelength re-radiated energy from the plasma.

7.2.2. Ignition and Propagation of LSD Waves

When comparing pulsed interactions at the HF/DF wavelengths with those at the CO_2 wavelength, it is important to consider the effects of the different pulse shapes.

With 10.6μm interaction an air plasma may be formed by the high intensity gain-switched spike at the leading edge of the pulse. At this stage in time the surface has not attained the vaporization temperature; ignition has originated from surface defect vaporization[28,30]. In the case of aluminium at an intensity of 10-30MW.cm^{-2}, the threshold fluence for this prompt ignition is about 1.7J.cm^{-2} [31]. Following the formation of a surface plasma, the high energy, low intensity laser tail interacts by forming an LSC or LSD wave - the LSD wave threshold being about 8MW.cm^{-2} [32,33]. In the absence of prompt ignition,

absorption is by the process of inverse Bremsstrahlung. This occurs at the target surface in the case of metals, but for many non-metals absorption is integrated over a finite depth.

The HF/DF laser pulses lack the gain-switched spike and rapid rise time of the CO_2 laser pulse. In consequence, plasma ignition occurs in the middle of the pulse[34-36]. The initial direct surface absorption is much larger than with CO_2, sothat the surface temperature rapidly rises. This increases the absorption coefficient and introduces the possibility of mass loss. Plasma ignition is possible by two mechanisms: bulk surface evaporation or from surface defects as before. The former process is more likely than with CO_2, as the bulk heating rate is larger; the latter process is less likely, as the inverse bremsstrahlung absorption increases with λ^2. Higher intensities are needed to maintain LSC waves than with CO_2, thus hot, high pressure plasmas are formed. Radiative transfer to the target is therefore much larger. The LSD wave threshold fluences are, as expected, ordered inversely with wavelength - the threshold for HF being much higher than with CO_2, the threshold for DF being intermediate.

7.3. References

1) Montes A., Hubbard M., Kler C. and Spalding I.J. Appl. Phys. Lett. 36, 652-4, 1980.

2) Dyer P.E., Ramsden S.A., Sayers J.A. and Skipper M.A. J. Phys. D: Appl. Phys. 9, 373-82, 1181, 1976.

3) Dick K. and Pepin H. Optics Commun. 13, 289-93, 1975.

4) Skipper M.A. PhD thesis, University of Hull, 1976.

5) Ehler A.W. J. Appl. Phys. 46, 2464-7, 1975.

6) Dyer P.E., James D.J., Pert G.J., Ramsden S.A. and Skipper M.A. Laser Interaction and Related Plasma Phenomena. 3, ed. Schwarz H.J. and Hora H. (New York: Plenum, 1974).

7) Chase J.B., Le Blanc J.M. and Wilson J.R. Phys. Fluids 16, 1142-8, 1973.

8) Elton R.C. NRL report 6738, 1968.

9) Bleach R.D. and Nagel D.J. J. Appl. Phys. 49, 3832-41, 1978.

10) Carlson T.A., Nestor C.W., Wasserman N. and Mc Dowell J.D. Atomic Data 2, 63, 1970.

11) Pepin H., Grek B., Rheault I. and Nagel D.J. J. Appl. Phys. 48, 3312-16, 1977.

12) Nagel D.J., Burkhalter, Doschek, Dozier, Feldman, Klein, and Whitlock, NRL annual report 7838, 93, 1974.

13) Büchl K., Eidmann K., Mulser P., Salzmann H., Sigel R., Witkowski S. Fourth Conference on Plasma Physics and Controlled Nuclear Fusion Research, Madison, Wisconsin, USA, paper CN-D-11, June, 1971.

14) Beverly R.E. Phys. Lett. A, 44, 321-2, 1973.

15) Dyer P.E., James D.J., Ramsden S.A. and Skipper M.A. Appl. Phys. Lett. 24, 316-7, 1974.

16) Eidmann K., Sigel R. Laser Interactions and Related Plasma Phenomena, 3B, ed. Schwarz H. and Hora H. Plenum, New York, 677, 1974.

17) Donaldson T.P., Hubbard M. and Spalding I.J. Phys. Rev. Lett. 7, 1348-51, 1976.

18) Martineau J., Repoux S., Rabeau M., Nierat G. and Rostaing M.

Optics Commun. 12, 307-11, 1974.

19) Mitchell K.B., Stratton T.F. and Weiss P.B. Appl. Phys. Lett. 27, 11-13, 1975.

20) Ripin B.H. Appl. Phys. Lett. 30, 134-6, 1977.

21) Yamanaka C., Yokoyama M., Nakai S., Sasaki T., Yoshida K., Matoba M., Yamabe C., Yamanaka T., Mizui J., Yamaguchi N. and Nishikawa K. 5th IAEA Conference on Plasma Physics and Controlled Nuclear Fusion Research, Tokyo, 1974.

22) Private communication to Hughes T.P. University of Essex, 1975.

23) Marcus S., Lowder J.E. and Mooney D.L. J.Appl. Phys. 47, 2966-8, 1976.

24) Mc Kay J.A., Bleach R.D., Nagel D.J., Schriempf J.T., Hall R.B., Pond C.R. and Manlief S.K. J. Appl. Phys. 50, 3231-40, 1979.

25) Metz S.A., Hettche L.R., Stegman R.L. and Schriempf J.T. J. Appl. Phys. 46, 1634-42, 1975.

26) Mc Kay J.A. and Schriempf J.T. Appl. Phys. Lett. 33, 877, 1978.

27) Mc Kay J.A., Schriempf J.T., Cronburg T.L., Eninger J.E. and Woodroffe J.A. Appl. Phys. Lett. 36, 125-7, 1980.

28) Walters C.T., Barnes R.H. and Beverly R.E. III, J. Appl. Phys. 49, 2937-49, 1978.

29) Maher W.E., Nichols D.B. and Hall R.B. Appl. Phys. Lett. 37, 12-14, 1980.

30) Weyl G., Pirri A. and Root R. AIAA Paper 80-1319, Snowmass, CO, 1980.

31) Pirri A.N., Kemp N.H., Root R.G. and Wu P.K.S. PSI TR-89, Physical Sciences Inc., Woburn, MA, 1977.

32) Boni A., Su F.Y., Thomas P.D. and Musal H.M. SAI 77-77a 567-LJ, Science Application Inc., La Jolla, CA, 1977.

33) Pirri A.N. Phys. Fluids, 16, 1435-1440, 1973.

34) Nichols D.B. and Hall R.B. Paper VI-6, AIAA Conference on Fluid Dynamics of High Power Lasers, Cambridge, MA., 1978.

35) Maher W.E. and Hall R.B. Bull. APS, 24, 1003, 1979.

36) Holmes B.S. AFWL-TR-80-31, Kirtland Air Force Base, NM, 1979.

CHAPTER 8

CONCLUSION

8.1. Summary

Characteristics of plasmas, produced by a pulsed unstable-resonator HF laser, with a range of solid targets in a vacuum have been presented. For this laser, the critical plasma density ($n_{ec} \sim 10^{20} cm^{-3}$) is intermediate to that obtained using CO_2 and Nd:glass lasers, allowing plasma production to be investigated in a potentially interesting new regime. Measurements employing soft x-ray detectors, charge collector probes and high-speed photography, together with the results of specular reflectivity, have been reported for target irradiances in the range 10^8 - $10^{11} W.cm^{-2}$. Scaling laws for the interaction have been established and in general found to agree with established theories and other experimental work. However, lack of data at 2.8μm has necessitated frequent references to experiments carried out at other wavelengths. To aid comparison and to establish wavelength scaling data, a gain-switched TEA CO_2 laser was used to study the interaction by employing the same diagnostic techniques as with the HF laser. Using 60ns FWHM pulses and irradiances upto $1.2 \times 10^{11} W.cm^{-2}$, the existence of a high energy electron component in the plasma was noted, probably as a result of the onset of a laser driven instability such as the parametric decay instability.

The formation and propagation of laser supported detonation waves has been studied for various targets in a gaseous environment using high speed photography. Measurements on plasmotron threshold, thermal coupling, reflectance and transmission through a laser-induced gas-breakdown plasma have also been performed and the results compared with existing theories and data.

8.2. Other Important Plasma Diagnostics

Measurements have been obtained elsewhere using ion mass spectrometry[1-4], UV[2,5-10], optical[8,10-13] and x-ray spectroscopy

[2,5-8,14-18], interferometry[19-25], x-ray pin-hole[14,17,26,27] and zone-plate photography[27], impulse measurements[28,29] and thin-foil transmission[20,30-32]. These investigations have been used to characterize various plasmas in order to study the interaction mechanism. Only for the very high irradiance situation are neutron[33-37] and alpha[37] emission an important diagnostic.

8.3. Suggestions for Future Work

8.3.1. Vacuum interaction focal-spot size

The focal-spot dimension affects the hydrodynamic flow of the laser produced plasma. Plasma spread from very small areas resembles point source expansion. The resulting steep plasma density gradients in the under-dense region are likely to suppress instabilities[38]. Hot electrons rapidly escape from the very localized heating zone.

Donaldson et al[39] note apparent inconsistencies between the temperature and reflectivity measurements of several workers at 0.694, 1.06 and 10.6μm laser wavelengths. They point out, however, that the focal spot size is an important variable that should be considered. Using large focal spot diameters and 35ps 1.06μm laser pulses focused onto plane Perspex targets, they obtained temperature and reflectivity scaling at irradiances between 2×10^{11} and $2 \times 10^{14} W.cm^{-2}$. The reflectivity results were consistent with classical inverse bremsstrahlung absorption, and their one-dimensional code predictions of the coronal electron temperature. The x-ray emission results were interpreted as giving the temperature of the cooler overdense plasma (the emission from this region dominates because of its n_e^2 dependence). Donaldson et al conclude that their large-spot results are consistent with a plane isodensity surface interaction; small spot interactions are expected to involve curved surfaces, where both refraction losses and resonance absorption are significant.

Unfortunately, the scaling laws obtained here were limited by the size of the lasers to small spot areas. It is suggested that, as higher power lasers are now becoming available, the scaling laws at the HF and CO_2 laser wavelengths be measured as a function of spot size.

This should clarify the situation and aid direct comparison with other workers' results.

8.3.2. Extension of Data

In the interest of extending the available data on HF and DF laser interactions, it is advisable to extend the measurements carried out in this thesis and elsewhere. The diagnostic methods employed in section 8.2. can be utilized and the target irradiances extended into the non-linear regime. In order to understand more fully the conflict between atomic number and shell ionization energies in x-ray production, it would be valuable to investigate a wider range of target materials and surfaces. X-ray emission peaking with HF and DF radiation is expected to occur at irradiances an order of magnitude higher than employed here. Ion spectroscopic measurements, together with bond energies, are necessary to clarify the irregularities in the ion scaling reported here. For the gaseous environment, the effects of varying the background gas should be more fully investigated. It would also be instructive to measure thermal coupling as a function of target angle. Two processes are important for plasma ignition at a surface: thermionic emission from surface defects followed by inverse-bremsstrahlung absorption. These two stages depend upon the surface fluence and the radiant flux respectively. With microsecond CO_2 laser radiation in air, the flux criterion has been found to dominate even at oblique incidence [40]. This situation needs clarifying for HF radiation and other parameters such as pulse length, ambient gas and target.

8.4. Acknowledgments

It is with pleasure that the author acknowledges and thanks members of the Applied Physics department at the University of Hull. It is obviously impossible to mention all by name who contributed in encouragement or in useful discussions. Firstly, I should like to thank my supervisors, D.J.James, P.E.Dyer and S.A.Ramsden. Some of the CO_2 interaction experiments were carried out in conjunction with Dr. M.A. Skipper. The experience of working alongside Dr. Skipper proved

invaluable in subsequent investigations. The assistance of Drs. B. Deka and G.Salvetti in HF interaction studies is greatfully acknowledged. In addition, their continued encouragement and friendship cannot be adequately expressed in words. Technical help, although in very high demand, has been of high standard. Thanks are given to the mechanical, optical and electrical workshop personnel, especially remembering B. Tait and P.Monk of the Molecular Gas Laser Group.

The receipt of two years' financial support from the SRC is acknowledged.

I should like to thank many friends who have contributed in making my studies enjoyable. Finally, the continued encouragement and assistance from my parents and from my very tolerant wife is greatfully acknowledged.

8.5. References

1) Bykovskii Yu.A., Degtyarenko N.N., Elesin V.F., Kozyrev Yu.P. and Sil'nov S.M. Zh. Eksp. Teor. Fiz. 60, 1306-19, 1971. Transl: Sov. Phys. JETP, 33, 706-11, 1971.

2) Boland B.C., Irons F.E. and Mc.Whirter R.W.P. J. Phys. B: Atom. Molec. Phys. 1, 1180-91, 1968.

3) Faure C., Perez A., Tonon G., Aveneau B. and Parisot D. Phys. Lett. 34A, 313-4, 1971.

4) Tonon G., Perez A., Faure C., Parisot D. and Aveneau B. X International Conference on Phenomena in Ionized Gases, Oxford, 1971. Contributed Papers, 232.

5) Fawcett B.C., Gabriel A.H., Irons F.E., Peacock N.J., Saunders P.A.H. Proc. Phys. Soc. 88, 1051-3, 1966.

6) Khan M.A. PhD thesis, University of Hull, 1974.

7) Basov N.G., Boikov V.A., Voinov Yu.P., Kononov E.Yu., Mandel' shtam S.L., Sklizkov. Zh. ETF Pis'ma 6, no.9, 849-51, 1967. Transl: Sov. Phys. JETP Lett. 6, 291-3, 1967.

8) McCall G.H., Benjamin R.F., Giovanielli D.V., Godwin R.P., Kephart J.F., Kohler D.R. and Lieber A.J. Los Alamos report LA-UR-74-490 and VIII International Quantum Electronics Conference, San Francisco, California, 1974.

9) Ehler A.W. and Weissler G.L. Appl. Phys. Lett. 8, 89-91, 1966.

10) Seka W., Schwob J.L. and Breton C. J. Appl. Phys. 41, 3440-1, 1970.

11) Irons F.E., McWhirter R.W.P. and Peacock N.J. Culham report CLM-P268, 1971.

12) Irons F.E. J. Phys. B: Atom. Molec. Phys. 6, 1562-81, 1973.

13) Peacock N.J., Hobby M.G. and Galanti M. J. Phys. B: Atom. Molec. Phys. 6, L298-304, 1973.

14) Pepin H., Grek B., Rheault F. and Nagel D.J. J. Appl. Phys. 48, 3312-6, 1977.

15) Irons F.E. and Peacock N.J. J. Phys. E: Sci. Inst. 6, 857-62, 1973.

16) Galanti M. and Peacock N.J. Culham Laboratory Report CLM-P401.

17) Donaldson T.P., Hutcheon R.J. and Key M.H. J. Phys. B: Atom. Molec. Phys. 6, 1525-44, 1973.

18) Yaakobi B., Bristow T.C. and Hauer A. Optics Commun. 14, 336-8, 1975.

19) Büchl K. J. Appl. Phys. 43, 1032-37, 1972.

20) Pepin H., Dick K., Martineau J. and Parbhakar K. Phys. Lett. 38A, 203-4, 1971.

21) Bruce C.W., Deacon J. and Vonderhaar D.F. Appl. Phys. Lett. 9, 164-6, 1966.

22) David C.D., Avizonis P.V., Weichel H., Bruce C. and Pyatt K.D. IEEE J. Quant. Elect. QE-2, 493-9, 1966.

23) David C.D. Appl. Phys. Lett. 11, 394-6, 1967.

24) Hugenschmidt M. and Vollrath K. C.R. Acad. Sci. Paris, 272B, 36-9, 1971.

25) Basov N.G., Boiks V.A., Gribkov V.A., Zakharov S.M., Krokhin O.N. and Sklizkov G.V. Zh. Eksp. i Teor. Fiz. 61, 154-61, 1971. Trans: Sov. Phys. JETP, 34, 81-4, 1972.

26) Nagel D.J., Burkhalter P.G., Dozier C.M., Holzrichter J.F., Klein B.M., McMahon J.M., Stamper J.A. and Whitlock R.R. Phys. Rev. Lett., 33, 743-6, 1974.

27) Skipper M.A. PhD thesis, University of Hull, 1976.

28) Ehler A.W. J. Appl. Phys. 37, 4962-6, 1966.

29) Gregg D.W. and Thomas S.J. J. Appl. Phys. 37, 2787-9, 4313-6, 1966.

30) Linlor W.I. Appl. Phys. Lett. 3, 210-11, 1963.

31) Linlor W.I. Phys. Rev. Lett. 12, 383-5, 1964.

32) Fabre E. and Vasseur P. J. Physique 29, Suppl. C3, 123-7, 1968.

33) Young F.C. IEEE Transactions on Nuclear Science NS-22, 718-23, 1975.

34) Basov N.G., Boiko V.A., Zakharov S.M., Kroklin O.N. and Sklizkov G.V. Zh. Eksp. i Teor. Fiz. Pis'ma 13, 691-4, 1971. Transl: JETP Lett. 13, 489-91, 1971.

35) Mead S.W., Kidder R.E., Swain J.E., Ranier E., Petruzzi J. Appl. Opt. 11, 345-352, 1972.

36) Yamanaka C. Laser Interaction and Related Plasma Phenomena. ed. Schwarz H.J. and Hora H. 2, 481-502, New York, Plenum Press, 1972.

37) See the Los Alamos and Lawrence Livermore reports.

38) Pant H.C., Sharma S., Nathan T.P.S. and Desai T. Appl. Phys. 23, 183-7, 1980.

39) Donaldson T.P., Balmer J.E. and Zimmermann. J. Phys. D: Appl. Phys. 13, 1221-33, 1980.

40) McKay J.A., Schriempf J.T., Cronburg T.L., Eninger J.E. and Woodroffe J.A. Appl. Phys. Lett. 36, 125-7, 1980.